

ABSTRACT

Title of Dissertation: Advancements in Label-free Biosensing Using Field-Effect Transistors and Aided by Molecular Dynamics Simulations

Nicholas Bernhard Guros, Doctor of Philosophy, 2019

Dissertation directed by: Associate Professor, Associate Chair, and Graduate Program Director, Dr. Jeffery B. Klauda, Department of Chemical and Biomolecular Engineering

Adjunct Professor, Dr. Arvind Balijepalli, National Institute of Standards and Technology

Biosensors are used to characterize or measure concentrations of physiologically or pathologically significant biomarkers that indicate the health status of a patient, for example, a biomarker associated with a specific disease or cancer. Presently, there is a need to improve the capabilities of biosensors, which includes their rate of detection, limit of detection, and usability. With respect to usability, it is advantageous to develop biosensors that can detect a biomarker that is not labeled, such as with a conventional fluorescent, magnetic, or radioactive label, prior to characterization or measurement by that biosensor. Such biosensors are known as label-free biosensors and are the primary focus of this work. Biosensors are principally evaluated by two standards: their sensitivity to detect a target biomarker at physiologically relevant concentrations and their specificity to detect only the target biomarker in the presence of other molecules. The elements of biosensing critical to improving these two standards are:

biorecognition of the biomarker, immobilization of the biorecognition element on the biosensor, and transduction of biomarker biorecognition to a measurable signal.

Towards the improvement of sensitivity, electrostatically sensitive field-effect transistors (FET) were fabricated in a dual-gate configuration to enable label-free biosensing measurements with both high sensitivity and signal-to-noise ratio (SNR). This high performance, quantified with several metrics, was principally achieved by performing a novel annealing process that improved the quality of the FET's semiconducting channel. These FETs were gated with either a conventional oxide or an ionic liquid, the latter of which yielded quantum capacitance-limited devices. Both were used to measure the activity of the enzyme cyclin-dependent kinase 5 (Cdk5) indirectly through pH change, where the ionic-liquid gated FETs measured pH changes at a sensitivity of approximately 75 times higher than the conventional sensitivity limit for pH measurements. Lastly, these FETs were also used to detect the presence of the protein streptavidin through immobilization of a streptavidin-binding biomolecule, biotin, to the FET sensing surface.

To study the biomolecular factors that govern the specificity of biomarker biorecognition in label-free biosensing, molecular dynamics (MD) simulations were performed on several proteins. MD simulations were first performed on the serotonin receptor and ion channel, 5-HT_{3A}. These simulations, which were performed for an order of magnitude longer than any previous study, demonstrate the dynamic nature of serotonin (5-HT) binding with 5-HT_{3A}. These simulations also demonstrate the importance of using complex lipid membranes to immobilize 5-HT_{3A} for biosensing applications to adequately replicate native protein function. The importance of lipid composition was further demonstrated using MD simulations of the ion channel alpha-hemolysin (α HL). The results of these simulations clearly demonstrate the lipid-protein structure-function relationship that regulates the ionic current through a lipid membrane-spanning ion channel. Finally, to demonstrate the impact of MD simulations to inform the design of FET biosensing, a strategy to use FETs to measure the ultra-low ionic currents through the ion channel 5-HT_{3A} is outlined. This strategy leverages critical elements of 5-HT biorecognition and ion channel immobilization extracted from MD simulations for the design of the proposed FET sensing surface interface.

Advancements in Label-free Biosensing Using Field-Effect Transistors and Aided
by Molecular Dynamics Simulations

by

Nicholas Bernhard Guros

Dissertation submitted to the Faculty of the Graduate School of the
University of Maryland, College Park, in partial fulfillment
of the requirements for the degree of
Doctor of Philosophy
2019

Advisory Committee:
Professor Jeffery Klauda, Chair
Amy Karlsson
Srinivasa Raghavan
Arvind Balijepalli
John Cumings

© Copyright by
Nicholas B. Guros
2019

© Copyright of Chapter 2 by
Nicholas B. Guros, Son T. Le, Siyuan Zhang, Brent A. Sperling, Jeffery B. Klauda,
Curt A. Richter, and Arvind Balijepalli
2019

© Copyright of Chapter 3 by
Son T. Le, Nicholas B. Guros, Robert C. Bruce, Antonio Cardone, Niranjana D.
Amin, Siyuan Zhang, Jeffery B. Klauda, Harish C. Pant, Curt A. Richter, and
Arvind Balijepalli
2019

© Copyright of Chapter 4 by
Nicholas B. Guros, Arvind Balijepalli, and Jeffery B. Klauda
2019

© Copyright of Chapter 5 by
Nicholas B. Guros, Arvind Balijepalli, and Jeffery B. Klauda
2019

Dedication

This work is dedicated to the memory of my grandfather, Frank S. Guros, who worked for over 30 years as an electrical engineer developing numerous electronic devices including field-effect transistors. His passion for the pursuit of understanding and improving technology inspired numerous members of our family to pursue careers in engineering, myself included.

Acknowledgements

I thank my advisers, Dr. Jeffery Klauda and Dr. Arvind Balijepalli for their tireless support and counsel throughout my doctoral education. Their patience, encouragement, and passion as mentors allowed me to fully pursue my interests as a graduate student and has wholly prepared me for a career in science and engineering. I further thank Dr. Jeffery Klauda for his support in providing me with the opportunity to travel to numerous conferences to share my work and to develop my skills as an effective scientific communicator, as well as for his deep knowledge of molecular dynamics simulations. I also further thank Dr. Arvind Balijepalli for his enthusiasm and wide-ranging expertise as we worked side-by-side in the laboratory and nanofab at NIST troubleshooting a wide-range of issues on the multidisciplinary endeavor that is FET biosensor development.

I further thank my colleagues at the University of Maryland's department of Chemical and Biomolecular Engineering who supported me through every aspect of graduate student life ranging from technical to administrative to personal. I also thank my colleagues at NIST including the mentorship provided by Drs. Joey Robertson, Son Le, Curt Richter, Antonio Cardone, and Siyuan Zhang who were always available to discuss any aspect of my work they thought they could assist with.

Lastly, I would like to thank all my friends and family for their support and patience during this endeavor, especially my fiancé Kristina Shultz who supported me tirelessly while working full-time and simultaneously obtaining a master's degree in public health. I could not have achieved this dream without all of your support, thank you.

Grant Numbers: 70NANB18H028 and 70NANB15H023

Computational Resources:

XSEDE: Extreme Science and Engineering Discovery Environment (XSEDE) allocation on Stampede, Darter, and Comet (MCB-100139)

MARCC: Maryland Advanced Research Computing Center (MARCC), jointly managed by Johns Hopkins University and the University of Maryland, College Park.

Anton2: On loan to Carnegie Mellon University (CMU) from D. E. Shaw Research, LLC for use as outlined in grant number R01GM116961 from the National Institutes of Health to CMU through the Biomedical Applications Group at the Pittsburgh Supercomputing Center, by grant number PSCA18011P.

Deeptthought and Deeptthought2: Simulations and analysis were also performed on the high-performance computing cluster (HPCC) of the Division of Information Technology at the University of Maryland, College Park.

Table of Contents

Dedication	ii
Acknowledgements	iii
Table of Contents	ii
List of Tables	v
List of Figures	vi
List of Abbreviations	viii
Chapter 1: Introduction to Biosensing	1
1.1 Overview of Biosensing	1
1.2 The Elements of Biosensing	4
1.2.1 Transduction and Measurement	4
1.2.2 Biorecognition and Immobilization	10
1.3 Improving Performance of Field-Effect Transistors for Biosensing	15
1.3.1 Overview and Transition from Silicon to 2-Dimensional (2D) Materials	15
1.3.2 Design and Fabrication of MoS ₂ FETs	17
1.3.3 Application for FET Biosensing: Transduction and Measurement	17
1.4 Improving Field-Effect Transistor Biosensing using Molecular Dynamics	18
1.4.1 General Overview, Force Fields, and Ensembles	18
1.4.2 Application for FET Biosensing: Biorecognition and Immobilization	22
1.5 Overview of Dissertation	23
Chapter 2: Reproducible Performance Improvements to MoS ₂ FETs for Applications in Biosensing	25
2.1 Introduction	25
2.1.1 Motivation	25
2.1.2 Challenges with Existing MoS ₂ FET Fabrication	26
2.1.3 Novel Fabrication Approach	28
2.2 Materials and Methods	29
2.2.1 FET Fabrication	29
2.2.2 FET Electrical Performance Characterization	31
2.2.3 Additional FET Performance Characterization	32
2.3 Results and Discussion	33
2.3.1 Monolayer MoS ₂ Field-Effect Transistor Fabrication	33
2.3.2 Monolayer MoS ₂ Field-Effect Transistor Performance	36
2.3.3 Monolayer MoS ₂ Characterization with Raman Spectroscopy, XPS and AFM	47
2.4 Conclusion	51
Chapter 3: Comparison of Solid-State and Liquid-Gated MoS ₂ FET Biosensors for Label-Free Enzyme Measurements and Direct Detection of Proteins	54
3.1 Introduction	54
3.1.1 Motivation: FETs for Measurements of pH and Protein Detection	56
3.1.2 Background: Ion-Sensitive FETs (ISFET) as Biosensors and FETs for Streptavidin Detection	59

3.2 Materials and Methods.....	61
3.2.1 Fabrication of Dual-gated Ionic Liquid-gated Field-Effect Transistors (FETs) and Design Comparison to Solid-state FETs.....	61
3.2.2 Quantum Capacitance Model and Time-Series Measurements and PID Control.....	62
3.2.3 C-V Measurements of Ionic Liquid Gates	64
3.2.4 Kinase Measurement Reagents	65
3.2.5 Streptavidin Measurement Reagents.....	66
3.2.6 Cdk5 γ - ³² P-ATP Measurements.....	67
3.3 Results and Discussion	68
3.3.1 Comparison of Solid-state and Ionic Liquid-gated Field-Effect Transistor Performance	68
3.3.2 Constant Current Mode Operation, Sensitivity, SNR, and LOD	71
3.3.3 Ion Sensitive pH Measurements	75
3.3.4 Kinase Activity Measurements	79
3.3.5 Streptavidin Binding Measurements.....	84
3.4 Conclusions.....	88
Chapter 4: The Impact of Lipid Type on the Immobilization of the α -Hemolysin Ion Channel.....	90
4.1 Introduction.....	90
4.1.1 Motivation.....	91
4.1.2 Simulation Approach	92
4.2 Materials and Methods.....	94
4.2.1 System setup and MD simulation Protocol.....	94
4.2.2 Analysis Methods.....	96
4.3 Results and Discussion	98
4.3.1. Membrane Equilibration	98
4.3.2 Membrane and Protein Hydrophobic Matching	100
4.3.3 Ionic Current and Distribution.....	108
4.3.4 Cap Truncation Effects	111
4.4 Conclusion	114
Chapter 5: Modeling the Biorecognition and Activation of the 5-HT _{3A} Serotonin Receptor with Different Membrane Lipids	117
5.1 Introduction.....	117
5.1.1 Background and Motivation	118
5.1.2 Simulation Approach	120
5.2 Materials and Methods.....	122
5.2.1 Simulation Setup.....	122
5.2.2 Analysis Methods.....	125
5.3 Results and Discussion	127
5.3.1 Equilibration and Stability	128
5.3.2 Structural Overview	131
5.3.3 5-HT Binding Events	135
5.3.4 Domain Interactions.....	140
5.3.5 Impact of Lipid Type	145
5.4 Conclusion	149

5.5 Transition to Proposed FET Measurements of 5-HT _{3A}	154
Chapter 6: Conclusions and Outlook: Using FETs to Study Low-Conductance Ion Channels Leveraging Lessons Learned from MD Simulations.....	156
6.1 Conclusions.....	156
6.2 Outlook: Introduction.....	157
6.2.1 Background: Method for Ion Channel Characterization.....	157
6.3 Outlook: Experimental Outline for Ion Channel Characterization with FETs.....	159
6.3.1 Materials and Methods: Immobilization.....	159
6.3.2 Experimental Setup.....	162
6.3.3 Interpretation of Results and Specificity.....	162
6.4 Outlook: Conclusion	163
Appendices.....	165
Bibliography	191
Publications, Awards, and Presentations	210

List of Tables

Table 1 – Performance parameters for EM-FGA and control FETs

Table 2 – Simulation parameters for α HL simulations

Table 3 – Surface area per lipid and hydrophobic thickness for lipid membranes in α HL simulations

Table 4 – Radial differences in hydrophobic thickness for lipid membranes in α HL simulations

Table 5 – Simulation parameters for 5-HT_{3A} simulations

List of Figures

- Figure 1 – Schematic definition of biosensor sensitivity and resolution
- Figure 2 – Elements of biosensing and outline of chapter topics
- Figure 3 – Circuit diagram and schematic of field-effect transistor (FET)
- Figure 4 – Example $I_D V_G$ transfer curves and $I_D V_D$ curves
- Figure 5 – Schematic $I_D V_G$ example of FET sensing
- Figure 6 – FET biosensing using a proportional-integral-derivative (PID) controller
- Figure 7 – Biorecognition and immobilization on a FET sensing surface
- Figure 8 – Direct vs. indirect FET sensing
- Figure 9 – Bulk MoS_2 and atomic diagram of MoS_2 crystal structure
- Figure 10 – Example of periodic boundary conditions for a molecular dynamics (MD) simulation unit cell
- Figure 11 – MoS_2 characterization with Raman spectroscopy and MoS_2 FET schematic and image
- Figure 12 – Process flow diagram for FET fabrication and comparison of exposed-material forming gas annealed (EM-FGA) vs. control FETs
- Figure 13 – $I_D V_G$ transfer curves and $I_D V_D$ curves for EM-FGA vs. control FET back-gates
- Figure 14 – $I_D V_G$ transfer curves and $I_D V_D$ curves for EM-FGA vs. control FET top-gates
- Figure 15 – X-ray photoelectron spectroscopy (XPS) spectra for MoS_2 before and after EM-FGA
- Figure 16 – Atomic force microscopy (AFM) images for MoS_2 before and after EM-FGA
- Figure 17 – Schematics of cyclin dependent kinase 5 (Cdk5) hyperactivation and phosphorylation of histone
- Figure 18 – Crystal structures for monomer and tetramer streptavidin
- Figure 19 – Images and schematics of solid-state FETs (SSFETs) and ionic liquid-gated FETs (LGFETs)
- Figure 20 – $I_D V_G$ transfer curves and α plots for dual-gated SSFET and LGFET operation
- Figure 21 – Diagram of FET as capacitances in series and α -threshold voltage relationship
- Figure 22 – Constant current mode operation and associated figures for α and SNR
- Figure 23 – Static pH measurements using an LGFET
- Figure 24 – Comparison of PID controlled pH measurements for SSFETs and LGFETs
- Figure 25 – Comparison of power spectral densities and SNR vs. pH for SSFETs and LGFETs
- Figure 26 – Comparison of Cdk5 activity obtained using radioactively labeled ATP, SSFETs, and LGFETs
- Figure 27 – Comparison of time series measurements of Cdk5 activity for SSFETs and LGFETs
- Figure 28 – Streptavidin binding measurements using a LGFET
- Figure 29 – Diagram of α HL and comparison of DPhPC and POPC molecular structures
- Figure 30 – Schematic of the hydrophobic accessibility of α HL and hydrophobic matching by lipid membranes
- Figure 31 – Representative cross-section snapshots of α HL *trans* entrance in DPhPC and POPC
- Figure 32 – α HL average channel radius profiles
- Figure 33 – Time series measurements of α HL ionic current and ionic distributions in the channel
- Figure 34 – Schematic of the hydrophobic accessibility of truncated α HL and hydrophobic matching by lipid membranes
- Figure 35 – Diagram of 5-HT_{3A} and comparison of POPC, SDPC, CHOL molecular structures
- Figure 36 – RMSD for the four 5-HT_{3A} simulation systems
- Figure 37 – Key 5-HT_{3A} simulation results and evidence of channel pre-activation

- Figure 38 – 5-HT_{3A} binding events including enthalpic contribution to binding energy and binding orientations
- Figure 39 – 5-HT_{3A} secondary structure shifts during pre-activation
- Figure 40 – 5-HT_{3A} secondary structure stabilization interactions
- Figure 41 – Comparison of lipid distribution for 5-HT_{3A} in varied membrane lipid type
- Figure 42 – Simplified diagram of the electrophysiological patch-clamp technique
- Figure 43 – Diagram of an example tethered-lipid membrane
- Figure 44 – Experimental set-up for characterization of an ion channel with a FET

List of Abbreviations

2D	2-dimensional	NPT	Isobaric-isothermal ensemble
5-HT	5-hydroxytryptamine (serotonin)	NVT	Isochoric -isothermal ensemble
5-HT _{3A}	5-hydroxytryptamine 3A serotonin receptor	p25	Pathogenic Cdk5 activator
ADP	Adenosine diphosphate	p35	Native Cdk5 activator
AFM	Atomic force microscopy	PBC	Periodic boundary conditions
ALD	Atomic layer deposition	PBS	Phosphate-buffered saline
ATP	Adenosine triphosphate	PID	Proportional-integral-derivative
BG	Back-gate	pLGIC	Pentameric ligand-gated ion channel
bp	Binding pocket	pM	Picomolar
BSA	Bovine serum albumin	POPC	1-palmitoyl-2-oleoyl-sn-glycero-3-phospho-choline
C36	CHARMM 36 force field	PUFA	Polyunsaturated fatty acid
C _{BG}	Back-gate capacitance	R _c	Contact resistance
Cdk5	Cyclin-dependent kinase 5	RMS	Root-mean-square
CHOL	Cholesterol	RMSD	Root-mean-square deviation
CMOS	Complementary metal oxide semiconductor	SA/lipid	Surface area per lipid
C _{TG}	Top-gate capacitance	SAM	Self-assembled monolayer
CVD	Chemical vapor deposition	SDPC	Polyunsaturated 1-stearoyl-2-docosahexaenoyl-sn-glycerol-3-phosphocholine
DI	Distilled	SiO ₂	Silicon dioxide
DPhPC	1,2-diphytanoyl-sn-glycero-3-phospho-choline	SNR	Signal-to-noise ratio
ECD	Extracellular domain	SSFET	Solid-state field-effect transistor
EM-FGA	Exposed-material forming gas anneal	TG	Top-gate
FEP	Free energy perturbation	TLM	Tethered-lipid membrane
FET	Field-effect transistor	TMD	Transition metal dichalcogenide
FGA	Forming gas anneal	TMD	Transmembrane domain
g _m	Transconductance	V _{BG}	Back-gate voltage
I _{DS}	Channel current	V _{DS}	Drain voltage
ISFET	Ion-sensitive field-effect transistor	V _{dW}	van der Waals
IUPAC	International Union of Pure and Applied Chemistry	V _{FB}	Flatband voltage
I-V	Current-voltage	V _o	Offset voltage
LG	Ionic liquid-gate	V _T	Threshold voltage
LGFET	Ionic liquid-gated field-effect transistor	V _{TG}	Top-gate voltage
LOD	Limit of detection	WS ₂	Tungsten disulfide
MD	Molecular dynamics	WSe ₂	Tungsten diselenide
MoO _x	Molybdenum oxide	XPS	X-ray photoelectron spectroscopy
MoS ₂	Molybdenum disulfide	α	Amplification
NAMD	Nanoscale molecular dynamics	αHL	α-hemolysin
nM	Nanomolar	λ _D	Debye length
NPAT	Isobaric-isothermal constant area ensemble	μFE	Field-effect mobility
		ψ _o	Surface potential

Chapter 1: Introduction to Biosensing

1.1 Overview of Biosensing

A biosensor is defined by the International Union of Pure and Applied Chemistry (IUPAC) as “a device that uses specific biochemical reactions mediated by isolated enzymes, immunosystems, tissues, organelles or whole cells to detect chemical compounds usually by electrical, thermal or optical signals”.¹ In other words, a biosensor is a tool that quantifies biological phenomena to provide information useful for the assessment of the health, status, or condition of a biological system. Every biosensor is designed to detect the presence of a specific biomolecule, known as a biomarker, that is independently identified as a representative indicator of health.¹ For example, in a clinical setting biosensors are used to detect the presence of a protein or DNA sequence associated with a given disease or cancer.²⁻³ Environmentally, biosensors are used to detect toxins in water or food samples or measure quantities like pH or osmolality, which are indirect measurements of sample healthy and quality.⁴⁻⁵

Label-free biosensors are a subset of biosensors that do not require the chemical labeling of a biomarker prior to its detection.⁶⁻⁸ Many biosensing assays require the labeling of biomarkers with either fluorescent,⁹ radioactive,¹⁰⁻¹¹ or magnetic labels¹² that permit the biomarker to be detected through an appropriate transduction mechanism, such as through optical intensity in the example of fluorescent labeling; however, labeling requires specialization in label handling and adherence to a biomarker, can be expensive and/or hazardous, such as in the case of radioactive labels,

and generally results in requiring more time and effort to perform a biosensing measurement. Moreover, the conformation of a biomarker, such as a protein, can be affected by the addition of a label, which can lead to the detection or characterization of a biomarker in a non-native state. Alternatively, label-free biosensors directly detect biomarkers and are not inhibited by the disadvantages of labeling. In this way, label-free biosensors provide a superior platform for biomarker detection; however, the replacement of conventional biosensors with label-free biosensors necessitates improvements to the performance, fabrication, and ease of use of label-free biosensors.

Biosensor performance is principally evaluated by two standards: sensitivity and specificity.¹ The sensitivity of a biosensor is measured as a response, i.e., a magnitude of signal change as a function of biomarker concentration or a change in a property associated with biomarker concentration (Figure 1). For example, a change in pH is caused from the evolution of a proton during hydrolysis of adenosine triphosphate (ATP) to adenosine diphosphate (ADP) during phosphorylation by a kinase, where the magnitude of pH change increases with increasing kinase concentration.¹³ Sensitivity is important because biomarker concentration indicative of disease may be extremely low, i.e., in the nanomolar (nM) or even picomolar (pM) range, which requires an exquisitely sensitive biosensor to detect. The specificity of a biosensor is its ability to detect a target biomarker and only that biomarker, i.e., adequate specificity is achieved when a false positive signal is not generated from the presence of other biomolecules similar to the biomarker. To demonstrate adequate specificity, control experiments that are intended to yield no response from the biosensor are performed with a sample composition otherwise identical to a sample of interest but without the

target biomarker.¹⁴ In short, specificity can be quantified through a signal of interest that is nominally greater than that obtained from a control experiment. In this way, the reporting of false positives can be mitigated which avoids erroneous conclusions such as the incorrect diagnosis of a disease.

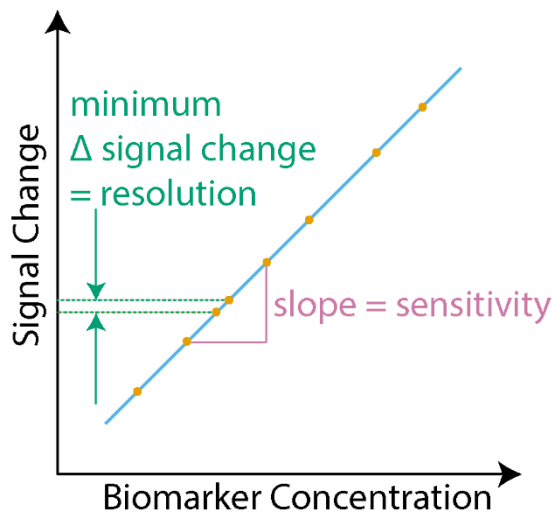


Figure 1. Schematic definition of biosensor sensitivity (*pink*) and resolution (*green*). Example data points colored *orange* and example linear regression best-fit line colored *light blue*.

Additional standards by which biosensor performance is evaluated include resolution, repeatability, and throughput.¹⁵ Resolution is a performance metric and is defined as the smallest signal change that can be discerned from two different concentrations of biomarker (Figure 1).¹ Repeatability, i.e., the ability of a biosensor to reproduce the same result over several measurements, is also an important performance metric and can be quantified through the standard error of a sample of measurements under identical conditions. Throughput is the speed at which a biosensor can detect a biomarker and can be critical for rapid diagnosis of a disease. All these considerations will be addressed throughout this work for charge sensitive electrical devices known as field-effect transistors (FETs), which were used as biosensors for this work.

1.2 The Elements of Biosensing

Biosensing is composed of four elements: biorecognition, immobilization, transduction, and measurement. The four elements have an interdependent relationship, as depicted in Figure 2.¹⁵ Figure 2 also serves as a diagram demonstrating which elements were principally developed with either Molecular Dynamics (MD) simulations or FET biosensing, where each is covered in individual chapters of this work, although their interdependence necessitates discussion of connected elements in context with the primary element discussed.

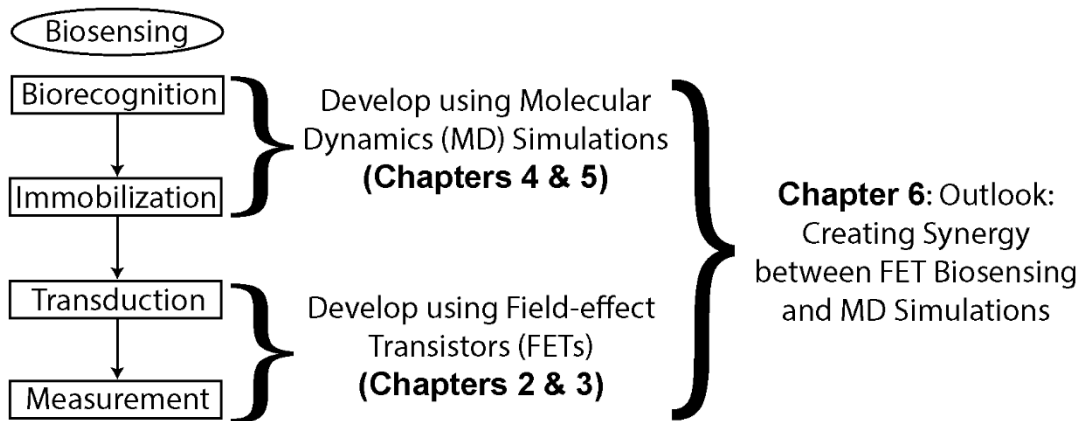


Figure 2. The four elements of biosensing (biorecognition, immobilization, transduction, and measurement) with the corresponding chapters where the improvement of each element is primarily discussed.

1.2.1 Transduction and Measurement

Transduction and measurement in this work were realized primarily with a FET. A FET is a three or four terminal electrical device. A potential is first applied between two terminals at the ends of a semiconducting channel, known as the source (*S*) and the drain (*D*) terminals, which creates an electrical current through the channel. Then, a potential is applied to one or more of the other terminals which are separated from the channel by a dielectric oxide and are known as gate (*G*) terminals. Gate terminals are

used to modulate, i.e., gate, the electrical current through the channel *via* the field-effect (Figure 3).¹⁶ In other words, the application of a voltage (V_{DS}) to the drain terminal produces a current (I_{DS}) through the semiconducting channel to the source terminal which is regulated *via* the field-effect through the application of a voltage (V_{TG}) or (V_{BG}) to a gate terminal. These gate terminals, top-gate (TG) and back-gate (BG), are named in this work for their orientation on top of or under the semiconducting channel.

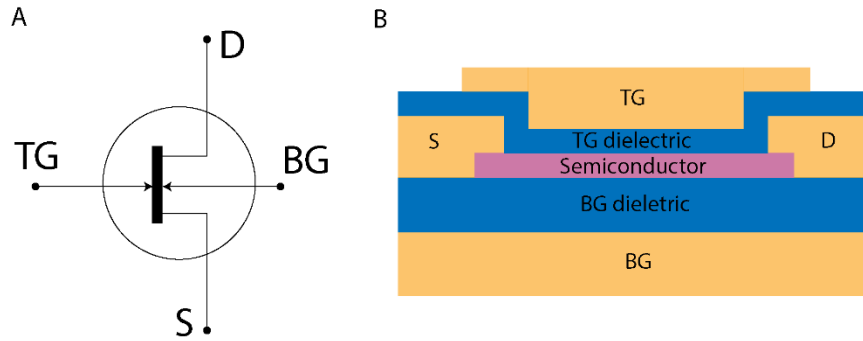


Figure 3. (A) Circuit diagram of a field-effect transistor (FET) denoting the source (S), drain (D), top-gate (TG), and back-gate (BG) terminals. (B) Schematic of a FET with the same terminal denotation (*orange*) and denotation of the gate dielectrics (*blue*) and semiconducting channel (*pink*). The schematic shown is not to scale.

Semiconducting channels can be *n-type* or *p-type* depending on their material properties.¹⁶ In *n-type* channels, the majority charge carriers are electrons as opposed to *p-type* channels where the majority charge carriers are holes. In solid state physics, a hole is defined as a vacancy, formed by an atom accepting an electron from elsewhere in a crystal lattice, that can move across the lattice as if it were positively charged.

The response of a FET semiconducting channel to a gate voltage is described through current–voltage (I - V) characteristics and is depicted using $I_{DS}V_G$ transfer

curves and $I_{DS}V_{DS}$ curves,¹⁶ examples of which are shown in for an *n-type* FET in Figure 4a (logarithmic $I_{DS}V_G$), Figure 4b (linear $I_{DS}V_G$), and Figure 4c (linear $I_{DS}V_{DS}$) where V_G represents either a top-gate or back-gate potential. I - V characteristics are divided into four regions: subthreshold, quadratic, linear, and saturation (Figures 4a and 4b).¹⁶ The subthreshold region, quadratic region, and linear region are respectively defined as where I_{DS} increases exponentially, quadratically, or linearly with the application of a gate voltage. The saturation region is defined as where I_{DS} no longer increases with the application of a gate voltage, i.e., the semiconducting channel is saturated with charge carriers. The transition between subthreshold and quadratic/linear regions occurs at the application of a gate voltage known as the threshold voltage (V_T) and is defined as the gate voltage at which an inversion of charge carriers occurs, resulting in the formation of a stable, conductive channel.¹⁶ The importance of these regions in FET operation for biosensing is described further in *Chapters 2 and 3*.

There are several other important definitions necessary to characterize FET performance. Drive current (I_{on}) is the maximum current permitted through the semiconducting channel and is related to the strength of signal obtainable for FET measurements. Related to I_{on} is the transconductance (g_m), defined as $\frac{\partial I}{\partial V}$, where the maximum g_m is used to obtain the field-effect mobility (μ_{FE}), which is a measurement of how quickly electrons can move through a semiconductor channel and also defines the strength of signal obtainable. Also important is the switching ratio (I_{on}/I_{off}), which defines the operational range over which a FET can be turned on and off, and subthreshold slope (more commonly reported as its inverse, subthreshold swing), which defines how quickly a FET switches from off to on.

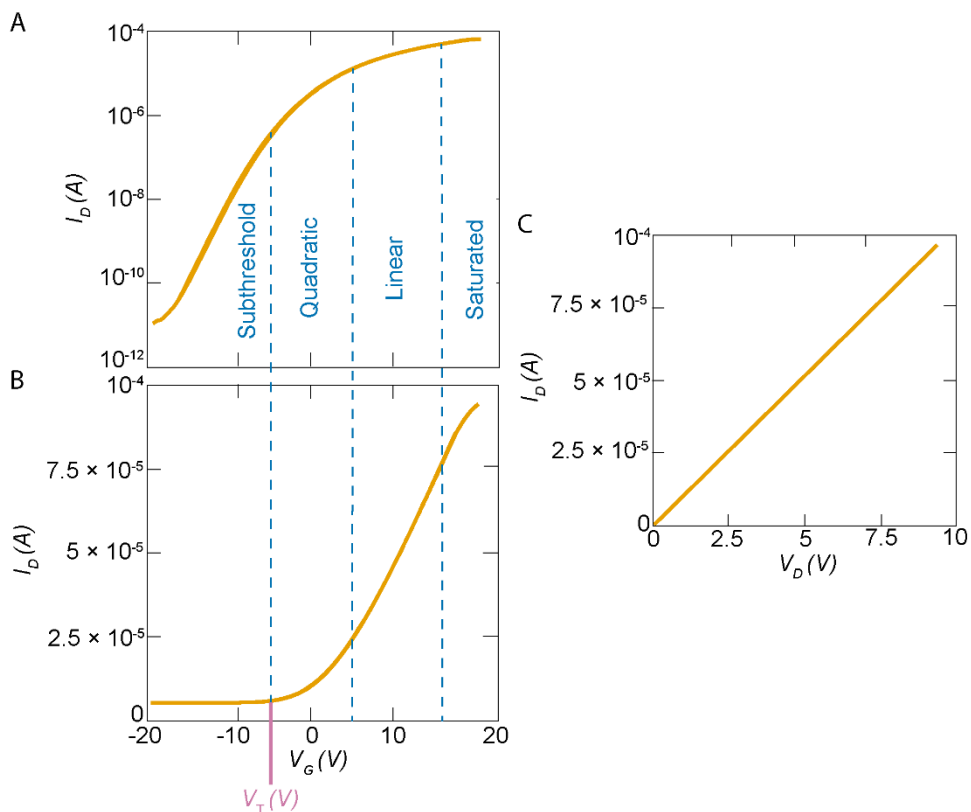


Figure 4. Example logarithmic (a) and linear (b) drain current-gate voltage ($I_D V_G$) relationships (orange) for a field-effect transistor (FET) denoting regimes of FET electrical behavior (blue) and threshold voltage (pink). (c) Example drain current-drain voltage ($I_D V_D$) relationship (orange) for the sample FET.

Transduction is the mechanism by which biorecognition is converted into a measurable signal.¹⁵ For conventional FET biosensors, biorecognition of a biomarker at one of the gate terminals must yield a sufficient change in electrostatic potential, proportional to biomarker charge and distance from the semiconducting channel, at the sensing gate. Charge from the biomolecules then modulates I_{DS} (by a value of ΔI_{DS}) analogous to applying an electrical potential to one of these terminals.

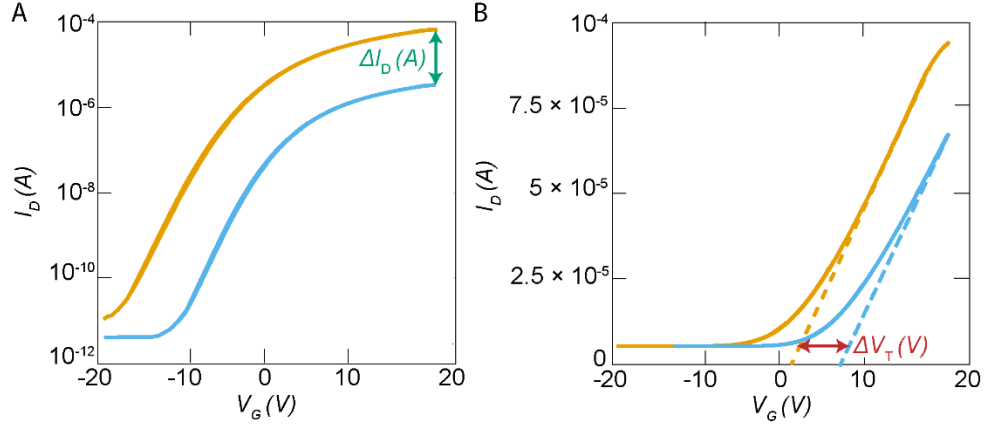


Figure 5. (a) Example logarithmic drain current-gate voltage ($I_D V_G$) relationships for a field-effect transistor (FET) before (*orange*) and after (*light blue*) the addition of a negative electrostatic potential on the gate sensing surface demonstrating a change (*green*) in drain current (I_D) at a given gate voltage (V_G). (b) Example linear drain current-gate voltage ($I_D V_G$) relationships for a FET before (*orange*) and after (*light blue*) the addition of a negative electrostatic potential on the gate sensing surface demonstrating a change (*red*) in threshold voltage (V_T).

Measurement is the mechanism by which a signal is acquired from transduction.¹⁵

For FET biosensors, this signal is conventionally quantified either in units of ΔI_{DS} or ΔV_T (Figure 5), where ΔV_T quantifies how the application of a potential to a gate terminal from biorecognition changes the gate voltage at which the FET switches on or off. The point of greatest charge sensitivity for a FET occurs at $g_{m,max}$,¹⁷⁻¹⁸ i.e., where $\frac{\partial I}{\partial V} = 0$, which is most readily discernable as the inflection point near 15 V in Figure 5B. Therefore, it is advantageous to operate a FET near this point by offsetting V_G by a voltage V_o so that a change in ΔV_G from biomarker binding yields the greatest possible ΔI_{DS} or ΔV_T . It is further advantageous to continually operate a FET biosensor at or near this point using a proportional-integral-derivative (PID) controller that applies a compensating potential to maintain I_{DS} at this point. This is shown in Figure 6, where the sensing surface is connected to the top-gate (TG) and a back-gate (BG) potential is applied to maintain constant I_{DS} . This is known as operating a FET in constant-current

mode and is only possible with dual-gated FETs where the semiconducting channel current can be regulated by both gates simultaneously. In constant current mode, ΔV_{BG} is reported instead of ΔI_{DS} or ΔV_T , i.e., the magnitude of potential needed to maintain a constant current through the semiconducting channel.

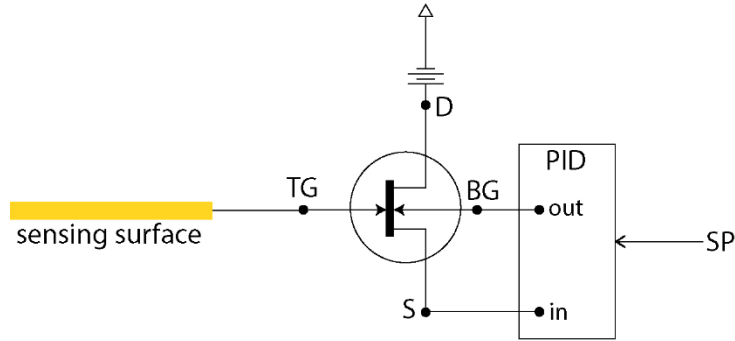


Figure 6. A proportional-integral-derivative (PID) controller can be used to operate a dual-gated field-effect transistor (FET) in constant-current mode, where a back-gate potential (V_{BG}) is applied to compensate for a biological top-gate potential (V_{TG}) applied to the sensing surface

The dual-gate design is also advantageous because a potential applied to one gate is amplified through capacitive coupling intrinsic to the capacitances of the gate oxides onto the other gate, where this amplification (α) is equivalent to the ratio of these capacitances for traditional gates with solid oxides with constant dielectric constants:

$$\alpha = \frac{C_{TG}}{C_{BG}} \quad (1)$$

where C_{TG} is the top-gate oxide capacitance and C_{BG} is the back-gate oxide capacitance. This relationship can be verified via experiment, as described in *Chapter 3*. In other words, the measured potential ΔV_{TG} is amplified by α such that the reported signal ΔV_{BG} becomes:

$$\Delta V_{BG} = \alpha \Delta V_{TG} \quad (2)$$

This amplification is discussed further in *Chapter 3*, where the advantages of using dual-gated monolayer MoS₂ FETs over traditional silicon FETs for biosensing is further discussed.

1.2.2 Biorecognition and Immobilization.

While the sensitivity of FETs permits the measurement of biomarkers at concentrations as low as nanomolar (nM) or even picomolar (pM), FETs alone do not indicate what biomolecule generates a measurable signal. In other words, FETs alone do not provide specificity for a given biomarker. To reconcile this, the sensing gate is functionalized with a biomolecule that has known affinity for a given biomarker, known as the biorecognition element.^{14, 19} Examples of biorecognition elements include an antibody (for a protein), a protein (for a ligand), or single-stranded DNA (for the complimentary single-stranded sequence) that are selected based on their nature to bind specifically to a given biomarker. Affinity for only the target biomarker is an essential feature of the biorecognition element in order to avoid non-specific binding of other biomolecules in a sample that could generate a false-positive result.

Proper immobilization of the biorecognition element is also critical for effective transduction and biorecognition.¹⁵ In FET biosensing, the biorecognition element is immobilized onto the sensing gate so that the change in surface potential ($\Delta\psi$) on the sensing gate is a function of the electrostatic charges of biorecognition element (q_o) and the bound biomarker (q) and not that of other biomolecules in the solution.⁸ The most simple way to define the relationship between $\Delta\psi$ and Δq (where $\Delta q = q - q_o$) is to model the gate oxide surface as a parallel plate capacitor with capacitance C :

$$\Delta\psi_o = \frac{\Delta q}{c} \quad (3)$$

However, because the biomarker is contained in an aqueous electrolyte solution (to hydrate and stabilize the biomarker), the effective charge of the biomarker is reduced due to charge screening. This relationship is best described by the Debye-Hückel model²⁰ which defines a length scale, relative to the position of the biomarker, known as the Debye Length (λ_D) over which the electrostatic potential of the molecule is not screened by ions:

$$\lambda_D = \sqrt{\frac{\epsilon_o \epsilon_r k_B T}{2 N_A e^2 I}} \quad (4)$$

where ϵ_o is the permittivity of free space, ϵ_r is the permittivity of aqueous solution, k_B is the Boltzmann constant, T is the absolute temperature, N_A is the Avogadro number, e is the elementary charge, and I is the ionic strength of the solution. For an aqueous solution at room temperature, $\lambda_D \propto \sqrt{1/I}$, where I is the parameter that defines the value of λ_D for a given experimental setup.

The Debye-Hückel model then defines the relationship between unscreened change in surface potential $\Delta\psi_o$ and the effective change in surface potential ($\Delta\psi_r$) as a function of the radial distance from the surface (r) as²⁰

$$\Delta\psi_r = \Delta\psi_o e^{-\frac{r}{\lambda_D}} \quad (5)$$

In other words, for a radial distance equal to one Debye length, the surface potential is screened by a factor of 1/e. Therefore, it is paramount in direct FET biosensing that the immobilization element allows for biomarker binding to occur within a Debye length of the surface. However, within the scope of the work, the Debye-Hückel model

only provides an approximation for the total surface potential created from a given concentration of biomarker and cannot be used to determine the exact number of biomarkers bound which requires an approximation of the surface coverage of the biorecognition elements and the assumption that these elements are rigid and in a fixed orientation, whereas practically they are highly flexible, yielding a radial distance r that is dynamic over a nominal range (Figure 7).

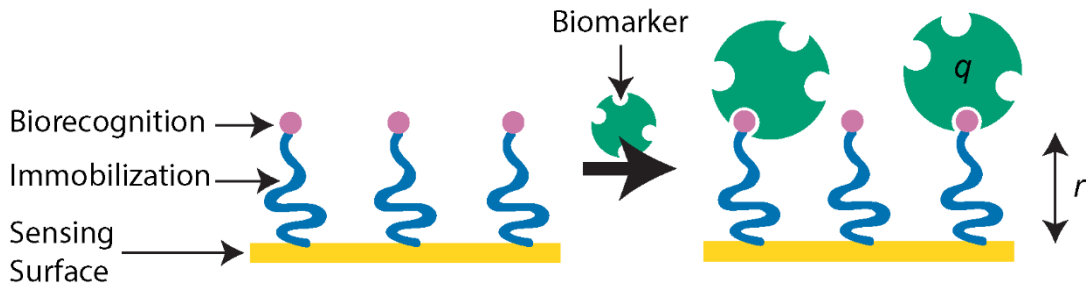


Figure 7. (left) A biorecognition element (*pink*) known to bind to a given biomarker (*green*) of charge q is adhered to the field-effect transistor (FET) sensing surface (*gold*) using an immobilization element (*blue*) at a distance r . The effective surface potential of a bound biomarker is defined using the Debye-Hückel Model (equations 4 and 5).

For more complex biorecognition elements, such as transmembrane proteins, the choice of biomolecules used to immobilize the transmembrane protein, namely membrane-forming lipids, is essential¹⁵ because these lipids have been demonstrated to directly impact the structure and function of a transmembrane protein, including the proclivity of that protein to bind to a given biomarker.²¹ It is also critical that the entire sensing surface is functionalized with either the immobilization element or a secondary surface-passivating biomolecule that does not interact with any of the biomolecules in the sample to mitigate non-specific interactions with the sensing surface.⁸ Passivation can also increase spacing between biorecognition elements to avoid their self-interactions and increase the accessibility of the biorecognition element to biomarkers in solution.

An advantage of FET biosensing is that the biorecognition element does not have to be directly immobilized on the sensing gate.¹⁴ A functionalized surface that is electrically connected to the sensing gate will still permit transduction of biomarker recognition to a measurable signal because the surface is an extension of the same electrical potential plane and is known as an extended gate. Extended gates permit remote sensing, which is advantageous because it bifurcates the measurement components, i.e., the FET and the sensing surface, where the FET is reusable between experiments of different conditions and the biorecognition containing surface, which is generally replaced between experiments, e.g., when biomarker concentration is varied to generate a dose-response curve.

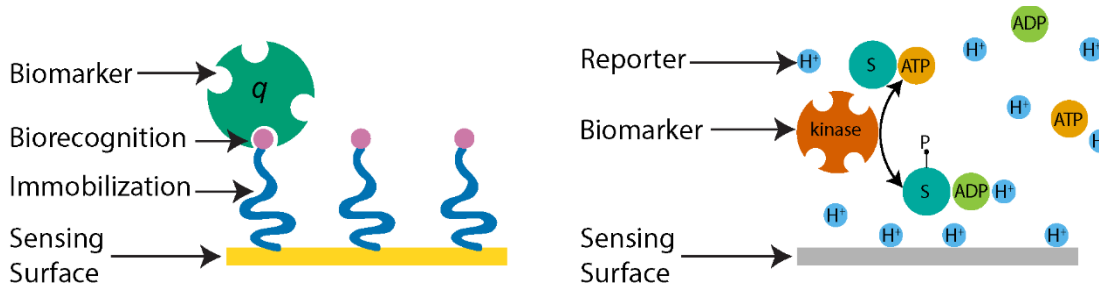


Figure 8. (a) A direct biosensor with a surface functionalized with a biorecognition element (*blue*) for field-effect transistor (FET) biosensing. (b) An indirect biosensor with a bare surface susceptible to sensing protons (H^+ , *light blue*), i.e., an ion-sensitive FET (ISFET), that are evolved from the hydrolysis of ATP by a kinase (*dark orange*).

Lastly, FETs that are sensitive to ions in an aqueous solution, so-called ion-sensitive FETs (ISFET),²² can serve as indirect biosensors.²³ ISFETs are similar to conventional biosensing FETs, but in ISFETs, the sensing gate is directly connected to both an ion sensitive surface and a reference electrode in solution.²² In this way, all interactions between ions and charged molecules are measured, as opposed to conventional FET biosensing where the surface is functionalized with a biorecognition

element and otherwise passivated to avoid direct interactions between charged molecules and the sensing surface (Figure 8).

The advantage of using ISFETs for biosensing is that biological information such as kinase activity or ion channel conductance can be determined indirectly through a reporter. For example, kinases are a type of enzyme that catalyze the transfer of a phosphate group from ATP to a substrate yielding ADP and a proton from the hydrolysis of ATP.²⁴ The rate of proton evolution from this phosphorylation, i.e., change in pH over time, is detectable by an ISFET through proton interaction with the sensing surface and can serve as an indirect measurement of kinase activity.²³ In this case, the biomarker is cyclin-dependent kinase 5 (Cdk5) activity as opposed to just Cdk5 concentration, and protons are a reporter rather than the biomarker themselves. Results from using this approach to quantify the activity of Cdk5 are presented in *Chapter 3* of this work.

The conductance of ion channels, a class of transmembrane proteins that regulate the flow of ions across lipid membranes, can be measured by immobilizing the ion channel in a lipid membrane above the sensing surface by a distance r using either a tethered-lipid membrane (TLM) or a nanodisc.²⁵ The lipid membrane restricts the number of ions interacting with the sensing surface over this distance r because ions can only reach the surface after passing through a channel that spans the membrane. A more detailed explanation of this proposed method to use ISFETs to measure ion channel conductance is presented in *Chapter 6*, and leverages FET biosensing techniques presented in Chapter 3 and conclusions regarding the immobilization of ion channels determined through MD simulations presented in *Chapters 4* and *5*.

1.3 Improving Performance of Field-Effect Transistors for Biosensing

1.3.1 Overview and Transition from Silicon to 2-Dimensional (2D) Materials

The first practical FETs were developed at Bell Labs by William Shockley in 1947²⁶. Since then, FET fabrication has been developed through the complementary metal oxide semiconductor (CMOS) process resulting in their use as the primary component of the modern integrated circuit in computers²⁷. Other common applications of FETs are as operational amplifiers²⁸, analog switches²⁹, choppers³⁰, current limiters³¹, and phase shift oscillators³². Since the early-2000s, the electrostatic sensitivity of FETs has been used for direct biosensing by numerous efforts, while ISFETs have been used since 1970 for indirect biosensing through measuring changes in solution pH including measurements of intravascular pH.²²

Until the mid-2000s, the primary semiconducting material used to fabricate FETs was silicon due to its electrical performance, ability to form good interfaces with dielectric oxides, and fabrication convention which was developed over the previous 50 years.¹⁶ In the mid-2000s, the electrical properties of 2-dimensional (2D) materials began to be explored, starting with graphene, i.e., a 2D hexagonal lattice of carbon atoms.³³⁻³⁵ Graphene has been proposed as a novel material that could revolutionize the field of nanoelectronics because of its impressive properties, which include high electron mobilities and mechanical strength.³³⁻³⁵ However, while promising for some applications, graphene does not have a direct bandgap and therefore does not act like a true semiconductor with switching behavior.³⁶⁻³⁷ In other words, an applied gate potential does not significantly regulate the channel current I_{DS} . Therefore, a potential applied to a sensing surface from a biomarker will not cause a discernable change in I_{DS} , which prohibits graphene FETs from being used as biosensors in their present state.

However, the development of graphene as a novel material for nanoelectronics spurred exploration into the semiconducting properties of other 2D materials known as transition metal dichalcogenides (TMD).^{36, 38-39} TMDs are crystalline structures composed of repeating motifs of MX_2 , where M is a transition metal atom and X is a chalcogenide atom, i.e., an atom belonging to group 16 of the periodic table (Figure 9).⁴⁰ Popular TMDs for nanoelectronics applications include sulfides, selenides, and tellurides, including molybdenum disulfide (MoS_2), tungsten disulfide (WS_2), and tungsten diselenide (WSe_2).⁴¹⁻⁴² In their bulk form, TMDs serve as excellent commercial lubricants where high temperature process conditions make water or aqueous lubricants not feasible.⁴³ However, when exfoliated to a monolayer of several layers, TMDs demonstrate advantageous electrical properties as presented in *Section 1.2.1*. These electrical properties provide an alternative to exceed the theoretical limitations of Moore's Law for silicon FETs that,⁴⁴ at peak miniaturization, demonstrate issues with power consumption, heat dissipation, gate-oxide leakage, electron mobility, and high signal-to-noise ratio (SNR).^{36, 38-40, 45}

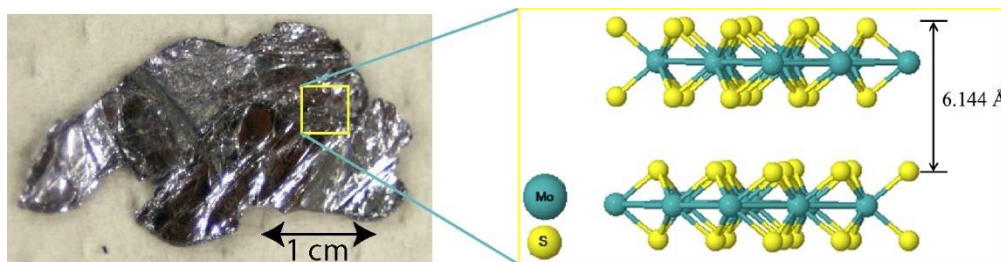


Figure 9. (left) Bulk molybdenum disulfide (MoS_2)* appears silver-gray in bulk form. (right) A single monolayer of MoS_2 ** is composed of repeating pattern of one Mo atom (green) for every two S atoms (yellow). *Figure from <https://www.mos2-info.com/mos2-mineral.jpg>. **Figure from [https://www.azonano.com/images/3605\(1\).jpg](https://www.azonano.com/images/3605(1).jpg).

1.3.2 Design and Fabrication of MoS₂ FETs

Over the past decade, rapid growth in the development of TMD FETs has demonstrated their promise as alternatives to silicon FETs. However, there are still significant challenges in the design and fabrication of TMD FETs which hinder their practical use for applications including biosensing. These challenges include the ability to produce large quantities of TMD FETs that demonstrate reproducible performance which is essential for performing conclusive biosensing experiments.⁴⁶⁻⁵⁰ *Chapter 2* of this work presents a novel method for the fabrication of monolayer MoS₂ FETs with reproducible performance which permitted the fabrication of a sufficient number of FETs to perform numerous biosensing measurements.

1.3.3 Application for FET Biosensing: Transduction and Measurement

While *Chapter 2* of this work focuses strictly on FET fabrication using MoS₂, the application of FETs for biosensing is presented in *Chapter 3*, including the use of MoS₂ FETs as ISFETs for ultra-sensitive pH measurements that serve as a proxy for Cdk5 activity and the use of FETs to detect the binding of streptavidin. Specifically, this work presents novel methods for the design of MoS₂ FETs including top-gating the FETs with an ionic liquid to yield quantum-capacitance limited FETs and comparing their performance to that of the solid-state (oxide top-gated) FETs first discussed in *Chapter 2*, both from a fundamental nanoelectronics perspective and for the application of biosensing. *Chapter 3* also presents improved methods of FET design and operation including operating FETs in constant-current mode using a PID controller to obtain time-series measurements and leveraging a dual-gated FET design to amplify a signal applied to the sensing surface.

1.4 Improving Field-Effect Transistor Biosensing using Molecular Dynamics

While FETs provide a powerful platform to quantify changes in electrostatic potential due to biological phenomena with state-of-the-art sensitivity, they do not intrinsically provide any information regarding the biological mechanisms responsible for these changes. Information related to these mechanisms can be obtained *a priori* through other experimental techniques, e.g., determining if streptavidin binds to a biotinylated surface using fluorescently-labeled streptavidin and optical microscopy to observe fluorescence; however, many mechanisms cannot be observed experimentally and require additional techniques to predict FET-measurable changes and the molecular factors that contribute to these changes. In the following section is described the role of one such predictive method, molecular dynamics (MD) simulations, in evaluating factors that govern biomarker biorecognition and immobilization of biorecognition elements in label-free biosensing.

1.4.1 General Overview, Force Fields, and Ensembles

MD simulations are a computational technique used to model the molecular interactions responsible for experimentally observed phenomena including macroscopic properties of biological systems.⁵¹⁻⁵² This technique can be used to observe events that occur on timescales too short to be observed experimentally and to create trajectories of these events that describe the transition between thermodynamic equilibrium states. Creation of these trajectories requires initial coordinates of atoms, such as the crystal structure of a protein, and a force field (FF) that describes the forces acted on atoms in the system by other atoms on in the system. Newton's laws of motion are integrated to obtain resultant changes in atom position and velocity relative to the

forces acted on an atom by other atoms over discrete timesteps and where the initial velocities of each atom are randomized. The CHARMM FF is one such FF used to describe these forces and the total potential energy (V) of a system as a function of atom position (\hat{R}):⁵³

$$\begin{aligned}
 V(\hat{R}) = & \sum_{bonds} K_b (b - b_0)^2 + \sum_{angles} K_\theta (\theta - \theta_0)^2 + \sum_{cross\ UB} K_{UB} (r_{1,3} - r_{1,3}^0)^2 + \sum_{improper} K_{im} (1 - \cos(2\phi)) \quad (5) \\
 & + \sum_{dihedrals} \left[\sum_j K_{\phi,j} (1 + \cos(n_j \phi - \delta_j)) \right] + \sum_{nonbonded\ pairs\ i,j} \epsilon_{ij} \left[\left(\frac{R_{min,ij}}{r_{ij}} \right)^{12} - 2 \left(\frac{R_{min,ij}}{r_{ij}} \right)^6 \right] + \sum_{nonbonded\ pairs\ i,j} \frac{q_i q_j}{\epsilon_D r_{ij}}
 \end{aligned}$$

where for the first term K_b is the bond force constant and $b - b_0$ is the distance from equilibrium that the atom has moved; for the second term K_θ is the angle force constant and $\theta - \theta_0$ is the angle from equilibrium between three bonded atoms; for the third term K_{UB} is the Urey-Bradley force constant and $r_{1,3} - r_{1,3}^0$ is the distance between the 1,3 atoms in the harmonic potential; for the fourth term K_{im} is the improper force constant and ϕ is the improper angle; for the fifth term, K_ϕ is the dihedral force constant, n is the multiplicity of the dihedral function, ϕ is the dihedral angle and δ plane shift; for the sixth term, i.e., the Lennard-Jones Potential, ϵ is the depth of the potential well, R_{min} is the distance at which the potential reaches its minimum and r is the distance between two atoms; for the seventh term, i.e., the electrostatic potential, ϵ_D is Coulomb's constant, q_i and q_j are the electrostatic charges of each atom, and r is the distance between the two atoms. In the CHARMM FF, intramolecular forces are quantified using the angles and bonds between bonded atoms, including cross Urea-Bradley (UB or 1-3 interactions), improper angles, and dihedral angles (where applicable). Intermolecular interactions, i.e., nonbonded pair interactions, are quantified through van der Waals (VdW) and electrostatic interactions, where VdW interactions are

modeled using the 6-12 Lenard-Jones potential. In this work two software packages, Nanoscale Molecular Dynamics (NAMD)^{52, 54} and Desmond,⁵⁵ were used to evaluate the CHARMM FF for sub-microsecond and multi-microsecond simulations, respectively.

Essential to calculating macroscopic properties from MD simulations is the thermodynamic ensemble used to model the system, where the ensemble is defined by the properties held constant in the simulation.⁵⁶⁻⁵⁷ These properties include the number of atoms (N), temperature (T), pressure (P), volume (V), surface tension (γ), and internal energy (E) and are selected to constrain a system in a thermodynamically feasible state. In this dissertation, the primary two ensembles used were the NPT (isobaric-isothermal) and NVT (isochoric-isothermal) ensembles, where the number of atoms and temperature are constrained constant in each, and either the pressure or volume is also constrained constant. Generally, the NPT ensemble is preferred because pressure, and not volume, is held constant in experiments. In this work, the NPT ensemble was used as often as possible, except in cases where a constant electric field was applied to the system, which requires a defined volume to be kept constant so the electric field is non-varying.

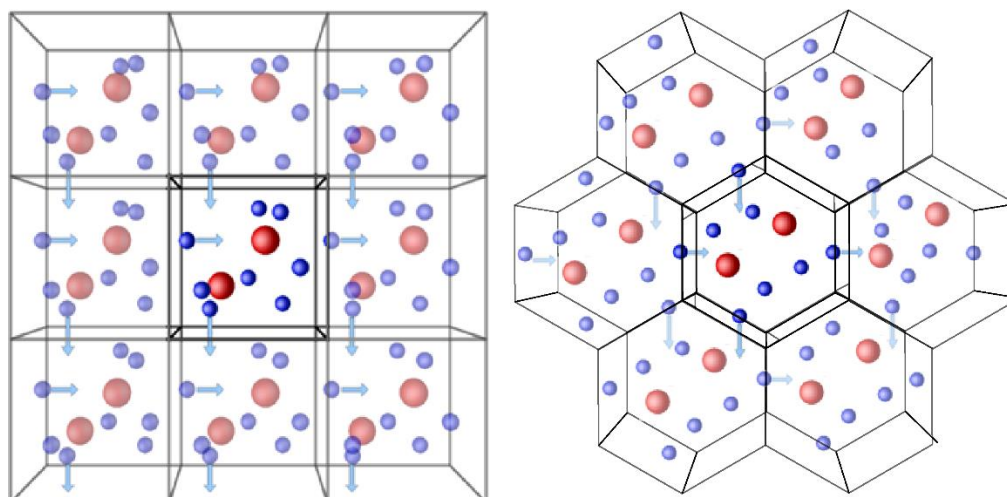


Figure 10. (left) Example of periodic boundary conditions (PBCs) for a molecular dynamics (MD) tetragonal simulation unit cell (Figure from reference 58). (right) Example of PBCs for a MD hexagonal simulation unit cell

In order to perform simulations using a unit cell, periodic boundary conditions (PBC) are used that impose the conditions of a cell boundary on the boundary of the opposite side of the cell (Figure 10).⁵⁸ PBC account for atoms that traverse the boundary of the unit cell and interactions on an atom by another atom across the boundary. In this work, a tetragonal unit cell was used which requires 26 identical images to account of all boundaries, but in some cases a hexagonal cell (Figure 10) was used which only requires 20 identical images. While N is held constant through neither creating nor destroying atoms, and V can be held constant by defining constant simulation cell dimensions, T and P require additional algorithms to be held constant. For simulations performed using NAMD, Langevin dynamics and the Langevin piston⁵⁹ Nosé-Hoover method,⁶⁰ where the piston controls are coupled to the temperature bath controlled by Langevin dynamics, were used to control T and P respectively.

1.4.2 Application for FET Biosensing: Biorecognition and Immobilization

MD simulations were performed in this work to better understand the biophysics that contribute to the biorecognition of biomarkers by FET sensing surface-adhered biomolecules (biorecognition elements) and the effects of immobilizing these biorecognition elements on the sensing surface. Specifically, for ion channels, it is advantageous to use lipids membrane to immobilize them onto a sensing surface, because ion channels natively function in lipid membranes. Moreover, the lipid membrane environment, including the type of lipids of which the membrane is composed, has been shown to regulate ion channel conductance.^{21, 61-65} Therefore, it is essential not just to study the effects of immobilizing ion channels in general using MD, but also to study how different types of lipids, each with unique structures, impact an ion channel's function.

To this end, *Chapter 4* is dedicated to demonstrating how membrane lipid type affects the conductance of the ion channel α -hemolysin (α HL). Specifically, in the context of this work, the MD simulations presented in this chapter serve as an example to demonstrate the ability of MD to discern differences in experimentally measurable parameters, e.g., ionic flux through the ion channel, when different membrane lipid types are present. Similarly, *Chapter 5* is dedicated to demonstrating differences in the function of the serotonin receptor and ligand-gated ion channel 5-HT_{3A} not only with respect to the number of ligands bound, but also with respect to the membrane lipid types immobilizing the protein. These simulations demonstrate both a mechanism of cooperative serotonin (5-HT) binding to 5-HT_{3A} and activation of the channel that further the understanding of 5-HT biorecognition by 5-HT_{3A} as well as the effects of lipid type on this mechanism. Ultimately, this information will be leveraged in future

work to select lipid types to appropriately immobilize 5-HT_{3A} on a FET-sensing surface to ensure channel function that is faithful to native conditions, as discussed in *Chapter 6*.

1.5 Overview of Dissertation

The primary purpose of this work is to demonstrate the benefits and potential of using FETs for biosensing applications and can be divided into four primary objectives:

- (i) Demonstrate an effective and repeatable method to fabricate FETs from monolayer MoS₂ with electrical performance sufficient to be used for biosensing applications (*Chapter 2*).
- (ii) Demonstrate the biosensing capabilities of these FET by detecting pH with sensitivity several times greater than the Nernst Limit as a proxy for Cdk5 activity and the addition of the streptavidin protein using a biotinylated sensing surface (*Chapter 3*).
- (iii) Demonstrate that MD simulations of the ion channels 5HT3 and α HL can be leveraged to predict the effects of biomarker biorecognition and immobilization in a lipid membrane on their structure and function for the subsequent interpretation of data obtained using FET biosensing (*Chapters 4 and 5*).
- (iv) Outline experiments that use FET biosensing as the primary tool to characterize 5HT3 and leverage conclusions from MD simulations to optimize the design of these experiments (*Chapter 6*).

Throughout this work, the four elements of biosensing, biorecognition, immobilization, transduction, and measurement will be discussed in context with

experiment or simulation results where appropriate to demonstrate how both FET measurements and MD simulations enhance the advancement of label-free biosensing. This work therefore serves not only as a summary of individual experiments and simulations with their own significant results, but also as a guide to create synergy between FET biosensing and MD simulations for the symbiotic advancement of their success.

Chapter 2: Reproducible Performance Improvements to MoS₂ FETs for Applications in Biosensing

(This chapter is published in: Guros, N.B., Le, S.T., Zhang, S., Sperling, B., Klauda, J.B., and Balijepalli, A., Robust Fabrication of Transistor Arrays from Large-Area Monolayer MoS₂. *ACS Applied Materials and Interfaces*. **2019**, 11, 16683–16692.)

2.1 Introduction

2.1.1 Motivation

Metal-mediated exfoliation has been demonstrated as a promising approach for obtaining large-area flakes of 2D materials to fabricate prototypical nanoelectronics for biosensing applications. However, several processing challenges related to organic contamination at the interfaces of the 2D material and the gate oxide must be overcome to realize robust devices with high yield. In this chapter, an optimized process is demonstrated to realize high-performance field-effect transistor (FET) arrays from large-area ($\approx 5000 \mu\text{m}^2$) monolayer MoS₂ with a yield of 85 %. A central element of this process is an exposed material forming gas anneal (EM-FGA) that results in uniform FET performance metrics (i.e., field-effect mobilities, threshold voltages, and contact performance) adequate for biosensing applications, presented in *Chapter 3* and *6*. Complementary analytical measurements show that the EM-FGA process reduces deleterious channel doping effects by decreasing organic contamination, while also reducing the prevalence of insulating molybdenum oxide, effectively improving the MoS₂-gate oxide interface. The uniform FET performance metrics and high device yield achieved by applying the EM-FGA technique on large-area 2D material flakes will help advance the fabrication of complex 2D nanoelectronics devices for biosensing

applications and demonstrates the need for improved engineering of the 2D material-gate oxide interface.

2.1.2 Challenges with Existing MoS₂ FET Fabrication

With the scaling of silicon complementary metal-oxide-semiconductor (CMOS) field-effect transistor (FET) technology approaching fundamental limits of device dimensions, power consumption, and heat dissipation,^{44, 66} an intense effort is underway to develop the next generation of switching devices for use in efficient computation and other low power applications such as biosensing.⁶⁷⁻⁶⁹ Over the last decade, progress in the use of 2D materials for numerous applications in the field of nanoelectronics has demonstrated the potential for these materials to transform the semiconductor industry.^{36, 38, 45} 2D materials have diverse electronic properties, ranging from semi-metals (e.g., graphene) to semiconductors (e.g., MoS₂, WSe₂, etc.) to insulators (e.g., hexagonal boron nitride).^{39, 70-72} Furthermore, even when these materials are made atomically thin (i.e., a single monolayer), they exhibit good electrical and mechanical properties⁷³⁻⁷⁵ making them ideal candidates for next generation electronics. A broad range of high-performance electronic devices such as FETs,^{7, 76} light-emitting diodes (LED),^{71, 77} photodetectors,⁷⁸⁻⁷⁹ and biosensors^{8, 14} have been realized from 2D materials showcasing their utility in applications where high sensitivity and low power operation are required. However, while the diversity of electronic properties and devices that can be obtained by using 2D materials is virtually limitless, their practical realization is hampered by device fabrication challenges, such as contamination at the interface of the material and gate oxide,⁸⁰⁻⁸² poor channel

doping control,^{47, 83-85} and high contact resistance,^{47, 86-87} resulting in unreliable device performance.

2D materials can be obtained from either geological sources or through chemical synthesis. Mechanical exfoliation³³ has been traditionally used to obtain 2D materials from geological sources, allowing the fabrication of prototype devices that demonstrate their remarkable properties. However, it is difficult to obtain 2D material flakes with areas large enough to fabricate arrays of nanoelectronics devices or logic circuits using this technique. To overcome this challenge, methods including chemical vapor deposition (CVD)^{46, 88-89} and physical vapor deposition (PVD)⁹⁰ are being developed to synthesize 2D material flakes with sufficiently large areas. Despite rapid progress in recent years, the performance of devices fabricated from 2D materials generated with these deposition methods has lagged behind the performance of those fabricated from geologically sourced 2D materials.^{89, 91-95} In the interim, metal-mediated exfoliation techniques that yield millimeter scale 2D materials⁹⁶⁻⁹⁸ can permit the realization of large arrays of devices and complex logic circuits. However, 2D material flakes obtained through metal-mediated exfoliation can suffer from both organic and metal contamination originating from multiple adhesive transfer steps, which can degrade device performance through uncontrolled channel doping and charge traps at the 2D material-gate oxide interfaces, making the fabrication of devices with these 2D material flakes difficult.^{96, 99-100} Therefore, new processes informed by better characterization of the interface between a 2D material and the gate oxide are needed to improve the performance and reliability of devices fabricated from metal-mediated sourced 2D materials in order to make their performance satisfactory for biosensing applications.

2.1.3 Novel Fabrication Approach

In this section, a process that improves the performance and reliability of FETs fabricated from MoS₂ monolayers obtained by gold-mediated exfoliation is presented.⁹⁶ To date, techniques such as ultra-high vacuum (UHV) annealing^{49, 101-102} and UV ozone (UV-O₃)¹⁰²⁻¹⁰⁵ have been applied to multilayer MoS₂ flakes obtained with traditional mechanical exfoliation to remove organic contamination. However, their use with monolayers has thus far been avoided because of the risk of destroying the material or generating insulating molybdenum oxide (MoO_x). Similarly, forming gas annealing (FGA) has been applied to MoS₂ FETs to improve metal-MoS₂ contact resistance and also remove organic contamination,^{102, 106} but such anneals are usually performed at temperatures between 200°C and 300°C, for short durations (2 – 4 hours), and after the deposition of a top-gate oxide to minimize the risk of material damage and mitigate the creation of sulfur vacancies.^{42, 106} Forming gas annealing for longer temperature and durations on exposed MoS₂ is thought to damage or destroy the material,⁴² but this data demonstrates that it does not.

The processing techniques developed as part of this work, namely an exposed material forming gas anneal (EM-FGA), allow high performance FET arrays to be reliably fabricated from MoS₂ obtained from metal-mediated exfoliation. FET performance improvements are a direct result of the EM-FGA improving the 2D material-gate oxide interfaces, which decreases deleterious channel doping without damaging the material, and eliminates the presence of insulating molybdenum oxide MoO_x. In this work, the physical and chemical basis for improved FET performance is demonstrated with complementary analytical measurements using Raman

spectroscopy, X-ray photoelectron spectroscopy (XPS), and atomic force microscopy (AFM) to demonstrate the effectiveness of the EM-FGA and its reliability for the fabrication of FETs and potentially other devices fabricated from 2D materials.

2.2 Materials and Methods

2.2.1 FET Fabrication

Low resistivity ($R < 0.005 \Omega\text{-cm}$) Si wafers with 70 nm SiO_2 were cleaned for 15 minutes at 75 °C in an agitated bath of 5:1:1 DI water/ammonium hydroxide/hydrogen peroxide. MoS_2 was prepared by gold-mediated exfoliation as described previously⁹⁶. MoS_2 was exfoliated from a bulk source onto adhesive tape which was then coated with 110 nm gold Au using electron beam deposition. Thermal-release tape was then used to transfer the gold-coated MoS_2 onto the wafers which were subsequently treated with oxygen plasma at 150 W and 30 cm^3/min at standard temperature and pressure (STP), 0 °C and 101 kPa, respectively (30 sccm), and 4 Pa (30 mTorr) for 4 minutes to remove residual contamination from the tape while the Au protected the MoS_2 . The Au was finally removed with Au etchant TFA (8 wt % Iodine, 21 wt % Potassium Iodide, 71 wt % water; Transene Inc., Danvers, MA) for 4 minutes and then cleaned with distilled (DI) water for 10 minutes, acetone for 30 minutes at 45 °C, and then rinsed with DI water and gently blown dry with N_2 .

After the transfer was complete, the presence of monolayers was confirmed with Raman spectroscopy. Source and drain contacts were patterned onto the entire wafer (i.e., not targeting specific monolayers) by using optical lithography with a stepper. The source and drain contacts were metallized with electron beam deposition of 2 nm Ti and 80 nm Au. Arrays were inspected for source and drain contact overlap of

monolayers using optical microscopy and targeted for channel patterning. $5\ \mu\text{m} \times 5\ \mu\text{m}$ MoS₂ channels were patterned using optical lithography and then etched into the monolayer with XeF₂ at 100 Pa (1 Torr) and 3 second pulses. For most monolayers, between 10 and 14 pulses were used to fully etch the monolayer. For Raman, XPS, and AFM analysis, samples were processed identically (except for electron beam metal deposition) to mimic processing conditions prior to the EM-FGA.

The EM-FGA was performed on the FETs for 24 hours in a tube furnace at 350 Pa (2.6 Torr) and 400 °C with 100 cm³/min forming gas at standard temperature and pressure (STP), 0 °C and 101 kPa, respectively (100 sccm) of 95:5 N₂/H₂. EM-FGA FETs were immediately transferred to a reactor for atomic layer deposition (ALD) of Al₂O₃ as opposed to control FETs where the FGA was performed after Al₂O₃ deposition. For ALD, saturating doses of trimethylaluminum and water vapor were alternately injected into a custom, warm-walled ALD reactor with a constant flow of ultra-high purity N₂ serving as a carrier gas for the reactants and as a purge gas between injections. The substrate was heated to 210 °C while the walls and gas lines were maintained at 110 °C. Under similar conditions, the deposition rate of Al₂O₃ was previously found using spectroscopic ellipsometry to be (0.103 ± 0.007) nm per cycle on SiO₂. A total of 200 cycles were performed to deposit ≈ 20 nm of top-gate Al₂O₃.

Finally, top-gates were patterned onto both sets of FETs using optical lithography and electron beam deposition to deposit 10 nm Ti and 100 nm Au. A second FGA was then performed for 4 hours in a tube furnace at 350 Pa (2.6 Torr) and 400 °C using 100 sccm of 95:5 N₂/H₂.

2.2.2 FET Electrical Performance Characterization

I - V characterization was performed during processing using a probe station and parameter analyzer. FETs were tested using standard $I_{DS}V_{DS}$ and $I_{DS}V_G$ measurement protocols for the back-gate where for $I_{DS}V_{DS}$, V_{DS} was swept from 0 V to 1 V and V_G was stepped three times from -10 V, 0 V, and 10 V, and for $I_{DS}V_G$, V_{DS} was stepped six times (0.05, 0.25, 0.45, 0.65, 0.85, 1.05) V and V_G was swept between -30 V to 25 V. A similar protocol was used for the top-gate, but for $I_{DS}V_{DS}$, V_G was set to either -4 V, 0 V, and 4 V, and for $I_{DS}V_G$, V_G was swept from either -6 V to 5 V. All back-gate measurements were made before deposition of the top-gate metal and all top-gate measurements were made with V_{BG} grounded.

The ideal V_T for a monolayer FET was calculated using the method outlined by Ma, et al.¹⁰⁷ where the local channel electrostatic potential (V_{ch}) and channel electron density (n_{ch}) must satisfy

$$C_q = q^2 g_{2D} \left[1 + \frac{\text{Exp}\left(\frac{E_g}{2k_B T}\right)}{2 \cosh\left(\frac{qV_{ch}}{k_B T}\right)} \right]^{-1}, \quad (6)$$

$$V_G = V_0 + V_{thermal} \ln \left(\text{Exp} \left(\frac{n_{ch}}{g_{2D} k_B T} \right) - 1 \right) + V_{ox}, \quad (7)$$

$$V_{ch} = V_0 + V_{thermal} \ln \left(\text{Exp} \left(\frac{n_{ch}}{g_{2D} k_B T} \right) - 1 \right), \quad (8)$$

where q is the elementary charge, g_{2D} is the 2D density of states within the channel, E_g is the band gap energy of MoS₂, k_B is the Boltzmann constant, T is the temperature, $V_0 = \frac{E_g}{2q}$, $V_{thermal} = \frac{k_B T}{q}$ is the thermal voltage, and $V_{ox} = \frac{q n_{ch}}{C_{ox}}$ is the voltage drop across the gate oxide. Equations (6) – (8) were solved numerically to obtain the ideal V_T for both a back-gate and top-gate interfaces with the monolayer MoS₂ FET.

Contact resistance was obtained using 4-point and 2-point probe measurements with the back-gate and top-gates floating. For the 4-point measurement, a constant $V_{DS} = 1$ V was applied to the first contact, V was measured across the second and third contacts where I was kept constant at zero, and the fourth contact was grounded to yield $R_{14,23} = \frac{V_{23}}{I_{14}} = R_{channel}$. For the 2-point measurement, a constant $V_{DS} = 1$ V was applied between the second and third contacts to yield $R_{23,23} = \frac{V_{23}}{I_{23}} = R_{channel} + 2 R_{contact}$. Rearranging these two equations for $R_{contact}$ (R_c) yields $R_{contact} = \frac{R_{23,23} - R_{14,23}}{2}$. $R_{23,23}$ and $R_{14,23}$ were found by taking the inverse of the slope of the best fit lines to the I - V data.

2.2.3 Additional FET Performance Characterization

2.2.3.1 Raman Spectroscopy

Raman spectra were acquired in a Renishaw InVia microscope spectrometer with laser excitation at 514 nm. All Raman peaks were calibrated based on the Si peak (520.7 cm^{-1}) and fitted with Gaussian-Lorentzian line shapes to determine the peak position, the line width, and the intensity of different components.

2.2.3.2 X-ray Photoelectron Spectroscopy

XPS Spectra were acquired on a Kratos Axis UltraDLD XPS/UPS system, under a base pressure of $0.135 \text{ } \mu\text{Pa}$ (10^{-9} Torr), using the monochromatic Al $K\alpha$ line. The XPS spectra were calibrated using adventitious carbon at ≈ 284.8 eV.

2.2.3.3 Atomic Force Microscopy

AFM images were acquired on an Asylum AFM with the tip in tapping mode to acquire both topographical and phase changes of the MoS₂ and the surrounding SiO₂ substrate.

2.3 Results and Discussion

2.3.1 Monolayer MoS₂ Field-Effect Transistor Fabrication

To realize monolayer MoS₂ FETs, MoS₂ was first transferred onto an oxidized Si substrate with an oxide (SiO₂) thickness of 70 nm using the gold-mediated exfoliation technique described in the *Section 2.2.1*.⁹⁶ Numerous flakes of the transferred material were measured using Raman spectroscopy to have monolayer thickness with an average area between 1000 μm² and 5000 μm² as seen from Figure 11a. The Raman peaks corresponding to the E¹_{2g} phonon mode (in-plane vibration for Mo and S at ≈ 386 cm⁻¹) and the A_{1g} mode (out-of-plane vibration for Mo and S at ≈ 403 cm⁻¹) were found to be in good agreement with the expected shift¹⁰⁸ for monolayer MoS₂ (thickness ≈ 0.7 nm) and yielded a frequency difference of 16.6 cm⁻¹ (Figure 11b, *orange*). Furthermore, the frequency difference between the A_{1g} and E¹_{2g} peaks increased to 22.4 cm⁻¹ for a bilayer and to 24.8 cm⁻¹ for bulk MoS₂ flakes (Figure 11c) in agreement with literature values.¹⁰⁸

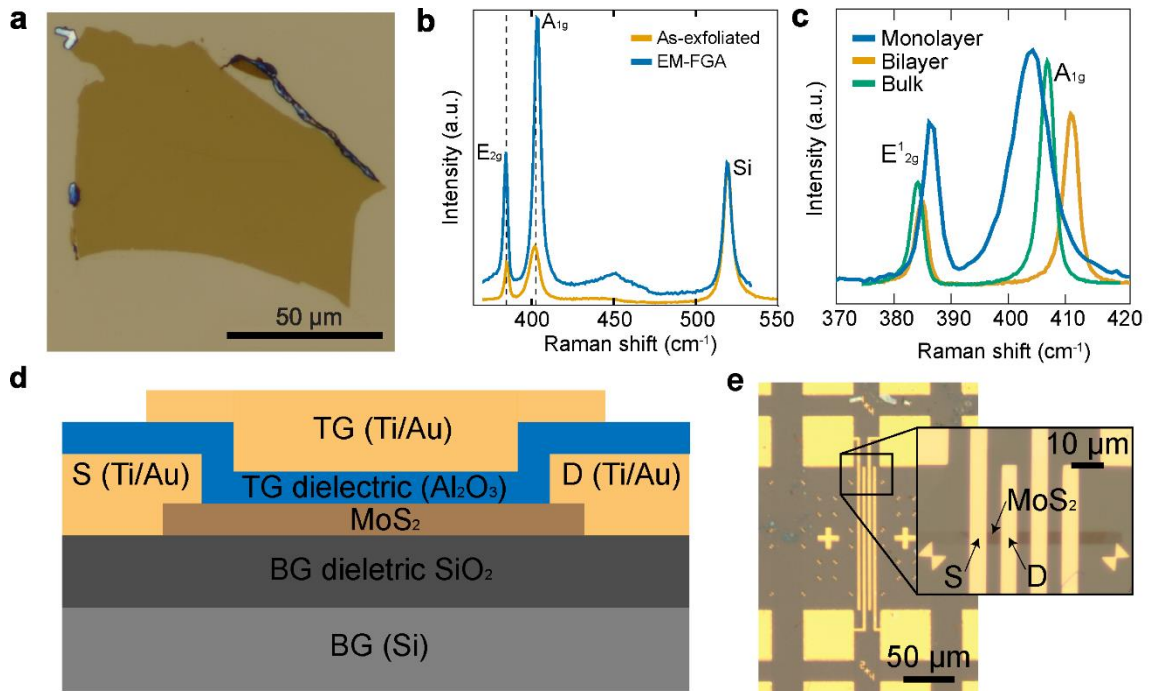


Figure 11. MoS₂ monolayer characterization and design of monolayer MoS₂ field-effect transistors (FET). (a) Large area ($\approx 5000 \mu\text{m}^2$) monolayers of MoS₂ were transferred onto a SiO₂ on Si wafer using the gold-mediated exfoliation method. (b) Raman spectra of the monolayer from (a) before (orange) and after (blue) an exposed material forming gas anneal. (c) Raman spectra for a monolayer (blue), bilayer (green), and bulk (orange) MoS₂ calibrated based on the Si peak at 520.7 cm^{-1} . (d) Cross-sectional schematic depicting a FET fabricated using monolayer MoS₂ (550 μm Si back-gate (BG), 70 nm SiO₂ BG oxide, monolayer (≈ 0.7 nm) MoS₂, 2 nm Ti/100 nm Au sources/drain contacts, 20 nm Al₂O₃ top-gate (TG) oxide, and 10 nm Ti/100 nm Au TG contact). (e) Optical image of a representative array of FETs prior to deposition of the top-gate dielectric and top-gate metal. Inset: Detail view of the FET array.

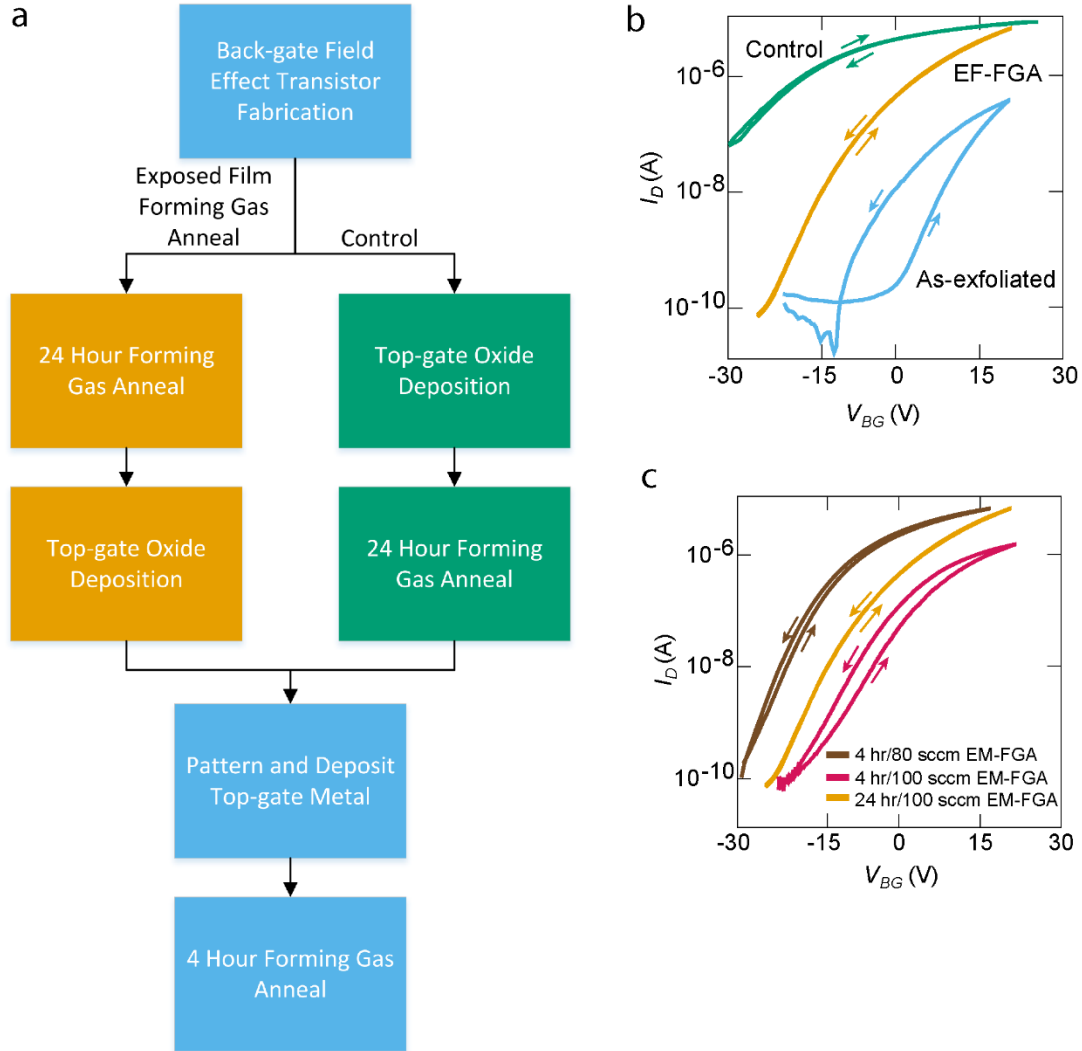


Figure 12. (a) Process flow diagram for the fabrication of field-effect transistor (FET) arrays. The *orange* steps (on the left) highlight the newly developed exposed material forming gas anneal (EM-FGA) sequence while the *green* steps (on the right) represent a conventional sequence for FET fabrication from 2D materials. The *blue* steps (top and bottom) are common to both processes. (b) Comparison of as-exfoliated (before FGA or top-gate oxide deposition) field-effect transistor (FET) back-gate performance to control FET and exposed material forming gas anneal (EM-FGA) FET back-gate performance. Representative transfer curves for as-exfoliated (*blue*), EM-FGA (*orange*) and control FETs (*green*) for $V_D = 1.05$ V. (c) Representative back-gate transfer curves for exposed material forming gas anneal (EM-FGA) field effect transistors (FET) performed for 4 hours and 80 cm^3/min forming gas at standard temperature and pressure (STP), 0 °C and 101 kPa, respectively (80 sccm) (*pink*), 4 hours at 100 sccm (*brown*), and 24 hours at 100 sccm (*orange*) measured after top-gate oxide deposition and prior to top-gate metal patterning.

A schematic of a monolayer MoS₂ FET is depicted in Figure 11d (see *Section 2.2.1* for fabrication details). Briefly, the source (*S*) and drain (*D*) contacts (2 nm Ti/80 nm Au) were patterned by using optical lithography and electron-beam metal deposition after gold-mediated transfer of monolayers. For each FET, a 5 μm × 5 μm channel was lithographically defined and subsequently etched. Figure 11e shows an optical image of an array of three FETs with a global back-gate (*BG*) and back-gate dielectric (*gray*, SiO₂). Next, the top-gate (*TG*) dielectric (*blue*, Al₂O₃) was deposited using atomic layer deposition (ALD) and the top-gate metal (10 nm Ti/100 nm Au) was patterned using optical lithography and electron-beam metal deposition. The large areas and relative abundance of exfoliated monolayers on the substrate allowed for batch fabrication of numerous monolayer FET arrays on a 4-inch wafer.

2.3.2 Monolayer MoS₂ Field-Effect Transistor Performance

Two sets of FETs were fabricated by using the process flow described in *Section 2.2.1* and shown in Figure 12a. A control set ($n=5$) was processed using the steps shown in Figure 12a on the right in *green*, in which a conventional annealing process was used, i.e., the entire set of five control FETs underwent a forming gas anneal (FGA) immediately after deposition of a top-gate oxide.^{42, 102} The second set of FETs ($n=20$) was fabricated with this new EM-FGA process as illustrated in Figure 12a on the left in *orange*. The anneal time and gas flow rate (Figure 12b) was varied and it was determined that an anneal temperature of 400 °C with 100 cm³/min forming gas for 24 hours at standard temperature and pressure (STP), 0 °C and 101 kPa, respectively (100 sccm), yielded an optimum improvement in performance. The back-gate performance of both the control and EM-FGA FETs was characterized after deposition

of the top-gate oxides, but without the top-gate metals. Next, top-gate metals were deposited onto both sets of FETs followed by a second shorter FGA (Figure 12a). Finally, the top-gate performance of all devices was measured while the back-gate was connected to ground.

Both the EM-FGA and control FETs demonstrated measurable improvement in back-gate performance compared to as-exfoliated (before FGA or top-gate oxide deposition) back-gate performance (Figure 12c; *blue*). On average, 85 % ($n=17/20$) of EM-FGA FETs showed consistent and improved performance relative to the control samples. Next, the electrical characteristics of the EM-FGA FETs compared to the control set is discussed.

2.3.2.1 Back-gate Performance

EM-FGA FET back-gate performance after top-gate oxide deposition and prior to top-gate metal deposition is shown by the representative *orange* transfer curve in Figure 13a for $V_{DS} = 1.05$ V (all transfer curves can be seen in Figure A1). The measurements were repeated for multiple (stepped) V_{DS} as seen in Figure 13b, where minimal hysteresis was observed. Average electrical performance parameters for all the measured devices are reported in Table 1. All devices demonstrated *n*-type behavior, consistent with previous observations for MoS₂ FETs.^{76, 109} Unless otherwise noted, error bars reported in this work represent the standard error.

Table 1. Performance parameters for EM-FGA and control FETs reported as means and standard errors. Several of these metrics are labeled as “N/A” because the large flat band shift in V_T for the control FETs precluded an accurate estimation of these metrics without inducing dielectric breakdown in the back-gate or top-gate oxide.

Parameter	EM-FGA (n=17)	Control (n=5)
<i>Back-gate</i>		
μ_{FE} (cm ² /V·s)	16.1 ± 2.4	13.5 ± 3.5
V_T (V)	2.4 ± 0.9	-21.1 ± 2.2
I_{on}/I_{off}	10 ⁵	N/A
I_{on} (μA/μm)	> 10	> 10
Subthreshold swing (V/decade)	4.6 ± 0.3	N/A
<i>Top-gate</i>		
μ_{FE} (cm ² /V·s)	2.8 ± 0.5	4.1 ± 0.3
V_T (V)	-1.8 ± 0.3	N/A
I_{on}/I_{off}	10 ⁶	N/A
I_{on} (μA/μm)	> 10	> 10
Subthreshold swing (mV/decade)	650 ± 24	N/A

On average, an I_{on}/I_{off} ratio of $\approx 10^5$ and a subthreshold swing of (4.6 ± 0.3) V/decade for the 70 nm SiO₂ back-gate interface was observed. At large positive V_{BG} , an I_{on} of was observed at least 10 μA/μm and a field-effect mobility (μ_{FE}), not correcting for source and drain contact resistance, of (16.1 ± 2.4) cm²/V·s that was determined using, $\mu_{FE} = \frac{g_{m,max} L/W}{C_{ox} V_D}$, where $g_{m,max}$ is the peak transconductance, L and W are the length and width of the channel respectively, and C_{ox} is the oxide capacitance per unit area, determined to be 49.3 nF/cm² for the 70 nm SiO₂ back-gate dielectric.¹¹⁰ To prevent the risk of dielectric breakdown, i.e., the application of a voltage that causes a portion a dielectric material to become conductive, irreversibly damaging the material, the application the range of V_{BG} was limited to ± 25 V. The threshold voltage (V_T), estimated by extrapolating the point of maximum slope on the transfer curve to the x -axis, was found to be (2.4 ± 0.9) V for the EM-FGA FETs. In contrast, the control

set exhibited a large and negative shift in V_T of (-21.1 ± 2.2) V, as shown by the representative *green* transfer curve in Figure 13a (all transfer curves can be seen in Figure A2). This shift in V_T is the key improvement in performance for the EM-FGA FETs that separates them from the control FETs.

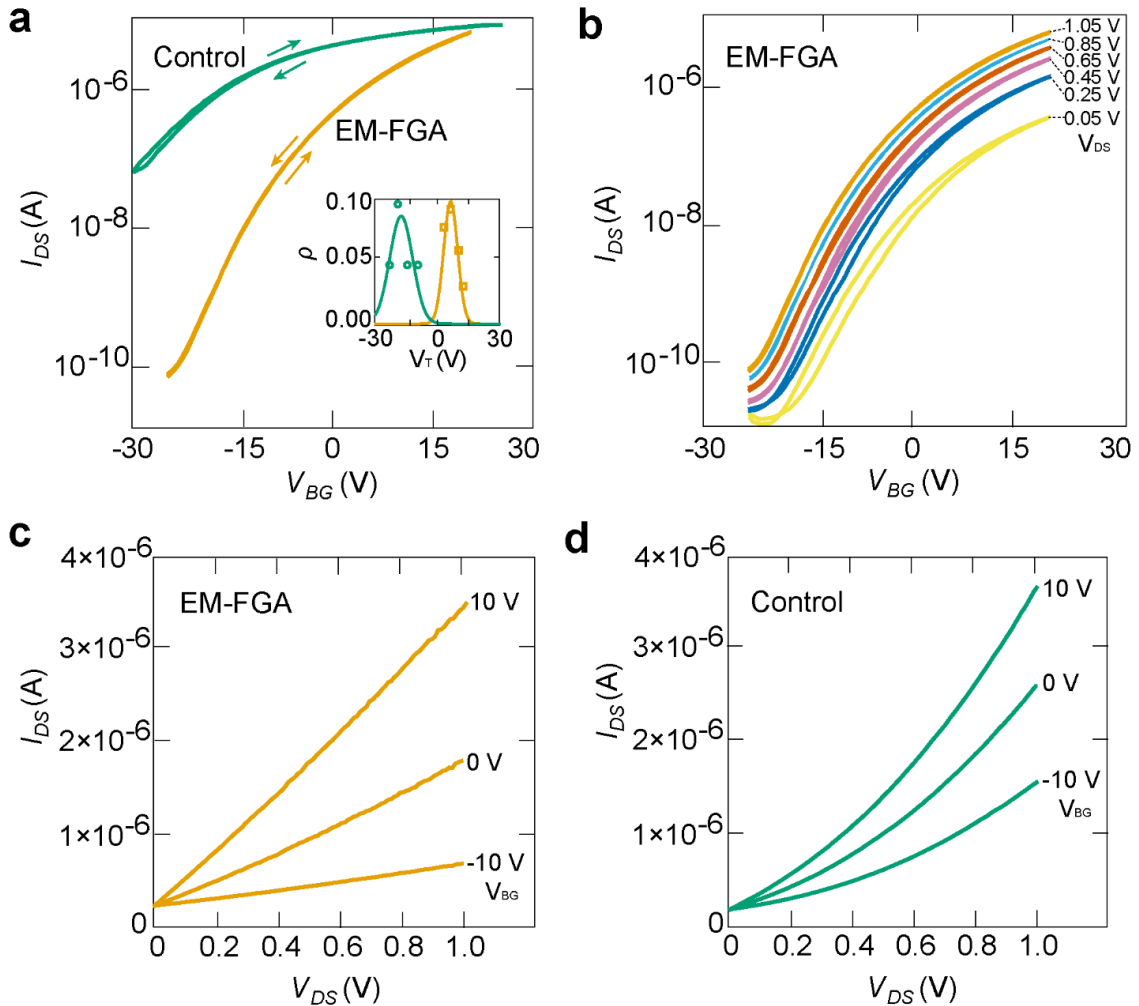


Figure 13. Characterization of field-effect transistor (FET) back-gate performance. (a) Representative transfer curves for an exposed material forming gas anneal (EM-FGA) FET (*orange*) and a control FET (*green*) for $V_{DS} = 1.05$ V. *Inset:* Distribution of V_T for the EM-FGA and control FETs. (b) Representative transfer curves for an EM-FGA FET at varying V_{DS} . (c) Representative $I_{DS}V_{DS}$ curves for an EM-FGA FET at varying V_{BG} demonstrate improved contact performance. (d) Representative $I_{DS}V_{DS}$ curves for a control FET at varying V_{BG} . All measurements were performed after deposition of a top-gate oxide and prior to the deposition of a top-gate metal.

Notably, a negative shift in V_T of the control set is consistent with previous observations of MoS₂ FETs after top-gate oxide deposition.^{102, 111} This shift could be explained by the presence of large trapped charges at the MoS₂-top gate oxide interfaces that dopes the channel and induces a flatband voltage (V_{FB}) shift. To quantify this behavior, V_{FB} is defined as: $V_{FB} = \phi_{MS} - \frac{Q_i}{C_{ox}}$, where ϕ_{MS} is the difference in the work function between the back-gate and the semiconducting MoS₂, Q_i is the density of fixed oxide and channel-contaminating charges, and C_{ox} is the back-gate oxide capacitance per unit area. Q_i can be quantified by substituting the definition of V_{FB} into the general gate bias equation, $V_G - V_{FB} = -\frac{Q_s}{C_{ox}} + \psi_s$, where V_G is the gate voltage, Q_s is the charge density of the MoS₂ channel, and ψ_s is the surface potential,¹⁶ yielding the equation $V_G - \phi_{MS} \mp \frac{Q_i}{C_{ox}} = -\frac{Q_s}{C_{ox}} + \psi_s$. The difference in experimental Q_i for the EM-FGA and control FETs with respect to the ideal case can be calculated by setting $V_G = V_T$, and assuming several other interface properties (ϕ_{MS} , C_{ox} , Q_s , and ψ_s) are the same for both cases. For the ideal case, Q_i is assumed as 0, yielding $\Delta V_{T(experimental-ideal)} = \frac{-Q_{i,experimental}}{C_{ox}}$.

For a monolayer MoS₂ FET, ideal V_T is defined as the V_G at which the quantum capacitance of the channel equals C_{ox} .¹⁰⁷ This definition must be used instead of the standard definition of V_T , which is only applicable to bulk semiconductor FETs, i.e., FETs with silicon as the semiconducting material.¹⁶ Using equations (6) – (8) outlined in *Methods*, the theoretical value of V_T was calculated to be +0.7 V for a FET for a monolayer MoS₂ channel on a 70 nm SiO₂ oxide. Therefore, the experimentally observed V_T of (2.4 ± 0.9) V for the EM-FGA case compares favorably to the

theoretical value. On the other hand, for the control FETs, V_T was measured as (-21.1 ± 2.2) V, which represents a large and negative shift from ideal V_T (Table 1), indicating the presence of substantial positive contamination that dopes the channel. The preceding results allowed the estimation of Q_i for both the EM-FGA and the control FETs. The estimated value of Q_i is closer to ideal for the EM-FGA FETs ($\approx -4.5 \times 10^{11}$ q/cm²) than for the control FETs ($\approx 6.7 \times 10^{12}$ q/cm²). The order of magnitude reduction in charge, due to the removal of positive contamination, strongly shifts V_T of the EM-FGA FETs in the positive direction and closer to the ideal value of +0.7 V. Furthermore, the estimated value of V_T for the EM-FGA devices is statistically consistent with the ideal value with 95 % confidence. This highlights the importance of the sequence of processing steps developed in this chapter (Figure 12) with respect to improving the quality of a 2D material-gate oxide interface.

The benefits of the EM-FGA also extend to improved contact performance in the EM-FGA devices relative to the control set. After the EM-FGA, the I_{DS} - V_{DS} response of the FETs as a function of V_{BG} was found to be Ohmic as seen in Figure 13c (all EM-FGA FET I_{DS} - V_{DS} responses can be seen in Figure A3). In contrast, Figure 13d demonstrates that the control devices exhibited rectifying characteristics indicating the presence of a Schottky barrier at those contacts (all control FET I_{DS} - V_{DS} responses can be seen in Figure A4). The difference in contact resistance (R_C) was quantified between the EM-FGA and control FETs using a four-point probe measurement technique (Figure A5) as described in *Section 2.2.1*. From these measurements, R_C was estimated to be (35 ± 3) k Ω - μ m for the EM-FGA FETs and (785 ± 32) k Ω - μ m for the control

FETs, where R_C for the EM-FGA FETs is ten-fold lower than previously reported for monolayer MoS₂ FETs.¹¹²

Forming gas annealing improves contact resistance (R_C) between metal source/drain contacts and MoS₂ through two mechanisms: 1) by removing organic contamination in the vicinity of the metal contacts, which generates a physical barrier between the metal contacts^{42, 49, 106} and 2) by locally doping the MoS₂ under the source and drain contacts with metal atoms.¹¹²⁻¹¹³ The EM-FGA FETs demonstrate lower R_C compared to the control FETs because the first mechanism is more effective without a top-gate oxide acting as a physical barrier to the removal of organic contamination by hydrogen gas. Furthermore, the second mechanism is more readily permitted in the EM-FGA FETs because organic contamination does not serve as a physical barrier to the doping of MoS₂ under the metal contacts with metal atoms. In contrast, the control FETs were annealed after the deposition of the top-gate dielectric, which shields the MoS₂-contact metal interface from hydrogen gas penetration, decreasing the effectiveness of organic contamination removal and subsequent doping of MoS₂ with metal atoms.

Many of the improvements displayed by the EM-FGA FETs were also observed for the control FETs. For example, minimal hysteresis was observed, while the drive current was found to be at least 10 $\mu\text{A}/\mu\text{m}$ at large positive V_{BG} and μ_{FE} was $(13.5 \pm 3.5) \text{ cm}^2/\text{V}\cdot\text{s}$ prior to correcting for the contact resistance (Table 1). However, the large shift in V_T for the control FETs precluded an accurate estimation of the I_{on}/I_{off} ratio and the subthreshold swing without inducing dielectric breakdown in the back-gate dielectric.

2.3.2.2 Top-gate Performance

One goal of this fabrication approach is to make dual-gated monolayer MoS₂ FETs for biosensing applications where the back-gate can be used to operate the FET in constant current mode (see *Chapter 1*). Therefore, after back-gate characterization, a top-gate metal was deposited onto both the EM-FGA and control FETs followed by a second, shorter FGA, to improve top-gate performance. EM-FGA FET top-gate performance is shown by the representative *orange* transfer curve in Figure 14a and reported for all measured devices in Table 1 (all transfer curves can be seen in Figure A6). On average, and similarly to the back-gate results, minimal hysteresis was measured, an $I_{\text{on}}/I_{\text{off}}$ ratio of $\approx 10^6$, and a subthreshold swing of (650 ± 24) mV/dec. At large and positive V_{TG} , a drive current of at least $10 \mu\text{A}/\mu\text{m}$ was measured and μ_{FE} of $(2.8 \pm 0.5) \text{ cm}^2/\text{V}\cdot\text{s}$ before correcting for the contact resistance (and assuming C_{ox} to be $398 \text{ nF}/\text{cm}^2$ for the top-gate oxide). V_{T} was found to be $(-1.8 \pm 0.3) \text{ V}$, estimated by extrapolating the point of maximum slope on the transfer curve to the x -axis.

To compare the experimental top-gate V_{T} of $(-1.8 \pm 0.3) \text{ V}$ to the ideal value, equations (6) – (8) were used to calculate ideal V_{T} for a top-gate FET with a monolayer MoS₂ channel under a 20 nm Al₂O₃ oxide. This value was found to be $+0.8 \text{ V}$. In contrast to the back-gate performance, the experimentally determined value of V_{T} does not compare favorably to ideality, indicating that the contaminants doping the channel affect top-gate performance more than back-gate performance. This may be, in part, due to trapping of these fixed charges at the interface degrading gate control. EM-FGA parameters will be further optimized in future work with the aim of reducing Q_{i} at the MoS₂-top-gate oxide interface and to shift top-gate V_{T} closer to ideality.

Finally, Figure 14b demonstrates that the device I_{DS} - V_{DS} characteristics were found to be Ohmic for the EM-FGA FETs (all I_{DS} - V_{DS} curves can be seen in Figure A7), in contrast to Figure 14c that demonstrates the rectifying behavior observed for the control FETs (all I_{DS} - V_{DS} curves can be seen in Figure A8), similar to the rectifying behavior observed for the control back-gates.

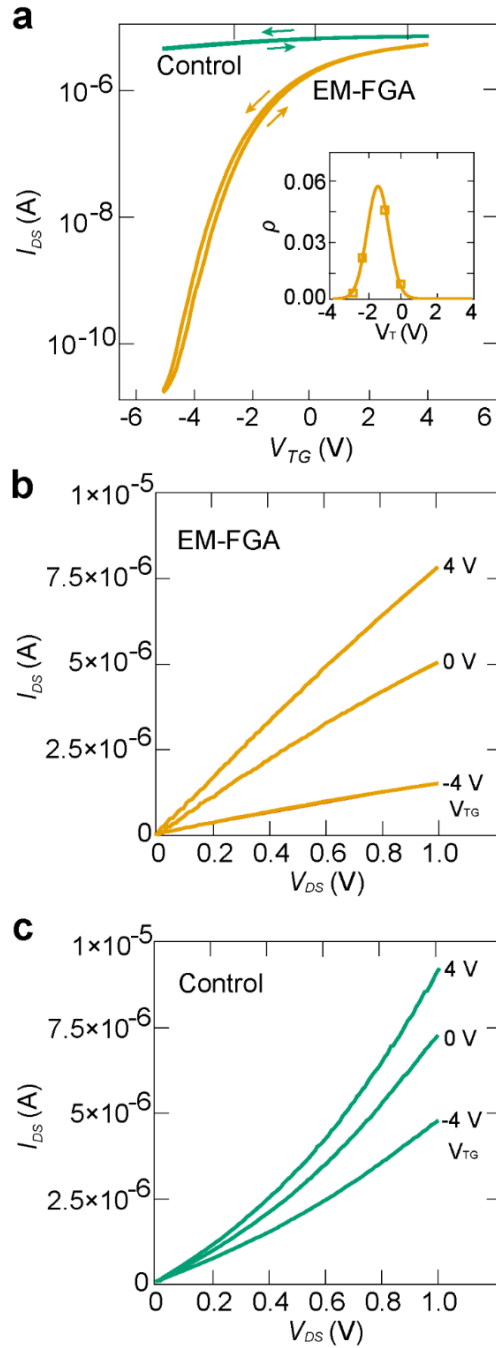


Figure 14. Characterization of field-effect transistor (FET) top-gate performance. (a) Representative top-gate transfer curves for an exposed material forming gas anneal (EM-FGA) FET (orange) and a control FET (green) for $V_{DS} = 1.05$ V. *Inset:* Distribution of V_T for the EM-FGA FETs (b) Representative $I_{DS}V_{DS}$ curves for an EM-FGA FET at varied V_{TG} demonstrating improvement to contact resistance. (c) Representative $I_{DS}V_{DS}$ curves for a control FET at varied V_{TG} . All measurements were made with $V_{BG} = 0$ V.

Similarly, to the back-gate, some aspects of top-gate performance for the control set were comparable to those of the EM-FGA set. Drive currents approached $10 \mu\text{A}/\mu\text{m}$ at large and positive V_{TG} , and μ_{FE} was found to be $(4.1 \pm 0.3) \text{ cm}^2/\text{V}\cdot\text{s}$ prior to correcting for the contact resistance (Table 1). However, also similar to the back-gate, a large and negative shift in V_{T} (Figure 14a, *green*) was observed in the top-gate for the control set, which again precluded an accurate estimation of the $I_{\text{on}}/I_{\text{off}}$ ratio, the subthreshold swing, and V_{T} for the control FETs without inducing dielectric breakdown in the gate dielectric (all transfer curves can be seen in Figure A9). Also, the large and negative shift in V_{T} for the control top-gates permitted a more accurate estimate of $g_{m,\text{max}}$ than the EM-FGA top-gates where $g_{m,\text{max}}$ is likely underestimated because I_{DS} is still increasing at 4 V, which was the maximum V_{TG} that could be applied without inducing dielectric breakdown (Figure 14a). This results in underestimations of $g_{m,\text{max}}$ and μ_{FE} for the EM-FGA FETs relative to the control FETs..

In summary, the observed performance benefits of the EM-FGA process are threefold: i) by drastically reducing the interface contamination and trap charges, a controlled V_{T} shift on both the back-gate and top-gate closer to the ideal value was achieved, which in turn improves performance and reproducibility of FETs fabricated using this approach closer to the level needed for integration in logic circuits,^{111, 114} ii) Ohmic metal-MoS₂ contacts were achieved, evident by the linear $I_{\text{DS}}-V_{\text{DS}}$ characteristics, with a low contact resistance, and iii) important FET characteristics including μ_{FE} , subthreshold swing, and $I_{\text{on}}/I_{\text{off}}$ ratio were maintained at values previously reported for FETs fabricated from MoS₂ sourced from traditional mechanical

exfoliation. Furthermore, the benefits of EM-FGA were achieved using only a tube furnace operating at relatively high pressures, i.e., 350 Pa (2.6 Torr), which makes the technique straightforward to implement without the need for highly specialized equipment.^{49, 102-103, 105, 109} The EM-FGA process is gentle and minimizes damage to the large monolayers obtained through metal-mediated exfoliation, unlike other commonly used cleaning techniques that utilize UV-ozone which has been shown to create disadvantageous MoO_x or even eliminate transistor behavior in FETs.^{102, 104, 115} It is expected that the EM-FGA to be a critical component of the streamlined processing of 2D materials obtained using increasingly widespread metal-mediated exfoliation techniques.^{97, 100, 116-117} Finally, to better describe the mechanism underlying improved FET performance in this work, several complimentary measurements were performed on the monolayers from which the FETs were fabricated, as described next.

2.3.3 Monolayer MoS₂ Characterization with Raman Spectroscopy, XPS and AFM

Raman spectroscopy, XPS, and AFM were used to quantify the effects of the EM-FGA on the morphology and chemical composition of MoS₂ monolayers obtained from metal-mediated exfoliation. All monolayers analyzed here were prepared using the process steps outlined in *Section 2.2.1*, identical to the monolayers used to fabricate the FETs, up to the deposition of the top-gate oxide.

2.3.3.1 Raman Spectroscopy

Raman spectra of monolayer MoS₂ are shown in Figure 11b. As discussed earlier, the separation between the E¹_{2g} and A_{1g} peaks in the spectrum were in agreement with the expected shift¹⁰⁸ for monolayer MoS₂ with a thickness of ≈ 0.7 nm and yielded a frequency difference of 16.6 cm⁻¹. The EM-FGA process increased the peak separation

frequency to 19.4 cm^{-1} , within the range observed for monolayer MoS_2 .¹⁰⁸ On the other hand, as seen from Figure 11b, samples processed with the EM-FGA demonstrated a dramatic overall increase in the peak intensity (*blue*) relative to the as-exfoliated sample (*orange*), and narrower E_{2g} peak widths (4.9 cm^{-1} compared to 7.3 cm^{-1}) suggesting the EM-FGA results in lower contamination and reduces defects in the MoS_2 crystal structure. A similar improvement to the material composition was previously observed for multilayer MoS_2 annealed with elemental sulfur.⁴⁸

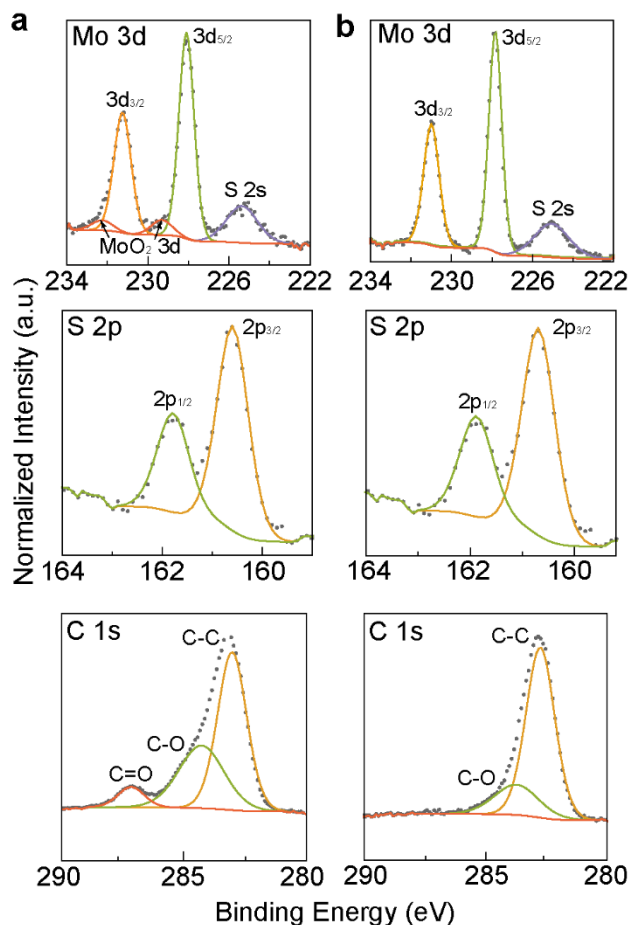


Figure 15. XPS spectra for MoS_2 sourced from metal-mediated exfoliation before and after exposed material forming gas annealing (EM-FGA). (a) XPS spectra for Mo, S, and C before the EM-FGA and (b) after the EM-FGA illustrating the elimination of MoO_2 and species containing $\text{C}=\text{O}$ bonds, and a reduction of species containing $\text{C}-\text{O}$ bonds while the presence of Mo^{4+} and S^{2-} were constant.

2.3.3.2 X-Ray Photoelectron Spectroscopy (XPS)

XPS spectra for three elements, Mo, S, and C, obtained from a MoS₂ monolayer before and after EM-FGA are illustrated in Figure 15. All spectral data are calibrated with the C 1s peak at a constant binding energy of ≈ 284.6 eV. Both before and after the EM-FGA, the Mo 3d shows two main peaks at 229.8 eV and 232.9 eV which are attributed to Mo 3d_{5/2} and Mo 3d_{3/2}, respectively, confirming the existence of Mo⁴⁺. The S XPS spectrum displays peaks at 162.7 eV and 163.81 eV that can be attributed to the doublet S 2p_{3/2} and S 2p_{1/2}, respectively, corresponding to the divalent sulfur ion (S²⁻) of MoS₂. However, the sample measured before the EM-FGA displays ≈ 5 % of MoO₂ on the channel, as evidenced by the two peaks at 231.0 eV (Mo 3d_{5/2}) and 234.0 eV (Mo 3d_{3/2}). These peaks are not observed after the EM-FGA, indicating that EM-FGA removes insulating and disadvantageous MoO₂ that forms on the surface of the monolayer.

Figure 15 also demonstrates changes in the C 1s peaks, which illuminate changes in organic contamination. The deconvolution of these peak illustrates the existence of organic compounds before EM-FGA due to the presence of C-C, C-O, and C=O bonds. After the EM-FGA, the intensity of C=O is not detectable and the intensity of C-O decreases, strongly indicating the removal of surface organic contamination. Furthermore, the C content was reduced by more than 90% after the EM-FGA, indicating that the EM-FGA method effectively reduces organic surface contamination.

2.3.3.3 Atomic Force Microscopy (AFM):

MoS₂ monolayers were also characterized using AFM imaging before and after the EM-FGA to assess changes in surface morphology as illustrated in Figure 16. The

topography of the underlying SiO₂ substrate changed visibly after the EM-FGA procedure (Figure 16a and 16b), but changes in the MoS₂ monolayer were more subtle. The average surface roughness measured on the SiO₂ substrate from the topography image reduced $\approx 40\%$ after the EM-FGA process from 892 pm to 510 pm. On the other hand, surface roughness appeared virtually unchanged for MoS₂. Complementary information was obtained by a careful analysis of the phase image of the same sample as seen in Figures 16c and 16d. In those images can be seen distinct and visible changes to both the SiO₂ and MoS₂ surfaces following EM-FGA. Prior to EM-FGA, the distribution of phase angles (Figure 16c, *inset*) on both the SiO₂ and MoS₂ surfaces was long-tailed indicating phase non-uniformity. This behavior was consistent with previous observations of contamination in graphene.¹¹⁸ Following EM-FGA, the phase angle distributions were considerably more uniform and followed a Gaussian distribution suggesting removal of surface contamination. The result agrees with the XPS measurements that show both removal of organic contamination and improvement to the stoichiometry of the MoS₂.

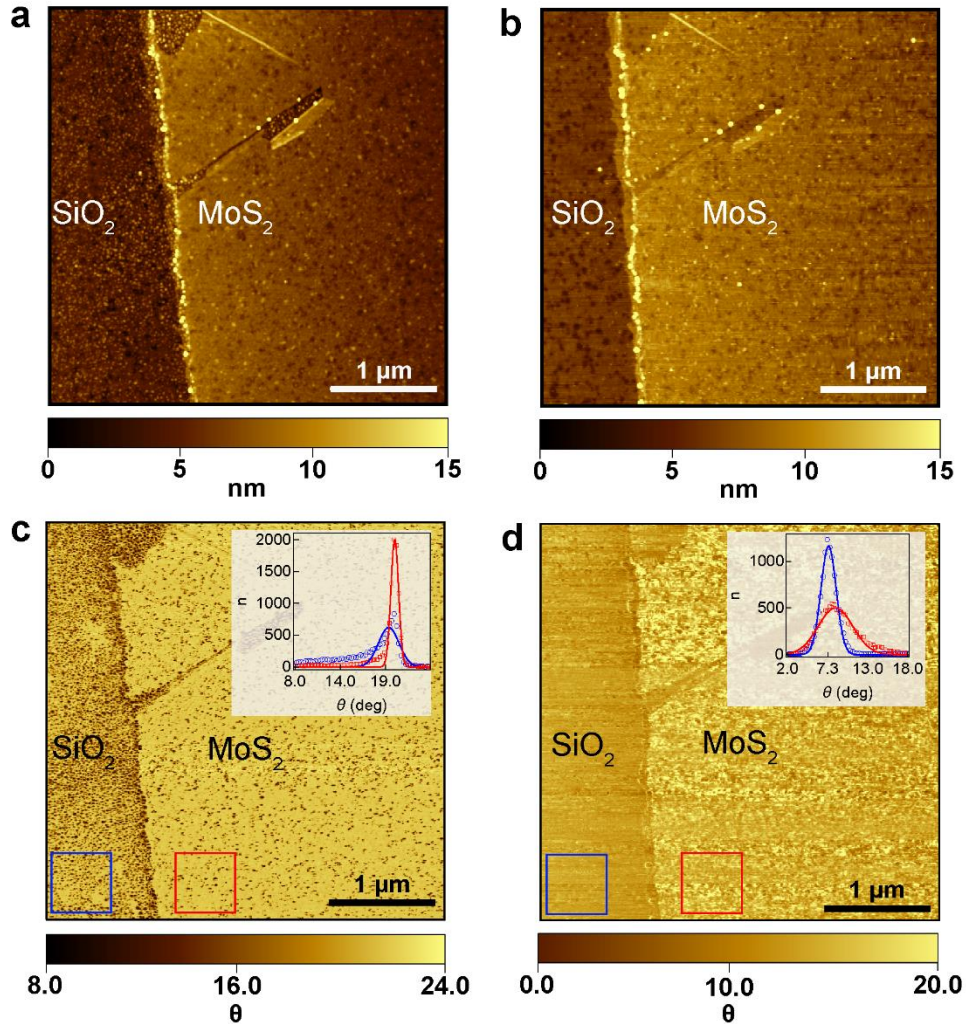


Figure 16. AFM images of a MoS₂ monolayer before and after exposed material forming gas annealing (EM-FGA). (a) Topographical image of a MoS₂ monolayer on SiO₂ before EM-FGA. (b) Topographical image of the MoS₂ monolayer from (a) on SiO₂ after EM-FGA. (c) Phase image of the MoS₂ monolayer from (a) on SiO₂. *Inset:* distributions of phase shift angles in the selected areas of the SiO₂ substrate (*blue*) and MoS₂ (*red*). (d) Phase image of the MoS₂ monolayer on SiO₂ from (b). *Inset:* distributions of phase shift angles in the selected areas of the SiO₂ substrate (*blue*) and MoS₂ (*red*).

2.4 Conclusion

Chapter 2 of this work presented a new process that markedly improved reproducibility and performance of FETs fabricated from MoS₂ monolayers sourced from metal-mediated exfoliation. The EM-FGA process improved both top and back-gate performance of the FETs, as quantified by nearly ideal and reproducible threshold

voltages, and Ohmic behavior of the source and drain contacts. Furthermore, common device metrics to estimate performance such as subthreshold slope, drive current, and field-effect mobility of the semiconducting MoS₂ were found to be comparable to previous reports of state-of-the-art FETs fabricated by mechanical exfoliation of MoS₂. These results demonstrate that the EM-FGA remarkably improves the MoS₂-gate oxide interfaces by removing trapped charges that can degrade electrical performance. As large area 2D material flakes become more commonplace due to continued interest in the metal-mediated exfoliation method,^{96, 116} the improved processing techniques reported here will be critical to enable the fabrication of components from 2D materials including FETs for biosensing applications.

The combination of the Raman, XPS, and AFM results support the conclusion that the EM-FGA improves the quality and composition of the MoS₂ monolayer resulting in improved FET performance. The improvements were found to be two-fold; (i) the EM-FGA process drastically decreased organic contaminants on the semiconducting material and surrounding back-gate dielectric, which can dope the channel and lead to an uncontrolled flatband voltage shift, and (ii) the EM-FGA process eliminated the presence of MoO₂ species which can be disadvantageously insulating. Lastly, the increase of anneal time performed on the exposed MoS₂ resulted in no observable detrimental effects on FET performance or destruction of the MoS₂.

The methods detailed in this work will have an immediate impact when realizing devices that use 2D materials sourced from metal-mediated exfoliation and could help in the development of 2D heterostructure devices where there is a stringent requirement for interface cleanliness and material quality, including FETs for biosensing

applications. In *Chapter 3*, the use of FETs fabricated using the methods demonstrated in *Chapter 2* for biosensing applications is presented. This includes comparing the performance of these FETs between two back-gate oxide thicknesses (70 nm and 300 nm) and top-gate material (either Al₂O₃ oxide or ionic liquid). Constant current mode operation of these FETs both as ISFETs (indirect biosensors) and sensing surface-modified FETs (direct biosensors) is presented as introduced in *Chapter 1*. Both liquid-gated FETs and oxide-gated (solid state) FETs were used for measuring pH and Cdk5 activity indirectly through pH, while the latter was also used for the detection of streptavidin, as presented in the final section of the chapter.

Chapter 3: Comparison of Solid-State and Liquid-Gated MoS₂ FET Biosensors for Label-Free Enzyme Measurements and Direct Detection of Proteins

3.1 Introduction

Using FETs as biosensors for measurements of enzymatic activity and protein detection requires FETs that demonstrate excellent sensitivity and high signal-to-noise ratios (SNRs) to achieve low limits of detection (LODs). In this chapter, electrical performance for solid-state FETs (SSFETs) and liquid-gate FETs (LGFETs) is compared to demonstrate the benefits of their dual-gate design. This dual-gate design permits the amplification of charge applied to the sensing gate as a function of either direct protein binding or their indirect characterization of protein activity, such as a pH change associated with the activity of an enzyme. Subsequently, their use as ISFETs and performance for measurements of pH is compared. The LGFETs demonstrate the ability to detect pH changes with ≈ 75 -fold higher sensitivity (4.4 V/pH) over the Nernst value of 59 mV/pH at room temperature and exhibit very low intrinsic noise resulting in a pH LOD of 92×10^{-6} at 10 Hz, which represents an order of magnitude improvement over state-of-the-art. The SSFETs demonstrate lower sensitivity for pH changes (0.25 V/pH), which is expected through an analysis of signal amplification, a function of their design and dielectric gates, but still demonstrate sufficiently low intrinsic noise to be used for pH changes associated with enzymatic activity. The low pH LODs demonstrated by these FETs shows promise for numerous applications ranging from pharmaceutical manufacturing to clinical diagnostics.

Here, the activity of the kinase cyclin-dependent kinase 5 (Cdk5), an enzyme implicated in Alzheimer's disease, was used as an example to demonstrate the ability of both LGFETs and SSFETs to measure Cdk5 activity, using pH as a reporter, at concentrations that are 5-fold lower than physiological values and with sufficient time-resolution to allow the estimation of both steady-state and kinetic parameters in a single experiment. The measurements were performed by using a pH sensing element that was connected electrically to the LGFET. This configuration allowed measurements with both a high intrinsic gain¹⁸ (i.e., sensitivity) and signal-to-noise ratio (SNR) that exceeded comparable silicon devices by more than an two orders of magnitude.¹¹⁹ The high sensitivity, low LOD and fast turnaround time of the measurements and the ability to perform measurements within current testing frameworks without resorting to surface modification¹²⁰⁻¹²² or hazardous radioactive labeling (that is currently used to measure the activity of kinases like Cdk5) will promote the development of early diagnostic tools and novel therapeutics to detect and treat neurological conditions years before currently possible.

Lastly, LGFETs were used as direct biosensors (see *Chapter 1, Figure 7*) to detect the binding of streptavidin to a biotinylated extended sensing surface, where concentrations as low as 20 nM were measured. These streptavidin measurements were used as an example to demonstrate the sensitivity of LGFETs with a model protein that is commonly used for proof-of-concept biosensing measurements. Ultimately, the high sensitivity demonstrated by these LGFETs can be used to detect the incorporation of ion channels into lipid membranes and the ionic flux through these ion channels, as discussed in *Chapter 6*. Therefore, it is essential to demonstrate the ability of LGFETs

to directly detect proteins (as shown in Figure 7), and to be used as ISFETs to measure changes in ion concentration (as shown in Figure 8).

3.1.1 Motivation: FETs for Measurements of pH and Protein Detection

Rapid and sensitive pH measurements using field-effect transistors (FETs) are used in diverse applications that include determining the effects of ocean acidification on marine ecology,¹²³ biomanufacturing,¹²⁴ and low cost DNA sequencers.¹²⁵ However, drastic improvements in sensitivity and the limit of detection (LOD) of electronic pH transduction are needed to accelerate their widespread use in important biotechnology applications.

One such example is the measurement of the function of enzymes, protein catalysts that accelerate biochemical reactions and serve an integral role in ensuring normal cellular function,¹²⁶ where small changes in the solution pH act as a reporter of their function.^{120, 127} Disruptions in normal enzyme function are known to give rise to debilitating neurological conditions including Alzheimer's and Parkinson's disease,¹²⁸ several cancers,¹²⁹ and even chronic neuropathic pain.¹³⁰ As part of normal cellular function, Cdk5 catalyzes the phosphorylation of substrate proteins by the hydrolysis of adenosine triphosphate (ATP) and the transfer of a single phosphate group. This results in the release of one or more protons into solution, and thereby a small change in the pH. The change in pH typically varies by less than 0.005 units¹³¹⁻¹³² under physiological conditions (i.e., for normal living organisms) or an order of magnitude lower than the resolution demonstrated with state-of-the-art ion-sensitive field effect transistors (ISFETs).^{125, 133}

Under normal physiological conditions, Cdk5 is tightly regulated by either the p35 or p39 inhibitory proteins (Figure 17).¹³⁴⁻¹³⁵ Oxidative stress causes a 10 kDa membrane anchored fragment of p35 to be cleaved, forming the pathological activator p25, resulting in deregulation and delocalization of the complex to the cytosol.¹³⁶ The resulting pathological complex, Cdk5/p25, has higher activity than its physiological counterpart, Cdk5/p35, and participates in the indiscriminate phosphorylation of numerous proteins, which are known to result in neurofibrillary tangles that are a hallmark symptom of Alzheimer's disease.¹³⁷

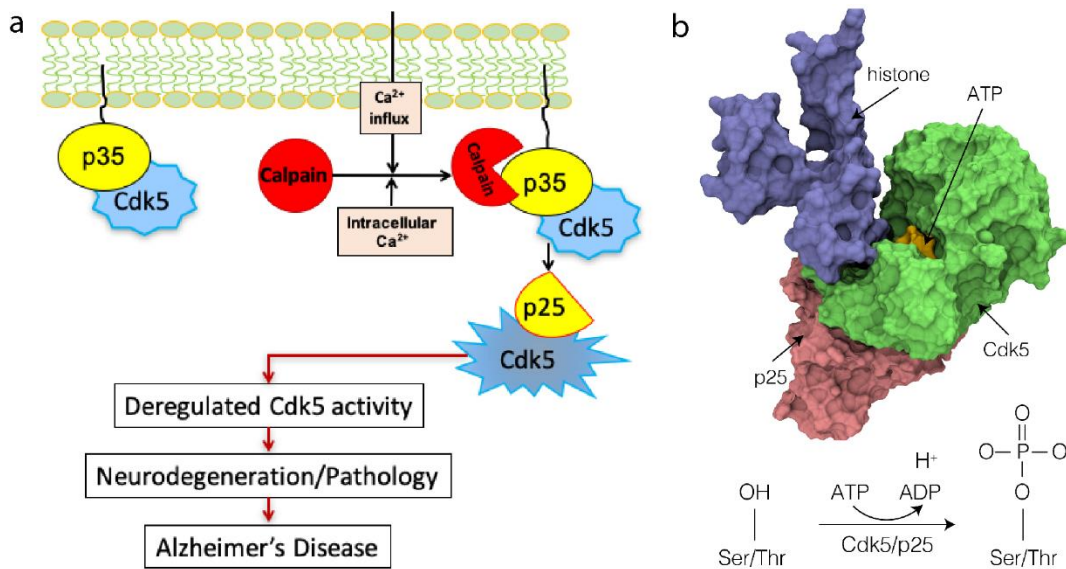


Figure 17. (a) The co-activator of Cdk5, p35, can be cleaved from oxidative stress resulting in a shortened, hyperactive form named p25.* The hyperactivity of Cdk5/p25 results in the over phosphorylation of substrates that is indicative of Alzheimer's disease. (b) Cdk5/p25 (red/green), phosphorylates serine and threonine side chains on the histone protein (purple) using ATP, which evolves ADP and protons (H⁺). *Figure 17a schematic courtesy of Harish Pant (National Institutes of Health).

Additionally, FETs have demonstrated promise as diagnostic tools to detect biomarkers such as proteins for the rapid diagnosis of cancer of disease.^{14, 127} Their exceptional sensitivity, label-free operation, size, and cost makes them an excellent alternative to traditional methods of protein detection such as enzyme-linked

immunosorbent assay (ELISA)⁹ and even label-free methods such as surface plasmon resonance (SPR),¹³⁸⁻¹³⁹ which requires bulky optical equipment. However, similar to pH detection, drastic improvements in sensitivity and LOD are needed to expand the use of FETs for biosensing applications, as well as improvements in the reproducibility of performance and unification of operation so that FET performance can be compared easily between assays that target the detection of various biomarkers. Efforts to improve the reproducibility of FET performance, which aims to minimize the calibration necessary to operate FETs for biosensing experiments, is covered in *Chapter 2*.

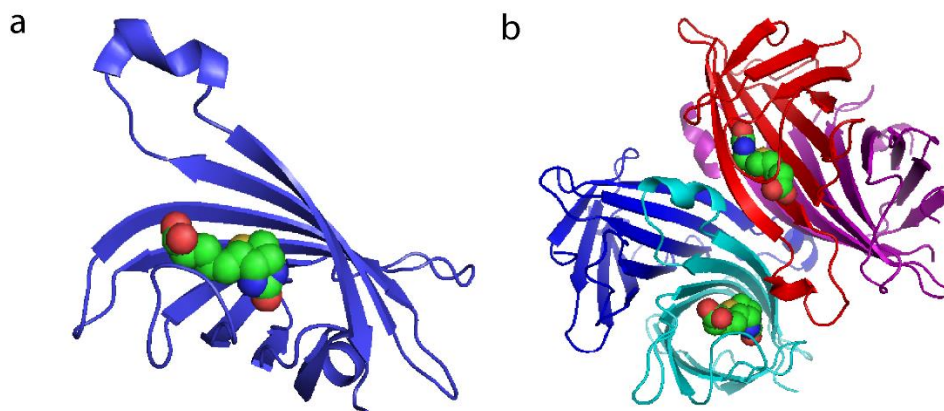


Figure 18. (a) A single monomer of streptavidin represented with secondary structure (*indigo*) bound to a biotin molecule represented by spheres (carbon, *green*; oxygen, *red*; nitrogen, *blue*; sulfur, *yellow*). (b) A native tetramer of streptavidin with tetramers colored *indigo*, *red*, *purple*, and *cyan*, with two biotin molecules colored with the same representation as in (a).

In this chapter, in addition to demonstrating the pH detection capabilities of FETs, the capability of FETs to detect the protein streptavidin is presented. Streptavidin was chosen because of its wide use as model protein for biosensing studies including previous studies of FETs.^{8, 140-143} Streptavidin (Figure 18) is widely used as a model protein for FET biosensing because it has a charge of $-7.2 e$ at pH 7.4 and has extremely

high affinity for the biomolecule biotin ($K_d \approx 10^{-15}$ M). Moreover, biotin can be immobilized onto a FET sensing surface using short hydrocarbon or polyethylene glycol (PEG) chains which it and subsequently bound streptavidin within a Debye length, λ_D of the sensing surface.¹⁴⁴⁻¹⁴⁶ Streptavidin's high affinity for biotin also yields high specificity which is an essential component of biosensing as discussed in *Chapter 1*. Lastly, streptavidin has been shown to have direct clinical relevance in capturing biomarkers such as biotinylated interferon γ (MIG) which is implicated in autoimmune diseases and inflammation.¹⁴⁷

3.1.2 Background: Ion-Sensitive FETs (ISFET) as Biosensors and FETs for Streptavidin Detection

Several techniques have been developed over the past century for more accurate measurements of solution pH. The Harned cell is the primary pH measurement standard,¹⁴⁸ but it requires an elaborate setup and long equilibration times making it unusable in the measurement of small and fast pH changes. As a result, pH measurements used in biotechnology applications rely extensively on electrode measurements or spectrophotometric techniques. These approaches lack adequate sensitivity and resolution for accurate measurements of enzyme mediated pH changes.¹⁴⁹⁻¹⁵⁰ In the past several years, there have been numerous developments in pH sensing technology using solid state devices that are potentially suitable for biological applications.^{125, 133, 151-152} Improved sensitivity and dynamic measurements have been demonstrated with ISFETs¹³³ and more recently dual-gate silicon FETs.¹⁵¹ In the latter case, pH sensitivity was shown to be approximately two-fold higher than the Nernst potential of 59 mV/pH at room temperature.¹⁵² Notably, the LOD of ISFETs has been reliably demonstrated to be 0.05 pH units.^{125, 133} The LOD for these devices could be

lower if the device parameters are optimized¹⁵³ or if the measurements are performed under a very narrow bandwidth.¹⁵⁴ However, resolution that is adequate for enzyme measurements under physiological conditions are yet to be experimentally realized with silicon FETs. These limitations have required FET-based enzyme catalyzed phosphorylation assays to be performed at concentrations that are about two orders of magnitude higher than physiological values, precluding their use in diagnostic and therapeutic development applications.^{121, 127, 155}

Several FET geometries, including nanowires,^{122, 141, 143, 145, 152, 154, 156-157} ribbons,^{127, 142, 158} and gaps,¹⁵⁹⁻¹⁶¹ have also been developed over the last couple decades for the detection of proteins such as streptavidin. These FETs are generally silicon-based, but more recently have been fabricated with 2D materials including MoS₂ and graphene. However, in addition to the aforementioned issues with reproducible fabrication and performance, the sensing gate or gate oxide is generally directly functionalized with a biorecognition element which only allows for a single experiment to be performed with a FET unless the sensing surface is regenerated, which is not trivial in most cases. Therefore, techniques such as extended gate configurations, as is explored by this work, are necessary to allow for the repeatable use of FETs for protein detection. Additionally, novel methods of FET operation, such as the closed-loop PID control explored in this work, are needed to improve SNR and ultimately LOD for protein detection using FETs.

3.2 Materials and Methods

3.2.1 Fabrication of Dual-gated Ionic Liquid-gated Field-Effect Transistors (FETs) and Design Comparison to Solid-state FETs

Fabrication details for the SSFETs is described in *Chapter 2*; however, for direct comparison to the LGFETs with respect to device geometry, a different FET array pattern was used, as shown by the optical image of an SSFET array (Figure 19a) where the *inset* shows a zoomed in image of the MoS₂ channel. Figure 19b shows a single SSFET from a FET array as hybrid schematic and circuit diagram. For the fabrication of LGFETs, instead of the deposition of a top-gate oxide, a small droplet of Diethylmethyl(2-methoxyethyl)ammonium bis(trifluoromethylsulfonyl)imide ionic liquid (DEME-TFSI IL; Sigma Aldrich, St. Louis, MO, p/n 727679, see Figure A10) was carefully applied onto the devices using a micromanipulator under an optical microscope. The droplet was sized to cover the MoS₂ monolayer and the gate electrodes,¹⁶²⁻¹⁶³ as seen in the optical image of LGFET array in Figure 19c and shown schematically for a single LGFET in Figure 19d. It is important to note that for good ionic liquid-gate coupling with the device's channel, the area of the gate electrodes that is in contact with the ionic liquid was designed to be much larger than the combined area of the source, drain contacts, and MoS₂ channel that are in contact with the ionic liquid. Gate leakage was verified by measuring the current across the ionic liquid upon application of a potential across two patterned gate electrodes.

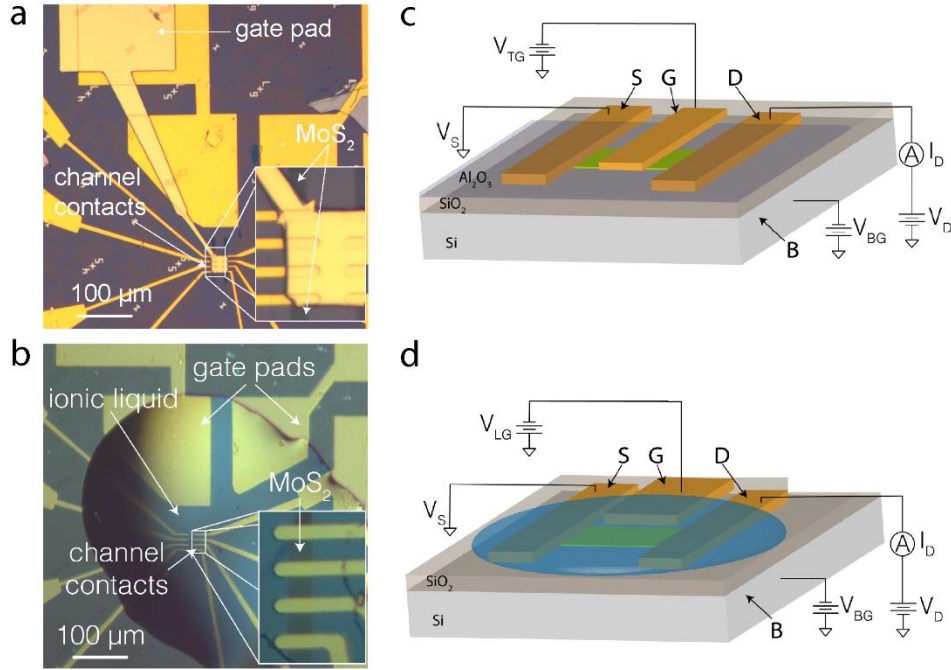


Figure 19. (a) Top view optical image of a solid-state field-effect transistor (SSFET) array. *Inset:* zoomed in view of the MoS₂ channel and source and drain contacts under a solid-state top-gate. (b) Hybrid schematic and circuit diagram of an SSFET. (c) Same as for (a) for an ionic-liquid gated FET (LGFET) with *inset* depicting the MoS₂ channel and source and drain contacts under an ionic liquid droplet. (d) Same as for (b) for a LGFET. Schematic abbreviations: *S* (source), *D* (drain), *G* (top-gate), *B* (back-gate), where abbreviations are used as subscripts for applied potentials and measured currents (where top-gates are specified as either *TG* (solid-state top-gate) or *LG* (ionic liquid-gated top-gate)).

3.2.2 Quantum Capacitance Model and Time-Series Measurements and PID Control

For a single layer MoS₂, SSFET, the relationship for α can be described with equation (1) (see *Section 1.2.1*) because the quantum capacitance of the MoS₂ (C_Q) is much greater than the capacitance of the top-gate oxide (C_{TG} , *i.e.*, $C_Q \gg C_{TG}$), which in this work was 20 nm of Al₂O₃ (see *Chapter 2*). However, for a single layer MoS₂ FET, C_Q is less than the capacitance of the ionic liquid (C_{LG}), and therefore a quantum capacitance model is needed for liquid-gated FETs. For single layer MoS₂ FET under positive ionic liquid-gate bias, the relationship between gate voltage, V_{LG} , and the channel charge carrier density, n_{ch} , is given by^{16, 107}

$$V_{LG} - V_{t,LG} - V_{FB} = \frac{E_g}{2q} - \frac{k_B T}{q} \ln \left[\exp \left(\frac{n_{ch}}{g_{2D} k_B T} \right) - 1 \right] + \frac{q n_{ch}}{C_{LG}} \quad (9)$$

where $V_{t,LG}$ is device threshold voltage, V_{FB} is the flat band voltage, E_g is material band gap, q is elementary charge, k_B is Boltzmann's constant, T is the temperature in Kelvin, g_{2D} is the band edge density of states, and C_{LG} is the liquid-gate capacitance. For a fixed V_{LG} , $V_{t,LG}$ is calculated as a function of channel carrier density:

$$V_{t,LG} = V_{LG} - V_{FB} - \left\{ \frac{E_g}{2q} - \frac{k_B T}{q} \ln \left[\exp \left(\frac{n_{ch}}{g_{2D} k_B T} \right) - 1 \right] + \frac{q n_{ch}}{C_{LG}} \right\} \quad (10)$$

Using equation 10 in combination with equations 6 – 8 (see *Section 2.2.2*), $V_{t,LG}$ and C_Q were calculated as a function of n_{ch} . Since C_{TG} and C_Q are in series as seen from Figure 21a, $C_{total(top)}(C_Q) = C_{LG} \times C_Q / (C_{LG} + C_Q)$. Similarly, the back-gate capacitance, $C_{total(back)} = C_{BG} \times C_Q / (C_{BG} + C_Q)$, where C_{BG} is the back-gate oxide capacitance. Moreover, since $C_Q \gg C_{BG}$ and $C_{BG} = \text{constant}$ under these limits, the expression for α is given by

$$\alpha = \frac{C_{total(top)}}{C_{total(back)}} \approx \frac{C_{LG} C_Q}{C_{BG}(C_{LG} + C_Q)} \quad (11)$$

and is limited by C_Q . At large values of n_{ch} , C_Q approaches its theoretical limit, $C_{Q,max}$, and α is constant. As n_{ch} decreases, C_Q decreases exponentially from $C_{Q,max}$ and a corresponding reduction in α is observed. The results of the model were compared with

experimentally measured values of α , which were extracted by taking the numerical derivative of V_{BG} ($V_{t,LG}$).

Time-series measurements were performed where the signal on the top-gate (V_{TG} or V_{LG}) was switched between an arbitrary function generator (HF2LI; Zurich Instruments, Zurich, Switzerland), a pH microelectrode (MI-4156; Microelectrodes, Bedford, NH), or the biotinylated sensing surface. An offset voltage V_o (GS200; Yokogawa Corporation, Tokyo, Japan) was then added to V_{TG} or V_{LG} using a summing amplifier (SR560; Stanford Research Systems Inc., Sunnyvale, CA). Each SSFET or LGFET was operated in a constant current mode using a PID controller that varied V_{BG} in response to changes in I_D . The channel current was first amplified using a current preamplifier (DLPCA-200; FEMTO, Berlin, Germany) with a transimpedance gain of 10^6 V/A. The amplified voltage was input to a digital PID controller (HF2LI; Zurich Instruments, Zurich, Switzerland), filtered using a 4-pole Bessel low pass filter (LPF) with a bandwidth of 5 kHz and then sampled at 25 kHz using a 14-bit analog to digital converter. The PID controller varied V_{BG} in response to changes in I_D with a bandwidth of 1 kHz ($K_P=496.1$, $K_I=9.242 \times 10^3$ s $^{-1}$ and $K_D=8.02$ μ s). The PID output was allowed to vary between -10 V to +10V to drive the back-gate voltage (V_{BG}).

3.2.3 C-V Measurements of Ionic Liquid Gates

In order to verify the capacitance (C_{LG}) of the ionic liquid, a LCR meter (E4980A; Agilent, Santa Clara, CA) was used to make 2-probe, AC capacitance measurements across the ionic liquid, measuring across a frequency range of 20 Hz to 2 MHz. Figure A11 shows representative results of these capacitive measurements, highlighting that at low frequency (where the FET operates for sensing) the capacitance

constant and approximately 1 nF (see Figure A11, *inset*). As seen in the inset, a negligible bias dependence of the capacitance was observed at all measured frequencies. The capacitance exhibits a less than 1% change over a ± 0.5 V range at the lowest frequency (20 Hz). Due to the FET design, there is not a constrained contact area of the ionic liquid on electrodes, therefore an optical estimate of $\approx 100 \mu\text{m} \times 100 \mu\text{m}$ was used as the area of metal plates that are in contact with the ionic liquid used in the capacitance measurement. This allowed an estimation of the specific gate capacitance to the liquid-gate to be $\approx 10.7 \mu\text{F}/\text{cm}^2$ at low frequency range (20 Hz to 2 kHz), in good agreement with values published in the literature.¹⁶⁴

3.2.4 Kinase Measurement Reagents

Activity measurements of Cdk5/p25 phosphorylation of histone H1 were performed by suspending 100 ng of the enzyme (C0745; Sigma Aldrich, MO) in 50 μL of 1 \times kinase buffer to obtain a final concentration of 18.5 nM. The Cdk5/p25 concentration was reduced five-fold for dynamic measurements to obtain a final concentration of 3.7 nM. A stock solution of 5 \times kinase buffer was prepared by suspending 25 mM β -glycerol (G9422; Sigma Aldrich, MO), 50 mM MgCl_2 (5980; Millipore, MA), 5 mM EGTA (E0396; Sigma Aldrich, MO), 2.4 mM EDTA (1002264786; Sigma Aldrich, MO), 1.25 mM MOPS (M1254; Sigma Aldrich, MO) in deionized water (DIW) and diluting further to form 1 \times kinase buffer. Solutions of the substrate protein were prepared by adding 2 mg/mL of histone H1 (10223549001; Sigma Aldrich, MO) to the assay to obtain the final concentrations as described in the main text. The phosphorylation reaction was triggered with a cocktail of dithiothreitol

(DTT) and ATP. The final concentration of the ATP and DTT solution was adjusted to 250 μ M and 5 mM in DIW respectively.

3.2.5 Streptavidin Measurement Reagents

Streptavidin detection measurements were performed by immobilizing biotin onto a gold sensing surface using a self-assembled monolayer (SAM) of biotin-terminated hydrocarbon chains provided by Sigma Aldrich (746622-1SET; Sigma Aldrich, MO). Gold sensing surfaces were prepared by depositing 10 nm of Ti and 200 nm of Au onto a 3" glass wafer with e-beam metal deposition and dicing the wafer into 9×9 mm dies. These dies were then cleaned with piranha and UV-ozone for 10 minutes each before functionalization with the SAM. 1 mg of the SAM was added to 1 mL of ethanol and then diluted 10X to yield 0.1X SAM in ethanol to achieve the optimal concentration for surface functionalization. After 1 hour, surfaces were rinsed in subsequent steps of excess ethanol, DIW, and 150 mM phosphate buffered saline (PBS, 1890535; Sigma Aldrich, MO) and assembled into a microfluidic cell composed of a well with the biotinylated surface as its base, inlet and outlet streams, and a top port which served as a port for a reference electrode that could be removed for streptavidin injection. An in-line reference electrode connected to the outlet stream was also tested to improve the usability of the cell. The surface area of the biotinylated well base exposed for to solution was approximately 7.1 mm^2 and the height of the well (to the base of the outlet port) was 7.1 mm, yielding a well volume of approximately 50 mm^3 .

Streptavidin, Alexa Fluor-488 conjugate (S11223; Sigma Aldrich, MO), was prepared by diluting a 2 mg/mL stock solution of streptavidin with PBS to final concentrations of 1 μ M, 200 nM, 100 nM, and 20 nM. The Fluor-488 fluorescence tag

permitted fluorescent measurements to be performed that verified the binding of streptavidin to the biotinylated surface (Figure A12). As a control for streptavidin binding, BSA was prepared by diluting a 5 mg/mL stock solution of BSA to a final concentration of 1 μ M. Either streptavidin or BSA were injected directly into the well using a micropipette so that kinetic information could be obtained by letting either protein diffuse to the surface, as opposed to flowing either protein in through the inlet and outlet streams, which were principally used to wash the cell and/or sensing surface in between experiments. A schematic of both the experimental setup for the kinase and streptavidin measurements is shown in Figure A13.

3.2.6 Cdk5 γ -³²P-ATP Measurements

Cdk5/p25 (C0745; Sigma Aldrich, MO) kinase activity was measured by collaborators at the NIH as described in the manufacturer's protocol with some modifications.¹⁶⁵ Briefly, kinase reaction was initiated by adding γ -³²P-ATP (final concentration of 50 μ M) to a preincubated substrate buffer cocktail and incubated at 30 °C for 1 hour. The reaction was terminated by spotting 20 μ l of the reaction mixture on a P81 phosphocellulose pad. Dried pads were washed 3 times in 75 mM phosphoric acid, followed by rinsing with 95% ethanol. The radioactivity of the spotted pads was measured in a liquid scintillation counter. Appropriate controls, without added phosphoryl acceptor substrates, were also run and the values were subtracted from the total counts obtained in the presence of substrate protein.

3.3 Results and Discussion

3.3.1 Comparison of Solid-state and Ionic Liquid-gated Field-Effect Transistor Performance

Performance for SSFETs and LGFETs fabricated with monolayer MoS₂⁷⁶ are shown for representative devices in Figures 20a and 20c, respectively, where the sensing surface was connected to the top-gate and where the silicon substrate was used as the back-gate. Extensive characterization of SSFETs can be found in *Chapter 2*, therefore this chapter will focus primarily on LGFET characterization and a comparison between SSFET and LGFET performance.

The devices described in this work are fundamentally different from dual-gate silicon FETs¹⁷⁻¹⁸ in that the asymmetric, capacitively coupled, gates in the SSFETs and LGFETs control the same atomically thin semiconducting channel giving rise to a large intrinsic gain in conjunction with ultralow noise performance. Furthermore, the measurement setup allowed LGFET performance to approach the intrinsic quantum capacitance limit of the channel material, as will be subsequently described.

The transfer characteristics of the SSFETs and LGFETs were measured by recording the drain current (I_D) as a function of the solid-state or ionic liquid top-gate potential (V_{TG} or V_{LG}) when the drain voltage (V_D) was held constant (as described in *Chapter 2*). The measurements were repeated for different back-gate voltages (V_{BG}) to estimate the signal amplification (α) due to the asymmetric capacitance of the top and back gates (Figures 20a and 20c). The SSFETs exhibited a dynamic range of ≈ 5 orders of magnitude in I_D and a subthreshold slope of 680 mV/dec while the LGFETs

exhibited a dynamic range of ≈ 5 orders of magnitude in I_D and a subthreshold slope of 145 mV/dec.

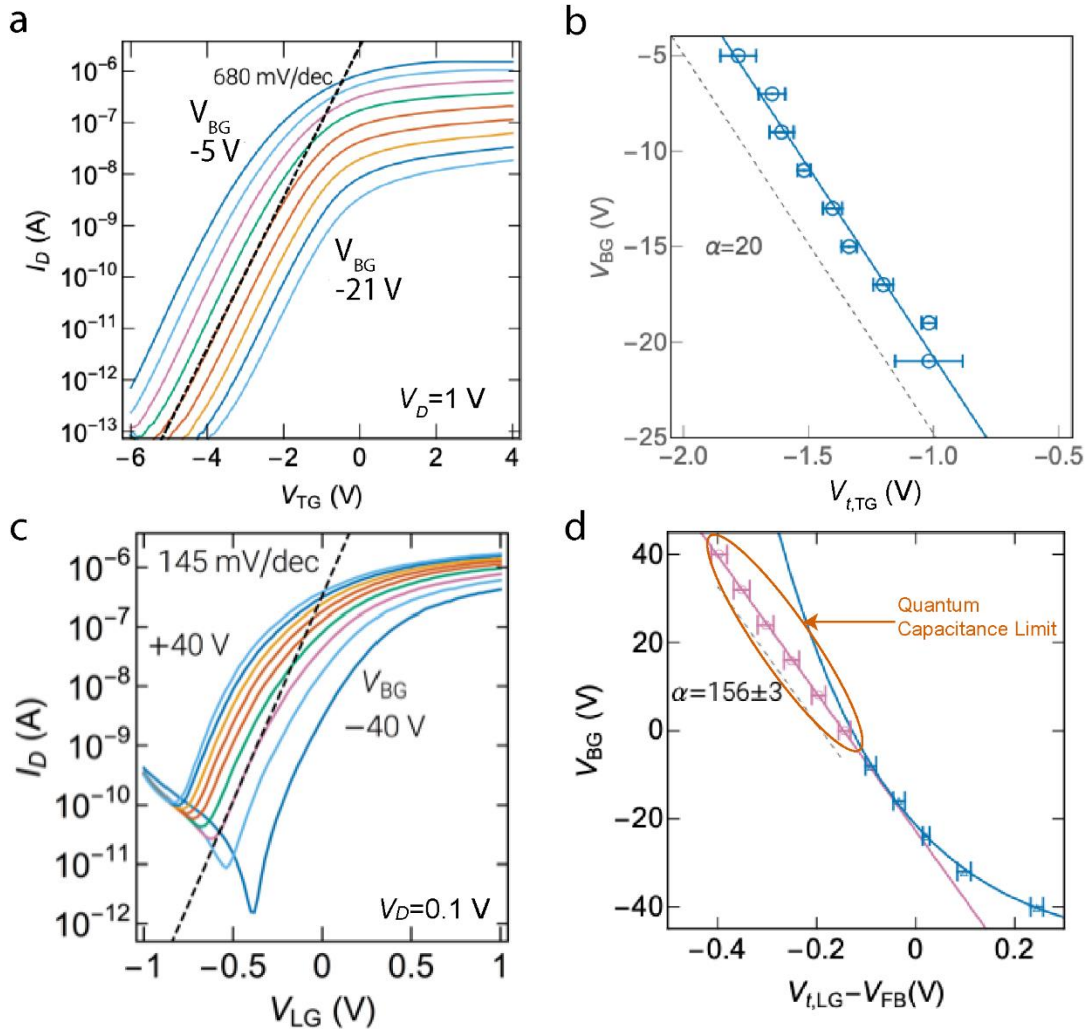


Figure 20. (a) Representative transfer curves for a solid-state field-effect transistor (SSFET) as a function of top-gate voltage (V_{TG}) and varying back-gate voltage (V_{BG}). (b) Relationship between threshold voltage (V_T) and V_{BG} , where the slope is the experimentally determined value for amplification (α) for a SSFET. (c) Representative transfer curves for a liquid-gated field-effect transistor (LGFET) as a function of liquid/top-gate voltage (V_{LG}) and varying back-gate voltage (V_{BG}). (d) Relationship between threshold voltage (V_T) and V_{BG} , where the slope is the experimentally determined value for amplification (α) for a SSFET in the quantum capacitance-limited region (orange), but not for outside this region. V_T is adjusted for V_{FB} to compare to theory (where the V_{FB} adjustment for (b) was small enough to be ignore).

For each curve in Figures 20a and 20c, the top-gate or liquid-gate threshold voltage ($V_{t,TG}$ and $V_{t,LG}$) was estimated from a linear extrapolation of the peak transconductance

to the x-axis, as shown in *Chapter 2*.¹⁶⁶ The value of $\alpha = dV_{BG}/dV_{t,TG}$ or $\alpha = dV_{BG}/dV_{t,LG}$ for representative devices was then determined numerically from the data in Figures 20b ($d=70$ nm) and Figure 20d ($d=300$ nm), where d is the thickness of the back-gate dielectric. Figure 20b depicts only one regime for V_{BG} as a function of $V_{t,TG}$ for the SSFET, as expected from the geometry (see *Section 3.2.2*) where α was constant and estimated to be 20 from the slope of the line in Figure 20b. Conversely, Figure 20d depicts two distinct regimes for V_{BG} as a function of $V_{t,LG}$ for the LGFET. At large and positive V_{BG} (Figure 20d, *pink*), where the device was in the limit of large 2D channel carrier density (n_{ch}), i.e., the quantum capacitance limit, α was constant and estimated to be 156 ± 3 . The error bars report the standard error defined as the standard deviation of the population mean. On the other hand, at negative V_{BG} and low n_{ch} (Figure 20d; *blue*), α decreased exponentially.

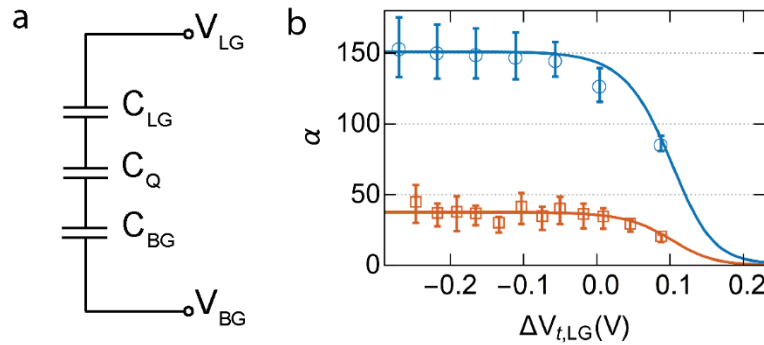


Figure 21. (a) Schematic for either a solid-state or liquid-gated dual-gated field-effect transistor (SSFET or LGFET). (b) Amplification (α) as a function of threshold voltage ($V_{t,LG}$) for two LGFETs with back-gate oxide thickness of 300 nm (*blue*) and 70 nm (*orange*). The solid line shows the theoretical model for quantum capacitance-limited device performance. Flatband voltage ($V_{FB} = -0.82$ V ($d=300$ nm) and $V_{FB} = +0.12$ V ($d=70$ nm) were subtracted from $V_{t,LG}$ to allow for direct comparison of the devices.

There is quantitative agreement between the model presented in sections 2.2.2 and 3.2.2 and measurements for two representative LGFET structures (with different back-gate oxide thicknesses), modeled as parallel capacitances (Figure 21a), shown in Figure 21b. In both cases, it was assumed $C_{BG}=0.0115 \mu\text{F}/\text{cm}^2$ ($d=300 \text{ nm}$) and $0.049 \mu\text{F}/\text{cm}^2$ ($d=70 \text{ nm}$), and $C_{LG}=10.7 \mu\text{F}/\text{cm}^2$ based on C-V measurements (see *Section 3.2.3*) and literature values.¹⁶⁴ $C_{Q,max}$ was directly calculated from Equation 11 to be $2.16 \mu\text{F}/\text{cm}^2$, and was in excellent agreement with the value of $2.2\pm 0.05 \mu\text{F}/\text{cm}^2$ extracted from a non-linear regression of the model to the data in Figure 21b. The only other free parameter in the model was the flat band voltage (V_{FB}), which depends in part on the fabrication process.⁸⁰ The extracted value of $C_{Q,max}$ was within $\approx 45 \%$ of the maximum theoretical value for monolayer MoS_2 , and more than two times higher than previous measurements.^{164, 167} This in turn allowed the devices to operate with high sensitivity when used for enzyme measurements. Furthermore, the ability to tune α with only the gate voltage is advantageous in biosensing applications to allow sensitivity to be offset for higher dynamic range.

3.3.2 Constant Current Mode Operation, Sensitivity, SNR, and LOD

The preceding results were used to maximize α when operating the SSFETS LGFETs in a constant current mode using a proportional-integral-derivative (PID) controller as shown in Figure 22a (SSFETs were also operated in constant current mode, but with α constant). The PID controller varied V_{BG} in response to V_{LG} to maintain a root mean square (RMS) channel current of 100 nA. PID performance was then compared with open loop operation where I_D was recorded in response to changes in V_{LG} . The signal connected to the ionic liquid-gate was setup to allow switching

between an arbitrary waveform generator to calibrate sensor performance or a biosensing element. In both cases, a fixed DC offset voltage (V_o) was added to V_{LG} to set the value of α (see *Section 3.2.2*).

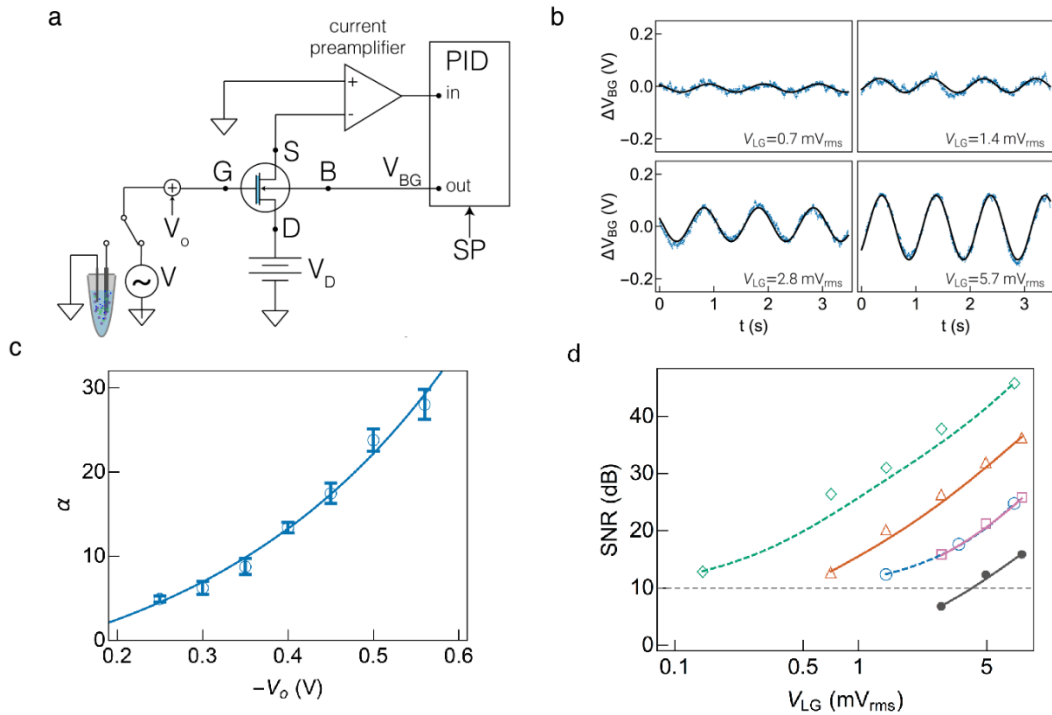


Figure 22. (a) SSFETs and LGFETs were set up in a constant current mode using a proportional-integral-derivative (PID) controller. I_D was held constant by continually adjusting V_{BG} in response to small changes to V_{TG} or V_{LG} . (b) The response of V_{BG} , under PID control, as a function of time is shown upon application of a 1 Hz AC sine wave signal with varying to the top-gate (shown as V_{LG} for a LGFET as an example with back-gate oxide thickness $d=300$ nm). (c) The amplification at the back-gate (α) increased with the applied liquid-gate offset voltage, V_o , allowing the device gain to be smoothly tunable. The error bars report the standard error. (d) The signal-to-noise ratio (SNR) was extracted with a bandwidth of 5 kHz as a function of AC signal amplitude for devices operated under PID control and in open loop (gray). For devices fabricated with either 300 nm (pink = 13; and orange = 42) or 70 nm (blue = 5; and green = 50) back-gate oxide thickness, the SNR under PID control was higher than under open loop operation.

An example of device calibration is shown where a 1 Hz sine wave was applied to V_{LG} for the LGFETs (Figure 22b). Figure 22b shows the change in V_{BG} ($d = 300$ nm) under PID control with $V_o = -0.56$ V for sine wave amplitudes of V_{LG} ranging from 0.7 to 5.7 mV_{rms}, which resulted in $\alpha = 28$. Tuning V_o allowed sensitivity to be smoothly

offset for dynamic range with the highest α realized when operating near the linear regime determined from Figure 20d. Using this approach, α was tuned smoothly from 5 ± 0.4 to 28 ± 1.8 when $d=300$ nm or from 5 ± 0.5 to 50 ± 1.5 when $d=70$ nm (Figure 22c). Moreover, the measured values of α were consistent with those in 21b, and more than an order of magnitude higher than dual-gate silicon FET measurements.¹⁸

The signal-to-noise ratio (SNR) is a true measure of sensor performance as introduced in *Chapter 1*. To determine if the higher sensitivity of these FETs, relative to dual-gate silicon devices,¹⁸ translated to an improved LOD, the noise in V_{BG} and I_D were measured for an LGFET to estimate the SNR in PID and open loop modes, and for an SSFET in PID mode once it was established that SNR is less in PID mode. Figure A14 shows a representative power spectral density (PSD) of the back-gate voltage under PID control ($d=300$ nm) and channel current during open loop operation for an LGFET and of the back-gate voltage under PID control ($d=70$ nm) for an SSFET. The broadband noise under PID control was estimated using the expression $\delta V_{BG} = \sqrt{\int_{BW} S_{V_{BG}} df}$, from DC to the low pass filter bandwidth of 5 kHz and found to be 5.8 mV_{rms} ($d=300$ nm; Figure A14) and 1.8 mV_{rms} ($d=70$ nm; Figure A14) for the measured LGFET, decreasing as expected with the back-gate oxide thickness, and 16.4 mV_{rms} ($d=70$ nm; Figure A14) for an SSFET. Furthermore, δV_{BG} was found to be invariant with V_o , and thereby α , over the measured range of biasing conditions. The channel current noise in the open loop case, $\delta I_D = \sqrt{\int_{BW} S_{I_D} df}$ was 700 pA_{rms} for the LGFET (Figure A14). The SNR was estimated using the expressions $20 \log_{10}(V_{BG}/\delta V_{BG})$ under PID control and $20 \log_{10}(I_d/\delta I_d)$ in open loop mode and shown

in Figure 22d as a function of V_{LG} . For a bandwidth of 5 kHz, SNR was found to increase ≈ 3 -fold ($\alpha=13$, $d=300$ nm) to ≈ 30 -fold ($\alpha=50$, $d=70$ nm) under PID control when compared to open loop operation.

The device structures described here are fundamentally different from silicon-based dual-gated FETs described in previous studies.¹⁷⁻¹⁸ In those devices, it was interpreted that two channels were formed and controlled independently by the top and bottom gates. In constant current mode, when the device was operated in the inversion-inversion regime, changes in the gate potential at one interface that drive the corresponding channel into strong inversion (increasing channel current), cause the other channel to be placed into weak inversion (with higher noise). Regardless of the polarity of the applied potential at the sensing gate, the overall channel current noise is dominated by the channel in weak inversion. Channel noise could be further limit SNR when the devices are operated in the inversion-depletion regime, for example as demonstrated with ultra-thin body double-gated silicon FETs.¹⁸ In this case, the noise is dominated by the depleted channel and should result in lower performance compared to the inversion-inversion regime. Furthermore, this effect becomes more pronounced with increasing gain. As a result, extensive work with such devices has shown no measurable improvement in SNR of silicon devices despite large improvements in the sensitivity.¹⁷ In contrast, ultra-thin channels formed with 2D materials have a single conducting channel controlled by both the top ionic liquid-gate and bottom SiO_2 back-gate. Because the channel can always be placed in the inversion regime, the relative noise is low over a wide range of biasing conditions leading to improved SNR with these devices.

3.3.3 Ion Sensitive pH Measurements

First, the LGFETs were used to remotely measure the pH of buffered solution with high sensitivity. In these static measurements, I_D was measured as a function of V_{BG} when a pH sensor measuring standard buffer solutions was connected to the liquid-gate as seen in Figure 23a (*inset*). The change in the back-gate threshold voltage, $V_{t,BG}$ for each measured pH from 4 to 10 is apparent from the data in Figure 23b and was found to be linear (Figure 23a) as a function of pH. The measurement sensitivity was estimated to be 4.4 V/pH or $\approx 75\times$ higher than the Nernst limit of 59 mV/pH at room temperature¹⁵² (Figure 23a; $\alpha=159$) and is a function of the device's intrinsic α . These measurements served as a demonstration of the maximum capabilities of an LGFET; subsequently both SSFETs and LGFETs were used to remotely measure pH over a physiologically relevant pH range ($\approx 6.7 - 7.5$ pH).

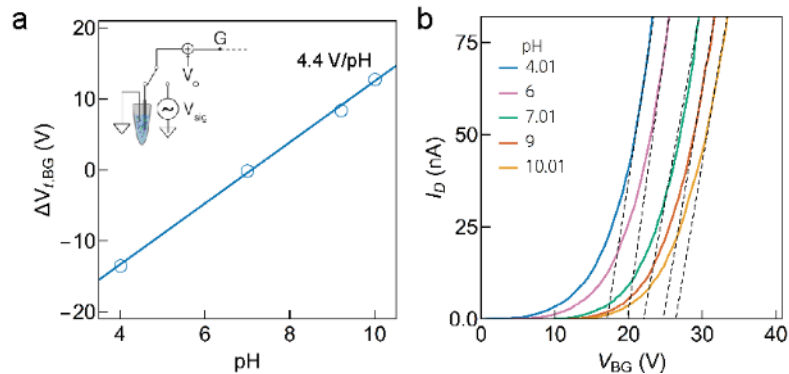


Figure 23. (a) Change in back-gate threshold voltage ($\Delta V_{t,BG}$) as a function of the solution pH showed a linear response over the measured range. When using a 300 nm SiO₂ back-gate, the pH sensitivity was found to be 4.4 V/pH. (*inset*) Measurements of pH were performed by connecting the ionic liquid-gate (G) to a pH sensing element. The dashed line shows the connection to the field-effect transistor (FET) in Figure 21a. (b) pH sensitivity of buffered electrolyte solutions was extracted from the shift in $\Delta V_{t,BG}$. These static measurements were performed over a wide range of solution pH from 4.01 to 10.01.

Solution pH over this physiologically relevant range was measured with LGFETs and SSFETs operated in constant current mode using PID control to minimize measurement noise. Figures 24a and 24b show time-series measurements of a PBS solution at a bandwidth of 10 Hz for a LGFET and SSFET, respectively. A switch was used to alternatively connect the ionic liquid-gate or the solid-state top-gate to the PBS solution and to ground. Figures 24b and 24d show the change in V_{BG} as a function of solution pH. A linear least-squares fit to the data returned a slope of 2.1 V/pH for the LGFET and 0.25 V/pH for the SSFET (Figures 24b and 24d). The maximum value of α obtained in the constant current mode was constrained by technical limitations in the control electronics, which precluded measurements at the maximum value of $\alpha=159$ for a LGFET as seen from the static pH measurements in Figure 23a.

The minimum detectable value of V_{BG} under PID control, which is inversely proportional to SNR, is a function of the measurement bandwidth when SNR=3 (or ≈ 10 dB). This in turn allowed the estimation of the LOD (also referred to as δpH) at a temperature of 300 K. At a bandwidth of 5 kHz, the minimum detectable V_{BG} was estimated to be 3.8 mV for an LGFET ($\alpha=50$, $d=70$ nm) resulting in a $\delta pH=0.0013$ pH units for these conditions. At the same 5 kHz bandwidth, the minimum detectable V_{BG} was estimated to be 15.2 mV for an SSFET ($\alpha=20$, $d=70$ nm) resulting in a $\delta pH=0.04$ pH units for these conditions. Since the measurements of the kinetics of biomolecules are relatively slow, LOD was further improved at higher bandwidth. When the signal was measured with a bandwidth of 10 Hz, a value of $\delta pH=92\times 10^{-6}$ pH units was extracted for the LGEET, representing a greater than 10-fold improvement over state-of-the-art ISFET measurements,^{14, 123, 133, 154} and a value of $\delta pH=0.0019$ pH units was

extracted for the SSFET. Importantly, in contrast to measurements made with dual-gate Si FETs, the LOD improved for the LGFETs with increasing α as discussed above.

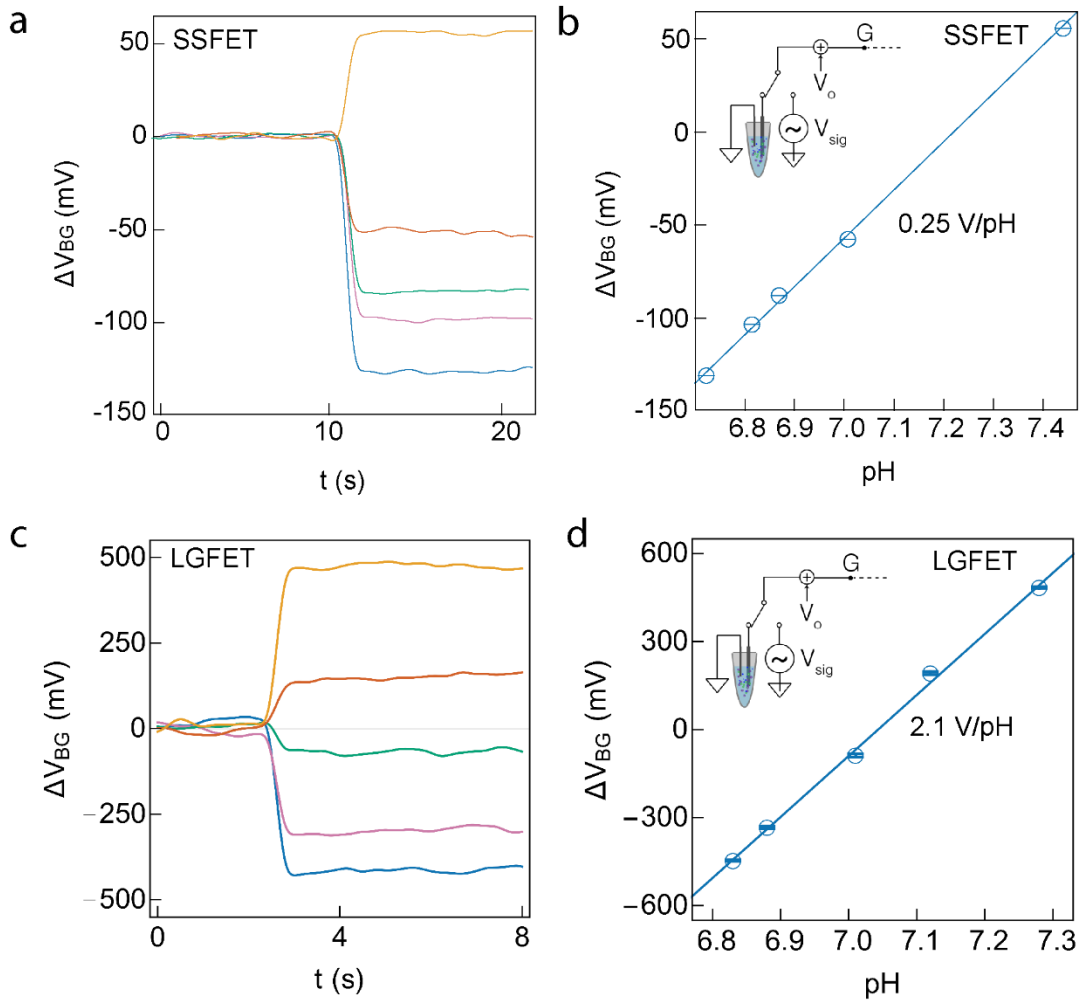


Figure 24. (a) Time-series measurements of V_{BG} response for a solid-state FET (SSFET) to buffered pH solutions. (b) Back-gate voltage (V_{BG}) response to varying pH buffer solutions in constant current mode with a bandwidth of 10 Hz shown for a SSFET with $\alpha = 8.5$ resulting in a sensitivity of 0.25 V/pH. The error bars represent the standard error. (*inset*) Measurements of pH were performed by connecting the top-gate (G) to a pH sensing element. The dashed line shows the connection to the field-effect transistor (FET) in Figure 21c. (c) Same as (a) for an ionic liquid-gated FET (LGFET) with $\alpha = 33$ resulting in a sensitivity of 2.1 V/pH. (d) Same as (b) for the same LGFET.

Measurement noise was estimated to be $\approx 60 \mu V_{rms}$ for the LGFETs and $\approx 700 \mu V_{rms}$ for the SSFETs by integrating the PSD of VBG from DC to 10 Hz. The noise spectra when measuring pH is shown in Figure 25a and Figure 25b for an LGET and a SSFET.

The SNR exhibited a minimum near pH 7 when V_{LG} or V_{TG} was small (≈ 68 dB at a sensitivity of 2.1 V/pH for an LGFET; ≈ 37 dB at a sensitivity of 0.25 V/pH for an SSFET) as shown in Figure 25c and 25d.

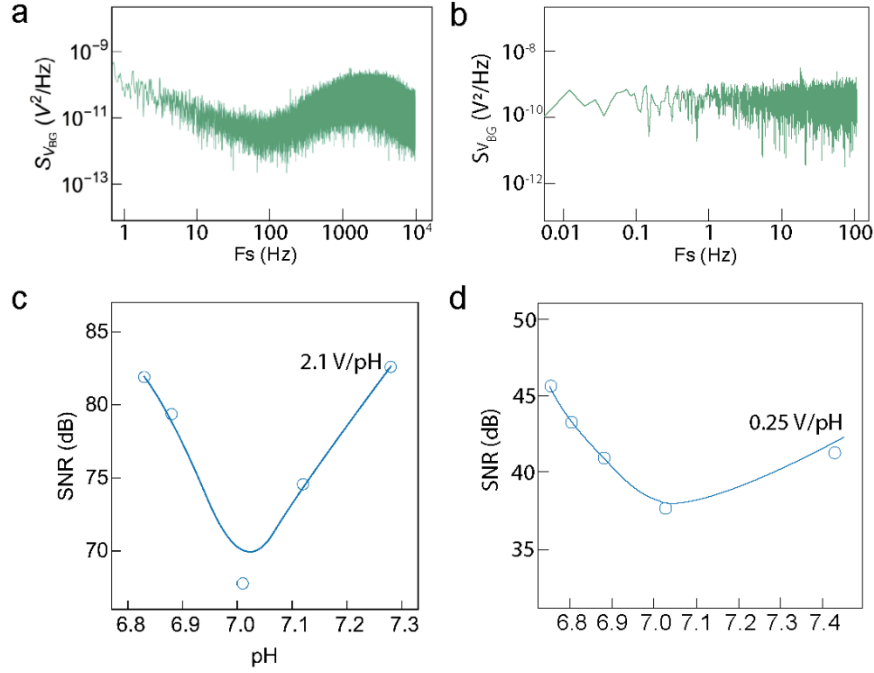


Figure 25. (a) Example of a power spectral density (PSD) for a LGFET used for pH measurements. (b) Example of a PSD for a SSFET used for pH measurements. (c) The LGFET measurement signal to noise ratio (SNR) was measured at a bandwidth of 10 Hz and found to average 75 dB. SNR was lowest in the vicinity of neutral pH (≈ 7) where liquid-gate voltage (V_{LG}) was very small. (d) The SSFET measurement signal to noise ratio (SNR) was also measured at a bandwidth of 10 Hz and found to average 42 dB. SNR was also lowest in the vicinity of neutral pH (≈ 7) where top-gate voltage (V_{TG}) was very small

The standard deviation of the back-gate voltage (σV_{BG}) measurements in Figure 24 were found to be 600 μV for the LGFET and 1210 μV for the SSFET. With the device gains, $\alpha=33$ and $\alpha=20$, LOD of the devices can be obtained using the expression $\sigma V_{BG}/(\alpha V_{Nernst})$, where $V_{Nernst}=59$ mV/pH is the Nernst voltage at room temperature. The LGFET pH LOD was determined to be 300×10^{-6} pH units and the SSFET pH

LOD was determined to be 1010×10^{-6} pH units. Furthermore, since SNR improves with increasing α as seen for an LGFET in 22c, the ultimate LOD of the LGFET at the maximum gain of the device ($\alpha=159$) is estimated to be 70×10^{-6} pH units. This is consistent with the value of 92×10^{-6} pH units extracted from an analysis of the noise floor (SNR 3; ≈ 10 dB) for a bandwidth of 10 Hz.¹⁵⁴

3.3.4 Kinase Activity Measurements

The multi-protein pathological complex, Cdk5/p25 (Figure 17), participates in the phosphorylation reaction shown in Figure 26a. Cdk5 mediated phosphorylation results in the release of a proton during ATP hydrolysis and the transfer of a single phosphate group to either a serine or threonine residue immediately preceding a proline.¹²⁰ Traditionally, this is measured using radioactively labeled adenosine triphosphate (ATP) analogs or fluorophores, which are expensive because they need specialized molecule labeling and handling, require hours to yield results, and often alter the kinase activity, thus limiting their effectiveness in rapid therapeutic screening.^{11, 168} Using this method, counts per minute (CPM) of radioactivity is measured under steady-state conditions for different concentrations and substrate which is then used to generate a plot of enzyme activity (Figure 26a). As a novel alternative to this method, LGFETs and SSFETs were used to measure the activity and kinetics of Cdk5 by detecting small changes in the solution pH during phosphorylation of the substrate protein, histone H1, and differences in their performance are discussed.

Figure 26b shows an example of how $\Delta V_{t,BG}$ values were estimated from an I_D-V_{BG} plot for different concentrations of histone H1 using an LGFET. These values were then used to generate Figure 26c, i.e., the relationship between histone H1

concentration and $\Delta V_{t,BG}$ under steady-state conditions, analogous to the substrate vs. CPM relationship traditionally presented. To account for instrument drift, each data point in the figure was measured differentially with a control sample that was identical to the measured vials except for the absence of ATP, thereby inhibiting the phosphorylation reaction. These differential measurements provide specificity for enzyme activity measurements in that they systematically eliminate changes to $\Delta V_{t,BG}$ caused by other factors such as negatively charged ATP.

The kinase activity was then estimated using, $s = \gamma \frac{[H1]}{k+[H1]}$, where k is a constant, $[H1]$ is the concentration of histone H1 and γ is a scaling constant. For the LGFET measurements in Figure 26c, k was estimated to be $17.5 \pm 1.3 \mu\text{M}$ from a non-linear regression of the model to the measured data, consistent with previously published activity measurements for the pathological Cdk5/p25 complex.¹³¹ The measurements in Figure 26c were compared against enzyme activity measurements obtained from a radioactively labeled γ -³²P-ATP assay, shown in Figure 26a.¹⁶⁹ The estimated value of $k=12.1 \pm 2.3 \mu\text{M}$ from those measurements was found to be statistically consistent with the LGFET measurements with 95 % confidence. The expected change in the solution pH was estimated using the expression $\frac{d[H^+]}{d \text{pH}} = 2.303 \frac{C_a K_a [H^+]}{(K_a + [H^+])^2}$, where C_a is the buffer concentration, K_a is the acid dissociation constant and $[H^+]$ is the proton concentration.^{132, 170} The change in pH was consistent with ≈ 3 phosphorylation sites on the substrate protein, assuming an electrolyte solution buffered with $C_a=250 \mu\text{M}$ 3-(*N*-morpholino)propanesulfonic acid (MOPS).

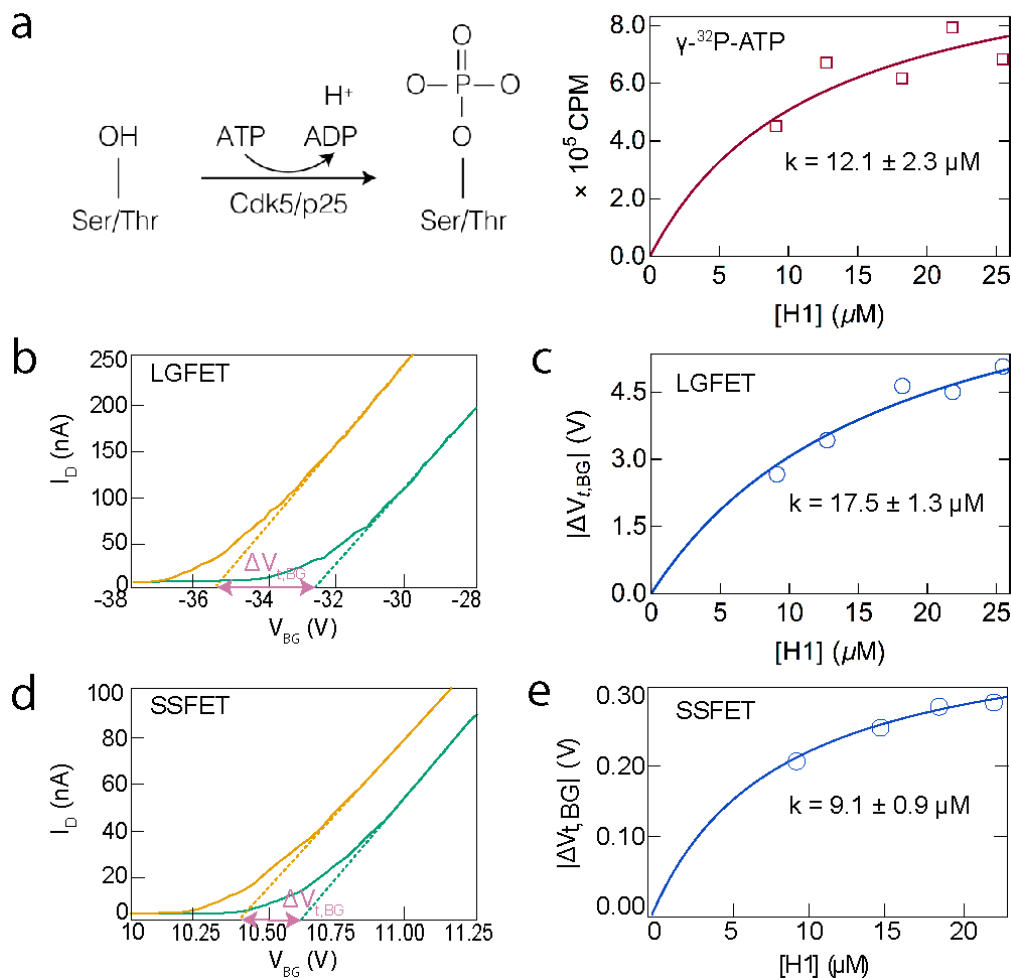


Figure 26. (a) *Left*, Cdk5/p25 phosphorylates serine and threonine side chains on the histone protein using ATP, which evolves ADP and protons (H^+). Radioactively labeled $\gamma\text{-}^{32}\text{P}$ (phosphate) is transferred to histone when such labels are used. *Right*, steady-state measurements of Cdk5 activity using radioactively labelled $\gamma\text{-}^{32}\text{P}$ -ATP as a reporter of Cdk5 activity. (b) Ionic liquid-gated field-effect transistors (LGFETs) measured the change in solution pH (quantified through threshold voltage ($V_{T,BG}$)) as a function of histone H1 concentration (H1) as a proxy for Cdk5 activity under steady-state conditions. (c) Solution pH was measured as change in $V_{T,BG}$, obtained from LGFET I_D - V_{BG} characteristics. (d) Solid-state field-effect transistors (SSFETs) used to obtain the same results as (b). (e) Solid-state field-effect transistors (SSFETs) used to obtain the same results as (c).

Figure 26d shows an example of how $\Delta V_{T,BG}$ values were estimated from an I_D - V_{BG} plot for different concentrations of histone H1 using an SSFET. Similarly to the LGFET, these values were used to generate Figure 26e. For the SSFET measurements in Figure 26e, k was estimated to be $9.1 \pm 0.9 \mu\text{M}$. The measurements in Figure 26e were

also compared against enzyme activity measurements obtained from a radioactively labeled γ - ^{32}P -ATP assay and found to be statistically consistent with 95 % confidence.

Both the LGFETs and SSFETs demonstrated adequate sensitivity and resolution to measure Cdk5 activity under steady-state conditions. However, over the range of histone concentrations used (9.2 – 25.8 μM for the LGFET and 9.2 – 22.1 μM for the SSFET), the LGFET demonstrated better sensitivity (0.13 V/ μM H1) than the SSFET (0.005 V/ μM H1), which is expected from the pH measurements shown in Figure 24. Furthermore, the LGFET demonstrated better resolution, i.e., the minimum difference between $\Delta V_{t,BG}$ (see *Figure 1*), which for these steady-state measurements was calculated to be 0.27 V, as opposed to the SSFET which demonstrated a resolution of only 0.078 V.

Advantageously, the FET-based measurements have a response time that allows the direct estimation of reaction kinetics and velocities as seen from Figure 27. The concentration of the Cdk5/p25 complex in these measurements was 3.8 μM (5-fold lower than the quantity used in Figure 26. For the LGFET (Figure 27a), a control sample without histone showed no change in the measured potential upon addition of ATP (*data not shown*). From Figure 27, it can be observed that upon addition of ATP there was a decrease in V_{BG} after ≈ 2 min. The polarity of V_{BG} is consistent with the release of protons into solution, which results in an increase in V_{LG} . The initial reaction velocities were estimated from a linear regression of the first 100 s data after a change in V_{BG} was detected and were found to increase monotonically with [H1]. Furthermore, the initial linear change in V_{BG} is consistent with an enzyme limited reaction.¹⁷¹ Finally, the time-course of each reaction in Figure 27 was fit with a first order rate law of the

form, $V_{BG} = \beta(1 - e^{-k_1 t})$, where β is a scaling constant and k_1 is a rate constant. The rate constant was consistent with previously reported values¹⁷¹⁻¹⁷² and estimated to be $k_1=0.18\pm 0.02$ per min, independent of the histone H1 concentration.

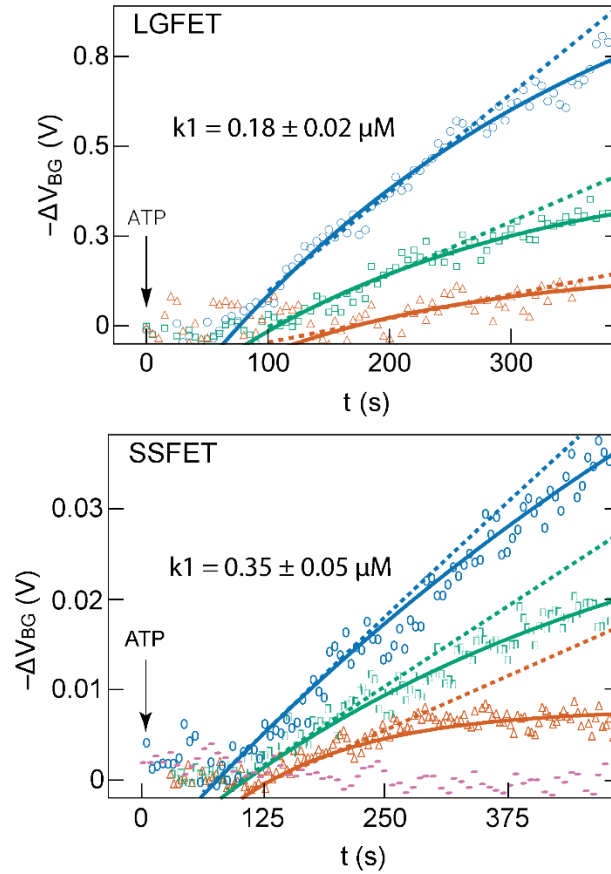


Figure 27. (a) Timeseries measurements of enzyme catalyzed phosphorylation obtained using a ionic liquid-gated field-effect transistor (LGFET) as a function of [H1] ($9.1 \mu\text{M}$ (*orange*), $12.7 \mu\text{M}$ (*green*), $18.2 \mu\text{M}$ (*blue*)) allow the direct estimation of the reaction dynamics. The solid lines depict the reaction kinetics model that describes the time course of phosphorylation, while the dashed lines represent an estimate of the reaction velocity during the first 100 s after a change in the signal was detected. (b) Same as (a) obtained using a solid-state FET with a control, $0 \mu\text{M}$ [H1], shown as *pink*.

For the SSFET (Figure 27b), a control sample without histone showed no change in the measured potential upon addition of ATP (*pink*). The decrease in V_{BG} in Figure 27b

is also consistent with the release of protons observed in Figure 27a, and using the same methods as the LGFET, k_I was estimated to be $k_I=0.38\pm 0.05$ per min, also independent of the histone H1 concentration, almost double the estimate obtained from the LGFET. Similarly to the steady-state measurements, while both the LGFETs and SSFETs demonstrated the ability to be used for real time measurements of Cdk5 kinetics, it is important to note that the better sensitivity of the LGFETs permitted measurements over a change of 0.8 V as opposed to only 0.035 V for the SSFETs.

3.3.5 Streptavidin Binding Measurements

The previous subsection described the use of FETs as indirect biosensors (see *Chapter 1, Figure 8*) to measure changes in pH, where pH served as a reporter for enzyme activity. In this subsection, FETs were used as direct biosensors (see *Chapter 1, Figure 7*) to detect the binding of the protein streptavidin to a biotinylated surface, where streptavidin is known to bind with high affinity to biotin. As discussed in the introduction of this chapter, streptavidin is commonly used in numerous biotechnology applications for protein detection because of this high affinity to biotin, as well as its relatively large electrostatic charge of $-7.2 e$ charge at pH 7.4 and stability in PBS. While specificity is determined for indirect FET biosensing by performing differential measurements relative to a control experiment, specificity for a biomarker can be achieved for direct biosensing by modifying the sensing surface with a biorecognition element that the biomarker binds to with high selectivity, for example, streptavidin to biotin.

However, because biotin must be immobilized some distance from the sensing surface, the ionic solution strength-dependent Debye Length ($\lambda_D \propto \sqrt{1/I}$, see

Chapter 1) becomes critical for achieving low limits of streptavidin detection, in that the applied surface potential from streptavidin is screened by ions in the electrolyte solution, i.e., it is reduced by a factor of $1/e$ for every radial distance λ_D it is bound from the surface. For 150 mM PBS, λ_D is calculated using equation (4) to be 0.76 nm. The value of λ_D increases to 2.41 nm and 7.61 nm for 0.1X, and 0.01X dilutions respectively. Therefore, it is advantageous to select or design an immobilization element that adheres the biorecognition element biotin within the dilution-dependent value of λ_D from the sensing surface to reduce the attenuation of the electric field from ionic screening. However, because the purpose of the streptavidin binding measurements in the scope of this work are proof-of-concept measurements, and it is not the primary goal of this work to minimize the LOD of streptavidin through FET biosensing, a standard biotin-terminated SAM provided by Sigma Aldrich was used for the following experiments (see *Section 3.2.5*).

Because the SAM details are proprietary, the exact distance the SAM immobilizes biotin from the surface is unknown, which prohibits calculating the distance streptavidin will be when bound to the sensing surface and assessing the subsequent electrolyte screening effects. However, it is also important to note that the Debye-Hückel model assumes rigid immobilization of biorecognition elements at a fixed distance and orientation from the sensing surface, whereas experimentally these elements are highly flexible and dynamic in solution, which can permit the orientation of bound streptavidin closer to the sensing surface in some cases. In short, while the Debye-Hückel model provides an initial estimation for how close to the surface a given biomarker must bind to reduce charge screening from the ionic solution, experiments

are still needed to determine the concentration of biomarker that a FET can practically detect.

Therefore, first a relatively high concentration of streptavidin, 1 μM in 1X PBS, was injected into a microfluidic cell (see *Section 3.2.5*) where the base of the cell was composed of a gold biotinylated surface connected to the top liquid-gate of an LGFET *via* an extended gate (an LGFET was chosen over a SSFET because the LGFETs exhibited better sensitivity for measurements of pH and Cdk5 activity). An in-line reference electrode was used to measure the change in surface potential from streptavidin binding relative to the solution potential (see *Section 3.2.5*). From this injection, an α -adjusted ΔV_{BG} of ≈ 60 mV was measured (Figure 28, *orange*, $\alpha = 50$), where ΔV_{BG} is the device drift-corrected back-gate potential applied by the PID controller to compensate for the increase surface potential applied to the extended top liquid-gate and $\alpha = \frac{\Delta V_{\text{BG}}}{\Delta V_{\text{LG}}}$ (see *Chapter 1*). Subsequently, the microfluidic cell was rinsed to remove any excess streptavidin, and a fresh biotinylated surface was prepared for an injection of 1 μM Bovine Serum Albumin (BSA). Because BSA is not known to bind to biotin, a BSA injection serves as a control for the streptavidin experiment to verify that the change of in surface potential was caused by streptavidin binding, and not, for example, by interactions between other charged particles (such as solution ions) and the sensing surface in the event the surface was not completely passivated by the SAM. Figure 28 demonstrates that the addition of 1 μM BSA yielded a ΔV_{BG} (*light blue*) no greater than device drift (*data not shown*) indicating that no detectable concentration of BSA bound to the biotinylated surface.

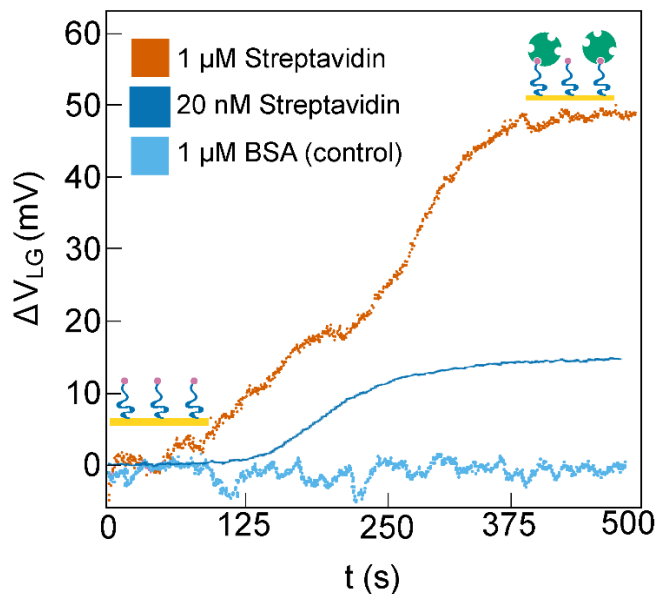


Figure 28. Liquid-gated field-effect transistors (LGFET) were used to measure the binding of streptavidin to a biotinylated sensing surface at concentrations as low as 20 nM.

Subsequently, a second LGFET ($\alpha = 14$) was used in an attempt to measure a lower concentration of streptavidin (20 nM). Here, 20 nM streptavidin in 1X PBS was injected into a microfluidic cell with a fresh biotinylated surface and a reference electrode was inserted into the top port of the microfluidic cell so a change in surface potential again could be measured against solution potential (see *Section 3.2.5*). An α -adjusted ΔV_{BG} of ≈ 15 mV was measured (Figure 28, *dark blue*), again not correcting for device drift.

While the limit of streptavidin detection by FETs is studied extensively in other works, the scope of this work is merely to demonstrate that the novel dual-gated, monolayer MoS₂ LGFETs used in this work are capable of detecting reasonably low concentrations of streptavidin (20 nM) through their amplification of the binding signal, linear response using a PID controller, and consistent operation in a high SNR regime. The ultimate goal of this work, as presented in *Chapter 6*, is to build a case that

these FETs can be used for the characterization of more complex proteins such as ion channels that are not currently being studied with FETs.

3.4 Conclusions

In *Chapter 3*, dual-gate SSFETs and LGFETs with atomically thin MoS₂ channels were demonstrated to be a robust and sensitive biosensing platform. The nearly 100-fold improvement in pH sensitivity above the Nernst value and order of magnitude improvement in the LOD over state-of-the-art silicon ISFETs at a bandwidth of 10 Hz for the LGFETs allowed the measurement of small changes in solution pH during enzyme mediated phosphorylation under physiological conditions. Additionally, SSFETs also demonstrated the necessary sensitivity and resolution to measure these small changes. This FET biosensing method eliminates the need for specialized labeling and hazardous material handling and can decrease the cost and complexity of enzyme activity assays appreciably. Another key advantage of the measurements is that they are time-resolved, enabling the estimation of both enzyme activity and kinetics in a single assay. Because signal transduction is performed remotely, the measurements are compatible with standard microtiter plates, and therefore amenable for use in high throughput screening to allow rapid evaluation of pharmaceutical candidates for neurological diseases.

The high sensitivity and SNR allowed measurements with 5-fold lower enzyme concentrations than physiological values and over an order of magnitude below previous demonstrations using FET. This in turn will enable new biomarker diagnostics from blood or cerebrospinal fluid to be developed for use at early stages of neurodegeneration where the changes to kinase activity are subtle and currently

undetectable.¹⁷³⁻¹⁷⁴ Importantly, these measurements can allow testing several years before any observable decline in cognitive function, allowing early interventions to be developed. The extended gate configuration of the sensors permit remote measurements, which allow them to be adapted for use in cell and tissue culture assays, where an increase in kinase activity has been correlated with pH imbalances.¹⁷⁵ Such measurements can allow assays that interrogate mechanistic behavior across multiple spatial scales – from test tube to cell culture experiments – to better quantify the origin of disease states.¹⁶⁵

Lastly, direct FET biosensing demonstrated with LGFETs for streptavidin detection indicates the ability of these FETs to directly measure the binding of a protein to a sensing surface. This will be essential for the proposed measurements outlined in *Chapter 6* that aim to characterize the function of ion-channels *via* indirect FET sensing of ionic flow through the channels, but at first must be able to detect when the channels incorporate into a lipid membrane. The following two chapters, *Chapter 4* and *5*, provide examples of how MD simulations can be used to model the effects of membrane lipid type on the function of ion channels the in the future will be immobilized in lipid membranes for FET biosensing.

Chapter 4: The Impact of Lipid Type on the Immobilization of the α -Hemolysin Ion Channel

(This chapter is published in: Guros, N.B., Klauda, J.B., and Balijepalli, A. The Role of Lipid Interactions in Simulations of the alpha-hemolysin Ion Channel-forming Toxin. *Biophysical Journal* **2018**, 115: 1720–1730.)

4.1 Introduction

To better understand the effect of the lipid membrane on the function of FET sensing surface-immobilized ion channels, MD simulations were performed on the ion channel alpha-hemolysin (α HL) in lipid membranes that were composed of either 1,2-diphytanoyl-sn-glycero-3-phospho-choline (DPhPC) or 1-palmitoyl-2-oleoyl-sn-glycero-3-phospho-choline (POPC). *Chapter 4* presents the highlights of these simulations, including the importance of lipid type in maintaining α HL structure and function, enabling direct comparison to biosensing experiments. While the two lipids studied are similar in structure, this chapter concludes that DPhPC membranes better match the hydrophobic thickness of α HL compared to POPC membranes. This hydrophobic match is essential to maintaining proper alignment of β -sheet loops at the *trans* entrance of α HL, which when disrupted creates an additional constriction to ion flow that decreases the channel current below experimental values. Agreement with experimental channel currents was further improved with sufficient lipid membrane equilibration and allowed the discrimination of subtle α HL conduction states with lipid type. Lastly, the effects of truncating the extramembrane cap of α HL and its role in maintaining proper alignment of α HL in the membrane and channel conductance is also explored. These results demonstrate the essential role of lipid type and lipid-protein interactions in simulations of α HL and serve as model to demonstrate how MD can be

used to predict the effects of immobilizing ion channels in lipid membranes for FET biosensing.

4.1.1 Motivation

Transmembrane proteins regulate the flow of ions, water, and biomolecules across membranes to control their concentrations within a cell, both through diffusion and active transport.¹⁷⁶⁻¹⁷⁹ Porins and ion channels like outer-membrane protein F (OmpF), potassium channel from *Streptomyces lividans* (KcsA), and gramicidin A (GrA) function in a wide variety of lipid membrane types, which impact their structure as well as function.¹⁸⁰⁻¹⁸² Previous experimental work reports the effects of membrane lipid composition, headgroup charge, and chain saturation, as well as membrane curvature and hydrophobic thickness on the conductive properties of porins and ion channels.^{61-62, 183-184} Tomita et al. reports that channel opening of β -barrel ion channels like α HL is maintained for a longer period of time in conical lipid membranes than in cylindrical shaped lipid membranes, resulting in a substantial difference in channel conductance.¹⁸⁵ Experimentally, evidence exists from as early as the 1980s demonstrating the difference in channel conductance for α HL in membranes composed of either phosphatidylcholine (PC) or a mixture of PC and phosphatidylserine (PS) lipids.¹⁸⁶ However, theoretical models comparing the effects of the lipid membrane type on ion channels are lacking, and are needed to reconcile differences between lipids used in modeling and experiment.

Beyond improving the biophysical understanding of ion channels, there is a practical need to understand the effect of lipid environment on ion channel function for biotechnology applications.¹⁸³ Specifically, α HL has been demonstrated as a strong

candidate for single molecule sensing applications because it forms an Ohmic channel across the lipid membrane.¹⁸⁷⁻¹⁸⁹ Channel current is reduced when a biomolecule obstructs the flow of ions as it passes through the channel; this reduction is proportional to the size and charge of the biomolecule,¹⁸⁷ potentially enabling clinical applications such as DNA and protein sequencing.¹⁹⁰⁻¹⁹² In the scope of this work, α HL also serves as an excellent model protein to demonstrate how immobilization of an ion channel in a lipid membrane affects its function, specifically with respect to the ionic current that an ion-sensitive FET could detect.

4.1.2 Simulation Approach

To date, there is a lack of MD simulation data that demonstrates the ability of MD to accurately reproduce experimentally-determined ionic current as a function of lipid membrane type, even through the use of various force fields (FFs, see *Chapter 1*)¹⁹³⁻¹⁹⁶. While MD has been used to assess the effects of ion type, pH, and electrical potential on α HL channel conductance,^{194, 197-198} studies on the effects of the lipid environment on α HL conductance are limited.^{180-182, 185} Generally, MD simulations of α HL are performed with either POPC, 1,2-dipalmitoyl-sn-glycero-3-phosphocholine (DPPC), or 1,2-dimyristoyl-sn-glycero-3-phosphocholine (DMPC) membranes, as noted by Desikan et al. who report the effects of these three lipid types using the MARTINI model; however, no conclusions regarding channel conductance are reported.¹⁹⁹

To address this shortcoming, this chapter reports the effects of lipid membrane type on α HL structure and channel conductance using all-atom MD simulations including the effects of immobilizing α HL in POPC versus DPhPC, the latter of which is

conventionally used for experimental measurements.^{196, 200-202} This was made possible only recently due to additions to C36 that include parameters for DPhPC.²⁰³ Furthermore, the importance of adequate equilibration for membranes containing α HL is examined.¹⁹⁶ Finally, this chapter describes the effects of truncating α HL similar to De Biase et al. by removing the cap (extramembrane) region to reduce the computational power necessary to perform such simulations, which increases with the number of atoms in the system.¹⁹³

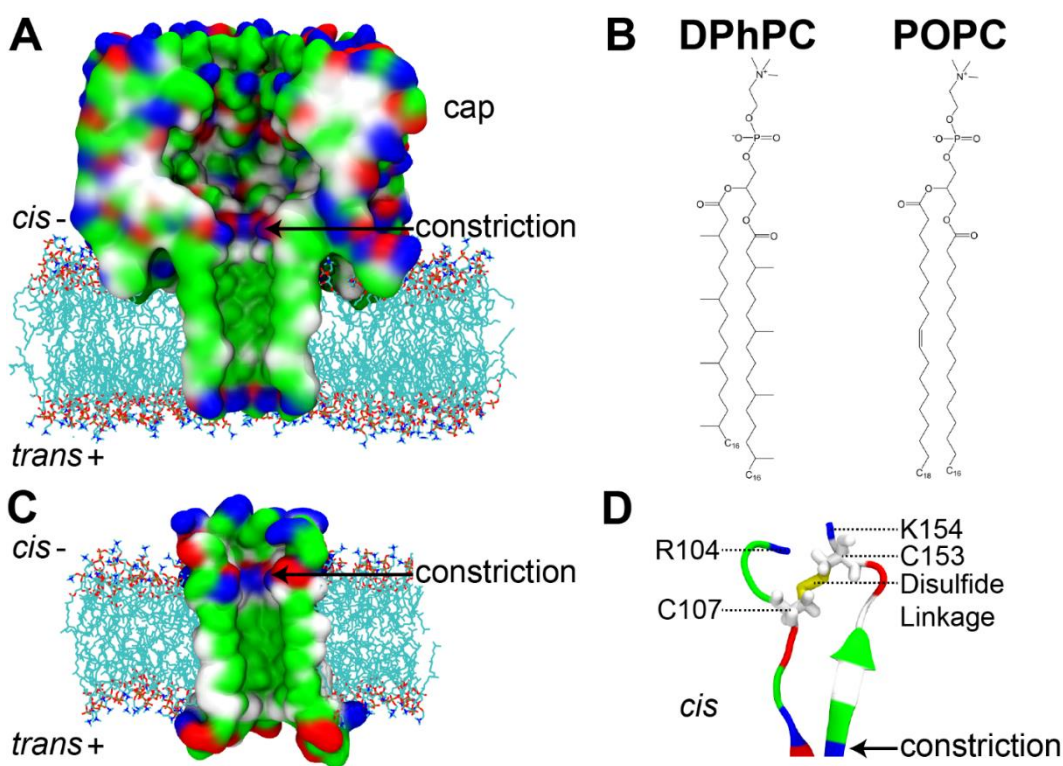


Figure 29. (A) Cross-section of α HL in a lipid membrane with α HL represented as an electrostatic surface colored by residue side-chain type (negative charge: *red*, positive charge: *blue*, polar: *green*, non-polar: *white*). Lipid heads and tails are represented with carbon: *cyan*, oxygen: *red*, nitrogen: *blue*, and phosphorous: *gold*. (B) Molecular structures of 1,2-diphytanoyl-sn-glycero-3-phospho-choline (DPhPC) and 1-palmitoyl-2-oleoyl-sn-glycero-3-phospho-choline (POPC) lipids depicting an unsaturated chain in the sn-2 position of POPC. (C) Cross-section of truncated α HL in a lipid membrane represented similarly as in (A). (D) Schematic of α HL truncation at R104 and K154 colored by residue side-chain type with disulfide linkage shown as *yellow*.

4.2 Materials and Methods

4.2.1 System setup and MD simulation Protocol

The CHARMM-GUI *Membrane Builder*²⁰⁴ was used to build protein-membrane systems (Figure 29A) with α HL (PDB ID: 7AHL²⁰⁵) or truncated α HL (Figure 29C) and lipid membranes composed of either DPhPC (CHARMM-GUI: PHPC) or POPC (Figure 29B). Each protein-membrane system was built in a tetragonal box containing a fully hydrated membrane, and sufficient K^+ and Cl^- ions to yield an overall 4M concentration, with an additional seven K^+ ions added to neutralize the system (Table 2). A high salt concentration was used to replicate experimental conditions used in biotechnology applications that use α HL. However, a higher salt concentration also results in additional electrostatic interactions between lipid head groups and salt ions, which increases the time needed for the lipid membrane to equilibrate.²⁰⁶

Eleven total trajectories are reported in this chapter (5 full-length and 6 truncated). For the full-length form, two simulations were simulated using a POPC membrane (Full_{POPC-SX}), two using a DPhPC membrane (Full_{DPhPC-SX}), and one using a POPC membrane and a 10 ns equilibration period (Full_{POPC-S3*}) reported by Balijepalli et al. (Table 2). Four additional trajectories were generated using the truncated form of α HL (β -barrel systems) in a POPC membrane (β -Barrel_{POPC-SX}) and two using the truncated form of α HL in a DPhPC membrane (β -Barrel_{DPhPC-SX}) in an attempt to replicate the conductance of the full form of α HL with reduced computational strain. These β -barrel systems contain α HL that is truncated at R104 and K154 (resulting in charged N- and C- terminals on R104 and K154) such that all residues with a charged side chain in the β -barrel portion were left intact (i.e., those involved in gating ions through the channel). The seven remaining segments were constrained to prevent β -strand unraveling by

removing non-gating residues I107 and F153 and replacing them with CYS residues that were linked via disulfide bonds (Figure 29D). The β -barrel systems trajectories are discussed in *Section 4.3.4*.

Table 2. Simulation parameters.

<i>System</i>	# of Lipids	# of waters	# of Ions (Cl ⁻ /K ⁺)	Channel Current (pA)
Full _{DPhC-S1}	288	39452	3664/3671	100.9
Full _{DPhC-S2}	288	39452	3664/3671	122.6
Full _{POPC-S1}	344	41106	3169/3176	60.9
Full _{POPC-S2}	344	41106	3169/3176	92.2
Full _{POPC-S3}	344	41106	3169/3176	116.7*
β -Barrel _{DPhC-S1}	288	23433	1814/1821	83.7
β -Barrel _{DPhC-S2}	288	23433	1814/1821	12.8
β -Barrel _{POPC-S1}	250	22380	1811/1818	89.9
β -Barrel _{POPC-S2}	250	22380	1811/1818	85.4
β -Barrel _{POPC-S3}	250	22380	1811/1818	33.0
β -Barrel _{POPC-S4}	250	22380	1811/1818	89.8
Experiment	-	-	-	150 \pm 3*

(*) - Denotes data published previously by Balijepalli et al.¹⁹⁶ Simulation data from Balijepalli et al. was obtained with 10 ns of membrane equilibration.¹⁹⁶

General MD simulation methods can be found in *Chapter 1*. These simulations used the TIP3P water model²⁰⁷⁻²⁰⁸ with the C36 FF²⁰⁹⁻²¹⁰ for lipids. The van der Waals interactions were smoothly switched off between 10 Å and 12 Å by a forced-based switching function.²¹¹ All the bond lengths involving hydrogen atoms were constrained using the SHAKE algorithm.²¹² Particle mesh Ewald²¹³ was used for electrostatic interactions with an interpolation order of 6 and a direct space tolerance of 10⁻⁶. NAMD⁵⁴ was used to perform the MD simulations at 298.15 K. After the standard CHARMM-GUI six minimization and equilibration steps (0.685 ns)²⁰⁴, the simulations were further equilibrated for 250 ns under constant semi-isotropic pressure (NPT; x = y and z varies independently) with the Nosé-Hoover Langevin-piston algorithm^{59, 214} to ensure complete membrane relaxation at a significantly high salt concentration, and

finally equilibrated for 10 ns under constant pressure and by fixing the membrane area (NPAT). All simulations were then run under constant volume and temperature (NVT) for 250 ns with a homogenous electrical field applied in the z direction proportional to -40 mV. An initial replicate was performed for 200 ns with a Langevin coupling coefficient of 1 ps^{-1} applied to only protein and lipid atoms. For additional replicates, a Langevin coupling coefficient of 1 ps^{-1} was applied to all non-hydrogen atoms to maintain constant temperature. The initial replicate served as a comparison set to verify the dampening effects to non-protein and non-lipid atoms would not significantly alter simulation results.

4.2.2 Analysis Methods

To assess adequate membrane relaxation, surface area per lipid was plotted over time. Surface area per lipid was calculated by taking the simulation cell x-y plane area (with the x-y ratio held constant at one) and subtracting the cross-sectional surface area of the β -barrel portion of α HL (1018 \AA^2) which spans the height of the membrane. The resulting value for the surface area occupied by lipids was divided by the number of lipids in one leaflet to yield an average value for surface area per lipid. Membranes were determined to be adequately equilibrated when the moving average of the surface area per lipid reached a stable value. When this moving average no longer fluctuated greater than 0.5 \AA^2 , membranes were determined equilibrated.

Membrane (hydrophobic) thickness was calculated from the average distance between carbonyl carbon atoms just below the lipid head groups in annular segments around the center of the protein. The average height (with the membrane centered at $z = 0$) of carbonyl carbon atoms was taken by averaging the z coordinates of all

carbonyl carbon atoms in either the outer or inner leaflet within a certain radial distance window relative to the center of the protein and subtracting the inner leaflet average from the outer leaflet average. These thicknesses are compared both to experiment and thicknesses determined through MD simulations performed by Zhuang et al.²¹⁵ calculated from the peaks of the electron density profiles for the carbonyl group. In this way, an identical comparison is made between hydrophobic thicknesses defined as the heights of the carbonyl carbon atoms, as opposed to comparing with the ‘2D_c’ distance which is the distance between the midpoints of the volume probability profile of a membrane’s hydrocarbon acyl chains.²¹⁶

The channel radius for the transmembrane region of α HL was calculated using the Hole program²¹⁷ over the length of the protein along its principal z axis orthogonal to the membrane. Channel radius values were averaged over 10 ns blocks to yield 25 unique block averages for each 250 ns trajectory. Average channel radius values over the entire 250 ns for each trajectory were also calculated. Protein tilt was calculated by taking the arccosine of the principal z axis of the transmembrane region of α HL orthogonal to the membrane.

Interaction energy between α HL and membrane lipids was calculated using CHARMM and includes contributions from electrostatic and van der Waals interactions. Three total interaction energies were calculated (defined in Table A1): protein – membrane, *trans* loops – membrane, and constriction – membrane.

Transmembrane current was calculated for the channel using Equation 13:

$$i = \frac{(N_{K^+} - N_{Cl^-}) \cdot q}{\Delta t} \quad (12)$$

where i is the current, N_{K^+} and N_{Cl^-} are the accumulations of crossings of potassium and chloride ions (respectively) across the channel at the plane $z = 0$ (the approximate center of the membrane), q is the charge of a single ion, and Δt is the time interval. The ionic current is calculated from the slope of the line created by plotting the change in accumulation of ion crossings through the channel over time. Reported values for the transmembrane current were calculated by taking block averages of the current over 20 blocks. Current values are reported in picoamperes assuming a charge of 1.6×10^{-19} C per ion and calculating the current over the course of the 250 ns trajectories.

4.3 Results and Discussion

4.3.1. Membrane Equilibration

Membrane equilibration, or relaxation, is critical for simulations of both pure lipid and protein-containing membranes to replicate experimental conditions. Previous MD simulations of α HL in a lipid membrane report equilibration periods as short as 10 ns,^{193-194, 196} using an energy relaxation criterion to determine convergence. The simulations presented in this chapter suggest that surface area per lipid (SA/lipid) is a better metric to determine membrane equilibration, particularly in the presence of an ion channel, where lipid packing around the protein modulates its function. For example, after a short 10 ns equilibration of α HL in a POPC membrane (FullPOPC-S3*), the reported SA/lipid was 25% greater than the experimental value for a pure lipid membrane.²¹⁶ It was found that an equilibration time of at least 200 ns was necessary to allow the SA/lipid to converge to its steady-state value (Figure A15). Notably, the equilibration time to reach steady-state was found to be independent of lipid type for either POPC or DPhPC in the presence of α HL.

SA/lipid averages and standard errors calculated from 20 ns blocks of the moving average are tabulated in Table 3. With longer equilibration, it was found that the simulated values of SA/lipid were within 2 % of experiment for pure DPhPC membranes (Full_{DPhPC-SX}), and within 1 % for pure POPC membranes (Full_{POPC-SX}). For both lipid types, SA/lipid decreased slightly in the presence of α HL compared to a pure lipid membrane. This may be a result of lipid rearrangement in the vicinity of α HL, as well as protein tilt, to accommodate the mismatch between the hydrophobic cores of the membrane and α HL.

Table 3. Surface area per lipid (SA/lipid; \AA^2) and membrane hydrophobic thickness (\AA) for pure POPC and DPhPC membranes obtained from experiment (Exp.) and MD, and from MD with α HL present (MD) specified as mean and standard error.

<i>System Name</i>	SA/Lip (\AA^2)			Hydrophobic Thickness (\AA)		
	Exp.-pure lipid ²¹⁶	MD-pure lipid ²¹⁵	MD- α HL present	Exp.-pure lipid ²¹⁶	MD-pure lipid ²¹⁵	MD- α HL present
Full _{DPhPC-SX}	78.0 \pm 1.6	77.5 \pm 0.2	76.4 \pm 0.4	27.5 \pm 0.5	27.2 \pm 0.2	27.6 \pm 0.02
Full _{POPC-SX}	62.7 \pm 1.3	63.7 \pm 0.3	62.9 \pm 0.4	30.2 \pm 0.6	29.3 \pm 0.3	29.6 \pm 0.02
Full _{POPC-S2}			78.5 \pm 0.8*			24.9 \pm 0.01*

(*) – Denotes from reference.¹⁹⁶

Average hydrophobic membrane thickness and standard errors calculated from 20 ns blocks of the moving average are also tabulated in Table 3. With longer equilibration, it was found that the simulated values of the hydrophobic membrane thickness were within 1 % of experiment for pure DPhPC membranes and within 2 % for pure POPC membranes. The hydrophobic membrane thickness increased slightly in the presence of α HL for DPhPC and decreased slightly for POPC. Without sufficient equilibration time (Full_{POPC-S3*}), POPC membrane thickness was 13 % smaller than the experiment and contributed to simulated ionic current through α HL twice that of a sufficiently equilibrated POPC membrane (Table 2).

4.3.2 Membrane and Protein Hydrophobic Matching

Previously, MD simulations of α HL were performed using POPC or DPPC lipids which are similar in structure (DPPC is fully saturated like DPhPC but does not have methyl-branched tails) and considered representative of mammalian lipid membranes.^{193-194, 196} but prevent effective comparison to experimental data in biotechnology applications where DPhPC membranes are used. To date, DPhPC lipids have been used in MD simulations of channels formed by DNA and antimicrobial peptides,²¹⁸⁻²²⁰ but have not been used with ion channels. In the following subsection, how α HL structure is affected by its hydrophobic match to both POPC and DPhPC membranes is presented, specifically with respect to the inner leaflet where improper matching can result in structural changes at the *trans* entrance of α HL.

4.3.2.1 Global Hydrophobic Match

The choice of membrane lipid type has been previously demonstrated to be critical to ion channel function and is a key motivation for understanding the effect of the membrane on the immobilization of ion channels to FET sensing surfaces.^{21, 61, 182, 185, 221-222} Notably, large differences in experimental observables of α HL due to the subtle differences in the structures of POPC and DPhPC (Figure 29B) occur.^{194, 216} Specifically, methylation along the hydrophobic tails of DPhPC leads to a $\approx 25\%$ increase in SA/lipid compared to POPC.²¹⁵ Furthermore, since DPhPC is saturated, it permits a more ordered membrane as opposed to POPC which has a single unsaturation in the *sn-2* position and lipid tails that are kinked.

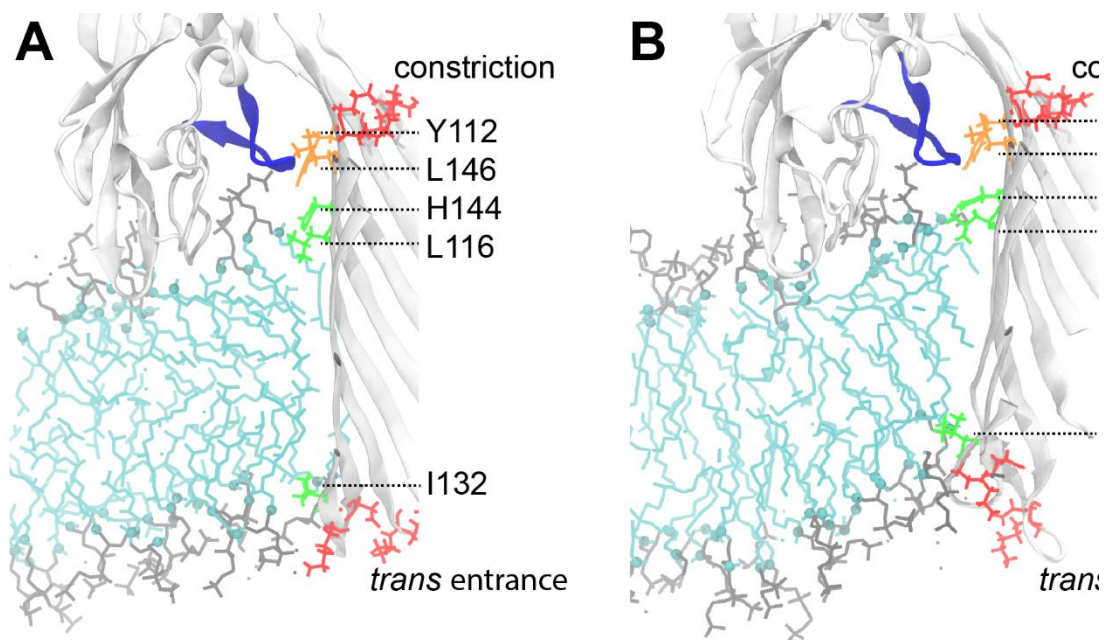


Figure 30. Schematic of the hydrophobic accessibility of α HL and subsequent match to the membrane for (A) DPhPC and (B) POPC. *White* – α HL secondary structure, *Blue* – first outer leaflet penetrating loop (Loop A) of α HL’s cap, *Orange* – Y112 and L146 which align to this loop, *Green* – H144, L116, and I132 which define the boundary for the hydrophobic accessibility of α HL, *Gray* – head group regions of membrane lipids, *Cyan* – hydrophobic region of the membrane, and *Red* – constriction and *trans* entrance residues with charged side chains.

Departures from experimental observables (Table 2, channel current) derive, in part, from the hydrophobic mismatch of the protein to the membrane, which is often used to predetermine the optimal lipid type to preserve ion channel function.²²³⁻²²⁵ However, determining the hydrophobic match between an ion channel and lipid membrane is not trivial. The hydrophobic thickness of the transmembrane region of α HL, defined here as the distance between the average heights of the hydrophobic residues of each heptamer that span the membrane (Y112 and L146 below the constriction and I132 above the *trans* entrance as seen in Figure 30A for DPhPC and Figure 30B for POPC), was calculated to be 37.3 ± 1.1 Å. However, each heptamer of α HL contains five loop motifs which, in part, form the extramembrane cap, and which penetrate the outer leaflet of the membrane (Figures 30A and 30B). Therefore, the

Orientation of Proteins in Membrane (OPM) database reports the net hydrophobic thickness of α HL to be $23.5 \pm 0.9 \text{ \AA}$,²²⁶ obtained by subtracting the penetration depth of these loops from the hydrophobic thickness of the transmembrane region of α HL.

The hydrophobic accessibility of α HL to the membrane is between these two values and is determined by the hydrophobic residues immediately above the *trans* entrance and the first outer leaflet penetrating loop of α HL's cap region (Figure 30, Loop A; *blue*). Loop A can be seen aligned with L146 in the transmembrane region (*orange*) before the constriction. However, because this loop is parallel to the membrane, it sterically hinders lipid alignment along the hydrophobic core of α HL, effectively creating an upper limit for the heights of charged lipid head group (*gray*). In turn, the membrane's upper hydrophobic terminus (*cyan*) aligns with residues H144 and L116. Herein, hydrophobic accessibility of α HL is defined as the distance between I132 above the *trans* entrance and the average of H144 and L116 as $26.8 \pm 0.6 \text{ \AA}$.

The result of the hydrophobic mismatch between membrane thickness and α HL's hydrophobic accessibility is twofold: membrane thickness near α HL decreases inducing negative curvature in the membrane and α HL tilts to orient its hydrophobic core into an energetically preferential conformation, which can be observed more readily in a POPC membrane (Figure 30B) than in a DPhPC membrane (Figure 30A). To better understand how membrane thickness decreases near α HL, Table 4 compares the hydrophobic membrane thickness for POPC and DPhPC per annular segment $r < 8 \text{ \AA}$ and $r > 8 \text{ \AA}$ from the edge of the hydrophobic core of the protein as described in *Section 4.2.2*. This thickness decreases negligibly for the Full_{DPhPC-SX}, however, it decreases by $\approx 5 \%$ for Full_{POPC-SX}, because the thicker POPC membrane must

compensate for the greater disparity between its thickness and α HL's hydrophobic accessibility. In addition to lipid membrane thickness deformation, ion channels attempt to minimize hydrophobic mismatch by tilting within the membrane.²²³ Full_{POPC-SX} tilt was almost three times as large as that of Full_{DPhPC-SX} (Table 3), indicating that α HL undergoes a greater change in its conformation to achieve hydrophobic matching with POPC compared to DPhPC. The difference in α HL tilt in DPhPC versus POPC lipids can be readily observed when comparing Figures 30A and 30B.

Table 4. Membrane hydrophobic thickness ($t_{r<8\text{\AA}}$ and $t_{r>8\text{\AA}}$) and α HL tilt specified as mean and standard error.

<i>System Name</i>	Membrane thickness (\AA): $t_{r>8\text{\AA}}$	Membrane thickness (\AA): $t_{r<8\text{\AA}}$	α HL tilt (degrees)
Full _{DPhPC-SX}	27.6 ± 0.02	27.5 ± 0.01	3.08 ± 0.04
Full _{POPC-SX}	30.0 ± 0.02	28.4 ± 0.01	8.68 ± 0.06

4.3.2.2 Membrane Inner Leaflet Distortion

Because steric hindrance between Loop A and residues Y112 and L146 result in an effective upper limit for the outer leaflet of the membrane to reside with respect to the hydrophobic core of α HL, curvature is induced on the inner leaflet near the *trans* entrance of the β -barrel. For Full_{POPC-SX}, the average depth of the inner leaflet extends past the *trans* entrance of α HL by 9.1 \AA resulting in significant local negative curvature in the POPC inner leaflet in an attempt to match the lower terminus of the hydrophobically accessible region of α HL (Figure 30B). In comparison, while Full_{DPhPC-SX} experiences a similar effective upper limit for the outer leaflet of the membrane, the average depth of the inner leaflet extends past the *trans* entrance of α HL by only 2.7 \AA (Figure 30A) and exhibits minimal local negative curvature at the inner

leaflet. This difference in membrane penetration depth is further described and compared to truncated α HL in Figure A16.

The induced local negative curvature on the inner POPC leaflet results in lipid kinking and increased membrane disorder while simultaneously α HL undergoes significant tilt driven by the need to hydrophobically match the membrane's hydrophobic core. The combination of these changes to the protein and membrane results in the charged lipid head groups deforming the *trans* entrance of α HL (Figure 31A). Specifically, the β -sheet *trans* entrance loops (residues V124 to L135) are perturbed from their native state into conformations where the loops bend inwards towards the center of the channel causing channel occlusion or outwards between head groups causing membrane distortion. These loops are natively stabilized by electrostatic interactions with neighboring loops, because D127 and K131 which contain oppositely charged side chains, within the loops are aligned with the residue of opposite charge alternatingly radially along the *trans* entrance of α HL. Figure 31C depicts the result of this destabilization with respect to channel occlusion by charged residues (depicted as red and blue) bending inwards towards the center of the channel.

In contrast, because DPhPC membranes are thinner and form a better hydrophobic match with α HL (Figure 31B), smaller curvature is observed compared to POPC, which results in less lipid kinking. Furthermore, decoupling of neighboring loop residues is not observed resulting in minimal channel occlusion (Figure 31D). The net result is a strong correlation ($R = 0.98$) between the average ionic current (Table 2) through the channel and the sum of the squares distances between neighboring β -sheet *trans* entrance loops, and better agreement with experimentally observed conductance.

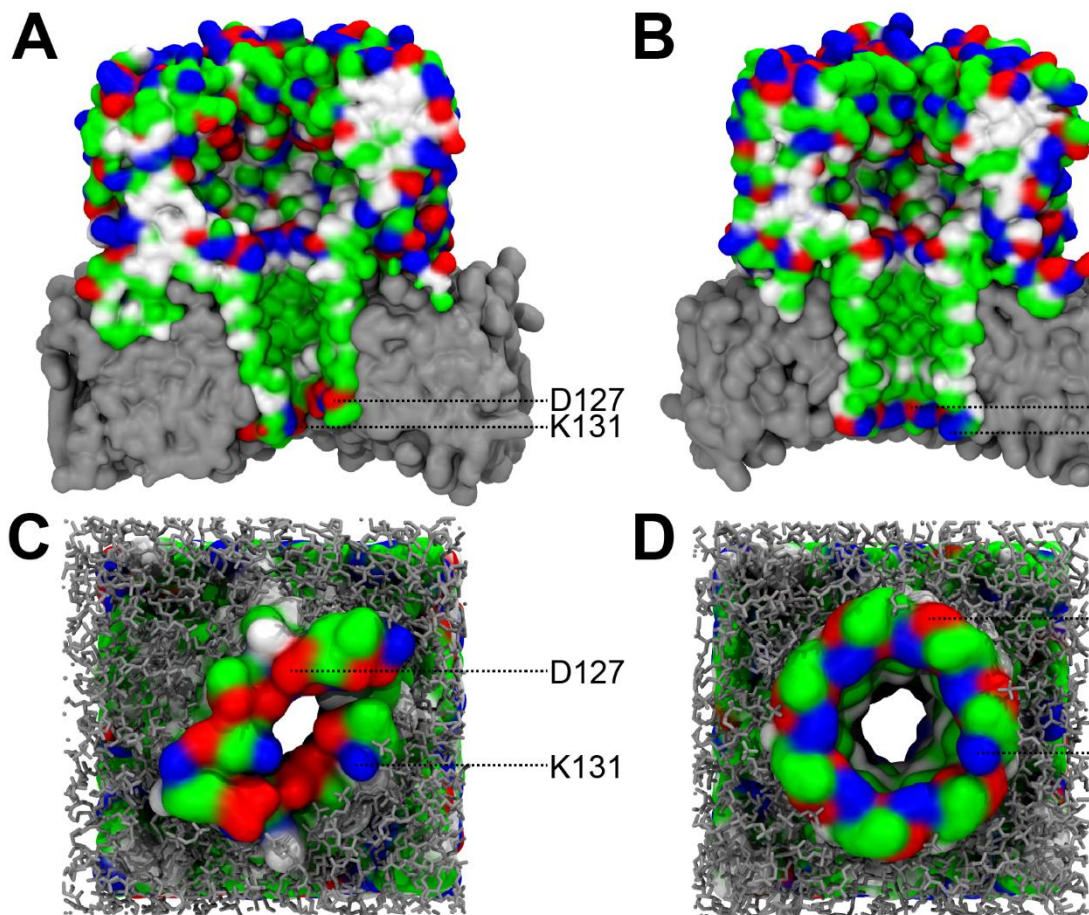


Figure 31. (A) Representative cross-section snapshot of FullPOPC-S1 depicting negative membrane curvature near the *trans* entrance resulting in deformation of the β -sheet *trans* entrance loops. (B) Representative cross-section snapshot of FullDPhC-S1 depicting minimal deformation of the β -sheet *trans* entrance loops. (C) Representative snapshot of FullPOPC-S1 looking up through α HL depicting channel occlusion. (D) Representative snapshot of FullDPhC-S1 looking up through α HL depicting minimal channel occlusion. Protein represented as an electrostatic surface with charged residues as red and blue. Lipids represented as a grey electrostatic surface (A) and (B) or lines (C) or (D).

4.3.2.3 Channel Constriction due to Hydrophobic Mismatch

Because the β -sheet *trans* entrance loops can create an additional constriction in the channel, the channel radius was calculated over the length of the transmembrane region of α HL to further assess correlation between channel constrictions and a reduction of ionic current. Channel radius was calculated over 0.25 Å segments and averaged over

time for the transmembrane region of α HL (Figure 32). Near the principal constriction ($z \approx 36 \text{ \AA}$), the average radius appears equivalent between Full_{DPhPC-SX} and Full_{POPC-SX}. However, towards the *trans* entrance where charged D127 and K131 reside, the average radius decreases to $\approx 4 \text{ \AA}$ for Full_{POPC-S1}, while increasing to $\approx 7 \text{ \AA}$ for Full_{DPhPC-SX} and $\approx 6 \text{ \AA}$ for Full_{POPC-S2*}. The correlation between the average channel radius between $-10 < z < 10 \text{ \AA}$ and average ionic current (Table 2) was found to be $R = 0.94$, that is a smaller *trans* entrance average radius is correlated to a reduction in ionic current. This correlation was calculated by taking the average channel radius between the aforementioned 20 \AA range for the four full system replicates as one variable and the corresponding average ionic current for that system as the second variable. Therefore, there is strong evidence that the destabilization of the β -sheet *trans* entrance loops manifests as an additional constriction to the channel radius which reduces the ionic current through the channel.

Figure A17 provides a more detailed depiction of channel radius fluctuation over time for each trajectory. The channel radius in Figure A16 is shown at 10 ns snapshots as a temperature map (blue: 0 ns, yellow: 125 ns, red: 250 ns). Full_{DPhPC-SX} displayed the least fluctuation in channel radius over time (Figure A16) and maintained a *trans* entrance radius of $5.5 < r < 6.5 \text{ \AA}$. In contrast, Full_{POPC-SX} displayed more significant fluctuations of $3 < r < 4.5 \text{ \AA}$ (Figure A166) at the *trans* entrance which partially accounts for the lower ionic currents observed relative to experiment. These *trans* entrance restrictions associated with channel collapse are correlated to reductions in channel current as described in Figure A18. Lastly, Full_{POPC-S3*} displayed the most

fluctuation of channel radius near the *trans* entrance ($5 < r < 7.5 \text{ \AA}$) due to insufficient equilibration and reduced protein-lipid interactions.

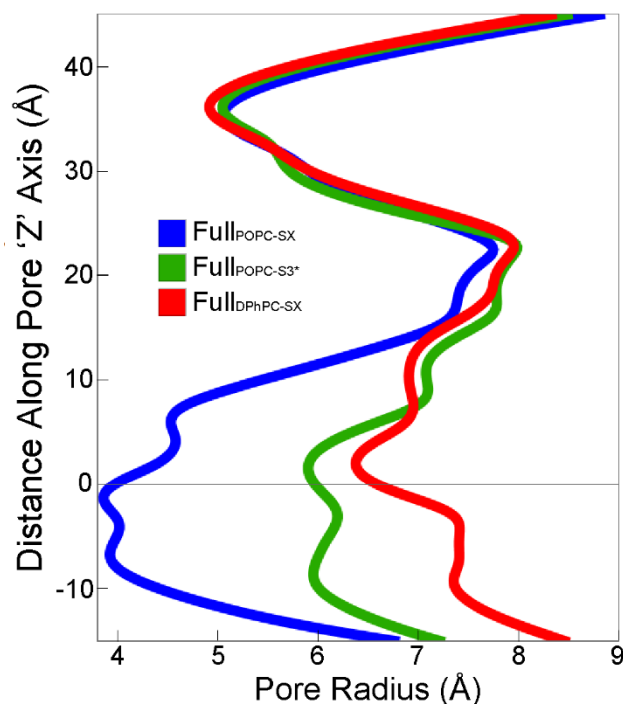


Figure 32. Average channel radius profiles. The average channel radius of α HL at the principal constriction is similar for all replicates, however it decreases significantly towards the *trans* entrance in a POPC membrane.

4.3.2.4 Favorability of Protein-lipid Interactions

Protein-lipid interaction energies were computed to support the hypothesis that DPhPC creates a more favorable environment for α HL compared to POPC due to better hydrophobic matching. The interaction energy between α HL and the membrane for Full_{POPC-SX} was $-126 \pm 1.8 \text{ kcal/mol}$, $\approx 38 \text{ kcal/mol}$ less attractive than that for Full_{DPhPC-SX}, which averaged $-164 \pm 0.4 \text{ kcal/mol}$. The interaction energy between α HL and the β -sheet *trans* entrance loops (defined in Table A1) for Full_{POPC-SX} was $-48.2 \pm 1.1 \text{ kcal/mol}$, $\approx 40 \text{ kcal/mol}$ less attractive than that for Full_{DPhPC-SX}, which averaged $-78.6 \pm 0.4 \text{ kcal/mol}$. Interaction energies between the principal constriction

and membrane were also computed and found to be negligible suggesting that the constriction is not influenced by membrane effects. These interaction energies indicate that DPhPC creates an environment that is more accommodating for α HL compared to POPC, specifically with respect to the β -sheet *trans* entrance loops that can strongly influence ion flow through the channel.

4.3.3 Ionic Current and Distribution

Membrane lipids do not directly restrict the flow of ions through α HL, but indirectly affect ionic current by altering α HL structure. The mean ionic current through the α HL channel is the primary experimental observable used to validate these simulations (Figure 33A) and was calculated using the net flux of ions across the channel with Equation 13. Best fit values for each trajectory are included in Table 2. First, the average transmembrane ionic current was calculated for the 200 ns replicate of Full_{DPhPC-SX} with Langevin coupling applied only to non-hydrogen protein and lipid atoms to verify the dampening effects did not significantly alter diffusion of water and ions. The current obtained from this replicate was 115.6 pA, which is only 3.3% greater than the average ionic current of the two 250 ns Full_{DPhPC-SX} replicates where a Langevin coupling coefficient of 1 ps^{-1} was applied to all non-hydrogen atoms. Clearly, the Langevin coupling on water and ions has a minimal effect on the calculated ion current and therefore Langevin coupling was applied to all atoms in subsequent ionic current analysis.

The average transmembrane ionic current obtained from two independent replicates of Full_{DPhPC-SX} was $74.5 \pm 7.2 \%$ of the experimental value. In contrast, ionic current obtained from two independent replicates of Full_{POPC-SX} was found to be only

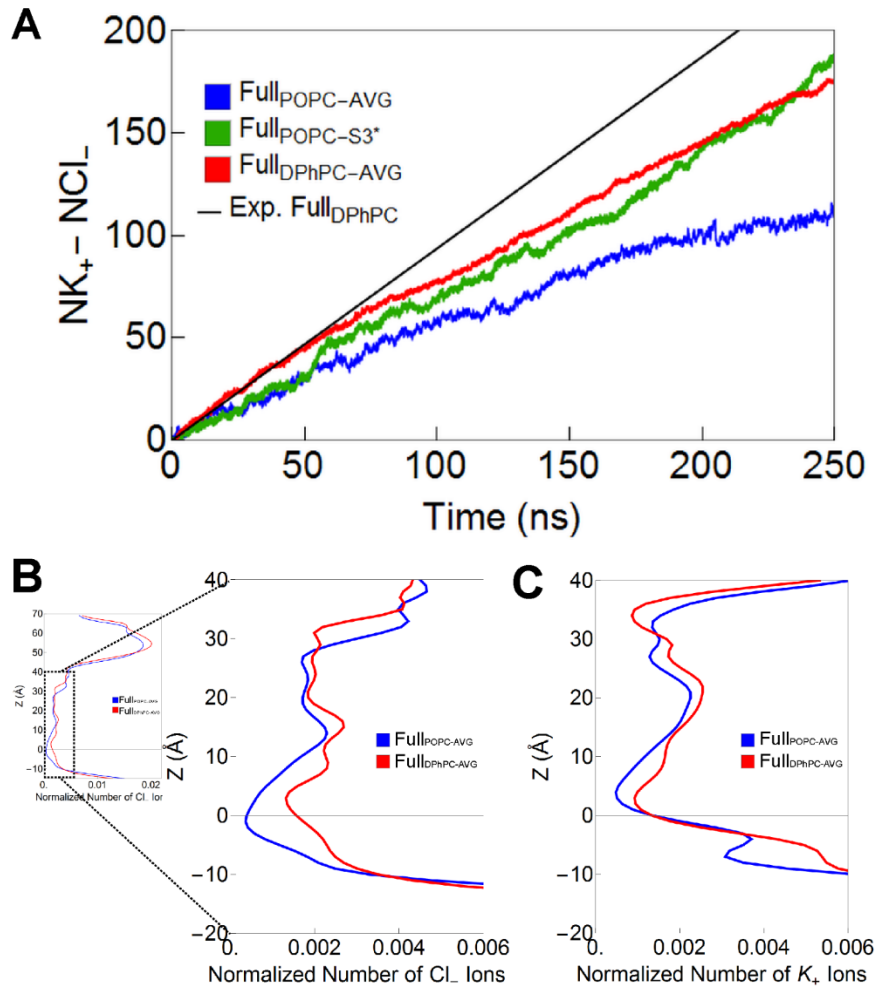


Figure 33. (A) Ionic current through α HL shown as the accumulation of ion crossings. (B) Probability density of Cl⁻ ion positions along the z axis of the channel. (right) Enlarged view of the transmembrane region. (C) Probability density of K⁺ ion positions along the z axis of the channel in the transmembrane region. Probability density of ion positions along the z axis of the channel was calculated with 1.0 Å bins. Only ions within a 25 Å radius of the channel axis were included. The distributions were calculated over the entire length of α HL and the standard error associated with each bin was $\leq 1\%$.

$51.9 \pm 11\%$ of the experimental value. Ionic currents initially match the experimental value for a short period of time, ≈ 10 ns for Full_{POPC}-S1 and ≈ 50 ns Full_{DPhPC}-SX, which is consistent with previous simulations.¹⁹⁴ However, simulated currents deviated from experiment when performed over longer timescales, indicating that longer timescales

are necessary to observe transient changes to ionic current and to probe changes in protein structure that cause these changes.

Ionic distributions are shown separately for K^+ (Figure 33B) and Cl^- (Figure 33C) ionic species over the transmembrane region of α HL to highlight the effects of lipid type. The constriction points are evident from minima in the distribution, which can then be correlated to specific protein-ion interactions. For α HL, electrostatic interactions between residues with charged sidechains govern the ability of ions to pass through the channel, which can be explained by the charged side chain-containing minima near the principal constriction (E111 and K147; $z \approx 36 \text{ \AA}$) and *trans* entrance (D127 and K131; $z \approx 0 \text{ \AA}$).

The principal constriction of α HL occurs near $z = 36 \text{ \AA}$ (with the membrane centered at the origin) along the principal axis of α HL and coincides with the minimum channel radius of the crystal structure. This constriction is formed by seven alternating E111 and K147 residue pairs (Figure 29A), one pair per heptamer, creating a ring of fourteen alternating positive and negative charged sidechains. This constriction is evident by minima which are more distinct for K^+ ions in FullPOPC-SX and FullDPhPC-SX than for Cl^- ions (Figure 33B, C), which is in agreement with previous studies which indicate that α HL is slightly anion selective.^{195, 227} Below the principal constriction, both FullDPhPC-SX and FullPOPC-S1 display an increased ion density with a maximum near $z = 15 \text{ \AA}$ for Cl^- ions and $z = 20 \text{ \AA}$ K^+ for ions and a lower density near the *trans* entrance (Figure 33B, C). Differences between FullDPhPC-SX and FullPOPC-SX are amplified at the *trans* entrance of α HL. Ion densities with FullPOPC-S1 were 50 % lower on average than FullDPhPC-SX for both ion species, indicating that *trans* entrance effects, and not the

principal constriction, appear to dominate the ionic distribution through α HL across a POPC membrane. Interestingly, the disparity between the *trans* entrance minima between lipid types is greater than that for the principal constriction, suggesting that deformation of the *trans* entrance due to hydrophobic mismatch to the membrane is the cause of deviation from experimental ionic currents.

4.3.4 Cap Truncation Effects

The final part of this chapter aims to accurately model the function of α HL through truncating the protein as described in *Section 4.2.2*. The primary benefit of this is to reduce the computational cost of performing simulations of α HL by reducing the system size. To date, simulations of a truncated form of α HL have been unable to describe experimentally observed currents,^{193, 228} however in several cases the *trans* entrance loops were truncated as well,²²⁹⁻²³⁰ which this section shows are essential in regulating the flow of ions through α HL.

A truncation scheme similar to past schemes which removes the cap of α HL, retaining the principal constriction, and connects the unconstrained tails of the seven heptamer pairs through disulfide bonds to preserve the β -barrel motif was used (Figure 29D). This truncation scheme is reasonable because the cap does not directly play a role in regulating ion flow, whereas the principal constriction and *trans* entrance loops do. However, the ionic currents through these truncated β -barrel systems (Table 2) do not accurately reflect experimental current or the ionic current through the full protein across the same lipid membrane type. Possible reasons for discrepancies between experimental and full system currents are presented in the following paragraphs.

Without the cap, there is no Loop A (Figure 30, Loop A; *blue*) to sterically hinder lipid alignment to the hydrophobic core of α HL, and no penetration by other loops to disturb lipid alignment. Therefore, instead of the corrected length for hydrophobic accessibility ($26.8 \pm 0.6 \text{ \AA}$), the full $37.3 \pm 1.1 \text{ \AA}$ of α HL's core is accessible to membrane lipids. This creates the opposite discrepancy between α HL's hydrophobic core and the hydrophobic core of DPhPC and POPC membranes (27.6 ± 0.02 and $30.1 \pm 0.02 \text{ \AA}$, respectively) which must be reconciled by conformational changes to α HL and the membrane. For both β -Barrel_{DPhPC-SX} and β -Barrel_{POPC-SX}, the result is induced positive curvature in both membrane leaflets to align the termini of the hydrophobic core with Y112 and L146 at the outer leaflet and I132 (or V124 for β -Barrel_{POPC-SX}) at the inner leaflet (Figure 34A and 34B). The *trans* entrance loops then extend below the inner leaflet height by 11.2 \AA for β -Barrel_{DPhPC-SX} and 6.4 \AA for β -Barrel_{POPC-SX} because the membrane exhibits positive curvature, as opposed to the negative curvature in the case of the full protein. Significant tilting can also be observed (Figure 34A and 34B), which is indicative of changes in α HL conformation to achieve energetically favorable hydrophobic matching.

The net result of membrane curvature and α HL tilt is that the *trans* entrance loops are now exposed to the aqueous phase instead of into alignment with the inner leaflet of the membrane, which is seen in the full systems (Figure 34). However, the correlation between the decoupling of the *trans* entrance loops, measured as the root-mean-squared-deviation (RMSD) between neighboring *trans* entrance loops, and channel radius near the *trans* entrance with ionic current are less clear ($R = 0.54$ and $R = 0.46$), which indicates the presence of an additional ionic current reducing factor,

hypothesized here to occur via residues with charged side chains (R104 and K154) immediately above the principal constriction (Figure 29D). This correlation was calculated by taking either the average channel radius or the trans entrance loops RMSD for the four full system replicates as one variable and the corresponding average ionic current for that system as the second variable. While the disulfide restraints did effectively maintain the β -barrel motif, they result in self-coupling between single β -strands (Figure A19A), while in the full systems coupling is observed between neighboring β -strands (Figure A18B). The coupled β -strands were constrained by the cap, which restrained them away from the center of the channel, preventing channel occlusion by R104 and K154.

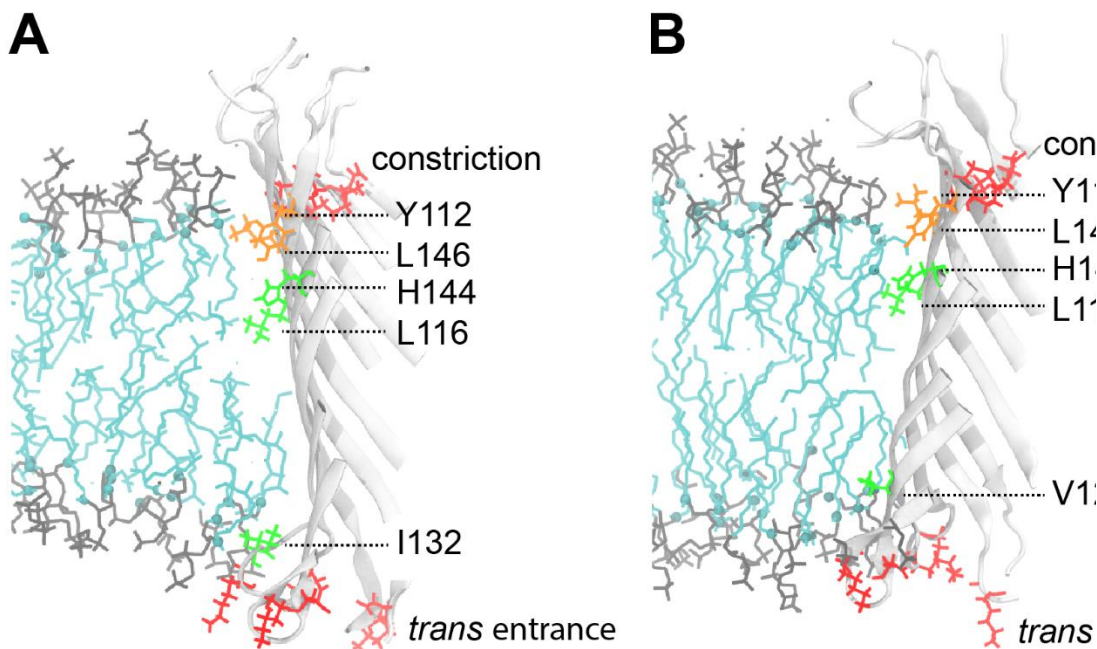


Figure 34. Schematic of the hydrophobic accessibility of α HL and subsequent match to the membrane for DPhPC (A) and POPC (B). *White* – α HL secondary structure, *Orange* – Y112 and L146 which define the upper boundary of hydrophobic accessibility, *Green* – H144 and L116 which now align well within the hydrophobic core of the membrane, and I132 or V124 which define the lower boundary for the hydrophobic accessibility.

Unfortunately, when constrained by disulfide bonds and not the cap, the termini of the β -strands, which contain R104 and K154, are more flexible and able to move towards the center of the channel creating an additional degree of channel occlusion and reduction of ionic current (Figure A18C), as opposed to the full system where these residues are restrained by the cap (Figure A18D). Overall, this truncation scheme was unable to faithfully depict α HL structure and function over 250 ns. This is particularly evident in β -Barrel_{POPC-S3}, where ionic current is approximately one third that of the three identical corresponding replicates and β -Barrel_{DPhPC-S2}, where ionic current is approximately one fourth that of the other identical corresponding replicate. In these replicates, the flexible termini containing R104 and K154 enter conformations of greater channel occlusion, which causes a reduction in ionic current. These conformations are not observed in every replicate, which creates significant statistical error around the mean ionic current. The effect of removing R104 and K154 to potentially stabilize the mean ionic current will need to be explored in subsequent simulations to accurately model the ionic current through α HL.

4.4 Conclusion

This chapter demonstrated a vastly improved all-atom model of the α HL ion channel in lipid membranes to better match experimental results in biotechnology applications. The results highlight the strong effect of proper membrane equilibration and lipid type on the structure and thereby function of the protein channel. With a better understanding of the lipid-protein structural relationship, more accurate and predictable FET biosensing measurements of ion channels like α HL can be achieved, as described in *Chapter 6*.

This chapter argued that SA/lipid is a more robust metric of measuring membrane equilibration rather than using energy criteria.^{203, 210, 215} Insufficient equilibration results in incomplete packing of lipids around α HL, reducing protein-lipid interactions, skewing protein-lipid hydrophobic matching, and subsequently causing deviations in the ionic current compared to experiment.

Ion channel function is sensitive to lipid type, which influences the membrane hydrophobic match. In this chapter it was demonstrated that otherwise identical systems of α HL in DPhPC result in ionic currents that are twice as high as α HL in POPC and show better overall agreement with experiment. Furthermore, differences in the hydrophobic match due to lipid type generate large structural changes at the *trans* entrance of α HL giving rise to an additional constriction point that limits the ionic current across the channel. This is in contrast to existing simulation work that assumes a rigid α HL structure and reports ionic currents that exceed the experiment by 50 %¹⁹³ or show good agreement at very short time scales.¹⁹⁴ Strong coupling between membrane type, structural changes, and channel conductance are consistent with results from other porins and ion channels such as OmpF, KcsA, and GrA.¹⁸⁰⁻¹⁸²

Finally, the preceding results were used as a guide to determine an optimal strategy to truncate the α HL ion channel to improve computational performance. Proper hydrophobic matching is even more essential to maintaining the function of the truncated ion channel because the removed cap domain no longer stabilizes the transmembrane region. Consequently, the *trans* entrance is exposed to the aqueous phase, which results in decoupling of stabilizing interactions. This will occur irrespective of how the truncation is done (disulfide or no disulfide bonds). This

analysis provides a physical basis for the higher ionic currents reported in previous truncation schemes that remove the trans entrance loops and the cap.^{193, 229-230}

In conclusion, the data in this chapter demonstrates that ionic currents calculated from all-atom MD simulations of the α HL ion channel show better agreement with experiment by using C36 DPhPC lipid membranes that better match the hydrophobic length of the channel and by sufficiently equilibrating the membrane. Using α HL as a model, these results demonstrate the potential effects of immobilizing an ion channel, such as on a FET sensing surface as described in *Chapter 6*, specifically with respect to how the type of lipid used for immobilization can affect channel current. The next chapter, *Chapter 5*, builds on these conclusions by presenting the results of MD simulations that aim to model the serotonin receptor and ion channel 5-HT_{3A}, specifically with respect to the predicted currents through the channel when activated.

Chapter 5: Modeling the Biorecognition and Activation of the 5-HT_{3A} Serotonin Receptor with Different Membrane Lipids

5.1 Introduction

Chapter 5 builds upon *Chapter 4* by providing a second example of how MD simulations can be used to model ion channel function and to assess the effects of the lipid membrane on ion channel current. Specifically, it demonstrates how MD can be used model ion channels that could be better characterized with FETs, where the setup for this FET characterization is described in *Chapter 6*, including how different lipid membrane types used in the immobilization of these ion channels regulate ion channel structure during activation. Also, significant details were elucidated regarding the mechanism of 5-hydroxytryptamine (5-HT, i.e., serotonin) binding to the 5-hydroxytryptamine 3A (5-HT_{3A}) serotonin receptor, i.e., the biorecognition of 5-HT_{3A} by an activating ligand.

Aided by efforts to improve their speed and efficiency, MD simulations provide an increasingly powerful tool to study the structure-function relationship of a specific family of ion channels, pentameric ligand-gated ion channels (pLGICs), which include 5-HT_{3A}. However, accurate reporting of the channel state and observation of allosteric regulation by agonist binding with MD remains difficult due to the timescales necessary to equilibrate pLGICs from their artificial and crystalized conformation to a more native, membrane-bound conformation *in silico*. Here, MD simulations of the 5-HT_{3A} for 15 – 20 μ s were performed to demonstrate that such timescales are critical to observe the equilibration of a pLGIC from its crystalized conformation to a membrane-bound conformation. These timescales, which are an order of magnitude longer than

any previous simulations of 5-HT_{3A}, allow the observation of dynamic binding and unbinding of 5-hydroxytryptamine (5-HT, i.e., serotonin) to the binding pocket located on the extracellular domain (ECD) and allosteric regulation of the transmembrane domain (TMD) from synergistic 5-HT binding. While these timescales are not long enough to observe complete activation of 5-HT_{3A}, the allosteric regulation of ion gating elements by 5-HT binding is indicative of a pre-active state, which provides insight into molecular mechanisms that regulate channel activation from a resting state. This mechanistic insight, enabled by microsecond-timescale MD simulations, allows a careful examination of the regulation of pLGICs at the molecular level, expanding the understanding of their function which provides insight for the design of FET biosensing experiments to further characterize this family of ion channels, which are described in detail in *Chapter 6*.

5.1.1 Background and Motivation

The homomeric 5-hydroxytryptamine 3A (5-HT_{3A}) serotonin receptor is a pentameric ligand-gated ion channel (pLGIC) located at the post-synaptic cleft that converts chemical signals to electrical responses in the central and peripheral nervous system.²³¹⁻²³² The primary chemical signal responsible for 5-HT_{3A} activation is the neurotransmitter 5-HT (i.e., serotonin). The binding of 5-HT causes conformational changes in the structure of 5-HT_{3A} that permit the flow of ions through the channel formed between its five monomer subunits, generating an action potential at the post-synaptic cleft.²³³ Clinically, pLGICs including 5-HT_{3A} regulate physiological functions such as nausea and are implicated in numerous psychiatric disorders including major depressive disorder, post-traumatic stress disorder, and Parkinson's disease.²³⁴⁻²³⁵

However, the mechanism by which agonist binding activates pLGICs and the structural basis that governs the transition between functional states is not well understood, and remains a critical element hindering the design of therapeutics for many psychiatric disorders.²³⁶⁻²³⁷ This mechanism is postulated to be more complex than a simple binary binding by activating ligands to a pLGIC, instead requiring the ‘priming’ of a pLGIC by dynamic binding through transitional pre-active states,²³⁸⁻²³⁹ a mechanism which is further supported by the conclusions of this work.

Molecular dynamics (MD) simulations are a useful technique for examining the basis of pLGIC function, including the mechanisms that govern rapid and dynamic transitions between states that cannot be observed through experimental techniques.²⁴⁰⁻²⁴² Numerous pLGICs have been investigated using all-atom MD simulations, including the nicotinic acetylcholine (nAChR),²⁴³ glutamate-gated chloride channel (GluCl),²⁴⁴ and glycine (GlyR)²⁴⁵ receptors, which has provided valuable insight into the structural response of pLGICs to agonist binding. MD simulations of 5-HT_{3A} have only been performed more recently, since its structure (excluding the intrinsically disordered intracellular domain) was first reported using X-ray crystallography in 2014 (PDB ID: 4PIR²⁴⁶) and later through cryo-electron microscopy (cryo-EM) in 2018 (PDB ID: 6BE1²⁴⁷). These *apo* structures, i.e., structures without 5-HT bound, have been reported as non-conductive,²⁴⁷⁻²⁴⁹ while more recently additional structures of 5-HT_{3A} have been resolved with various agonists and antagonists and have been reported as both conductive and non-conductive.^{248, 250} Such states are initially assigned based on pore radius through the channel, where a minimum pore radius greater than that of

a given wetted ion, such as Na⁺ or K⁺, represents a pLGIC in a conductive state because it is sufficiently wide to permit the translocation of ions.

However, assigning states to these static structures is not trivial due to limitations in structural resolution, symmetry assumptions, removal of highly flexible residues, and the addition of molecular components that may artificially constrain the protein in a given conformation, such as the nanobodies used in the original crystallization of 5-HT_{3A}.²⁴⁶ Therefore, MD simulations are performed to confirm the assignment of a state using careful analysis of structural dynamics including the pore radius profile, changes to the agonist-binding regions, and changes to secondary structure elements in the TMD and extracellular domain (ECD). However, most simulations generally suffer from inadequately short timescales, usage of non-native membrane lipids, and a lack of validation of critical simulation parameters including protein equilibration, membrane equilibration, and ligand representation in a force field that if not properly validated, may bias a pLGIC in a non-native conformation, subsequently yielding an inaccurate assignment of channel state.

5.1.2 Simulation Approach

In *Chapter 5*, all-atom MD simulations of both *apo* and 5-HT-bound 5-HT_{3A} starting with PDB ID: 4PIR²⁴⁶ were performed to determine the native protein state under conditions comparable with experiment. These simulations build upon previous MD simulations of full-length 5-HT_{3A}²⁴⁸⁻²⁵⁰ in several notable ways. Firstly, each simulation was performed for 15 – 20 μs, which is an order of magnitude longer than any previous simulations of 5-HT_{3A}. This chapter demonstrates that such timescales are necessary to adequately equilibrate 5-HT_{3A} using C36 for lipids²⁰⁹⁻²¹⁰ and for

proteins²⁵¹ in a lipid membrane and to observe the dynamic nature of 5-HT binding during channel priming, i.e., observation of a pre-active state. Secondly, a ternary lipid membrane composed of 1-palmitoyl-2-oleoyl-SN-glycero-3-phosphocholine (POPC), polyunsaturated 1-stearoyl-2-docosahexaenoyl-sn-glycerco-3-phosphocholine (SDPC), and cholesterol was used to mimic the neuronal lipid environment in which 5-HT_{3A} resides,²⁵² whereas past simulations used only POPC to represent the lipid environment.²⁴⁸⁻²⁵⁰ The importance of lipid membrane type cannot be understated. It has been shown experimentally that cholesterol and polyunsaturated lipids interact directly with pLGICs such as nAChR,²⁵³⁻²⁵⁷ which is largely homologous in structure to 5-HT_{3A}, to strongly regulate receptor structure and conductance. Lastly, several levels of simulation validation were included to ensure this model accurately represents experiment, including sufficient lipid membrane equilibration to ensure realistic lipid packing and careful parameterization of 5-HT for the CHARMM General Force Field (CGenFF)⁵³ using free energy perturbation (FEP) simulations to determine its solvation free energy, ensuring the accurate representation of 5-HT binding to 5-HT_{3A}. These two parameters are specifically highlighted because insufficient lipid packing can result in a reduction of protein-lipid interactions around the TMD and because improper ligand parameterization can result in an unrealistic affinity of 5-HT to the binding pocket of 5-HT_{3A}. Together, these simulations provide a framework for how microsecond-timescale MD simulations must be used to examine the equilibration of pLGICs from a crystalized conformation and to examine allosteric regulation from ligand binding that can help reveal the nature and functional state of the ion channel. This framework can be used for other pLGIC conformations, including the recently

resolved open conformation of 5-HT_{3A},²⁵⁸ to model the ionic current through such ion channels providing useful predictions for the expected ionic gradient detectable by a FET sensing surface (see *Chapter 1*).

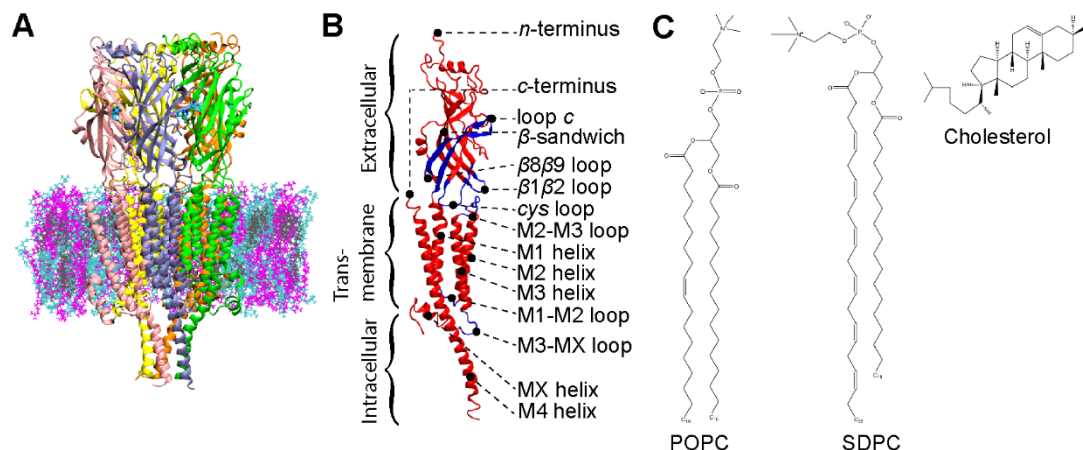


Figure 35. (A) Cross-section of 5-hydroxytryptamine 3A (5-HT_{3A}) in a lipid membrane with 5-HT_{3A} represented by secondary structure and colored by monomer (A, green; B, purple; C, pink; D, yellow; E, orange), lipids represented as lines and lipid type represented by color: 1-palmitoyl-2-oleoyl-SN-glycero-3-phosphocholine (POPC), *cyan*; 1-stearoyl-2-docosahexaenoyl-sn-glycerco-3-phosphocholine (SDPC), *magenta*; cholesterol, *gray*), and 5-HT also represented as lines (*aqua*). (B) A single monomer of 5-HT_{3A} represented by secondary structure and colored as red and blue to create contrast for specific secondary structure motifs. (C) Lipid structures of POPC, SDPC, and cholesterol.

5.2 Materials and Methods

5.2.1 Simulation Setup

The CHARMM-GUI *Membrane Builder*²⁰⁴ was used to build protein-membrane systems (Figure 35A) with 5-HT_{3A} (PDB ID: 4PIR²⁴⁶) and lipid membranes composed of either 7:7:6 SDPC/POPC/cholesterol, which has been shown to mimic the neural membrane environment,²⁵² or POPC. The unresolved M2-M3 loop was added using *Modeller*.²⁵⁹ The 57 unresolved intracellular and intrinsically disordered residues linking the M4 helix to the MX helix were not added; however, the membrane served as a scaffold and ensured that the M4 helix did not separate from the rest of the TMD. A single monomer of 5-HT_{3A} depicting relevant secondary structure motifs is depicted

in Figure 35B. Four total trajectories are reported in this study. The first system is 5-HT_{3A} with no 5-HT added (5-HT_{3A-Apo}), i.e., the *apo* system. The next two systems are 5-HT_{3A} with either ≈ 5 mM 5-HT (5-HT_{3A-5mM}) or ≈ 15 mM 5-HT (5-HT_{3A-15mM}) added to the system, i.e., 5 and 15 5-HT molecules respectively. The last system is also 5-HT_{3A} with ≈ 5 mM (5-HT_{3A-5mM-POPC}) added to the system, i.e., five 5-HT molecules, except the membrane was composed of only POPC lipids to compare the effects of a POPC versus mixed lipid membrane, where lipid structures are shown in Figure 35C. Each protein-membrane system was built in a tetragonal box containing a fully hydrated membrane, and sufficient K⁺ and Cl⁻ ions to yield an overall 0.15 M concentration (physiological), with an additional 25 K⁺ ions added to neutralize the *apo* system and proportionally less K⁺ ions when 5-HT (charge: +1) was added to the 5 mM, 15 mM, and 5 mM-POPC systems (Table 1).

These simulations used the TIP3P water model²⁰⁷⁻²⁰⁸ with C36 for lipids²⁰⁹⁻²¹⁰ and for proteins.²⁵¹ The van der Waals interactions were smoothly switched off between 10 Å and 12 Å by a forced-based switching function.²¹¹ All the bond lengths involving hydrogen atoms were constrained using the SHAKE algorithm.²¹² Particle mesh Ewald²¹³ was used for electrostatic interactions with an interpolation order of 6 and a direct space tolerance of 10⁻⁶. NAMD⁵⁴ was used to perform the equilibration of the simulations at 310.15 K and Anton2²⁶⁰ was to perform the production runs of the simulations also at 310.15 K.

For the equilibration, after the standard CHARMM-GUI six minimization and equilibration steps (0.685 ns),²⁰⁴ the simulations were further equilibrated for 250 ns under constant semi-isotropic pressure (NPT; $x = y$ and z varies independently) with

the Nosé-Hoover Langevin-piston algorithm^{59, 214} to ensure complete membrane relaxation which has been demonstrated previously as necessary,²¹ and finally equilibrated for 10 ns under constant pressure and by fixing the membrane area (NPAT).

Next, 5-HT was docked to 5-HT_{3A} using *AutodockVina* and including flexible side chains.²⁶¹ The center of the docking search space was specified as the center of mass of the ten residues previously identified as important for 5-HT binding.^{232, 249} A search space of (30 × 30 × 30) Å was used to ensure all possible conformations of 5-HT and flexible side chains were surveyed. The conformation which yielded the lowest energy was selected for each of the five binding pockets, all of which were practically identical, except for minor variations that arose from side chain rearrangement during the 250 ns equilibration period. An example of a 5-HT molecule docked into a binding pocket is shown in Figure A20.

CGenFF was used to obtain initial parameters for 5-HT,²⁶² which were modified based on free energy perturbation (FEP). FEP was used to determine ΔG° for 5-HT in aqueous and octanol phases which were used as inputs for the relationship $\log P_{Oct/Wat} = \frac{(\Delta G^\circ_{Wat} - \Delta G^\circ_{Oct})}{RT}$, where $\log P_{Oct/Wat}$ is the base-ten logarithm for the partition coefficient, a ratio of the concentrations of 5-HT between water and octanol, ΔG°_{Wat} and ΔG°_{Oct} are the Gibbs free energies of 5-HT in water and octanol in kcal mol⁻¹, respectively, R is the gas constant in kcal K⁻¹ mol⁻¹, and T is temperature in K. The partition coefficient $P_{o/w}$ is experimentally determined for 5-HT, therefore ΔG°_{Wat} and ΔG°_{Oct} calculated from FEP must yield the experimentally determined

$P_{\text{Oct/Wat}}$ using the above relationship. To achieve this end, the charge parameters of 5-HT are changed from those initially provided by CGenFF to satisfy these conditions.

For production runs, all simulations were performed on Anton2⁵⁵ under constant volume and temperature (NVT) and semi-isotropic pressure for 15 – 20 μs with a homogenous electrical field applied in the z direction proportional to -60 mV to match experimental conditions where an electric field is applied to generate a current through 5-HT_{3A}²⁶³⁻²⁶⁴. The Anton Multigrator framework²⁶⁵ with a Nosé-Hoover thermostat^{60, 266} and a MTK barostat²¹⁴ was used with a 2.5 fs time step, short-range electrostatic interactions were calculated with a cutoff of 9 Å, and long-range electrostatic interactions were calculated using the u-series method.⁵⁵

5.2.2 Analysis Methods

Surface area per lipid was calculated by taking the simulation cell x - y plane area (with the x - y ratio held constant at one) and subtracting the average cross-sectional surface area of the TMD of 5-HT_{3A} which spans the height of the membrane, similarly to αHL (see *Chapter 4*). The resulting value for the surface area occupied by lipids was divided by the number of lipids in one leaflet to yield an average value for mean surface area per lipid. Membranes were determined to be adequately equilibrated when the moving average of the surface area per lipid reached a stable value. When this moving average no longer fluctuated greater than 0.5 \AA^2 , membranes were determined equilibrated.

Root-mean-square deviation (RMSD) for the protein backbone was calculated using CHARMM where only amine nitrogen, carbonyl carbon, and alpha carbon atoms were selected (no side-chain atoms). RMSD was also calculated for each secondary

structure motif as well to help determine which motifs contributed to overall perturbations in backbone RMSD, specifically in the transmembrane (TMD) versus extracellular (ECD) domains. A list of the residue numbers in each motif are included in Table A2.

Pore radii for all simulations and the crystal structures for PDB IDs 4PIR and 6HIN were calculated using the Hole program²¹⁷ over the length of the protein in the 'z' direction orthogonal to the membrane and averaged over 240 ps blocks. Snapshots of the TMD were obtained using Visual Molecular Dynamics (VMD)²⁶⁷ and aligned to 6HIN using the MultiSeq Plugin. All other snapshots including those of the binding pockets, domain interactions, transitions of loop *c*, and the lipid membrane were also obtained using VMD.²⁶⁷

Binding events were determined by distance between 5-HT and the ECD. A maximum distance of at least 4 Å between 5-HT and the ECD for at least 50 ns was considered a significant binding event. Interaction energies (enthalpic contribution) were calculated using CHARMM and includes contributions from electrostatic and van der Waals interactions to verify 5-HT-ECD interactions. Extent of loop *c* opening was calculated by taking the distance between D202 and R65 of neighboring monomers which form a salt bridge that stabilizes the binding pocket and 5-HT binding.

Lipid density was obtained by projecting the *z* coordinate of the carbonyl carbon for each lipid onto the *x-y* plane at 240 ps steps. SDPC penetration of the TMD of 5-HT_{3A-5mM} was quantified to be when any non-hydrogen atom of SDPC was within 5 Å of the TMD helices M1-M4 which can only occur when SDPC is within an individual monomer and not between neighboring monomers due to the diameter of each helix.

The same criteria were used to quantify the penetration of the TMD of 5-HT_{3A-5mM} monomer-D by all three lipid types, including the binding pocket formed for cholesterol due to the expansion of the TMD. The intra-TMD area was calculated by taking the cross-sectional area of the quadrilateral whose corners were the center of masses of the TMD helices M1-M4.

5.3 Results and Discussion

Accurately modeling the native structure of 5-HT_{3A} is an essential step to unraveling the structural elements that govern its function on a molecular level. To this end are described three keys to achieving accurate modeling of the ion channel: the equilibration of 5-HT_{3A} from a crystalized conformation to a more native, membrane-bound conformation; the allosteric regulation of its TMD from dynamic binding of 5-HT to its principal binding pockets located on its ECD; and differences in systems with varied 5-HT concentration and lipid membrane composition. Table 5 defines the key parameters for these systems: three are composed of 5-HT_{3A} embedded in a POPC/SDPC/Cholesterol membrane without 5-HT (*apo*), with \approx 5 mM 5-HT (five docked 5-HT), and with \approx 15 mM 5-HT (five docked 5-HT plus ten 5-HT added to the aqueous phase). A fourth system is composed of 5-HT_{3A} embedded in a POPC membrane with \approx 5 mM 5-HT (five docked 5-HT) to directly compare differences that arise from lipid membrane composition (Table 5). An example docking pose of 5-HT can be found in Figure A20.

Table 5. Simulation parameters for the four 5-HT_{3A} systems simulated with membranes composed of 1-palmitoyl-2-oleoyl-SN-glycero-3-phosphocholine (POPC), 1-stearoyl-2-docosahexaenoyl-sn-glycerco-3-phospho-choline (SDPC), and cholesterol (CHOL) or POPC only.

<i>System</i>	# POPC	# SDPC	# CHOL	# of waters	# of ions (Cl ⁻ /K ⁺)	Time (μ s)
5-HT _{3A} -Apo	126	126	108	43395	138/163	20
5-HT _{3A} -5mM	126	126	108	48528	150/170	15
5-HT _{3A} -15mM	126	126	108	48994	153/163	15
5-HT _{3A} -5mM-POPC	250	0	0	41552	132/152	15

5.3.1 Equilibration and Stability

Both membrane and protein equilibration are critical for accurate simulations of membrane embedded transmembrane proteins. To demonstrate adequate membrane equilibration, the average surface area (SA)/lipid for the mixed (POPC/SDPC/cholesterol) and POPC membranes was calculated during 250 ns of system equilibration at constant pressure and temperature (NPT) until the moving average for each case converged to an equilibrium value (Figure A21), similarly to α HL (see *Chapter 4*). For POPC, the equilibrium SA/lipid was $(63.5 \pm 0.5) \text{ \AA}^2$, demonstrating good agreement with the experimental average of $(62.7 \pm 1.3) \text{ \AA}^2$,²¹⁶ where the error bars represent the standard error. The average SA/lipid for the POPC/SDPC/cholesterol membrane was found to be $(51.6 \pm 0.4) \text{ \AA}^2$, which is expectedly lower than the experimental SA/lipid of a pure POPC, due to the membrane condensing effects of cholesterol.²⁶⁸ Unless noted otherwise, all errors are defined as the standard deviation of the mean.

Adequate protein equilibration during microsecond production at constant volume and temperature (NVT) is demonstrated in Figure 36A through backbone root-mean-square deviation (RMSD) of 5-HT_{3A}, excluding the MX helix (located at the terminus

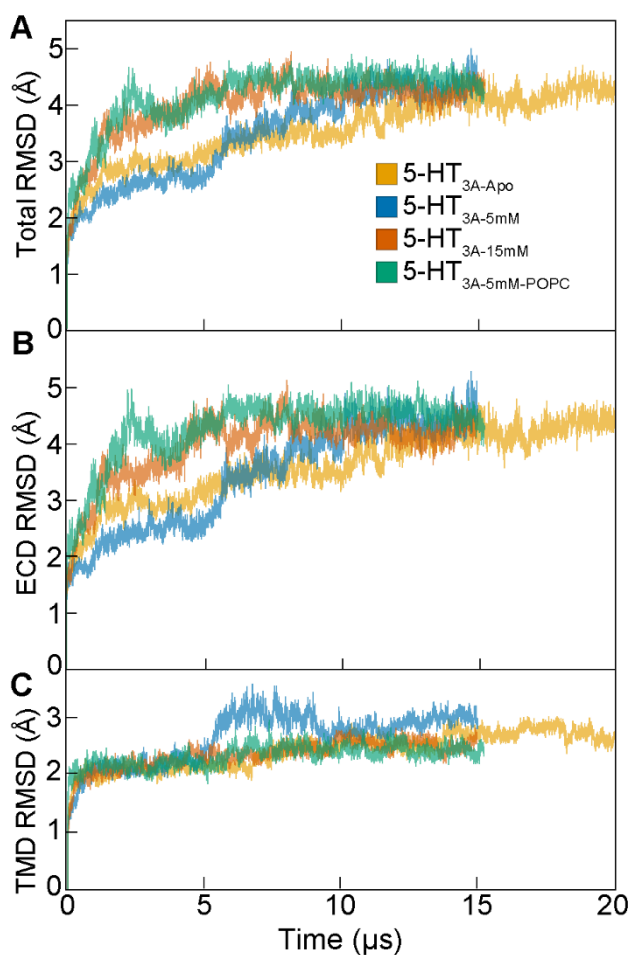


Figure 36. (A) Total backbone root-mean-square deviation (RMSD) for the four 5-HT_{3A} systems simulated. (B) RMSD of the extracellular domain (ECD) for the four systems. (C) RMSD of the transmembrane domain (TMD) for the four systems.

of the M3 helix, see Figure 35). Figure 36A demonstrates that all three 5-HT-bound structures stabilize by 10 μs in both mixed and POPC membranes (as listed in Table 5), whereas 5-HT_{3A-Apo} stabilizes by 14 μs . The additional equilibration time in the *apo* case is likely due to increased flexibility of loop *c* of the binding pocket that is stabilized through 5-HT binding in the other systems. The MX helix was excluded from the backbone RMSD because it is highly flexible due to the lack of 57 intracellular and intrinsically disordered residues linking it to the M4 helix that were unresolved during

the crystallization of 5-HT_{3A}.²⁴⁶ RMSD per secondary structure element (where definitions by residue number can be found in Table A2) was also calculated and is shown in Figure A22 to demonstrate the highly flexible nature of the MX helix compared to the other secondary structure elements.

Backbone RMSD for the ECD (Figure 36B) and TMD (Figure 36C) was also calculated to assess the structural response in the ECD to 5-HT binding and subsequent allosteric regulation of the TMD. Differences in the ECD RMSD trends for 5-HT_{3A-Apo} and 5-HT_{3A-15mM} are unremarkable (Figure 36B). ECD RMSD for 5-HT_{3A-5mM-POPC}, on the other hand, demonstrates a distinct departure from the other three trends between 2 – 3 μ s (Figure 36B). However, this departure does not appear correlated to a departure in TMD RMSD (Figure 36C) and can be explained by rapid opening and closing of the flexible loop *c* on multiple monomers which ultimately does not result in allosteric regulation of the TMD. Conversely, ECD RMSD for 5-HT_{3A-5mM} demonstrates a distinct departure from the other three trends between 5 – 10 μ s (Figure 36B) which appears correlated to a distinct departure in TMD's RMSD between 5 – 10 μ s (Figure 36C). RMSD per secondary structure element is shown in Figure A23, including the elements that contribute most significantly to this departure, including the M2-M3 loop, the *cys*-loop, and the β 8- β 9 loop, which exist at the interface between the ECD and TMD and are reported to be involved in the allosteric activation of 5-HT_{3A}.^{236, 248,}
²⁶⁹ The cause of these departures in 5-HT_{3A-5mM} RMSD were subsequently explored, specifically as to how they relate to allostery between the binding of 5-HT to its principal binding pockets on the ECD and resultant structural shifts between domains, as discussed further in *Section 5.3.4*.

5.3.2 Structural Overview

The assignment of ion channel state between conductive and non-conductive is generally determined through the pore radius profile which demonstrates the pathway available for ion translocation through the channel (see *Section 5.2.2*). In Figure 37A, pore radius profiles are shown for the initial crystal structure, PDB ID: 4PIR,²⁴⁶ (*light blue, dashed*) and for 5-HT_{3A-Apo} (*orange*) averaged over 20 μ s after the 250 ns of equilibration from the crystal structure, where the standard error of the pore radius is within the thickness of the trend line. PDB ID: 4PIR is non-conductive because while the entire ECD is hydrated and accessible to ion translocation, the minimum pore radius is $< 2 \text{ \AA}$ through the TMD (*gray*), below the threshold needed to permit the passage of hydrated K⁺ ions. Figure A24 clearly shows the contrast between PDB ID: 4PIR and an open conformation of 5-HT_{3A} (PDB ID: 6HIN²⁵⁰), which would permit the translocation of ions with a slight movement of pore-lining helices and the L260 sidechain.

The minimum pore radius along the ECD of 5-HT_{3A-Apo} deviates by less than 1 \AA from the crystal structure. This allows the ECD to remain hydrated and thereby accessible to ion translocation. However, the pore closes across the TMD ($-50 \text{ \AA} < z < 0 \text{ \AA}$) as demonstrated by the pore radius approaching a minimum value of 0 \AA for 20 μ s of simulation time (Figure 37A, *gray* region). Furthermore, the snapshot of the TMD shown in Figure 37B reveals that symmetry is maintained between the M2 helices of each monomer in this closed conformation, as depicted by the red-dashed line connecting the centers of the pore-lining M2 helices and shown in the associated plot of the interior angle θ for each of the five monomers (Figure 37C). Any fluctuations in the orientation appear cooperative and mostly in parallel to these lines of symmetry,

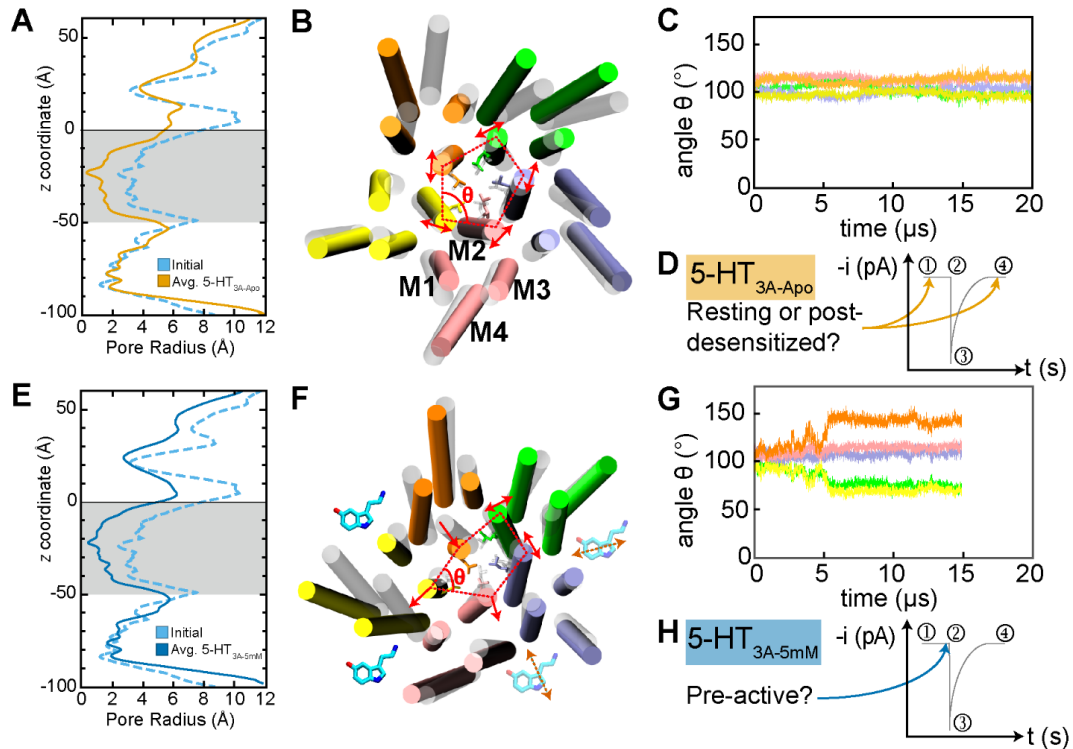


Figure 37. (A) Pore radius profiles for the starting structure (*light blue, dashed*) and 5-HT_{3A-Apo} (*orange*) averaged over 20 μ s with the transmembrane domain (TMD) shaded *gray* and error bars smaller than the thickness of the profile trend. (B) TMD snapshot for 5-HT_{3A-Apo} (including L260) shown as secondary structure and lines (respectively), with the initial structure as transparent white and the final structure colored by monomer (A, *green*; B, *purple*; C, *pink*; D, *yellow*; E, *orange*), with lipids, water, and ions removed for clarity. Representative helix labels for M1-M4 shown for monomer C with red, dashed lines connecting the centers of pore-lining M2 helix to demonstrate symmetry and *red, solid* arrows indicating the principal direction of M2 fluctuation. (C) Interior angle θ for the five monomers in (A) versus time. (D) Representative trend of current (*i*, pA) versus time (*t*, s) for the lifecycle of a 5-HT_{3A} receptor with instantaneous currents shown for the resting (1), pre-active (2), activated/open (3), and desensitized (4) states. Arrows indicate the possible states suggested by 5-HT_{3A-Apo}. (E) Pore radius profiles for the starting structure and 5-HT_{3A-5mM} (*blue*) averaged over 15 μ s with the TMD shaded in *gray* and error bars smaller than the thickness of the profile trend. (F) TMD snapshot of 5-HT_{3A-5mM} depicted the same as (C) with cartoon 5-HT indicating 5-HT-binding between monomers for the entire 15 μ s (*solid*) and transient binding (*transparent with dashed arrows*). (G) Same as for (C), but for 5-HT_{3A-5mM}. (H) Same as for (D), but for 5-HT_{3A-5mM}.

as opposed to orthogonal to the center of the pore. Figure 37D shows the lifecycle of activation for 5-HT_{3A} and indicates that this conformation is most consistent with a non-conductive resting state; however, a post-desensitized state cannot be ruled out,

which is also functionally non-conductive, but exists after the activation and desensitization of 5-HT_{3A} and is unresponsive to 5-HT binding.

In Figure 37E, pore radius profiles are shown for the initial crystal structure, PDB ID: 4PIR, (*light blue, dashed*) and for 5-HT_{3A-5mM} (*blue*) averaged over 15 μ s after the 250 ns of equilibration from the crystal structure, where the standard error of the pore radius is within the thickness of the trend line. The average minimum pore radius along the ECD of 5-HT_{3A-5mM} deviates by less than 1 \AA from the crystal structure, but remains hydrated and accessible to ion translocation (Figure 37E). Similarly to 5TH_{3A-Apo}, the pore radius across the TMD ($-50 \text{ \AA} < z < 0 \text{ \AA}$) approaches a minimum value of 0 \AA and the pore remains closed for 15 μ s (Figure 37E, *gray* region). Alone, this result suggests that the presence of bound 5-HT only impacts the ECD and not the TMD of 5-HT_{3A}, suggesting a lack of allostery and a desensitized state of 5-HT_{3A}. However, in Figure 37F a snapshot of the TMD of 5-HT_{3A-5mM} demonstrates that there is a significant antisymmetric shift between monomers D (*yellow*) and E (*orange*). Such an antisymmetric shift is depicted by a similar M2 helix center connecting red-dashed line and red arrows to demonstrate the direction of monomer shift conversely to the symmetric closure observed in 5-HT_{3A-Apo} and by the associated plot of the interior angle θ for each of the five monomers (Figure 37G) that demonstrates significant deviations in interior angle symmetry. The shift begins around 5 μ s and appears correlated to the departures in RMSD of both the ECD and TMD at around 5 μ s (Figures 2B and 2C). The shift dynamics (data not shown) can be summarized as follows: M2-D shifts outwards from the center of the pore in a cooperative fashion with M1-D, M3-D, and M4-D (M2-C also displays an outward shift, but to a lesser extent),

which would result in incremental pore opening if not for M2-E subsequently shifting inwards toward the center of the pore in a cooperative fashion with M1-E, M3-E, and M4-E and occupying the space voided by M2-D, resulting in the final conformation shown in Figure 37F. M2-A and M2-B display fluctuations parallel to the pore center similar to the M2 helices of 5-HT_{3A-Apo}.

Shown schematically in Figure 37F, 5-HT binds within binding pockets (bp) formed between pairs of monomers in the ECD (removed for clarity), for example bpCD is formed between the complementary monomer C and primary monomer D, while bpDE is formed between complementary monomer D and primary monomer E (an example of the initial binding pose is shown in Figure A20). The asymmetric shifts observed in 5-HT_{3A-5mM} appear correlated to 5-HT binding in these binding pockets. Monomer D is bound on either side by two 5-HT, and subsequently undergoes a conformational change as described in the previous paragraph. On the other hand, monomer C is only bound by 5-HT on its complimentary face and subsequently displays a minor M2 conformational change, while monomer E is only bound by 5-HT on its primary face and subsequently displays significant M2 collapse into the channel. Furthermore, Figure 37F shows that monomers A and B do not undergo observable conformational changes, and do not appear to be allosterically regulated by 5-HT. 5-HT appears to only rebinds transiently to bpAB and bpBC and does not rebind substantially to bpEA, in contrast to the binding observed in bpCD and bpDE. Because the conformational changes caused by the binding of only two 5-HT does not result in the channel opening sufficiently to permit the translocation of ions,^{239, 270} an activated state cannot be assigned to the simulated conformation 5-HT_{3A}. However, because this

5-HT binding causes conformational changes to a single monomer of 5-HT_{3A} that resemble the initialization of channel opening, it can be concluded that 5-HT appears to be priming the receptor for activation, i.e., the conformation resembles a pre-active state, as indicated by in Figure 37H, and not a desensitized or post-desensitized state.

Symmetric pore closure is also observed in 5-HT_{3A-5mM-POPC} and in 5-HT_{3A-15mM} (Figure A25), similar to 5-HT_{3A-Apo}. In 5-HT_{3A-5mM-POPC} (Figure A25A), only one 5-HT is bound over the duration of the simulation and no large conformational change is observed in the TMD, suggesting that the binding of a single 5-HT is also insufficient to cause channel opening or even priming of the channel. However, monomer D of 5-HT_{3A-15mM} (Figure A25B, *yellow*) is bound on either side by 5-HT, similar to 5-HT_{3A-5mM}, but does not demonstrate a large outwards shift in M2-D from the center of the pore, in contrast to the shift observed for M2-D of 5-HT_{3A-5mM}. Subsequently, the nature of the binding events at each 5-HT concentration to determine differences in 5-HT binding which result in different apparent outcomes with respect to monomer D between these two systems. Additionally, a full comparison of the TMD conformations for all four systems compared to the open conformation (PDB ID: 6HIN) is shown in Figure A26.

5.3.3 5-HT Binding Events

Numerous binding events were observed in 5-HT_{3A-5mM} and 5-HT_{3A-15mM} throughout each 15 μ s simulation. Here, binding is defined as when 5-HT is within 4 Å of the ECD of 5-HT_{3A} for at least 50 ns to exclude inconsequential collisions between the two biomolecules. Binding events ranged from completely stable to transient, in some cases lasting the entire 15 μ s simulation time. The number of 5-HT molecules

bound to 5-HT_{3A} at a given point in time are plotted in Figure 38A for 5-HT_{3A-5mM} and Figure A27A for 5-HT_{3A-15mM}. While initial docking orientations and binding energies were nearly identical after the 250 ns equilibration (which resulted in minor structural changes to the binding pocket, see *Section 5.2.1*), bound 5-HT ultimately sampled a range of conformations in each of the five binding pockets where the stability of each binding event varied substantially between orientations.

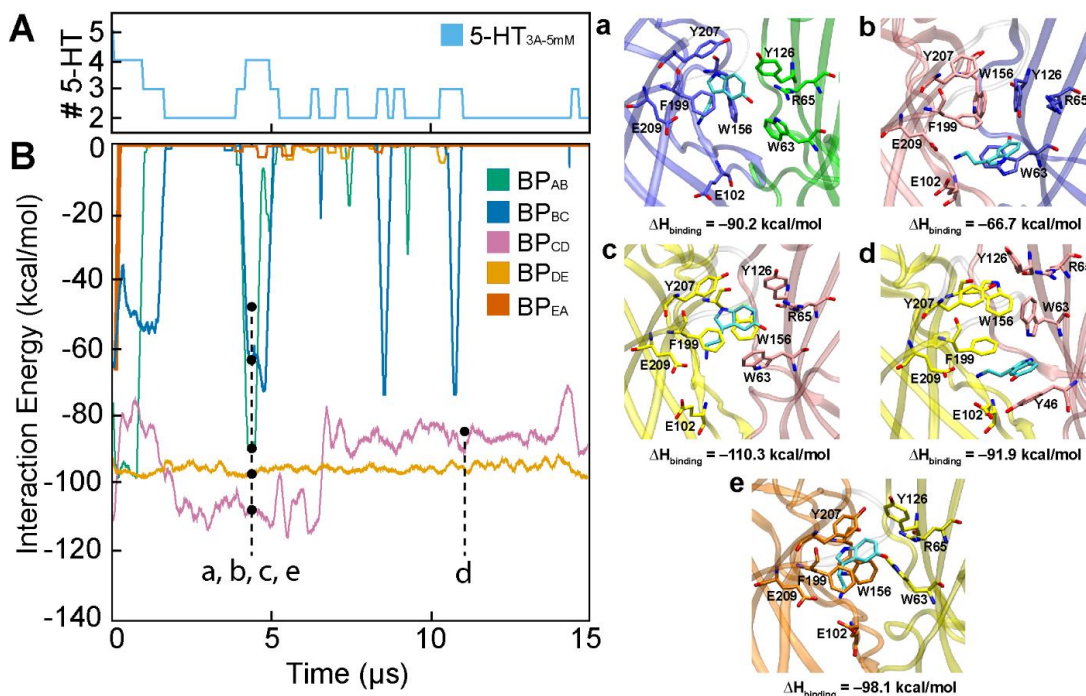


Figure 38. (A) Total binding events of 5-HT with 5-HT_{3A-5mM}. (B) enthalpic contribution to binding energy between 5-HT and the extracellular domain (ECD) where letters correspond to binding orientations on the right: bpAB (a, ≈ 4.6 μ s), bpBC (b, ≈ 4.6 μ s), bpCD (c, ≈ 4.6 μ s), bpCD (d, ≈ 14.7 μ s), and bpDE (e, ≈ 4.6 μ s) and monomers colored as: A, green; B, purple; C, pink; D, yellow; E, orange.

For 5-HT_{3A-5mM}, bpCD and bpDE were occupied by a single 5-HT for the duration of the simulation, whereas bpAB and bpBC experienced transient binding of 5-HT, i.e., several instances of binding and rebinding for different durations (Figure 38B). bpEA experienced no significant binding events after the unbinding of 5-HT within the first 50 ns, due likely to the opening of loop *c* on monomer A which contributes substantially

to the stability of 5-HT in the binding pocket and which remained in an open conformation for the duration of the simulation. Binding poses corresponding to the five markers in Figure 38B are shown for bpAB, bpBC, bpCD, and bpDE in Figure 38 with panel letters corresponding to the marker letter. Four binding poses are shown at around 4.6 μ s, where the highest number of 5-HT are bound (four) for $\approx 1 \mu$ s, which occurs immediately prior to structural changes in the ECD and TMD demonstrated in Figures 36 and 37. Lastly, a binding pose at around 11.4 μ s is shown for bpCD to demonstrate a significant change in binding orientation not observed for bpDE that is stable for the duration of the simulation and suggests an alternative binding pocket for 5-HT which could be related to the binding dynamics of pre-activation.

Each panel in Figure 38 depicts the residues of 5-HT_{3A} involved in the binding of 5-HT, residues that are generally conserved between events with some exceptions. For bpAB (where transient binding is observed), E209 of the primary monomer forms a salt bridge with the amine group of 5-HT, the hydroxyl group of 5-HT only experiences transient stabilization through charge-dipole interactions with R65, and the indole group experiences only transient stabilization through effective π - π stacking with Y207 and F199 (Figure 38a). Meanwhile, bpBC displays dual electrostatic stabilization of 5-HT through E209 and E102, but only transient π - π stacking with W63 and F199 and has virtually no interaction with R65 (Figure 38b). The transient binding in these pockets appears to be governed by the breaking of a salt bridge between D202 of the primary monomer and R65 of the complimentary one; loop *c* of the primary monomer locks at the salt bridge, over the binding pocket (Figure A28). Because binding-pocket residues Y207, W156, F199, and E209 are located on loop *c*, it is not surprising that

only transient binding is observed when loop *c* opens from the binding pocket, whereas loop *c* remains locked by the D202-R65 salt bridge for bpCD and bpDE.

The binding poses for bpCD and bpDE are nearly identical at around 4.6 μ s, with E209 and E102 interacting electrostatically with the amine group of 5-HT and R65 and the hydroxyl group of 5-HT interacting through charge-dipole interactions (Figure 38c and 38e). Simultaneously, the indole group of 5-HT is stabilized through π - π stacking with W156 and F199 and occasionally with Y207. The aforementioned D202-R65 salt bridge keeps loop *c* residues Y207, F199, and E209 near the binding pocket's complimentary residues and ultimately enables more residues to stabilize 5-HT in the pocket (Figure A27). Lastly, Figure 38d shows that the binding orientation for bpCD results in a decrease in the enthalpic contribution starting at around 7.2 μ s, but is still sufficiently stable to maintain a bound conformation with 5-HT_{3A}. A similar electrostatic stabilization between the amine group of 5-HT and E209 and E102 is observed, however the only other stabilization interactions are π - π stacking with Y46 and transient π - π stacking with F199.

Presumably, the additional 5-HT in 5-HT_{3A-15mM} would yield better activation than in 5-HT_{3A-5mM}; however, due to conflicts between multiple 5-HT in a single binding pocket and channel blocking (data not shown), better activation was not achieved. Experimentally, concentrations as low as 10 μ M are used yield complete channel activation,^{239, 270} but achieving such a low concentration *in silico* would require an impractical volume of water for MD simulations. Notably, the enthalpic contributions to binding energy in 5-HT_{3A-5mM} for bpCD and bpDE are more favorable than any of the sustained (and most of the transient) binding events observed in 5-HT_{3A-15mM}

(Figure A27B). For example, 5-HT is bound to bpAB for over 10 μ s in 5-HT_{3A-15mM} (Figure A27a), initially bound in an orientation as favorable as bpDE in 5-HT_{3A-5mM}. However, this orientation shifts to one where 5-HT is bound only to the bottom interface of the binding pocket (Figure A27b), resulting in an interaction with only a single conserved binding residue (E209) and an enthalpic contribution to binding energy of ≈ -40 kcal/mol. Binding pockets bpCD and bpDE, which are also occupied for a large portions of the simulation, demonstrate similarly unfavorable orientations (Figure A27e and A27g), which is a possible explanation that while sustained, these binding events do not result in the outward M2 shifts observed in 5-HT_{3A-5mM} and why evidence of pre-activation was not readily observed in 5-HT_{3A-15mM}. Binding orientations with enthalpic contributions to binding energy on par with those for bpCD and bpDE of 5-HT_{3A-5mM} are also observed in 5-HT_{3A-15mM} (Figures A27c, A27d, A27f, and A27h), however these events are not as long in duration as those in 5-HT_{3A-5mM}, further explaining why M2 shifts indicative of pre-activation are not observed in 5-HT_{3A-15mM}. Moreover, the salt bridge between R65 and D202 was not maintained for any of the binding pockets in 5-HT_{3A-15mM}, resulting in the opening of loop *c* to various extents in all five binding pockets. Notably, 5-HT remained bound in several instances without the additional stability provided by loop *c*, but these events appeared insufficient with respect to allosterically converting 5-HT binding to changes in the TMD. Subsequently, specific residue-based evidence for the allosteric mechanism by which the binding events observed in bpCD and bpDE of 5-HT_{3A-5mM} regulate structural shifts in the TMD of monomer D is presented as they relate to pre-activation and possible causes for the inwards collapse of M2-E.

5.3.4 Domain Interactions

The mechanism that governs the transition between states of 5-HT_{3A} lies in the allostery between 5-HT binding and secondary structure elements in the TMD and ECD, namely the M2-M3 loop (TMD), the β 1- β 2 loop (ECD), the β 8- β 9 loop (ECD), and the pre-M1 region (TMD/ECD),^{236, 248, 269} which are shown for 5-HT_{3A-5mM} monomers C, D, and E in Figure 39A. The β 1- β 2 loop, the β 8- β 9 loop, and the pre-M1 region are all directly connected to residues involved in 5-HT binding through β -strands and all interact either directly or indirectly with the M2-M3 loop. The M2-M3 loop is critical to channel gating because it acts as a spring that regulates the orientation M2, which is critical because separation between neighboring M2 helices is needed to allow the turning of L260 away from the center of the pore (shown in an open conformation PDB ID: 6HIN²⁵⁰ as an indication of a conductive state, Figure 24), and outwards tilt and/or translation of M2 allows this separation of helices to occur. The M2-M3 loop has been reported as natively restrained in the *apo* form,²⁴⁸ which is also observed here, meaning that pore opening is an active process that requires the release of the loop from a native restraint.

The disparity between the conformational change observed in monomer D and the collapse observed in monomer E initiates with the M2-M3 loop which in monomer D coils into a helix that causes M2-D to tilt outwards along with M3-D (Figure 39A). The opposite occurs in the M2-M3 loop of monomer E which becomes more elongated allowing M2-E to tilt inwards along with M3-E. Coiling of M2-M3-D is permitted because of a shift in β 1- β 2-D away from M2-M3-D (and towards β 1- β 2-E), while β 1- β 2-E and β 1- β 2-C do not demonstrate significant shifts (Figure 39A). Distances between the center of masses of the five β 1- β 2 loops are shown in Figure 39B for 5-

HT_{3A-5mM} to demonstrate the deviation from the average distance between β 1- β 2 loops and the distances between β 1- β 2-D and its neighbors and in Figure 39C for 5-HT_{3A-Apo} which serves as a control case (no 5-HT is bound). Of the β 1- β 2 loops, as proposed, only β 1- β 2-D shifts because bpDE residues D-Y46, D-W63, and D-R65 all lie on β -strands 1 and 2 of monomer D which at the onset of binding are pulled toward the primary monomer E through 5-HT in bpDE as the intermediary, while the pentamer D residues of bpCD are pulled toward the complimentary monomer C through 5-HT in bpCD as the intermediary, causing a twisting of monomer D which includes twisting of β 1- β 2-D. Neither monomers C or E are bound on either side by 5-HT, so they do not display the same twisting as seen in monomer D, but rather are constrained in only one direction by 5-HT binding. Moreover, this twist of monomer D and coiled orientation of M2-M3-D is stabilized by a salt bridge that forms between D271 of M2 and K54 of β 1- β 2-D which locks monomer M2-D in a conformation that reduces channel occlusion (Figure 40A). Alternatively, because β 1- β 2-E does not exhibit a twisting motion, K54 of monomer E is stabilized by forming a salt bridge with D52 and E53 of β 1- β 2-D when β 1- β 2-D twists toward β 1- β 2-E (Figure 39A). The twisting of β 1- β 2-D further allows D271 of M2-E to also form a salt bridge with K54 of monomer D, but unlike D271 of M2-D, this salt bridge constrains M2-E in an orientation that creates channel occlusion instead of decreasing restriction through the channel (Figure 40B).

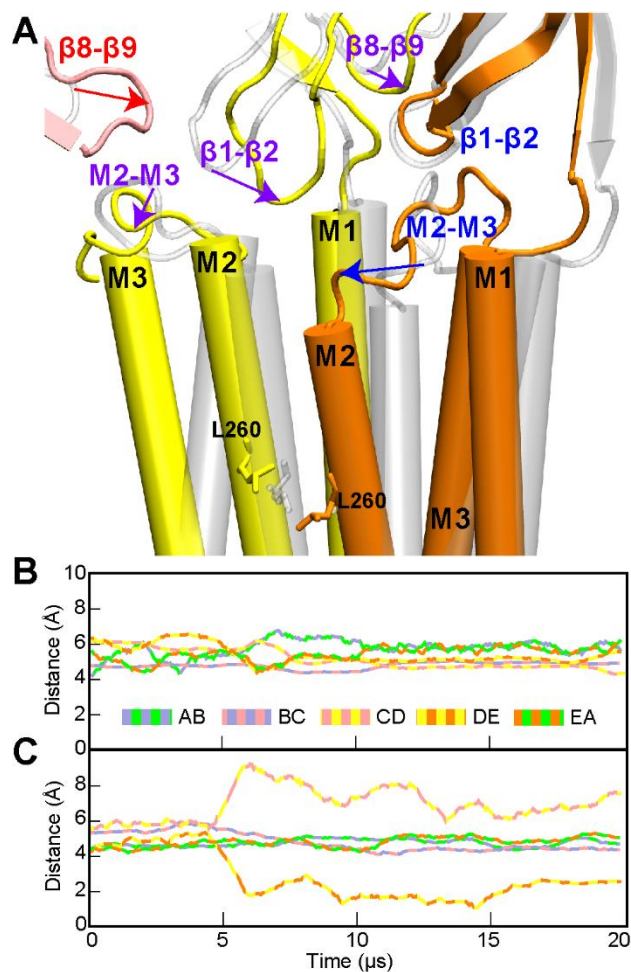


Figure 39. (A) Principal shifts in secondary structure motifs at the transmembrane domain (TMD)/extra cellular domain (ECD) interface for 5-HT_{3A-5mM} due to sustained binding events in bpCD and bpDE. Monomers C (*pink*), D (*yellow*), and E (*orange*) shown as secondary structure with initial structures colored as transparent white. Monomers A and B, and all M4 helices removed for clarity. Distances between the center of masses of the $\beta 1$ - $\beta 2$ loops colored by monomers for 5-HT_{3A-Apo} (B) and 5-HT_{3A-5mM} (C).

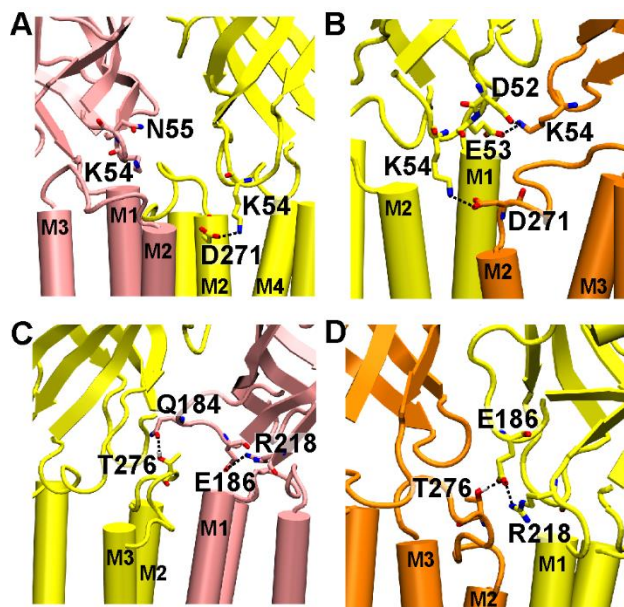


Figure 40. Stabilizing interactions depicted as secondary structure and colored by monomer (C, *pink*; D, *yellow*; E, *orange*) with relevant residues depicted as sticks and atoms following the standard coloring scheme. (A) K54 of $\beta 1$ - $\beta 2$ -D forms a salt bridge with D271 of M2-D stabilizing it in a conformation that reduces channel occlusion. $\beta 1$ - $\beta 2$ -D shifts with the twisting of monomer D and does not interact with $\beta 1$ - $\beta 2$ -C. (B) K54 of $\beta 1$ - $\beta 2$ -D also forms a salt bridge with D271 of M2-E stabilizing it in a closed conformation. Meanwhile, K54 of $\beta 1$ - $\beta 2$ -E forms salt bridges with D52 and E53 of $\beta 1$ - $\beta 2$ -D, the only $\beta 1$ - $\beta 2$ loop that shifts due to twisting of monomer D. (C) T276 of M2-M3-D is stabilized with hydrogen bonding with Q184 of $\beta 8$ - $\beta 9$ -C conversely to (D) where T276 of M2-M3-E is stabilized with hydrogen bonding with E186 of $\beta 8$ - $\beta 9$ -D instead due to differences in shifts of the $\beta 8$ - $\beta 9$ loops that arise from either partial or complete binding of their associated monomers. Both instances of hydrogen bonding are stabilized by a salt bridge between E186 of $\beta 8$ - $\beta 9$ of R218 of the pre-M1 region.

Additionally, differences in shifts observed in the $\beta 8$ - $\beta 9$ loops of monomers C and D appear to play a role in stabilizing the conformation of monomer D that reduces channel occlusions and the conformation of monomer E that increases it. The M2-M3 loop is natively constrained by hydrogen bonding to the $\beta 8$ - $\beta 9$ loop and pre-M1 region of the complimentary monomer, constraints which are broken, but then reconfigured between T276 of M2-M3-D and Q184 of $\beta 8$ - $\beta 9$ -C in the form of hydrogen bonding (Figure 40C). However, due to an upwards shift in $\beta 8$ - $\beta 9$ -D as a result of twisting observed in monomer D, T276 of M2-M3-E and E186 of $\beta 8$ - $\beta 9$ -D also form a hydrogen bond (Figure 40D), but much like the D271-K54 salt bridge, this hydrogen bond contributes to lock M2-M3-D in a conformation that reduces channel occlusion and M2-M3-E in a conformation that increases it. In both cases a salt bridge is formed between E186 and R218 (Figure 40C-D) which strengthens the configurations governed by hydrogen bonding with T276.

In summary, bound only to the primary face of 5-HT_{3A-5mM} monomer C, 5-HT appears to regulate the $\beta 8$ - $\beta 9$ loop which is connected through β -strand linkage to the primary face, but not to the $\beta 1$ - $\beta 2$ loop which is only connected to the complimentary face (Figures 39 and 40). Conversely, bound only to the complimentary face of 5-HT_{3A-5mM} monomer E, 5-HT appears to regulate the $\beta 1$ - $\beta 9$ loop which is connected through β -strand linkage to the complimentary face, but not to the $\beta 8$ - $\beta 9$ loop which is only connected to the primary face, preventing the M2-M3-E loop from expanding outwards, and allowing M2-E to collapse inwards (Figures 39 and 40). Only in the case of 5-HT_{3A-5mM} monomer D, is full allosteric regulation and activation of a 5-HT_{3A} monomer observed, in contrast to its neighboring monomers which are only partially

bound by 5-HT. Significant shifts of these loops in the other monomers of 5-HT_{3A-5mM} and in the three other systems were not observed, indicating that the binding of 5-HT that allosterically regulates monomer D of this system is indicative of pre-activation, whereas at least three bound 5-HT are required to achieve complete activation.^{239, 270}

Lastly, changes in the TMD are not solely related to agonist binding in pLGICs, and can also be regulated by antagonists, glycosylation, phosphorylation, and the lipid membrane itself. This last effect of lipid interactions is relevant to the conformational transition of monomer D in 5-HT_{3A-5mM}. Therefore, subsequently discussed is the differences between the three systems with a membrane composed of a 7:7:6 mixture of POPC/SDPC/cholesterol and the final system with a membrane composed of pure POPC, as defined in Table 5.

5.3.5 Impact of Lipid Type

These simulations are unique compared to past simulations of 5-HT_{3A} because they are the first to use a lipid membrane composition representative of a neuronal membrane (a 7:7:6 mixture of POPC/SDPC/cholesterol) and the first to compare simulations of a pLGIC in two different membrane lipid compositions (this mixture versus pure POPC). This is particularly important with respect to probing the role which lipids have on the immobilization of 5-HT_{3A} for applications like FET biosensing. POPC is commonly used for simulations of mammalian proteins because it is considered representative of mammalian lipid membranes, however both polyunsaturated fatty acid (PUFA) lipids such as SDPC and cholesterol have been found to make up a significantly high percentage of the lipids found in 5-HT_{3A}-containing membranes.²⁵³ While to date there is a lack of evidence demonstrating the

direct effects of these lipids on 5-HT_{3A}, there is evidence demonstrating that these lipids interact directly with and regulate the function of other pLGICs such as the nAChR, the *Gloeobacter violaceus* ligand-gated ion channel (GLIC), and the γ -aminobutyric acid receptor (GABA), which are largely homologous in structure to 5-HT_{3A}.^{253-257, 271-274} This indicates a need to study the effects of these lipids on 5-HT_{3A} to determine if they play a role in regulating its function similar to other pLGICs. Therefore, in this subsection differences in lipid distribution and lipid interaction with 5-HT_{3A} between 5-HT_{3A-5mM} and 5-HT_{3A-5mM-POPC} are reported, as depicted by representative snapshots for the two simulations in Figure 41A and 41B, respectively.

The first observable difference in lipid distribution is greater clustering of SDPC (*cyan*) compared to POPC (*magenta*) around the TMD of 5-HT_{3A-5mM}, quantified by the average number of SDPC within 3.5 Å of 5-HT_{3A} (46.2 ± 0.03) compared to POPC (35.6 ± 0.02). SDPC demonstrates a tendency to transiently penetrate the TMD with its saturated chain (Figure 41A, small *red* circle), in contrast to POPC (Figures 41A-B). The TMD of each 5-HT_{3A-5mM} monomer is transiently penetrated by at least one SDPC (with the exception of monomer E), as shown in Figure A29. Sustained penetration of the TMD is only observed in the 5-HT_{3A-5mM} monomer D (Figure 41A, large *red* circle), which experiences twisting and expansion due to sustained 5-HT binding to both its primary and complimentary faces (see *Section 3.2, Structural Overview*). Occupation of the TMD within monomer D (*yellow*) can also be seen in Figure 41C (indicated by a red circle) which depicts lipid density for the three lipid types in 5-HT_{3A-5mM} over the entire 15 μ s and average center of masses for helices M1-M4.

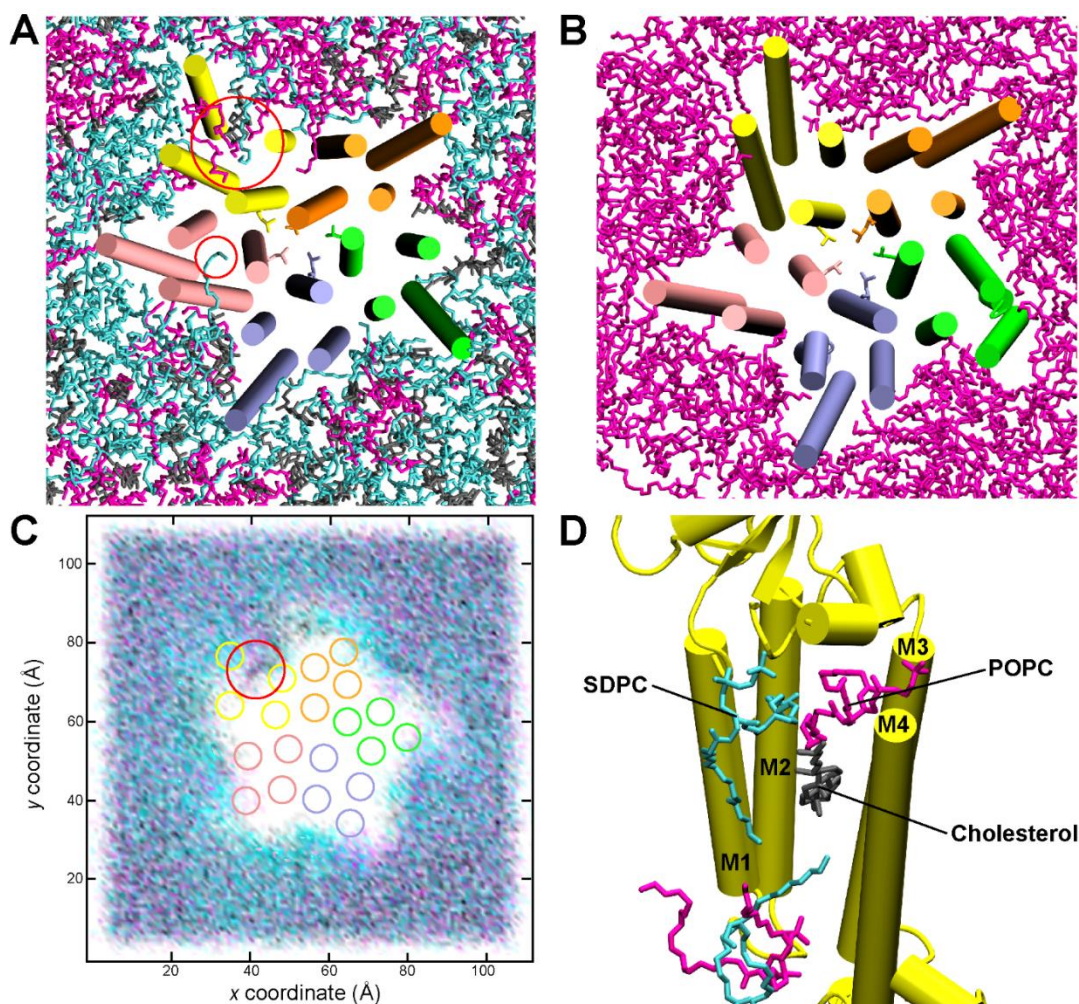


Figure 41. (A) Representative snapshot of 5-HT_{3A-5mM} colored by monomer (A, *green*; B, *purple*; C, *pink*; D, *yellow*; E, *orange*) depicting transient penetration of the TMD by 1-stearoyl-2-docosahexaenoyl-sn-glycerco-3-phosphocholine (SDPC, *cyan*) and sustained penetration by 1-palmitoyl-2-oleoyl-SN-glycero-3-phosphocholine (POPC, *magenta*), SDPC, and cholesterol (*gray*). (B) Representative snapshot of 5-HT_{3A-5mM}-POPC depicting no such penetration when only POPC is present. (C) Lipid density over 15 μs for 5-HT_{3A-5mM} depicting clustering of SDPC around the TMD and sustained penetration of the TMD. (D) Snapshot of 5-HT_{3A-5mM} monomer D (*yellow*) shown as secondary structure with penetrating lipids shown as sticks and other lipids removed for clarity.

Figure A30 demonstrates the relationship between the expansion of the intra-helical space within helices M1-M4 of monomer D, represented by the area formed between a quadrilateral whose four corners are the center of masses of these helices, and lipids that penetrate the intra-helical space as it expands. At the onset of this expansion at around 5 μs, the saturated tail of a SDPC lipid packs into the intra-helical space,

followed by the saturated tail of a POPC lipid that also packs into the intra-helical space at around 6 μ s. Over the next six microseconds, the entire POPC lipid packs within the intra-helical space, which is followed by the packing of a second POPC lipid that replaces the saturated tail of the SDPC lipid. This second POPC lipid is subsequently replaced by a single cholesterol at around 12 μ s, followed by the packing of a SDPC lipid at around 13 μ s into the intra-helical space. Finally, the packing of two additional lipids, one POPC and one SDPC lipid, into the intra-helical space, but towards the bottom of this space to result in the final conformation observed in Figure 41D, which is stable for the remaining 3 μ s of the simulation. This packing of three different lipid types stabilizes the final conformation of monomer D and is not observed in any other monomers in this replicate or in the 5-HT_{3A}-Apo and 5-HT_{3A}-15mM simulations.

In addition to the monomer D-penetrating cholesterol, which demonstrated sustained hydrogen bonding to Y442 on M4-D, two more cholesterols were identified as hydrogen bonding with a Glu residue on M3-A and an Arg residue on M4-B, respectively, for the final 10 μ s of the simulation, though no significant changes in 5-HT_{3A} structure were associated with the binding of these cholesterols to the TMD. Notably, the sustained hydrogen bonding of cholesterol to Y442 of M4-D was only made possible through the trapping of cholesterol via π - π interactions with monomer D (Figure A31). The first stable interaction with monomer D was π - π stacking with F439 of M4-D for \approx 50 ns, which transitioned to π - π stacking with F242 of M1 for \approx 50 ns and finally to hydrogen bonding with Y442 (Figure A31). Direct hydrogen bonding with Y442 would likely not be possible without first π - π stacking with Y442 and/or F439 which face outwards into the membrane on the M4 and M1 helices,

respectively. The end result is a stable binding pocket for cholesterol within monomer D of the TMD, which maintains the final conformation of the monomer (FigureA31).

5.4 Conclusion

In this chapter, all-atom MD simulations using the first resolved structure of 5-HT_{3A}, PDB ID: 4PIR.²⁴⁶ This allowed both the observation of an equilibrated membrane-bound conformation of the pLGIC, and the allosteric regulation of its structure by 5-HT. These microsecond-scale simulations permitted the depiction, for the first time, of a dynamic representation of 5-HT binding, and allosteric regulation during the pre-activation or priming of 5-HT_{3A}. From these results it can be concluded that a pre-active rather than fully activated state was observed because the ion channel through 5-HT_{3A} remained closed to ion translocation even with stable binding of two 5-HT ligands in the five possible binding pockets on the ECD. During this state, a twisting and expansion of the 5-HT_{3A} monomer bound on both sides by these 5-HT was observed, indicative of the channel being primed for activation. The observed structural changes during 5-HT binding is in agreement with the proposed mechanism of pLGIC activation.²⁴⁴ However, because only two 5-HT ligands remained bound for the full 15 μ s simulation, with the other three 5-HT ligands transiently bound, full activation of the channel was not observed. This is in agreement with kinetic models of experimental data that indicate at least three 5-HT ligands must remain bound to achieve a measurable current through 5-HT_{3A}.^{239, 270}

Notably, the kinetic models of 5-HT_{3A} that best describe experimental data require the inclusion of a pre-active state, designated by 5-HT binding that primes the pLGIC for activation,^{239, 270} proposed to enhance cooperativity.²⁷⁵⁻²⁷⁶ While there was an

observed transition of a bound 5-HT neighboring a second bound 5-HT to a less enthalpically favorable orientation, the entropic favorability of this orientation is difficult to obtain with limited sampling. Therefore, it cannot be fully quantified whether 5-HT binding caused higher affinity for 5-HT in a neighboring binding pocket as hypothesized for other pLGICs.²⁷⁵⁻²⁷⁶ However, other conformational changes from 5-HT binding which appear to prime the ECD-TMD interface for channel activation were presented, such as the stabilization of an open conformation of the M2 helix through stabilization of the M2-M3 loop of the TMD by the β 1- β 2 and β 8- β 9 loops of the ECD, in agreement with previous observation.^{248, 250} The stable binding of only two of five 5-HT ligands to 5-HT_{3A} further allowed the reporting of, for the first time, differences in allosteric regulation based on monomers that are bound on either the primary, complimentary, or both faces by 5-HT.

Critically, these observations of 5-HT_{3A} pre-activation are based on the assumption that the starting structure, PDB ID: 4PIR,²⁴⁶ represents a resting state and not a desensitized state as previously hypothesized.²⁴⁷ To this end, the accurate representation of 5-HT_{3A} *in silico* was promoted by embedding the pLGIC in a lipid membrane representative of the native membrane, measuring structural equilibration with RMSD, and comparing differences between 5-HT-bound and *apo* conformations. The lipid membrane environment, including the adequate packing of lipids in the membrane, has been shown to be essential for accurate MD simulations of ion channels, and can even regulate ion channel conductance.^{21, 61-65} *Chapter 5* reports for the first time the use of a well-equilibrated POPC/SDPC/Cholesterol lipid membrane that mimics the native neuronal membrane (specific benefits of adding SDPC and

cholesterol are presented at the end of the discussion). 250 ns of equilibration was necessary to achieve membrane equilibration, i.e., lipid packing, as reported through SA/lipid (Figure A21) for the POPC/SDPC/Cholesterol membranes (as well as pure POPC membranes). This equilibration is important because if the membrane is not natively packed it promotes the TMD to spontaneously expand outwards into the membrane, which may be erroneously observed as channel opening. Previous simulations of 5-HT_{3A} that used pure POPC membranes²⁴⁸⁻²⁵⁰ have not reported metrics such as SA/lipid that would indicate sufficient lipid packing, and may have erroneous conclusions based on less packed membranes.

Protein structure determined through crystallization is not necessarily representative of the native structure under physiological conditions, especially when nanobodies are needed to resolve the structure, such as the 5-HT_{3A} structure used here.²⁴⁶ To reconcile this, structural changes from a crystalized structure of 5-HT_{3A} to a more native state are reported and required up to 12 μ s to relax. Notably, *apo* 5-HT_{3A} took the most time to stabilize (12 μ s), whereas 5-HT-bound forms took less time (8 μ s – 10 μ s), which is likely due to loop *c* and other binding pocket residues that are restrained by 5-HT binding, but exhibit greater flexibility without 5-HT in the *apo* case. This essential RMSD metric to confirm 5-HT_{3A} equilibration in the lipid membrane was not reported for previous simulations that only equilibrated 5-HT_{3A} for at most 60 ns, whereas these results indicate that these timescales are orders of magnitude less than what is required to achieve structural equilibration.²⁴⁸⁻²⁵⁰ Similarly to under-equilibrated lipid membranes, incomplete equilibration of protein structure can lead to the erroneous observations regarding 5-HT_{3A} structure.

A conductive or open state can be easily discerned from the translocation of hydrated ions across the pLGIC. However, assigning a channel state to a closed pLGIC (i.e., a pre-active, desensitized, or resting state) is more difficult, requiring a comparison between the *apo* and ligand-bound conformations. The pore radius profiles for all four systems reported demonstrate that the TMD pore closes for both *apo* and 5-HT-bound conformations of 5-HT_{3A} to less than the radius of a hydrated K⁺ ion, resulting in a closed conformation. In 5-HT_{3A-Apo}, this closure is symmetric through the TMD, and there is little change to the pore radius profile of the ECD compared to the crystalized conformation, suggesting a resting state either before activation or after desensitization (Figure 37). Similarly, previous MD simulations of *apo* 5-HT_{3A} (PDB IDs: 4PIR and 6BE1) also report that the *apo* conformation remains closed to ion translocation and resembles a resting state.^{248, 250}

Conversely to 5-HT_{3A-Apo}, 5-HT_{3A-5mM} demonstrated asymmetric closure through the TMD in combination with evidence of pre-activation, which has not been observed previously for 5-HT_{3A}.²⁴⁸⁻²⁵⁰ Notably, asymmetric closure in 5-HT_{3A-5mM} was observed with the expansion of at least one monomer through the TMD due to 5-HT-binding. Therefore, this conformation likely represents a desensitized state which would not demonstrate an allosteric response from 5-HT binding, in contrast to a previous hypothesis.²⁴⁷ Previous MD simulations of 5-HT_{3A} have not conclusively demonstrated activation of the pLGIC with five 5-HT ligands bound for the entire simulation, including a lack of maintaining an initially open conformation in an activated state.²⁴⁸⁻²⁵⁰ Evidence of partial activation that was observed may be an artifact of insufficient

protein equilibration, insufficient lipid packing, and the application of artificial restraints that bias the structure of 5-HT_{3A} in a given conformation.²⁴⁸⁻²⁵⁰

In short, closure through the TMD of 5-HT_{3A} is not unprecedented, but the timescales used in these simulations, an order of magnitude greater than any previous work, allowed for the observation of the unbinding and rebinding of 5-HT to 5-HT_{3A}, and the priming of 5-HT_{3A} after the structure was allowed to equilibrate to a more native conformation. While the unbinding of 5-HT from 5-HT_{3A} is a novel observation, ligand unbinding has been observed previously for other pLGICs including GluCl,²⁴⁴ where four of five glutamate ligands became unbound before 500 ns, with only one rebinding transiently over the final 1 μ s. This unbinding resulted in channel closure similarly to that observed for these simulations, described as ‘spontaneous relaxation of the channel’, and supported a conclusion that crystalized conformations of pLGICs may be in a pre-active state that require microsecond timescales to observe priming or pre-activation.²⁴⁴

Lastly, evidence demonstrating the direct effects of lipids on 5-HT_{3A}, including from cholesterol and PUFA lipids, is lacking compared to other pLGICs.²⁵³ This chapter presents the sustained interactions between cholesterol and the TMD of 5-HT_{3A}, specifically that cholesterol, along with POPC and SPDC, penetrate the TMD of 5-HT_{3A-5mM} monomer D (Figure A32) as it twists and expands due to 5-HT binding and stabilize it in a presumed pre-active state. This suggests that lipid types other than POPC are required to modulate the 5-HT_{3A-5mM} response to 5-HT binding including the stabilization of the pre-active state. Also observed was hydrogen bonding between cholesterol and M4, which also has not been previously reported, and appears critical

to catch cholesterol through π - π bonding before it is able to fully penetrate the TMD. Experimentally, cholesterol has been included in lipid membranes to study the structure of 5-HT_{3A},^{246, 277} but few conclusions have been reported besides the distribution of 5-HT_{3A} in the membrane changing from evenly distributed to tightly packed clusters as a result of the removal of cholesterol.²⁷⁷ However, because the structure of 5-HT_{3A} is largely homologous to other pLGICs including the nAChR, GLIC, and GABA receptors, whose amplitude of channel conductance and rate of desensitization are regulated by cholesterol²⁵³⁻²⁵⁷ and PUFA lipids²⁷¹⁻²⁷⁴, it is likely that cholesterol and PUFA lipids play a role in regulating the structure and function of 5-HT_{3A}. Notably, MD simulations have previously demonstrated a binding site for cholesterol on GABA,²⁷¹ which demonstrated that cholesterol interacts with the M2 helix of the TMD, strongly suggesting the regulation of channel conductance. While no direct interactions between M2 and cholesterol were observed, previously²⁷¹ cholesterol was docked at the M2 helix, as opposed to these simulations which required the diffusion of lipids to penetrate 5-HT_{3A5mM} monomer D. Additional simulations of 5-HT_{3A} will be needed to fully understand the role of cholesterol and PUFA lipids in regulating 5-HT_{3A} function, including ones that leverage the potential cholesterol binding site by homology to GABA.²⁷¹

5.5 Transition to Proposed FET Measurements of 5-HT_{3A}

The previous two chapters, *Chapter 4* and *Chapter 5*, provided examples of how MD simulations are used to model ion channel function including the ionic current through the channel, including the effects of lipid membranes on the ion channels. These predictions can be particularly useful for applications such as FET biosensing,

which provide an excellent ion-sensitive platform for characterizing ion channels, but require the immobilization of ion channels above the sensing surface with lipid membranes, which as described in *Chapter 4*, can significantly impact channel current. *Chapter 5* also provided significant impact regarding the biophysical mechanisms of the biorecognition of 5-HT by 5-HT_{3A} which has implications in understanding the activation mechanism of 5-HT_{3A} as characterized with FET biosensing. The final chapter of this work provides a brief summary of how ion channels are currently characterized, and briefly describes how novel FET fabrication (*Chapter 2*) and novel FET design, as used for other ultra-sensitive protein measurements (*Chapter 3*), can be used for the characterization of ion channels.

Chapter 6: Conclusions and Outlook: Using FETs to Study Low-Conductance Ion Channels Leveraging Lessons Learned from MD Simulations

6.1 Conclusions

The primary purpose of this work was to demonstrate the benefits and potential of using FETs for biosensing applications. The following four objectives were achieved in the six chapters that make up this work:

- (i) An effective and repeatable method to fabricate FETs from monolayer MoS₂ with electrical performance sufficient to be used for biosensing applications was demonstrated in *Chapter 2*.
- (ii) The ability of these FETs to detect pH with sensitivity several times greater than the Nernst Limit as an indirect measurement of Cdk5 activity and to directly detect streptavidin binding was demonstrated in *Chapter 3*.
- (iii) MD simulations of the ion channels 5-HT_{3A} and α HL were used to model their immobilization in lipid membranes and biomarker biorecognition (in the case of 5-HT_{3A}) in *Chapters 4 and 5* which provides valuable insight into the effects of lipid membrane type on ion channel immobilization and the biophysical phenomena that govern biorecognition, as they pertain to FET biosensing.
- (iv) Experiments that use FET biosensing to characterize ion channels such as 5-HT_{3A} are outlined in *Chapter 6* which provides an accumulation of all the conclusions elucidated in this work.

This work demonstrated how experimental and simulation methods can be used to advance the application of label-free biosensing, which will serve as a useful tool for medical diagnosis and therapeutic characterization in the immediate future.

6.2 Outlook: Introduction

6.2.1 Background: Method for Ion Channel Characterization

Ion channels such as 5-HT_{3A} are typically characterized with experimental techniques such as patch-clamp, an electrochemical biosensing method which was developed in the early 1980s.²⁷⁸ A simplified diagram of how patch-clamp is performed is shown in Figure 42, where a glass micropipette filled with electrolyte solution is used to isolate a patch of cellular membrane containing a single ion channel, e.g., of a neuronal cell. A working electrode is inserted into this micropipette and connected to a reference electrode that is added to the surrounding solution, creating an electrical circuit over which a change in potential can be measured.²⁷⁸ The effective electrical circuit is the glass micropipette (R_P) in series with two parallel elements, the capacitance of the membrane (C_M) and the resistance of the ion channel (R_{IC}), where R_P and C_M are presumed constant R_{IC} , a resistance to ionic current, changes as a function of the activation of the channel by a given agonist. Generally reported is the channel current, using the applied potential, the channel resistance, and Ohm's Law ($V=IR$).²⁷⁸

While patch-clamp generally leverages an amplifier to increase the electrical signal obtained from such a measurement, the resolution is not sufficient to characterize the channel current though native 5-HT_{3A}.^{232, 236, 263, 279} This is presumed to be because of several arginine residues at the *trans* entrance of 5-HT_{3A} which serve as a selectivity

filter for negatively charged ions,^{232, 236} rendering very low channel currents (< 1 pA). Therefore, novel sensing techniques, such as ion-sensitive FET biosensing are needed to characterize the ultra-low currents through 5-HT_{3A}, to provide a platform to study the effectiveness of therapeutics, such as activation inhibitors, on the ion channel. FETs are also significantly less expensive to produce when mass-produced, potentially providing a significant cost reduction compared to the patch-clamp technique.

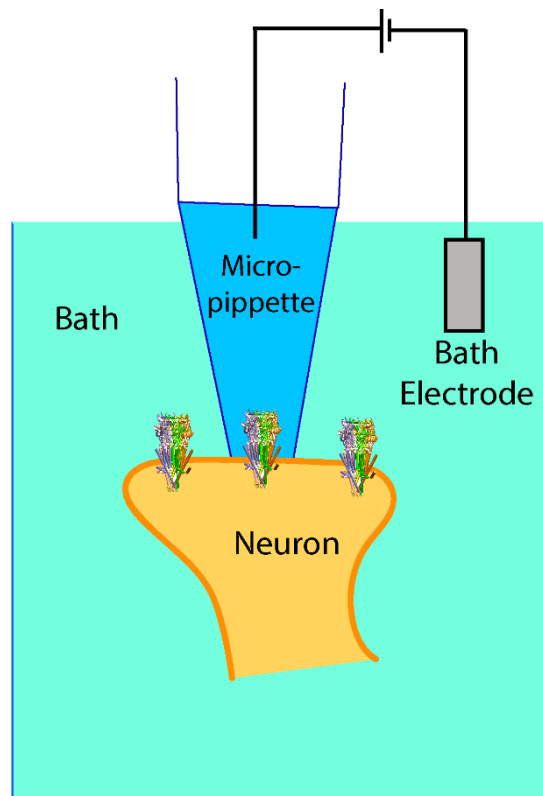


Figure 42. Simplified diagram of the patch-clamp technique. A micropipette is used to isolate a patch of a cell (e.g., neuron) membrane containing an ion channel. An electrode is inserted into the pipette and connected to a reference electrode in the bath water forming an electrical circuit over which a potential difference is measured. The potential is converted to a channel current where the ion channel acts as a resistor to ionic current.

6.3 Outlook: Experimental Outline for Ion Channel Characterization with FETs

6.3.1 Materials and Methods: Immobilization

The immobilization of ion channels on a sensing surface such that their native function is faithfully recreated requires a lipid membrane composed of lipid types necessary to maintain this function (see *Chapters 4* and *5*). A popular tool used to achieve this is a tethered-lipid membrane (TLM), which is depicted in Figure 43.^{200, 220, 280} TLMs have been used to study numerous ion channels, including α HL, the ion channel that was the subject of *Chapter 4*.^{200, 220, 280-282} TLMs are composed of two lipids types, the first is a mobile lipid known to form a bilayer membrane (Figure 43, *red*), and the second is the same lipid but with the head group removed and replaced with a hydrocarbon chain (Figure 43, *long blue/red* chains with *brown* termini) that terminates with some functional group (Figure 43, *yellow*) known to bind to the sensing surface, collectively known as the tethering lipid. The hydrocarbon chain of the tethering lipid serves to create sufficient space between the lipid membrane and the sensing surface, so that the ion channel of interest can be inserted into the membrane without sterically clashing with the sensing surface. This is not to be confused with the spacer molecule (Figure 43, *short blue/red* chain) that is added with the tethering lipid to permit the even spacing of tethering lipids along the sensing surface, as to not create clusters of tethers where ion channels would sterically clash with the tether chains.

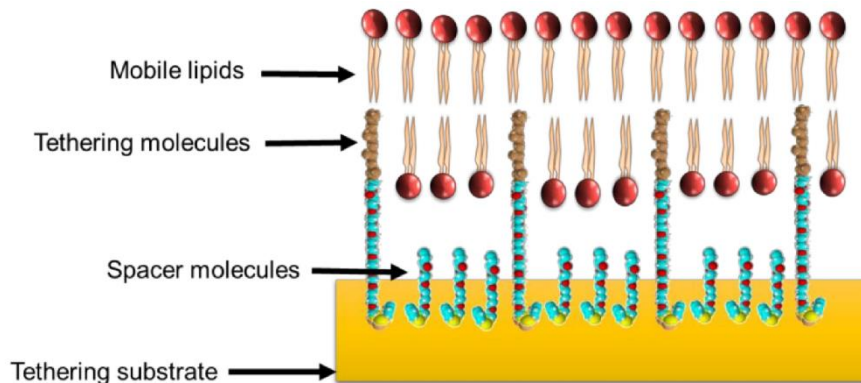


Figure 43. Schematic of a tethered-lipid membrane (TLM). First, spacer molecules (*short blue/red chains*) and tethering molecules (*long blue/red chains with brown termini*) are adhered to the surface (*gold*). Next, mobile lipids (*red*) are added, spontaneously forming a lipid membrane bilayer. Figure adapted from reference 281.

TLMs can be created by first adding a mixture of spacer molecules and tether lipids onto a cleaned sensing surface which spontaneously create a monolayer and then adding mobile lipids that spontaneously create a bilayer membrane from this monolayer.^{200, 220, 280-282} The remaining lipids are then rinsed away forming a pristine TLM. Spacer molecules and tethered lipids of varied length are commercially available to accommodate for ion channels of different length and size.²⁸¹⁻²⁸² Essential to performing FET measurements with this setup will be short spacer molecules to allow for the sensing surface to detect ions with minimal screening from the Debye-Hückel Model (see *Chapter 1*). The formation of a robust TLM can be verified with techniques such as impedance spectroscopy,²⁸³⁻²⁸⁴ where a robust TLM should demonstrate a strong capacitive component and a weak resistive component, where the latter is indicative of defects in a membrane.

The insertion of non-gating ion channels such as α HL can be measured through increases in the resistive component of these impedance measurements,²⁰⁰ however, because ion channels like 5-HT_{3A} require activation, more sophisticated techniques will

be required to verify their incorporation into the TLM, such as direct FET sensing, as described for streptavidin in *Section 3.3.5*. The significant electrostatic potential of an ion channel such as 5-HT_{3A} is well within the limit of detection of the monolayer MoS₂ FETs discussed in *Chapter 2* and *3*, providing that the lipid tethers are sufficiently short to keep the ion channel near the sensing surface and that sufficiently low concentrations of electrolyte are used to avoid electrostatic potential screening effects as predicted by the Debye-Hückel Model (see *Chapter 1*).

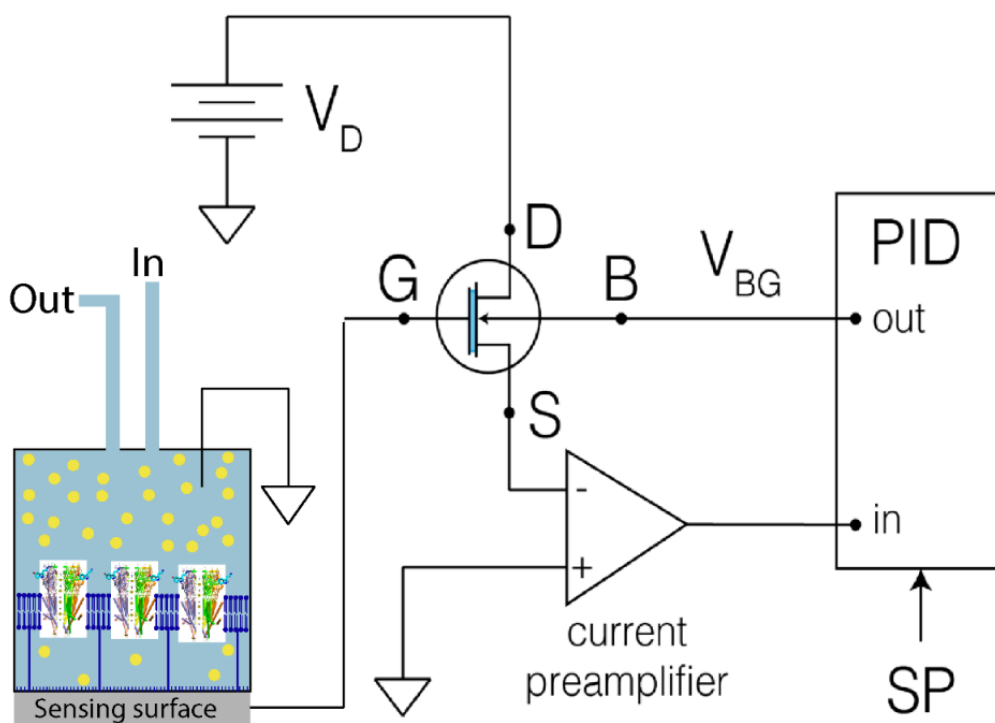


Figure 44. Schematic of proposed FET biosensing measurements for the characterization of ion channels. Details of the circuit diagram are the same as in Figure 22a for pH sensing. For ion channel characterization, ion channels will be connected near the sensing surface *via* a tethered-lipid membrane (TLM). Direct FET biosensing will be used to detect the incorporation of ion channels into the TLM and indirect FET biosensing will be used to detect ionic currents at the onset of activation by an ion channel agonist

As introduced at the start of this section, the choice of mobile lipid type is essential to maintaining ion channel function, as demonstrated with MD simulations in

Chapters 4 and 5. For 5-HT_{3A} the use of a mixture of POPC, SDPC, and cholesterol lipids was shown to be important for maintaining ion channel function with these MD simulations, and therefore a similar mixture should be considered for the TLM in the experiments outlined in this section.

6.3.2 Experimental Setup

After direct FET sensing measurements confirm the incorporation of closed 5-HT_{3A} into the TLM, the same configuration for the indirect FET measurements described in *Chapter 3* will be used where the sensing surface is utilized as an ion-sensitive surface. Figure 44 shows the same circuit diagram for this setup, except with the sensing surface shown with a TLM (*dark blue*) attached and 5-HT_{3A} inserted into the TLM. In Figure 44, ions are shown as *yellow*, where the addition of the agonist 5-HT will open up the 5-HT_{3A} ion channels and the application of a potential to the surface will drive ions through the channels.

6.3.3 Interpretation of Results and Specificity

As an ion-sensitive FET operating in constant current mode under PID control, the measured output will be ΔV_{BG} , where ΔV_{BG} will increase with the opposite polarity of the ions driven to the surface, which will have the opposite polarity of the potential applied to the solution. Furthermore, it will be important to use a buffered electrolyte solution to avoid unwanted changes in pH that could be interpreted as changes in the ionic potential on the sensing surface. In this way, the only element governing a measured change in potential is the TLM bound 5-HT_{3A} that restricts the flow of ions to the surface, which will yield high specificity for such an experiment, in that only an activator like 5-HT should be able to open 5-HT_{3A} and create ion flow to the sensing

surface. Nevertheless, control experiments with other small molecules such as 5-HT_{3A} inhibitors will need to be performed, to ensure that the binding of a small molecule to 5-HT_{3A} or the TLM will be create a significant FET signal. In the event the FET is sensitive enough to measure activator binding, differential measurements will be performed to account for this additional charge, much like the control measurements to account for the additional charge of ATP for the Cdk5 measurements presented in *Chapter 3*.

The key to maximizing sensitivity in FET biosensing is the distance that the charged biomarker can be sensed by the sensing surface, as demonstrated by the Debye-Hückel Model. Therefore, it will also be essential for these indirect biosensing experiments to leverage a spacer molecule that is as short as possible to minimize the distance between the ions and maximize the electric field they impose onto the sensing surface. Spacers are varying length are available for the creation of TLMs, therefore selection of spacers should not demonstrate to be a major challenge in these experiments.

6.4 Outlook: Conclusion

In conclusion, this chapter provides a brief outline for how FETs can be leveraged for the characterization of ion channels. The use of TLMs to recreate the function of these ion channels, with membrane lipid types found in the tissues that these proteins are natively found, should provide to be an adequate immobilization platform that permits the native biorecognition of agonists by the ion channels. The excellent performance characteristics of dual-gated, monolayer MoS₂ FETs should permit sufficiently low LODs to detect the ultra-low currents though ion channels such as the homomeric 5-HT_{3A} serotonin receptor.

This chapter builds upon numerous lessons learned demonstrated in the preceding four chapters, which were only elucidated through the novel experiments and simulations performed as part of this work. In summary, this final chapter demonstrates synergy between FET biosensing and MD simulations, specifically as to how FET biosensing can be used to characterize ion channels whose structure-function relationship can be best modelled with MD. Specifically, while current MD simulations (*see Chapter 5*) have only provided mechanistic information regarding the pre-activation of 5-HT_{3A}, future simulations will be used to model the channel current through an activated/open conformation of 5-HT_{3A}. These simulations will provide predictions on the ionic current through activated 5-HT_{3A}, which is unknown from experiment.^{232, 236} Presently, as part of this work, these MD simulations are being performed on recently resolved open/activated conformations of 5-HT_{3A} that were resolved with 5-HT bound to the structure.^{250, 258} Ultimately, FET measurements will be used to quantify the actual ionic current to validate these models with experimental data, which will also provide information useful to assigning channel state, i.e., activated versus desensitized.

Appendices

Appendix Figures.

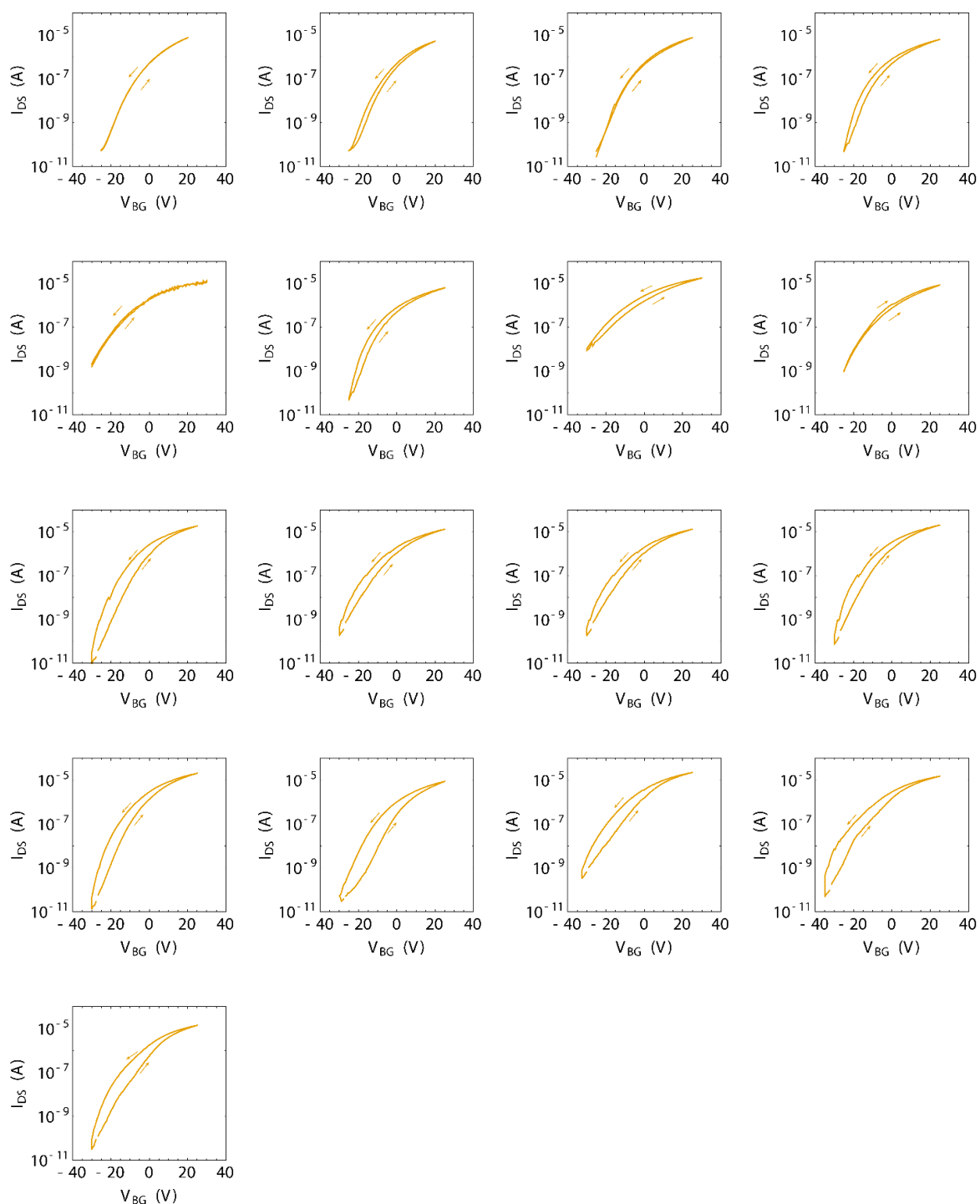


Figure A1. Transfer curves for all 17 exposed material forming gas anneal (EM-FGA) field-effect transistors (FET) for $V_{DS} = 1.05$ V demonstrating back-gate performance. All measurements were performed after deposition of a top-gate oxide and prior to the deposition of a top-gate metal.

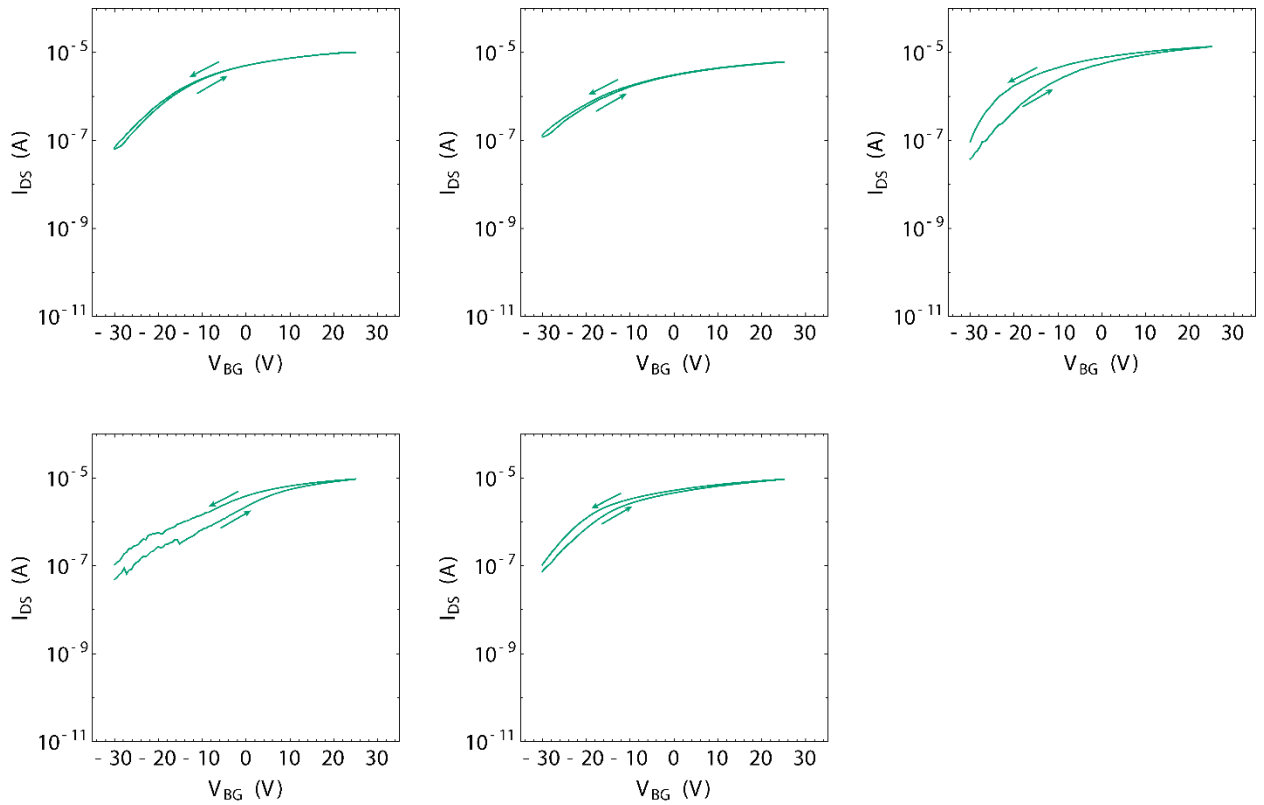


Figure A2. Transfer curves for all 5 control field-effect transistors (FET) for $V_{DS} = 1.05$ V demonstrating back-gate performance. All measurements were performed after deposition of a top-gate oxide and prior to the deposition of a top-gate metal.

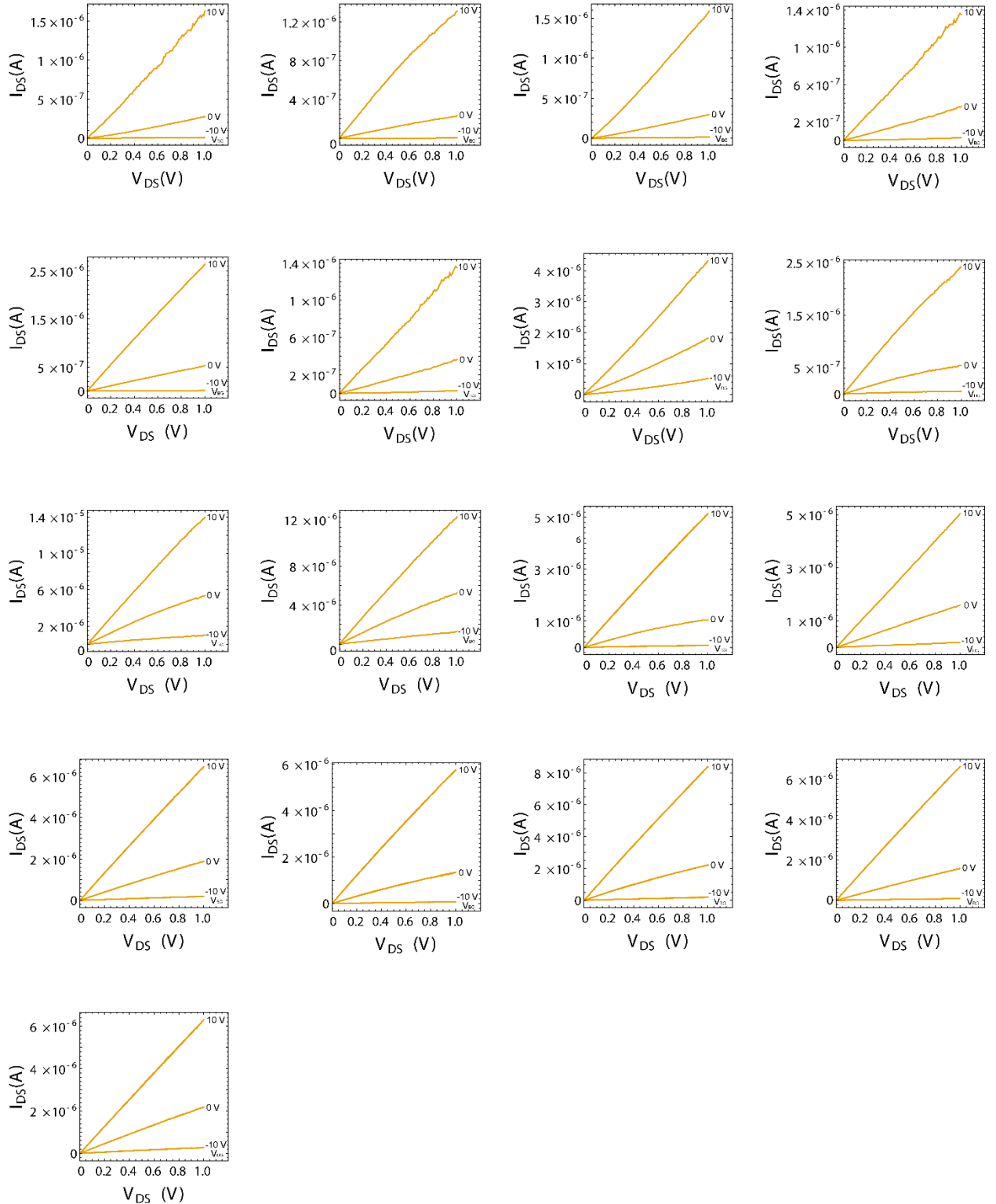


Figure A3. I_{DS} - V_{DS} curves for all 17 exposed material forming gas anneal (EM-FGA) field-effect transistors (FET) at varying V_{BG} (10 V, 0 V, and -10 V) demonstrate improved contact performance. All measurements were performed after deposition of a top-gate oxide and prior to the deposition of a top-gate metal.

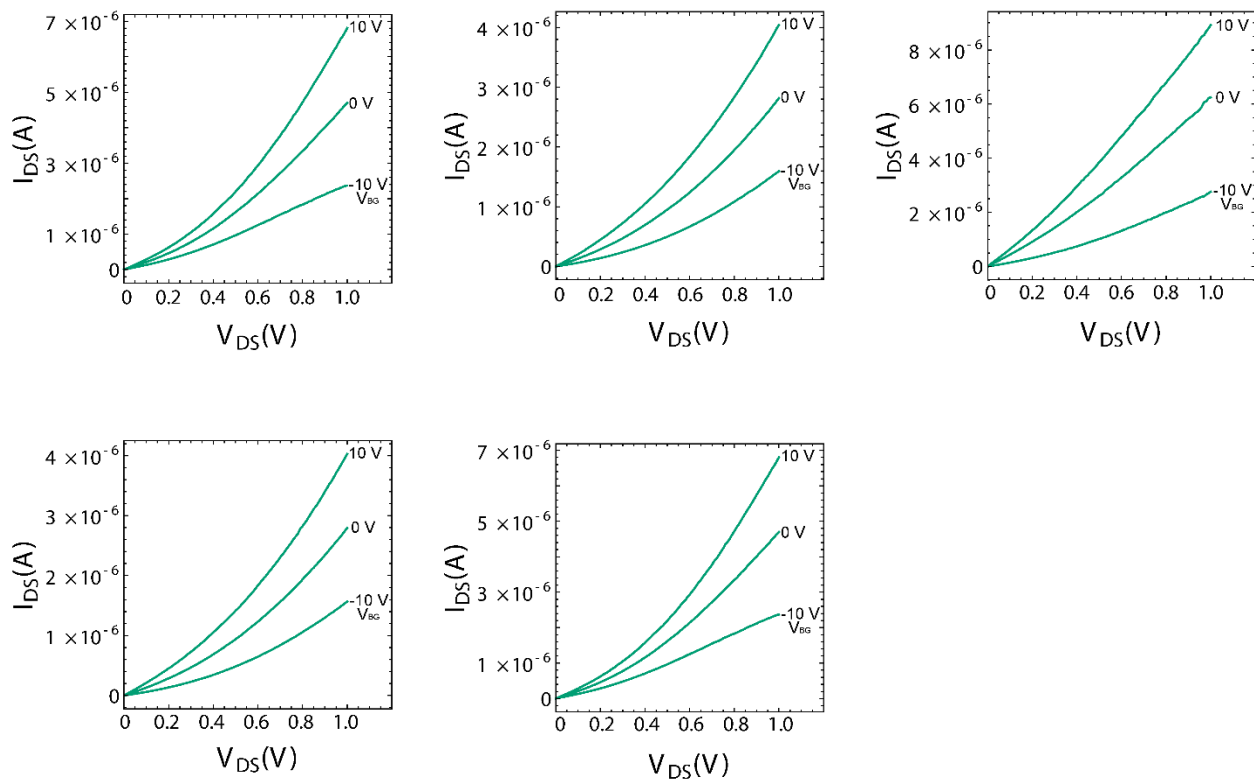


Figure A4. I_{DS} - V_{DS} curves for all 5 control field-effect transistors (FET) at varying V_{BG} (10 V, 0 V, and -10 V). All measurements were performed after deposition of a top-gate oxide and prior to the deposition of a top-gate metal.

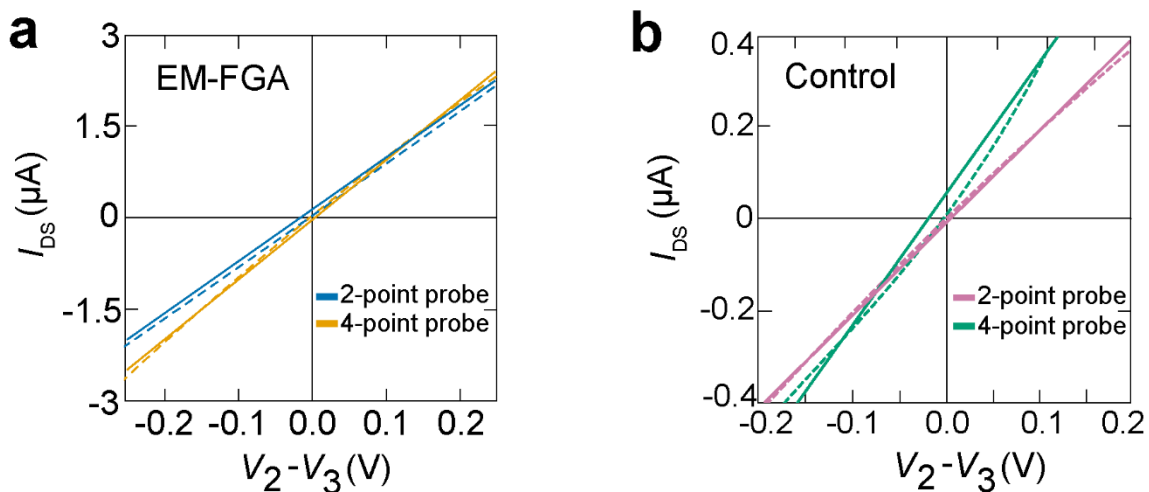


Figure A5. (a) 2-point and 4-point probe I - V curves used to calculate contact resistance for an EM-FGA FET and the same I - V curves for a control FET (b).

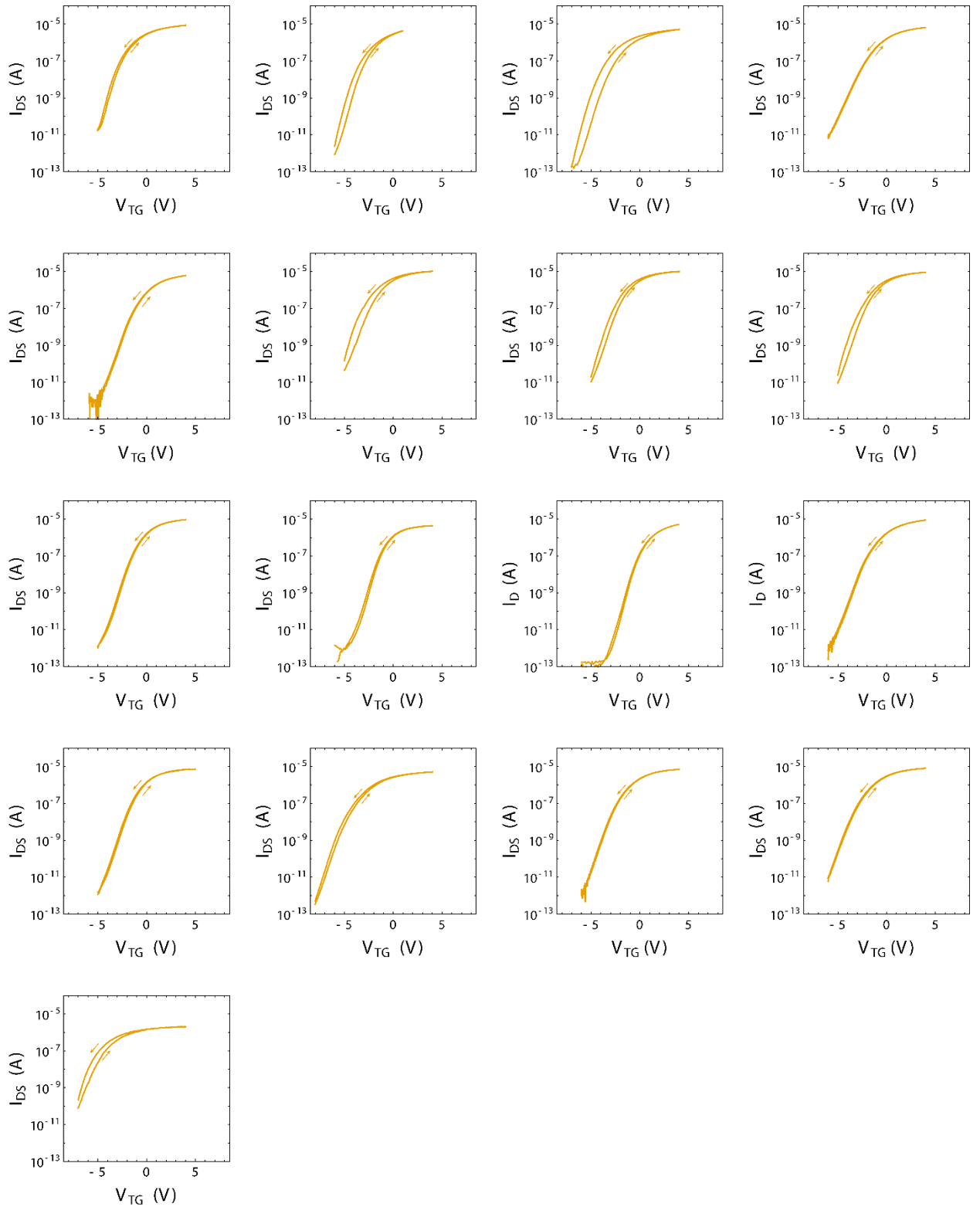


Figure A6. Transfer curves for all 17 exposed material forming gas anneal (EM-FGA) field-effect transistors (FET) for $V_{DS} = 1.05$ V demonstrating top-gate performance. All measurements were performed after deposition of a top-gate oxide and a top-gate metal.

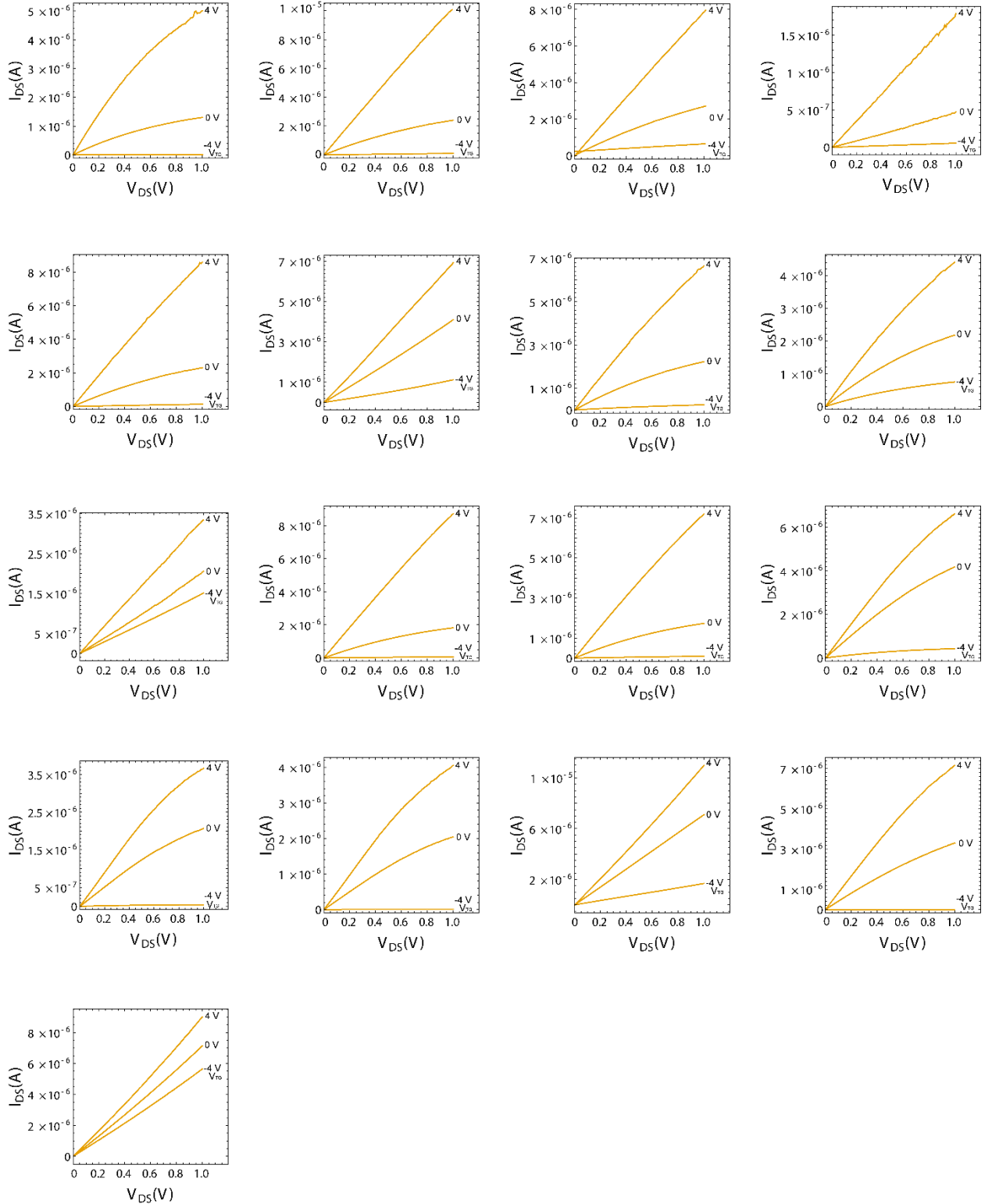


Figure A7. I_{DS} - V_{DS} curves for all 17 exposed material forming gas anneal (EM-FGA) field-effect transistors (FET) at varying V_{TG} (4 V, 0 V, and -4 V) demonstrate improved contact performance. All measurements were performed after deposition of a top-gate oxide and a top-gate metal.

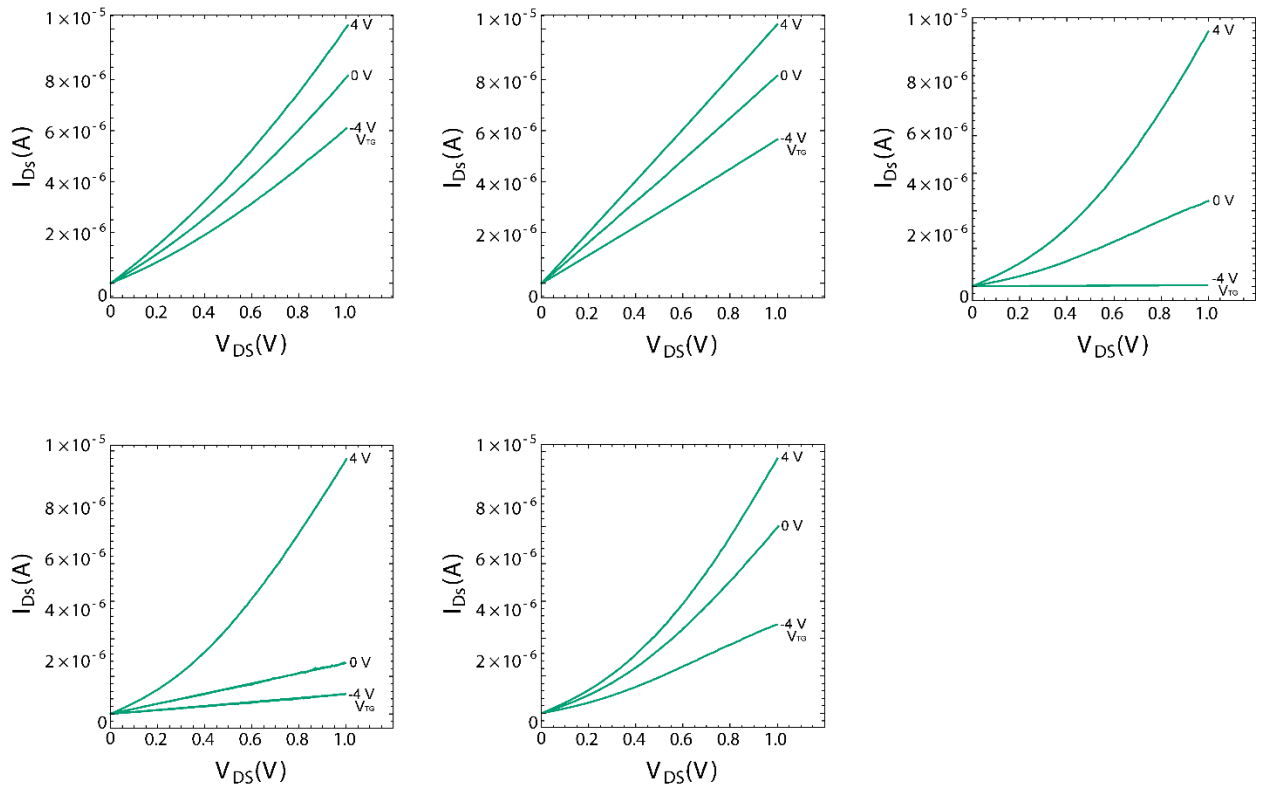


Figure A8. $I_{DS}V_{DS}$ curves for all 5 control field-effect transistors (FET) at varying V_{TG} (4 V, 0 V, and -4 V). All measurements were performed after deposition of a top-gate oxide and a top-gate metal.

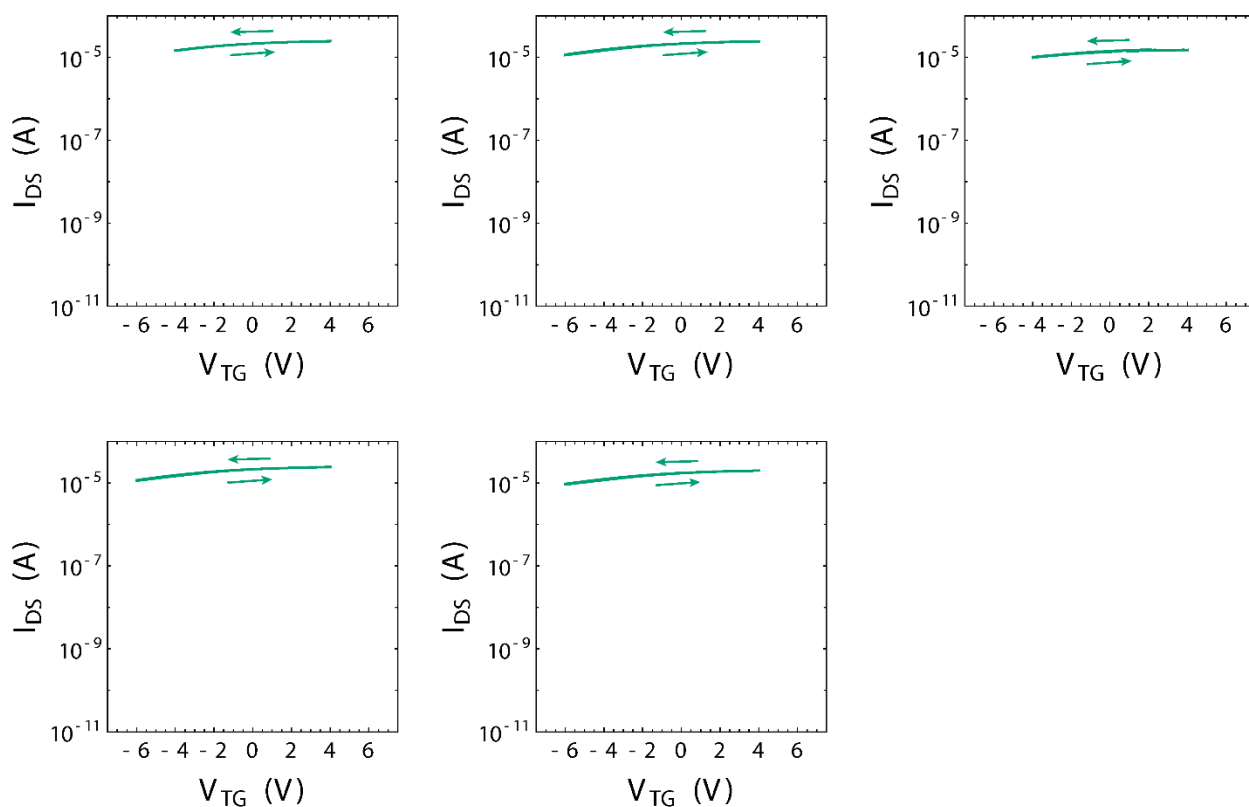


Figure A9. Transfer curves for all 5 control field-effect transistors (FET) for $V_{DS} = 1.05$ V demonstrating top-gate performance. All measurements were performed after deposition of a top-gate oxide and a top-gate metal.

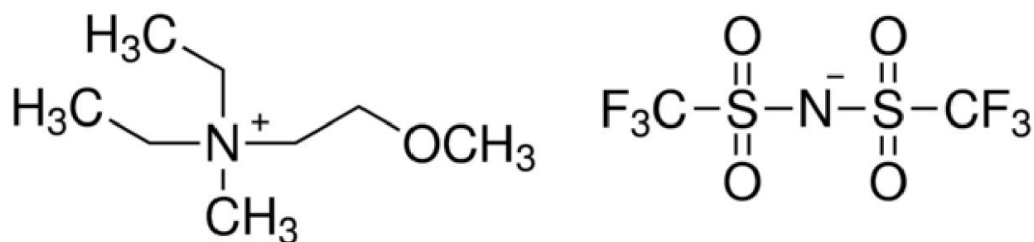


Figure A10. Chemical structure of Diethylmethyl(2-methoxyethyl)ammonium bis(trifluoromethylsulfonyl)imide, the ionic liquid using to top-gate the ionic liquid-gated field-effect transistors (LGFETs)

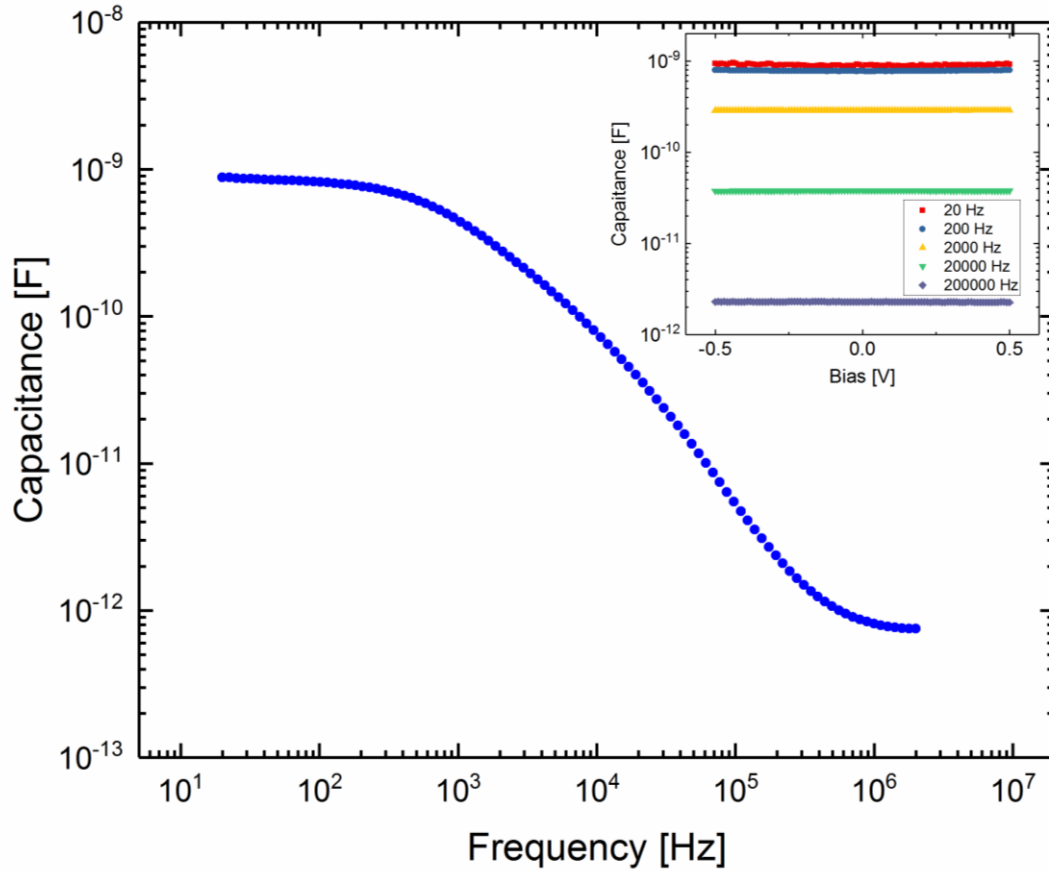


Figure A11. AC Capacitance data for ionic liquid on gold electrodes. $V_{AC} = 10$ mV, bias = 0 V. (*inset*) Capacitance with fixed frequency and measured with a variable voltage bias. Quantum capacitance was extracted following a standard practice used previously when analyzing the performance of ionic liquid gated MoS₂ field effect transistor.^{107, 162} The extracted value compares favorably with both theory and previous experiment data confirming the approach of the method used here.

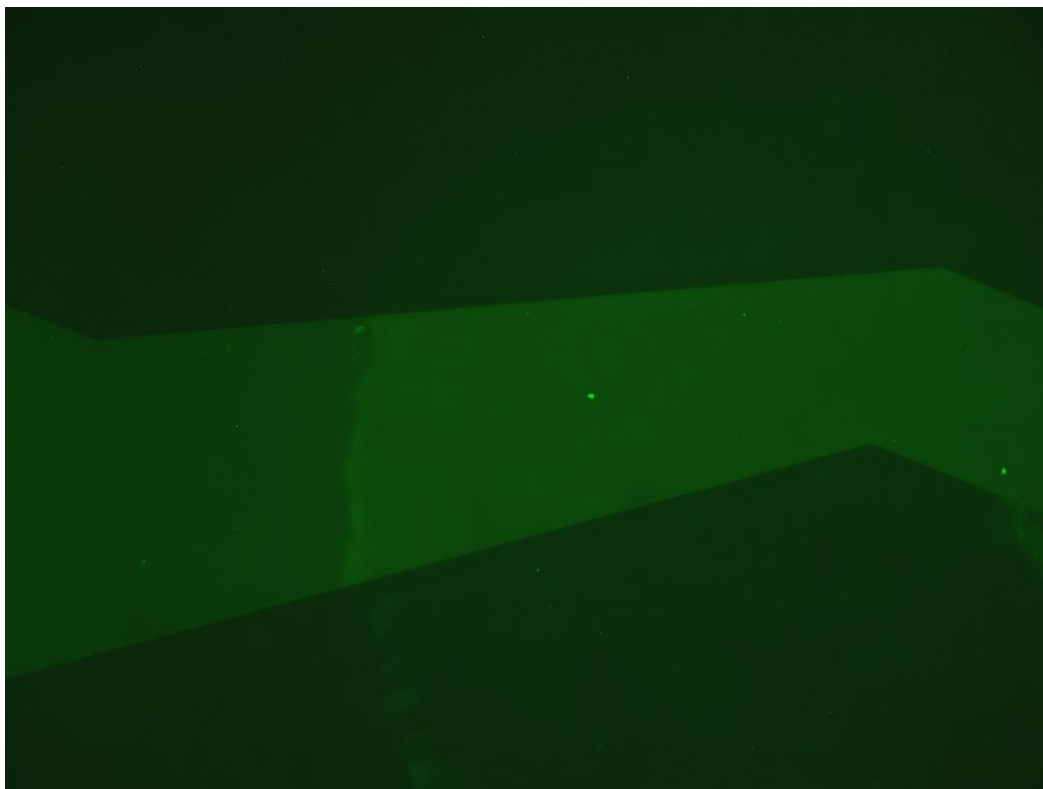


Figure A12. The fluorescently tagged Streptavidin Alexa Fluor-488 permitted fluorescent measurements to be performed that verified the binding of streptavidin to the biotinylated surface. False green coloring was added in post-processing to enhance contrast: black regions are the SiO₂ substrate, the dark green region (*left*) is the biotinylated gold outside the area partitioned with a rubber o-ring for streptavidin binding, and the light green region (*right*) is the biotinylated gold inside the area partitioned with a rubber o-ring where fluorescent streptavidin bound to the substrate.

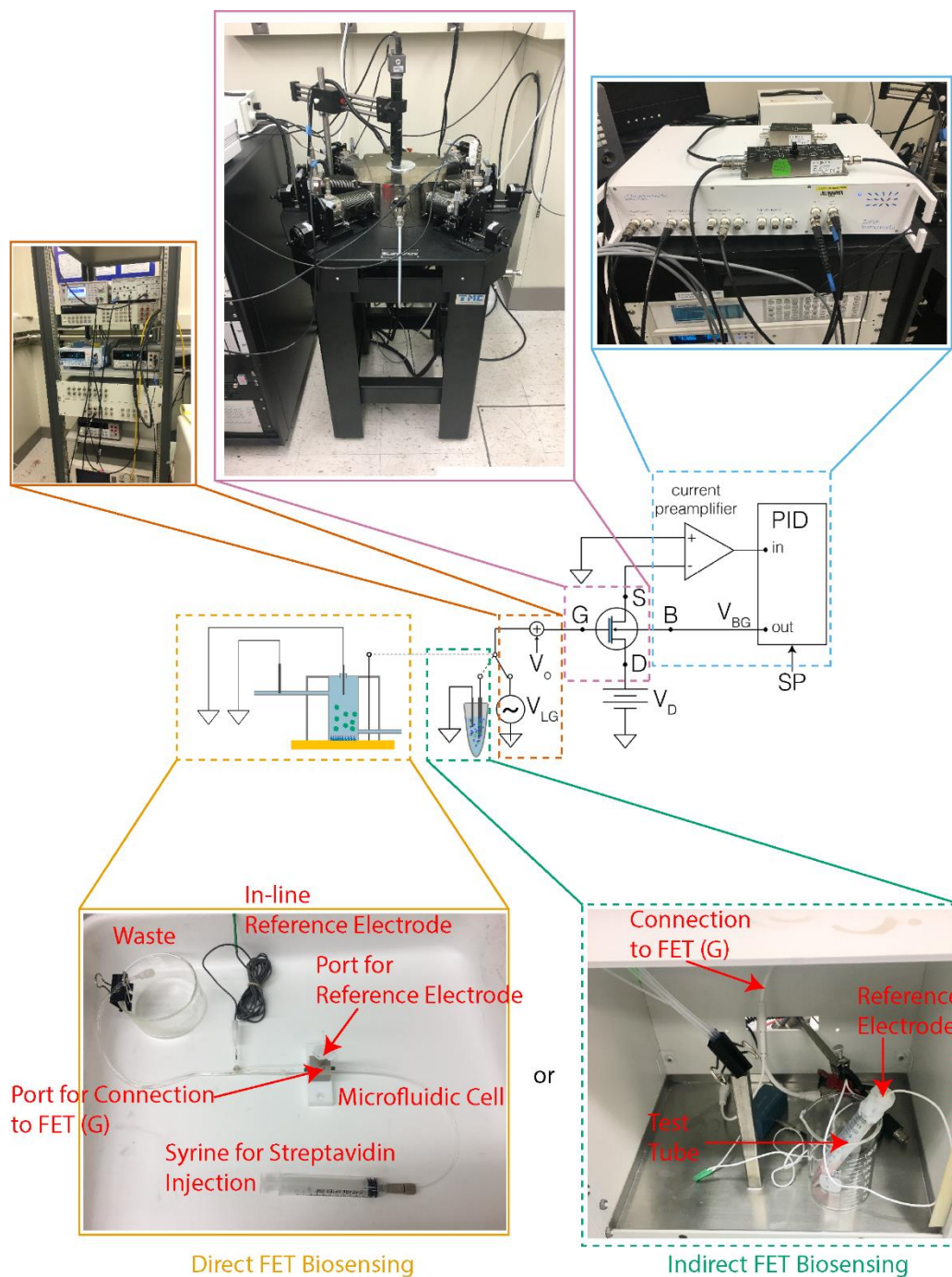


Figure A13. Schematic and associated images of both direct FET biosensing for streptavidin detection (*orange*) and indirect FET biosensing for measurements of pH or enzymatic activity (*green*). For streptavidin measurements, either an in-line reference electrode or reference electrode inserted into the injection port were used. FET shown in *reddish purple*, PID controller and current preamplifier shown in *sky blue* and wave function generator and offset voltage shown in *vermillion*.

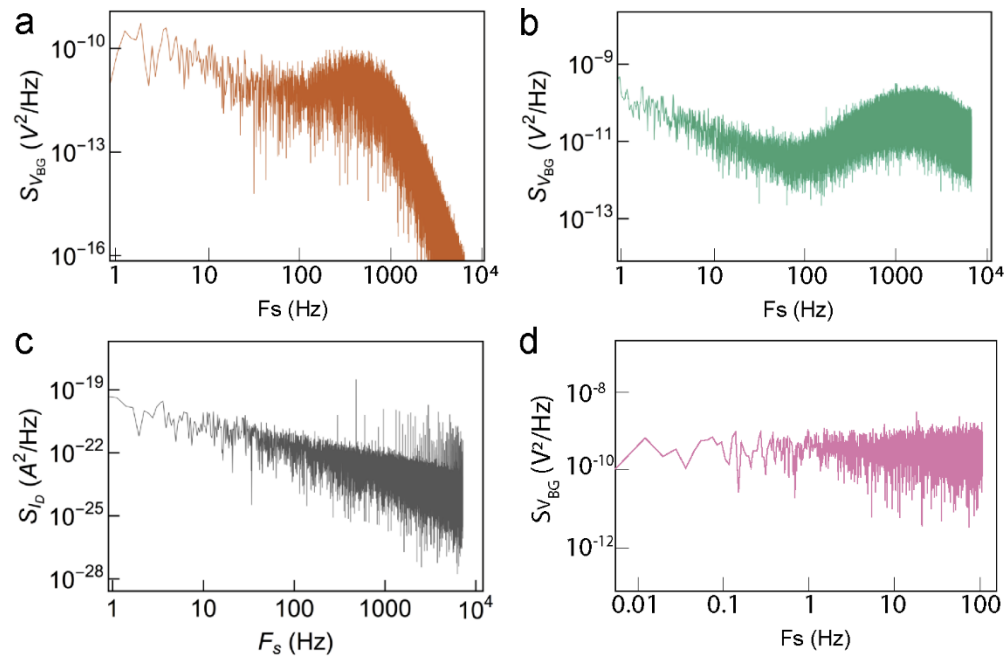


Figure A14. Power spectral densities for a ionic liquid-gated FET (LGFET) of (a) V_{BG} (300 nm SiO_2) and (b) V_{BG} 70 nm SiO_2 under PID control, of (c) I_D (300 nm SiO_2) under open loop operation, and for a solid-state FET (SSFET) of (d) V_{BG} (300 nm SiO_2), which were used to estimate the signal to noise ratio (SNR).

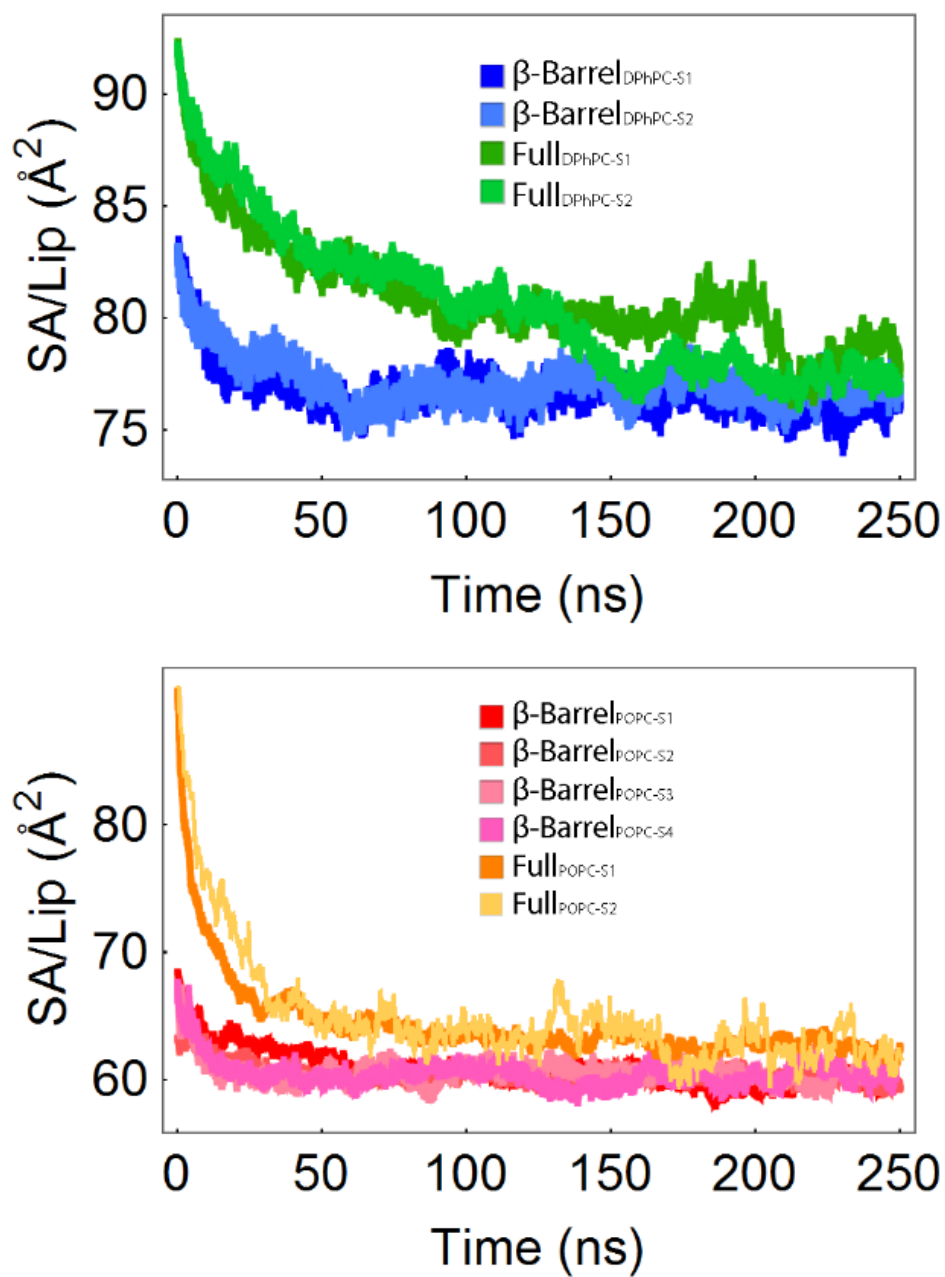


Figure A15. Lipid surface area (SA) versus time depicting convergence to stable SA/lipid values after sufficient membrane equilibration.

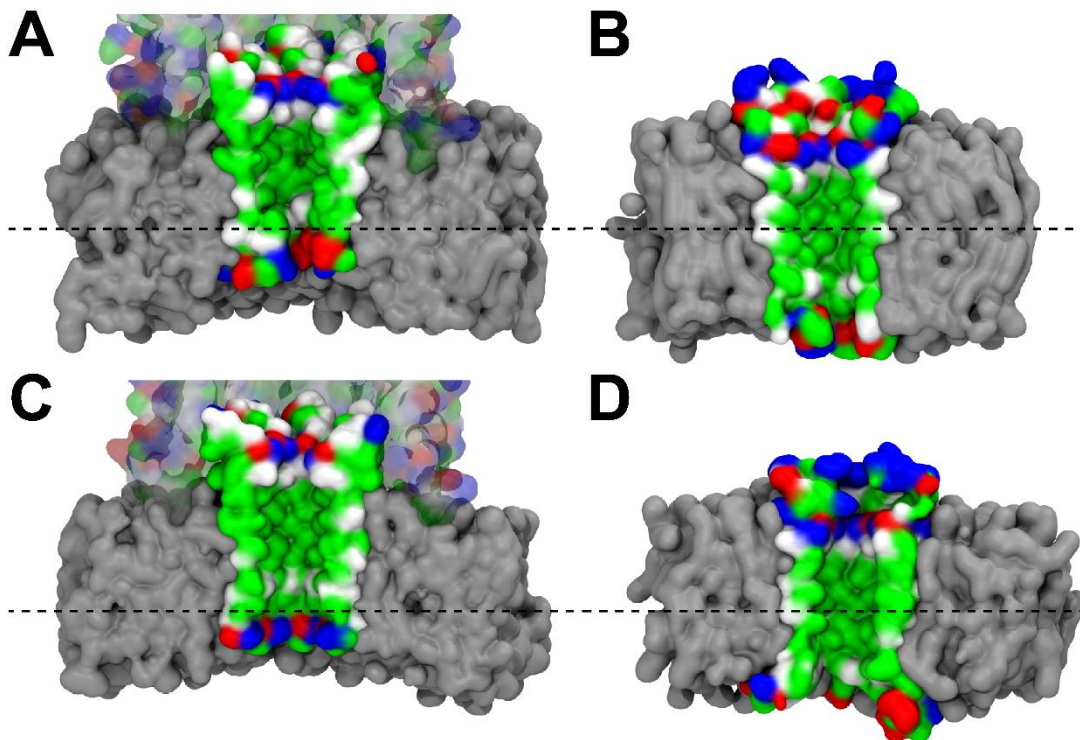


Figure A16. (A) Representative cross section snapshot of truncated β -barrel_{POPC-S1} depicting the β -barrel of α HL extending downwards into the membrane exposing the β -strand *trans* entrance loops to the aqueous phase which destabilizes the loops. (B) Representative cross section snapshot of Full_{POPC-S1} for comparison of relative height of α HL in the membrane. (C) Representative cross section snapshot of truncated β -barrel_{DPhC-S1} depicting the β -barrel of α HL extending downwards into the membrane also exposing the β -strand *trans* entrance loops to the aqueous phase which destabilizes the loops. (D) Representative cross section snapshot of Full_{DPhC-S1} also for comparison of relative height of α HL in the membrane. α HL is shown as an electrostatic surface colored by residues charge type. Lipid membrane is shown as a gray electrostatic surface.

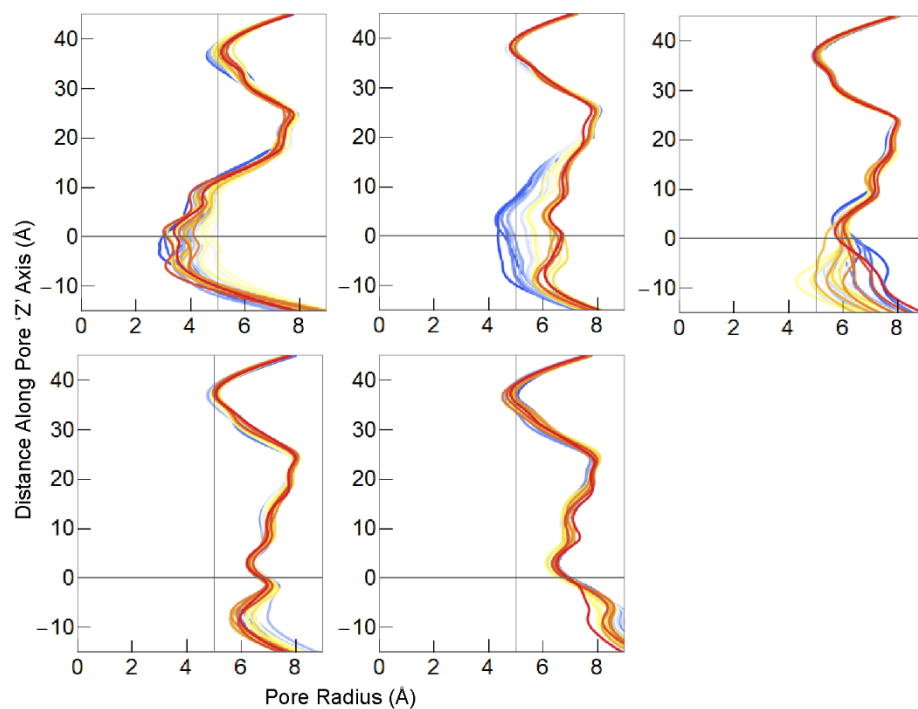


Figure A17. Channel radius profiles of the transmembrane region shown over time as a temperature map (blue: 0 ns, yellow: 125 ns, red: 250 ns). Top row from left to right: Full_{POPC-S1}, Full_{POPC-S2}, Full_{POPC-S3*}; bottom row from left to right: Full_{DPhPC-S1}, Full_{DPhPC-S2}

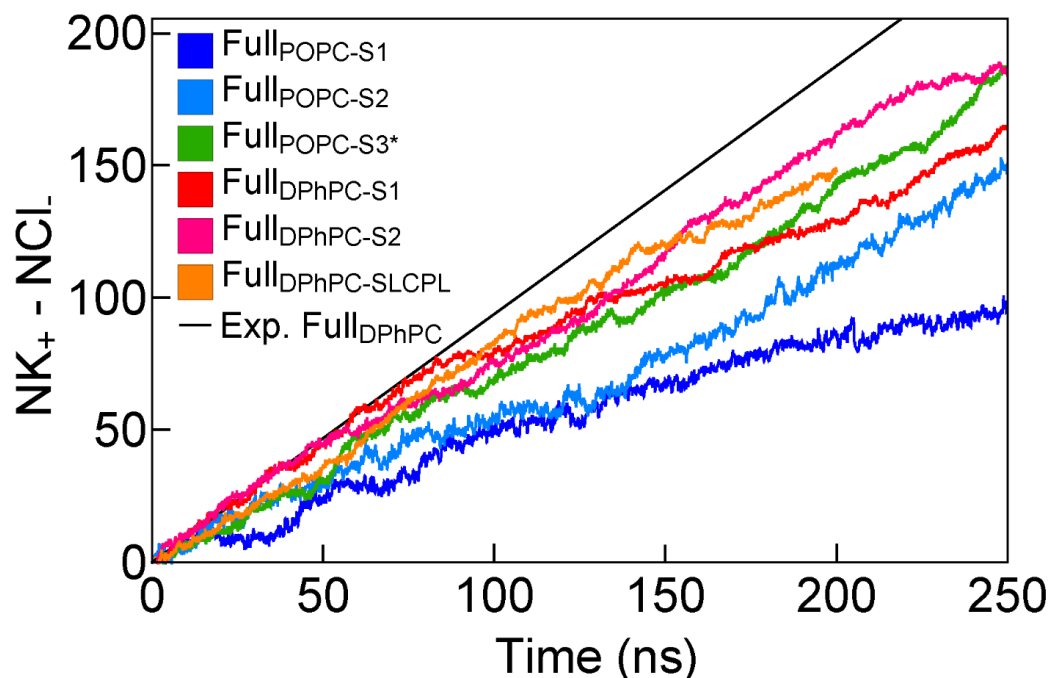


Figure A18. Ionic current through α HL shown as the accumulation of ion crossings for individual replicates. While average trends (Figure 5A) demonstrate overall differences between POPC and DPhPC, individual trends show $\text{Full}_{\text{DPhPC-SX}}$ display excellent agreement to experimental current through ≈ 60 ns and less variability between replicates in contrast to $\text{Full}_{\text{POPC-SX}}$ which display agreement to experimental current only through ≈ 20 ns and significant variability after 150 ns. The divergence in channel current for $\text{Full}_{\text{POPC-SX}}$ after 150 ns is correlated to pore collapse which is not observed as significantly in DPhPC membranes. $\text{Full}_{\text{DPhPC-SLCPL}}$ (Langevin coupling applied only to non-hydrogen protein and lipid atoms) demonstrates an insignificant difference in DPhPC currents when Langevin coupling is applied to only non-hydrogen protein and lipid atoms or too all non-hydrogen atoms (including water).

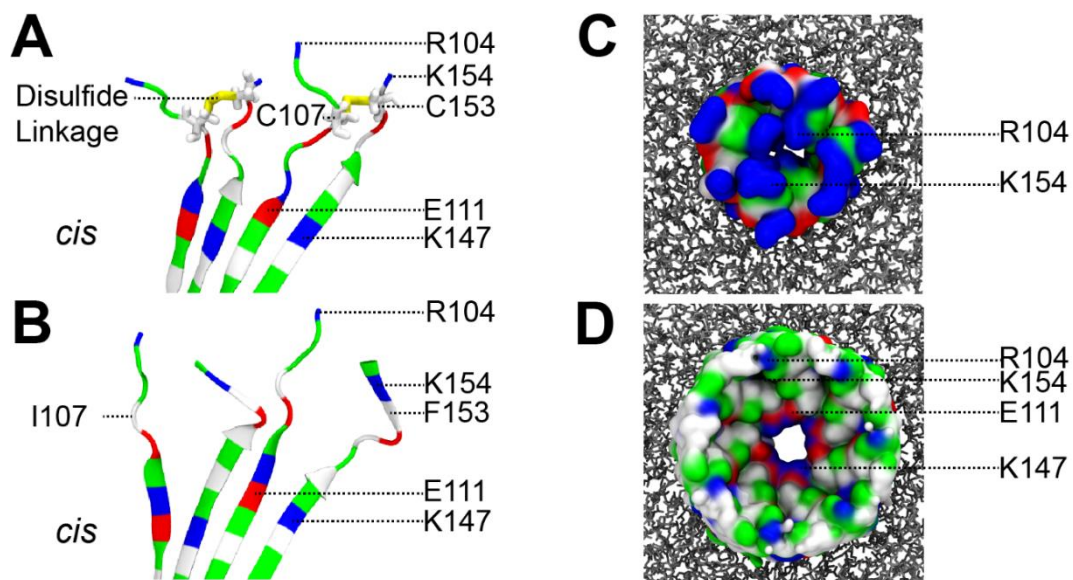


Figure A20. (A) Barrel_{DPhPC-SX} depicting disulfide linkages (*yellow*) between β -strands to prevent unravelling. (B) Full_{DPhPC-SX} depicting coupling between neighboring β -strands and not individual strands. (C) Channel occlusion and obfuscation of the principal constriction by R104 and K154. (D) Restraint of R104 and K154 by the cap prevents additional channel occlusion above the principal constriction. α HL shown by secondary structure with residues colored by side-chain charge type.

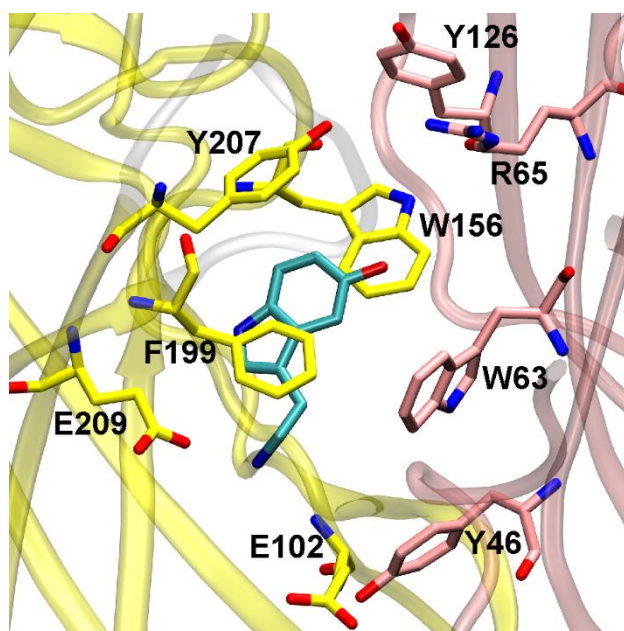


Figure A20. Example binding pose of 5-HT obtained using *Autodock Vina*.

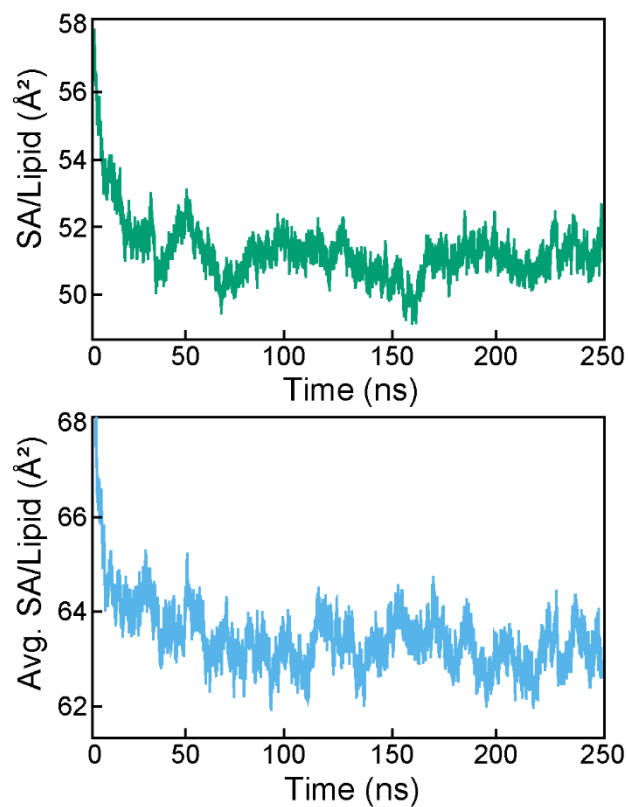


Figure A21. Average surface area per lipid (SA/lipid) during constant pressure and temperature (NPT) equilibration of the mixed 7:7:6 1-stearoyl-2-docosahexaenoyl-sn-glycerco-3-phosphocholine (SDPC)/1-palmitoyl-2-oleoyl-SN-glycero-3-phosphocholine (POPC)/cholesterol (top, *green*) membrane and POPC (bottom, *blue*) membrane.

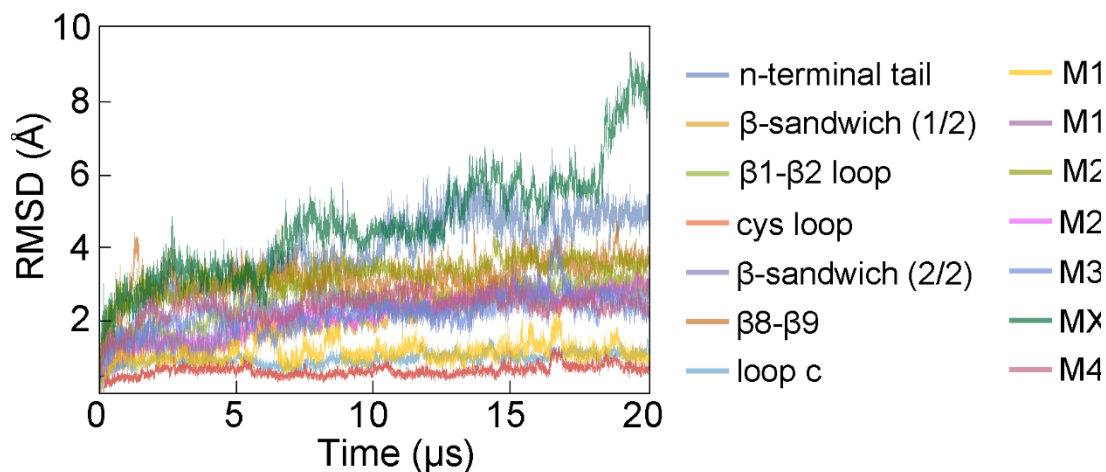


Figure A22. Total backbone root-mean-square deviation (RMSD) of the secondary structure motifs (Table S1) for 5-HT_{3A-Apo}.

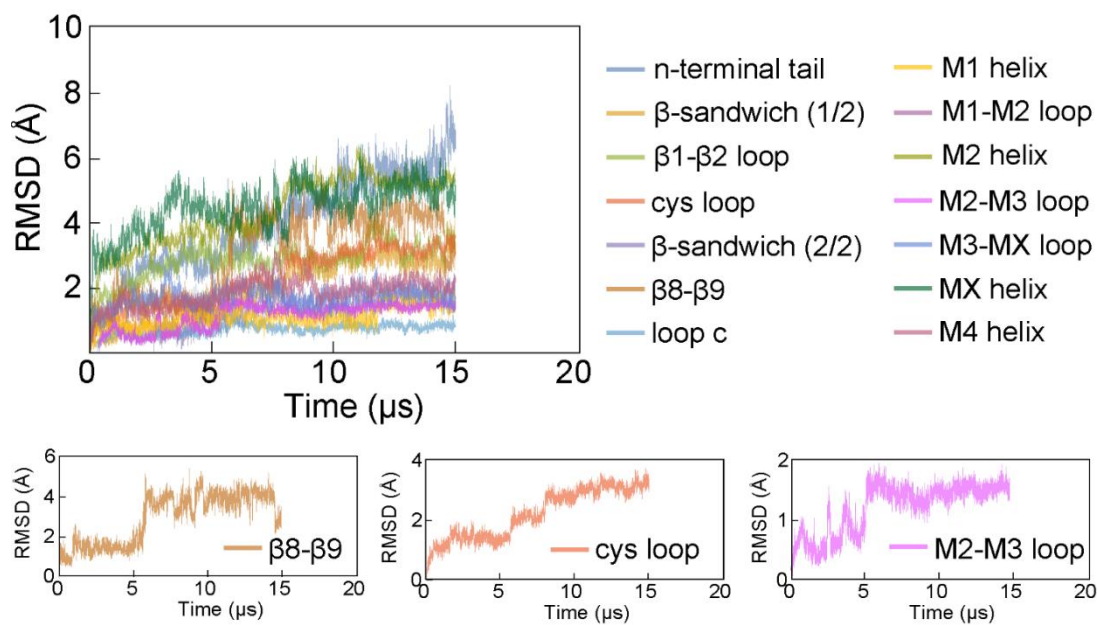


Figure A23. (Top Row) Total backbone root-mean-square deviation (RMSD) of the secondary structure motifs (Table S1) for 5-HT_{3A-5mM}. (Bottom Row) Total backbone RMSD highlighted for the β 8- β 9, *cys*, and M2-M3 loops.

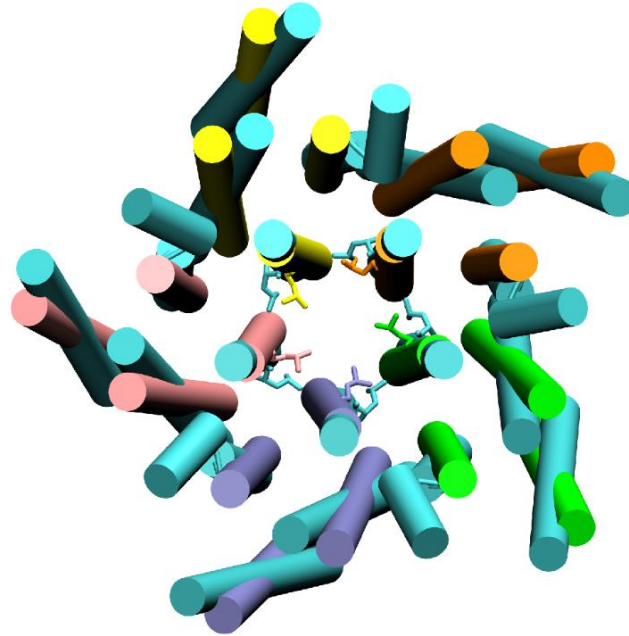


Figure A24. Transmembrane domain (TMD) of an open conformation of 5-HT_{3A} (PDB ID: 6HIN, *cyan*) overlaid with the closed conformation of 5-HT_{3A} (PDB ID: 4PIR) colored by monomer (A, *green*; B, *purple*; C, *pink*; D, *yellow*; E, *orange*) where L260 is shown for both structures as sticks.

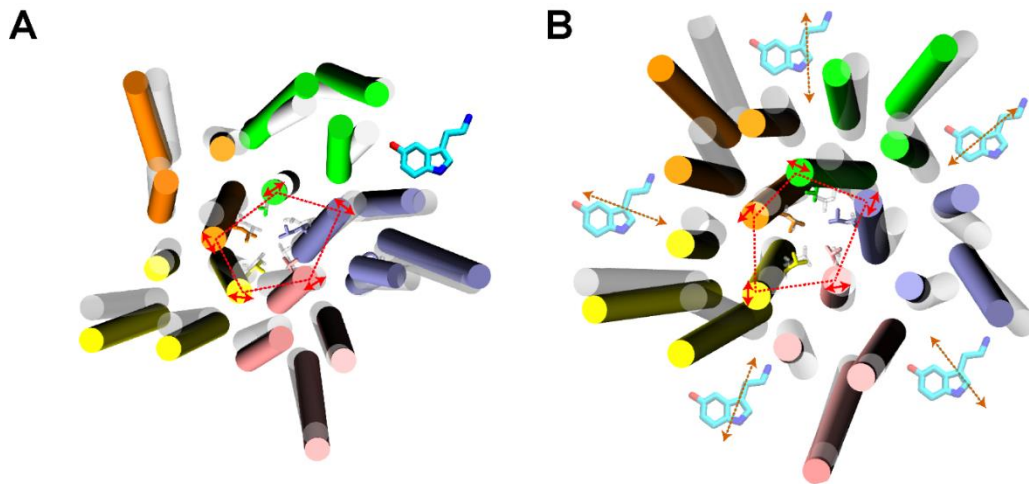


Figure A25. (A) Transmembrane domain (TMD) snapshot for 5-HT_{3A-5mM-POPC} (including L260) shown as secondary structure and lines (respectively), with the initial structure as transparent white and the final structure colored by monomer (A, *green*; B, *purple*; C, *pink*; D, *yellow*; E, *orange*), with lipids, water, and ions removed for clarity. Representative helix labels for M1-M4 shown for monomer C with red, dashed lines connecting the centers of pore-lining M2 helix to demonstrate symmetry and *red*, solid arrows indicating the principal direction of M2 fluctuation with cartoon 5-HT indicating 5-HT-binding between monomers for the entire 15 μ s (*solid*) and transient binding (*transparent with dashed arrows*). (B) Same as (A) for 5-HT_{3A-15mM}

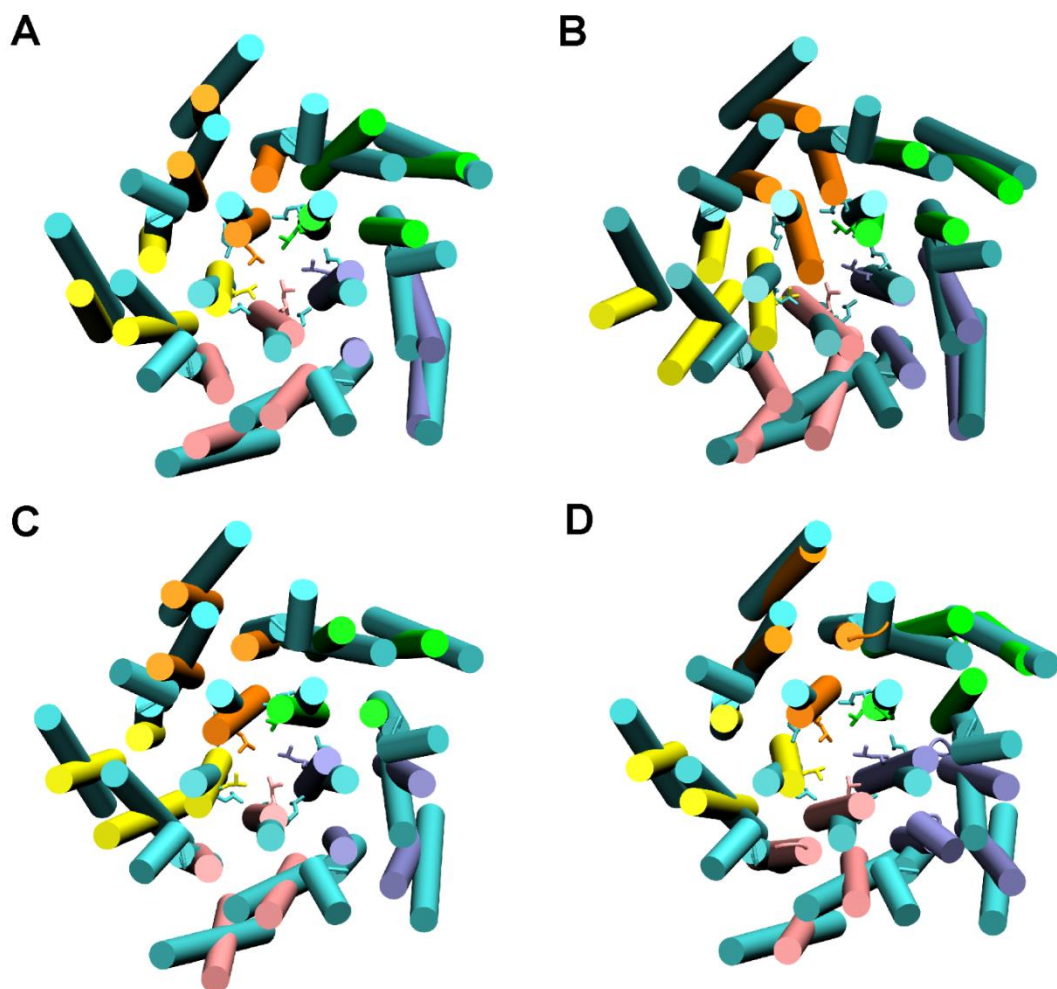


Figure A26. Comparison of representative transmembrane domain (TMD) snapshots from Figure 3 and Figure S6 overlaid with the open conformation of 5-HT_{3A} (PDB ID: 6HIN, cyan) colored by monomer (A, green; B, purple; C, pink; D, yellow; E, orange), with lipids, water, and ions removed for clarity: (A) 5-HT_{3A-Apo}, (B) 5-HT_{3A-5mM}, (C) 5-HT_{3A-15mM}, and (D) 5-HT_{3A-5mM-POPC}. The primary constriction residue L260 is shown as sticks.

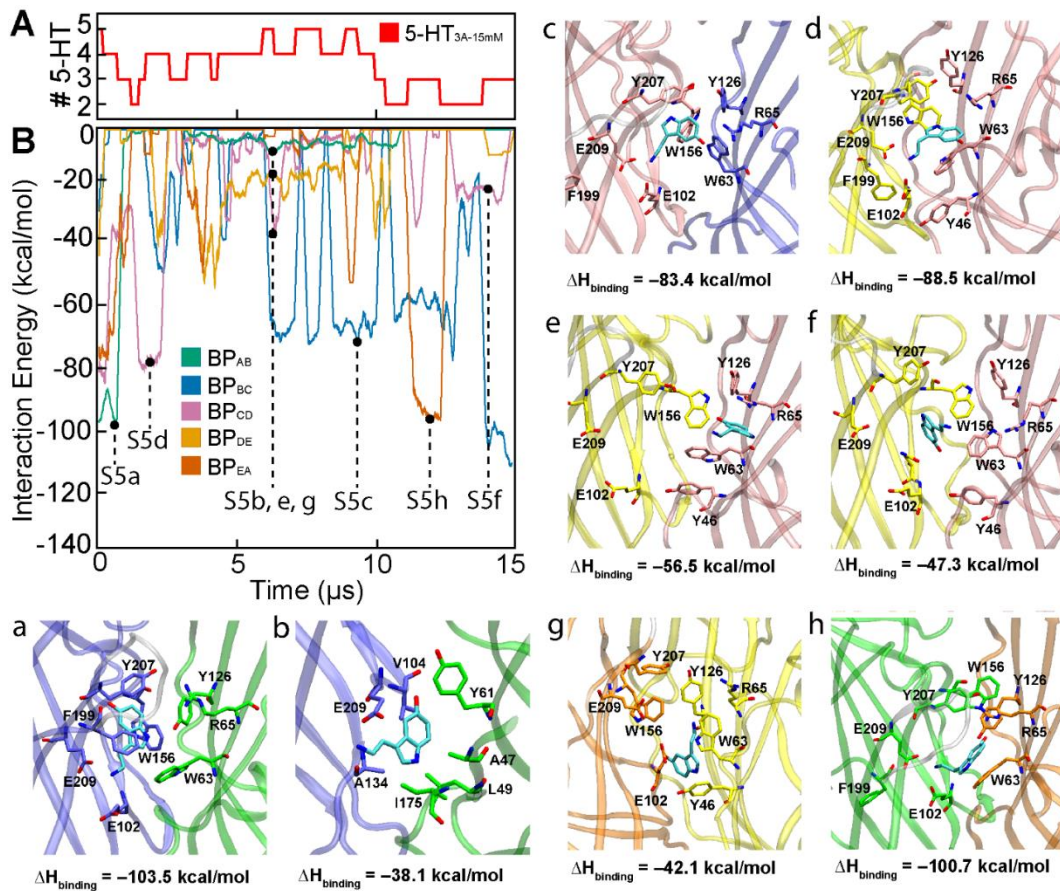


Figure A27. (A) Total binding events of 5-HT with 5-HT_{3A-15mM}. (B) enthalpic contribution to binding energy between 5-HT and the extracellular domain (ECD) where letters correspond to binding orientations on the bottom and right: bpAB (a, ≈ 1.2 μ s), bpAB (b, ≈ 6.4 μ s), bpBC (c, ≈ 9.1 μ s), bpCD (d, ≈ 2.2 μ s), bpCD (e, ≈ 6.4 μ s), bpCD (f, ≈ 14.1 μ s), bpDE (g, ≈ 6.4 μ s), and bpEA (h, ≈ 12.2 μ s).

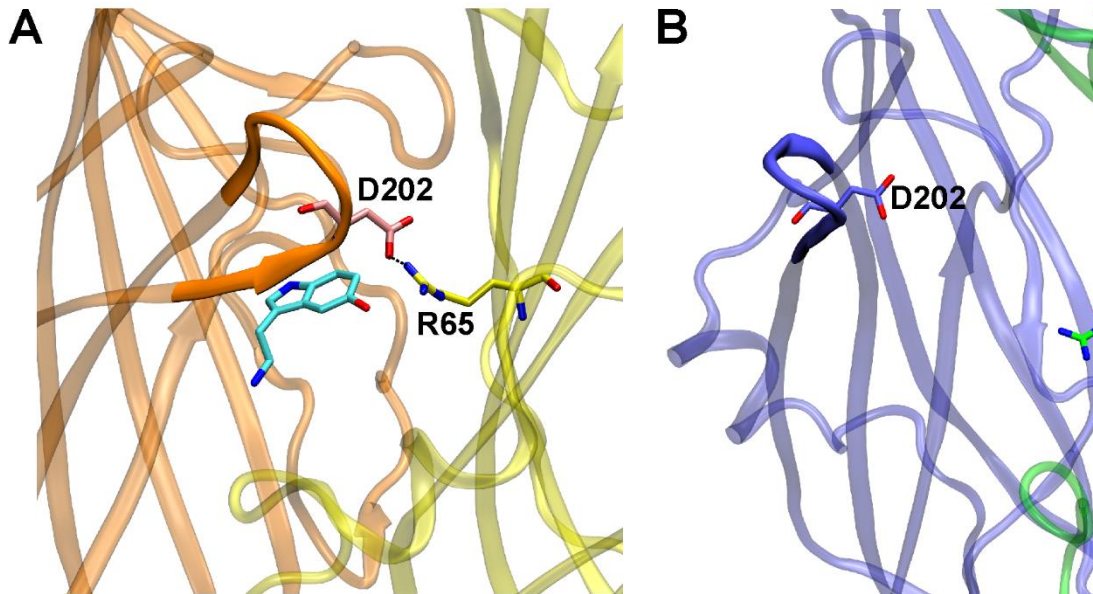


Figure A28. (A) Secondary structure of a binding pocket with D202 and R65 represented with sticks to demonstrate the essential salt bridge that helps maintain an optimal binding environment for 5-HT (cyan). (B) When this salt bridge is broken, 5-HT rapidly unbinds from the binding pocket because several of the residues involved in 5-HT binding are located near D202 of loop *c* which swings open without stabilization from the D202-R65 salt bridge.

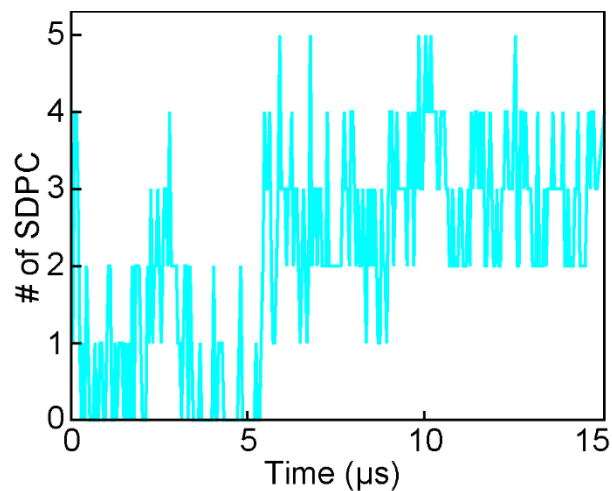


Figure A29. Total number of SDPC penetrating the transmembrane domain (TMD) of 5-HT_{3A-5mM}.

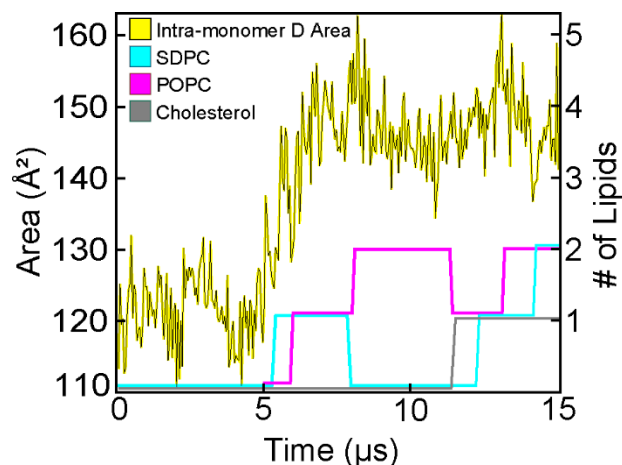


Figure A30. Correlation between the intra-transmembrane domain (TMD) area of monomer D (left axis) and number of lipids penetrating this area (right axis). Legend: SDPC: 1-stearoyl-2-docosahexaenoyl-sn-glycerco-3-phosphocholine, POPC: 1-palmitoyl-2-oleoyl-SN-glycero-3-phosphocholine.

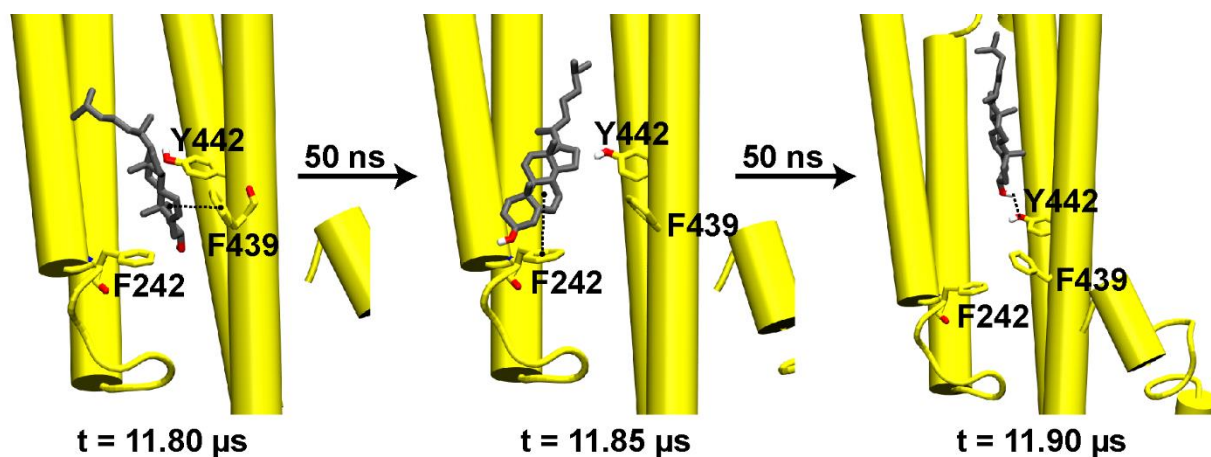


Figure A31. Trapping and transition of cholesterol (*gray*) within 5-HT_{3A-5mM} monomer D (*yellow*) with relevant side chains depicted as lines. Cholesterol is initially stabilized through π - π stacking with F439 of M4, but switches to π - π stacking with F242 of M1. After stabilization within monomer D, cholesterol flips orientation and is ultimately stabilized through hydrogen bonding with Y442 of M4.

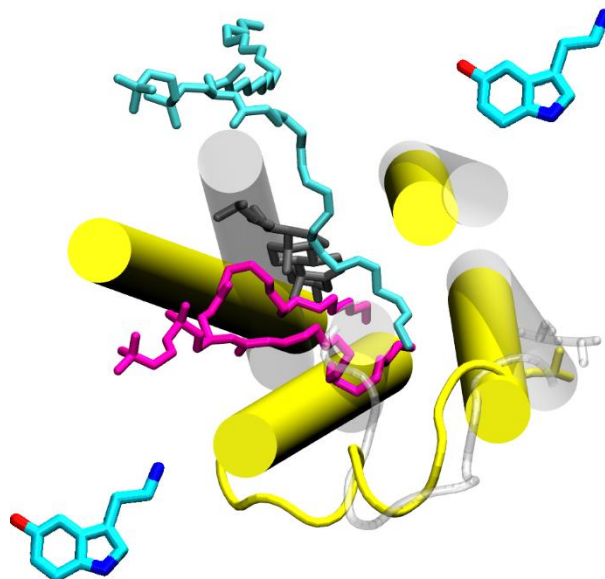


Figure A32. Initial (*white*, transparent) and final (*yellow*, solid) conformations of the transmembrane domain (TMD) helices M1-M4 and the M2-M3 loop of 5-HT_{3A-5mM} monomer D before and after twisting and expansion due to 5-HT binding to the extracellular domain (ECD) on either side of the monomer (shown schematically). Also depicted are the three primary lipids that penetrate the intra-TMD space created from this conformational shift.

Appendix Tables.

System Name	Protein – Membrane	<i>trans</i> entrance – Membrane	Constriction – Membrane
Definition (selection)	Entire protein – entire lipid membrane	Residues from V124 to L135 (including D127 and K131 with charged side chains) – entire lipid membrane	Residues E111 and K147 – entire lipid membrane

Table A1. Definitions (selections) of α HL regions and membrane for interactions energy calculations

Table A2. Relevant secondary structure motifs and associated residue numbers.

<i>Secondary Structure Motif</i>	Residue #s
<i>n</i> -terminal tail	8:36
β -sandwich (1/2)	37:134
(β 1- β 2 loop)	52:57
<i>cys</i> loop	135:147
β -sandwich (2/2)	148:176
β 8- β 9 loop	177:180
Loop <i>c</i>	181:219
M1 helix	220:244
M1-M2 loop	245:248
M2 helix	249:272
M2-M3 loop	273:281
M3 helix	282:308
M3-MX loop	309:317
MX helix	318:334
M4 helix	399:459

Bibliography

1. IUPAC. Compendium of Chemical Terminology, n. e., Blackwell Scientific Publications: Oxford.
2. Malhotra, B. D.; Chaubey, A., Biosensors for Clinical Diagnostics Industry. *Sensors and Actuators B: Chemical* **2003**, *91* (1-3), 117-127.
3. Rasooly, A.; Jacobson, J., Development of Biosensors for Cancer Clinical Testing. *Biosensors and Bioelectronics* **2006**, *21* (10), 1851-1858.
4. Rodriguez-Mozaz, S.; de Alda, M. J. L.; Barcelo, D., Biosensors as Useful Tools for Environmental Analysis and Monitoring. *Analytical and Bioanalytical Chemistry* **2006**, *386* (4), 1025-1041.
5. Rogers, K., Recent Advances in Biosensor Techniques for Environmental Monitoring. *Analytica Chimica Acta* **2006**, *568* (1-2), 222-231.
6. Sang, S.; Wang, Y.; Feng, Q.; Wei, Y.; Ji, J.; Zhang, W., Progress of New Label-Free Techniques for Biosensors: A Review. *Critical Reviews in Biotechnology* **2016**, *36* (3), 465-481.
7. Sarkar, D.; Liu, W.; Xie, X.; Anselmo, A. C.; Mitragotri, S.; Banerjee, K., Mos₂ Field-Effect Transistor for Next-Generation Label-Free Biosensors. *ACS Nano* **2014**, *8* (4), 3992-4003.
8. Lowe, B. M.; Sun, K.; Zeimpekis, I.; Skylaris, C.; Green, N. G., Field-Effect Sensors – from Ph Sensing to Biosensing: Sensitivity Enhancement Using Streptavidin-Biotin as a Model System. *Analyst* **2017**, *142* (22), 4173-4200.
9. Engvall, E.; Perlmann, P., Enzyme-Linked Immunosorbent Assay, Elisa: Iii. Quantitation of Specific Antibodies by Enzyme-Labeled Anti-Immunoglobulin in Antigen-Coated Tubes. *The Journal of Immunology* **1972**, *109* (1), 129-135.
10. Rennie, M. J., An Introduction to the Use of Tracers in Nutrition and Metabolism. *Proceedings of the Nutrition Society* **1999**, *58* (4), 935-944.
11. Goldstein, D. M.; Gray, N. S.; Zarrinkar, P. P., High-Throughput Kinase Profiling as a Platform for Drug Discovery. *Nature Reviews Drug Discovery* **2008**, *7* (5), 391.
12. Berliner, L. J.; Reuben, J., *Spin Labeling: Theory and Applications*. Springer Science & Business Media: 2012; Vol. 8.
13. Le, S. T.; Guros, N. B.; Bruce, R. C.; Cardone, A.; Amin, N. D.; Zhang, S.; Klauda, J. B.; Pant, H. C.; Richter, C. A.; Balijepalli, A., Quantum Capacitance-Limited Mos₂ Biosensors Enable Remote Label-Free Enzyme Measurements. *arXiv preprint arXiv:1902.10234* **2018**.
14. Tarasov, A.; Gray, D. W.; Tsai, M.-Y.; Shields, N.; Montrose, A.; Creedon, N.; Lovera, P.; O'Riordan, A.; Mooney, M. H.; Vogel, E. M., A Potentiometric Biosensor for Rapid on-Site Disease Diagnostics. *Biosensors and Bioelectronics* **2016**, *79*, 669-678.
15. White, I., Biosensing Concepts - Bioe631. **2016**.
16. Taur, Y.; Ning, T. H., *Fundamentals of Modern VLSI Devices*. Cambridge University Press: 2013.
17. Go, J.; Nair, P. R.; Alam, M. A., Theory of Signal and Noise in Double-Gated Nanoscale Electronic P H Sensors. *Journal of Applied Physics* **2012**, *112* (3), 034516.

18. Wu, T.; Alharbi, A.; You, K.-D.; Kisslinger, K.; Stach, E. A.; Shahrjerdi, D., Experimental Study of the Detection Limit in Dual-Gate Biosensors Using Ultrathin Silicon Transistors. *ACS Nano* **2017**, *11* (7), 7142-7147.
19. Kim, D.-S.; Park, J.-E.; Shin, J.-K.; Kim, P. K.; Lim, G.; Shoji, S., An Extended Gate Fet-Based Biosensor Integrated with a Si Microfluidic Channel for Detection of Protein Complexes. *Sensors and Actuators B: Chemical* **2006**, *117* (2), 488-494.
20. Huckel, E.; Debye, P., Zur Theorie Der Elektrolyte. I. Gefrierpunktserniedrigung Und Verwandte Erscheinungen. *Physics Z* **1923**, *24*, 185-206.
21. Guros, N. B.; Balijepalli, A.; Klauda, J. B., The Role of Lipid Interactions in Simulations of the A-Hemolysin Ion-Channel-Forming Toxin. *Biophysical Journal* **2018**, *115* (9), 1720-1730.
22. Bergveld, P., Development of an Ion-Sensitive Solid-State Device for Neurophysiological Measurements. *IEEE Transactions on Biomedical Engineering* **1970**, (1), 70-71.
23. van der Schoot, B. H.; Bergveld, P., Isfet Based Enzyme Sensors. *Biosensors* **1987**, *3* (3), 161-186.
24. Genck, W., *Biochemistry*. Cengage Learning: 2013.
25. Chan, Y.-H. M.; Boxer, S. G., Model Membrane Systems and Their Applications. *Current Opinion in Chemical Biology* **2007**, *11* (6), 581-587.
26. Shockley, W., A Unipolar "Field-Effect" Transistor. *Proceedings of the IRE* **1952**, *40* (11), 1365.
27. Millman, J., *Electronic Devices and Circuits*. McGraw-Hill: Singapore, 1985.
28. Kubota, Y.; Shiraki, I., Series Connected Multi-Stage Linear Fet Amplifier Circuit. Google Patents: 2001.
29. Rugg, H. W., An Integrated Fet Analog Switch. *Proceedings of the IEEE* **1964**, *52* (12), 1572-1575.
30. Eugene, M. C., Dual Mos-Fet Chopper-Summer Circuit in a Closed Loop Servo. Google Patents: 1969.
31. Brown, L. T., Series Current Limiter. Google Patents: 1985.
32. Rofougaran, A.; Rael, J.; Rofougaran, M.; Abidi, A. In *A 900 Mhz Cmos Lc-Oscillator with Quadrature Outputs*, Solid-State Circuits Conference, 1996. Digest of Technical Papers. 42nd ISSCC., 1996 IEEE International, IEEE: 1996; pp 392-393.
33. Novoselov, K. S.; Geim, A. K.; Morozov, S. V.; Jiang, D.; Zhang, Y.; Dubonos, S. V.; Grigorieva, I. V.; Firsov, A. A., Electric Field Effect in Atomically Thin Carbon Films. *Science* **2004**, *306* (5696), 666-669.
34. Zhang, Y.; Tan, Y.-W.; Stormer, H. L.; Kim, P., Experimental Observation of the Quantum Hall Effect and Berry's Phase in Graphene. *Nature* **2005**, *438* (7065), 201.
35. Novoselov, K. S.; Geim, A. K.; Morozov, S.; Jiang, D.; Katsnelson, M.; Grigorieva, I.; Dubonos, S.; Firsov, AA, Two-Dimensional Gas of Massless Dirac Fermions in Graphene. *Nature* **2005**, *438* (7065), 197.
36. Mas-Balleste, R.; Gomez-Navarro, C.; Gomez-Herrero, J.; Zamora, F., 2d Materials: To Graphene and Beyond. *Nanoscale* **2011**, *3* (1), 20-30.
37. Kim, S.; Nah, J.; Jo, I.; Shahrjerdi, D.; Colombo, L.; Yao, Z.; Tutuc, E.; Banerjee, S. K., Realization of a High Mobility Dual-Gated Graphene Field-Effect Transistor with Al₂O₃ Dielectric. *Applied Physics Letters* **2009**, *94* (6), 062107.

38. Novoselov, K.; Mishchenko, A.; Carvalho, A.; Neto, A. C., 2d Materials and Van Der Waals Heterostructures. *Science* **2016**, *353* (6298), aac9439-9431-aac9439-9411.
39. Akinwande, D.; Brennan, C. J.; Bunch, J. S.; Egberts, P.; Felts, J. R.; Gao, H.; Huang, R.; Kim, J.-S.; Li, T.; Li, Y., A Review on Mechanics and Mechanical Properties of 2d Materials—Graphene and Beyond. *Extreme Mechanics Letters* **2017**, *13*, 42-77.
40. Manzeli, S.; Ovchinnikov, D.; Pasquier, D.; Yazyev, O. V.; Kis, A., 2d Transition Metal Dichalcogenides. *Nature Reviews Materials* **2017**, *2* (8), 17033.
41. Li, H.; Wu, J.; Yin, Z.; Zhang, H., Preparation and Applications of Mechanically Exfoliated Single-Layer and Multilayer Mos₂ and Wse₂ Nanosheets. *Accounts of Chemical Research* **2014**, *47* (4), 1067-1075.
42. McDonnell, S.; Addou, R.; Hinkle, C. L.; Wallace, R. M., Physico-Chemical Characterisation of Mos₂/Metal and Mos₂/Oxide Interfaces. *2D Materials for Nanoelectronics* **2016**, *17*, 163-206.
43. Spalvins, T., Morphological and Frictional Behavior of Sputtered Mos₂ Films. *Thin Solid Films* **1982**, *96* (1), 17-24.
44. Solomon, P., Device Innovation and Material Challenges at the Limits of Cmos Technology. *Annual Review of Materials Science* **2000**, *30* (1), 681-697.
45. Gupta, A.; Sakthivel, T.; Seal, S., Recent Development in 2d Materials Beyond Graphene. *Progress in Materials Science* **2015**, *73*, 44-126.
46. Sik Hwang, W.; Remskar, M.; Yan, R.; Kosel, T.; Kyung Park, J.; Jin Cho, B.; Haensch, W.; Xing, H.; Seabaugh, A.; Jena, D., Comparative Study of Chemically Synthesized and Exfoliated Multilayer Mos₂ Field-Effect Transistors. *Applied Physics Letters* **2013**, *102* (4), 043116-043111-043116-043113.
47. McDonnell, S.; Addou, R.; Buie, C.; Wallace, R. M.; Hinkle, C. L., Defect-Dominated Doping and Contact Resistance in Mos₂. *ACS Nano* **2014**, *8* (3), 2880-2888.
48. Liu, K.-K.; Zhang, W.; Lee, Y.-H.; Lin, Y.-C.; Chang, M.-T.; Su, C.-Y.; Chang, C.-S.; Li, H.; Shi, Y.; Zhang, H., Growth of Large-Area and Highly Crystalline Mos₂ Thin Layers on Insulating Substrates. *Nano Letters* **2012**, *12* (3), 1538-1544.
49. Young, C. D.; Bolshakov, P.; Zhao, P.; Smyth, C.; Khosravi, A.; Hurley, P.; Hinkle, C. L.; Wallace, R. M. In *Investigation of Critical Interfaces in Few-Layer Mos₂ Field Effect Transistors with High-K Dielectrics*, The Electrochemical Society, 2017; pp 839-839.
50. Li, L.; Long, R.; Prezhdo, O. V., Why Cvd Grown Mos₂ Samples Outperform Pvd Samples: Time-Domain Ab Initio Analysis. *Nano Letters* **2018**, *18* (6), 4008-4014.
51. Karplus, M.; McCammon, J. A., Molecular Dynamics Simulations of Biomolecules. *Nature Structural & Molecular Biology* **2002**, *9* (9), 646-652.
52. Kalé, L.; Skeel, R.; Bhandarkar, M.; Brunner, R.; Gursoy, A.; Krawetz, N.; Phillips, J.; Shinozaki, A.; Varadarajan, K.; Schulten, K., Namd2: Greater Scalability for Parallel Molecular Dynamics. *Journal of Computational Physics* **1999**, *151* (1), 283-312.
53. Vanommeslaeghe, K. H., E. Acharya, C. Kundu, S. Zhong, S. Shim, J. E. Darian, E. Guvench, O. Lopes, P. Vorobyov, I. and MacKerell, Jr. A.D., Charmm General Force Field (Cgenff): A Force Field for Drug-Like Molecules Compatible with

the Charmm All-Atom Additive Biological Force Fields. *Journal of Computational Chemistry* **2010**, *31*, 671-690.

54. Phillips, J. C.; Braun, R.; Wang, W.; Gumbart, J.; Tajkhorshid, E.; Villa, E.; Chipot, C.; Skeel, R. D.; Kale, L.; Schulten, K., Scalable Molecular Dynamics with Namd. *Journal of Computational Chemistry* **2005**, *26* (16), 1781-1802.

55. Shaw, D. E., Anton 2: Raising the Bar for Performance and Programmability in a Special- Purpose Molecular Dynamics Supercomputer. *Proceedings of the International Conference for High Performance Computing, Networking, Storage and Analysis* **2014**, SC14.

56. Leach, A. R.; Leach, A. R., *Molecular Modelling: Principles and Applications*. Pearson education: 2001.

57. Frenkel, D.; Smit, B., *Understanding Molecular Simulation: From Algorithms to Applications*. Elsevier: 2001; Vol. 1.

58. Sébastien Le Roux, V. P. Model Box Periodic Boundary Conditions - P.B.C. <http://isaacs.sourceforge.net/phys/psc.html#fpbc>.

59. Feller, S. E.; Zhang, Y.; Pastor, R. W.; Brooks, B. R., Constant Pressure Molecular Dynamics Simulation: The Langevin Piston Method. *The Journal of Chemical Physics* **1995**, *103* (11), 4613-4621.

60. Nosé, S., A Unified Formulation of the Constant Temperature Molecular Dynamics Methods. *The Journal of Chemical Physics* **1984**, *81* (1), 511-519.

61. Aguilera, V. M., Carmina Verdiá-Báguena, and Antonio Alcaraz, Lipid Charge Regulation of Non-Specific Biological Ion Channels. *Physical Chemistry and Chemical Physics* **2014**, *16* (9), 3881-3893.

62. Tucker, S. J.; Baukowitz, T., How Highly Charged Anionic Lipids Bind and Regulate Ion Channels. *The Journal of General Physiology* **2008**, *131* (5), 431-438.

63. Valenzuela, S. M.; Alkhamici, H.; Brown, L. J.; Almond, O. C.; Goodchild, S. C.; Carne, S.; Curmi, P. M.; Holt, S. A.; Cornell, B. A., Regulation of the Membrane Insertion and Conductance Activity of the Metamorphic Chloride Intracellular Channel Protein Clic1 by Cholesterol. *PLoS One* **2013**, *8* (2), e56948.

64. Noriko Tomitaa, M. M. M., David J. Niedzwieckia, Makoto Ohtab, Liviu Movileanu, Does the Lipid Environment Impact the Open-State Conductance of an Engineered β -Barrel Protein Nanopore? *Biochimica et Biophysica Acta* **2013**, *1828* (3), 1057-1065.

65. Corradi, V.; Sejdiu, B. I.; Mesa-Galloso, H.; Abdizadeh, H.; Noskov, S. Y.; Marrink, S. J.; Tieleman, D. P., Emerging Diversity in Lipid-Protein Interactions. *Chemical Reviews* **2018**.

66. Frank, D. J., Power-Constrained Cmos Scaling Limits. *IBM Journal of Research and Development* **2002**, *46* (2.3), 235-244.

67. Nikonov, D. E.; Young, I. A., Overview of Beyond-Cmos Devices and a Uniform Methodology for Their Benchmarking. *Proceedings of the IEEE* **2013**, *101* (12), 2498-2533.

68. Hutchby, J. A.; Bourianoff, G. I.; Zhirnov, V. V.; Brewer, J. E., Extending the Road Beyond Cmos. *IEEE Circuits and Devices Magazine* **2002**, *18* (2), 28-41.

69. Bernstein, K.; Cavin, R. K.; Porod, W.; Seabaugh, A.; Welser, J., Device and Architecture Outlook for Beyond Cmos Switches. *Proceedings of the IEEE* **2010**, *98* (12), 2169-2184.

70. Liu, Y.; Weiss, N. O.; Duan, X.; Cheng, H.-C.; Huang, Y.; Duan, X., Van Der Waals Heterostructures and Devices. *Nature Reviews Materials* **2016**, *1* (9), 1-17.
71. Wang, Q. H.; Kalantar-Zadeh, K.; Kis, A.; Coleman, J. N.; Strano, M. S., Electronics and Optoelectronics of Two-Dimensional Transition Metal Dichalcogenides. *Nature Nanotechnology* **2012**, *7* (11), 699-712.
72. Jariwala, D.; Sangwan, V. K.; Late, D. J.; Johns, J. E.; Dravid, V. P.; Marks, T. J.; Lauhon, L. J.; Hersam, M. C., Band-Like Transport in High Mobility Unencapsulated Single-Layer Mos₂ Transistors. *Applied Physics Letters* **2013**, *102* (17), 173107-173107-173107-173104.
73. Radisavljevic, B.; Kis, A., Mobility Engineering and a Metal–Insulator Transition in Monolayer Mos₂. *Nature Materials* **2013**, *12* (9), 815-820.
74. Sengupta, R.; Bhattacharya, M.; Bandyopadhyay, S.; Bhowmick, A. K., A Review on the Mechanical and Electrical Properties of Graphite and Modified Graphite Reinforced Polymer Composites. *Progress in Polymer Science* **2011**, *36* (5), 638-670.
75. Suk, J. W.; Piner, R. D.; An, J.; Ruoff, R. S., Mechanical Properties of Monolayer Graphene Oxide. *ACS Nano* **2010**, *4* (11), 6557-6564.
76. Radisavljevic B, R. A., Brivio J, Giacometti V, Kis A, Single-Layer Mos₂ Transistors. *Nature Nanotechnology* **2011**, *6* (3), 147-150.
77. Yin, Z.; Zhang, X.; Cai, Y.; Chen, J.; Wong, J. I.; Tay, Y. Y.; Chai, J.; Wu, J.; Zeng, Z.; Zheng, B., Preparation of Mos₂–Moo₃ Hybrid Nanomaterials for Light-Emitting Diodes. *Angewandte Chemie International Edition* **2014**, *53* (46), 12560-12565.
78. Esmaeili-Rad, M. R.; Salahuddin, S., High Performance Molybdenum Disulfide Amorphous Silicon Heterojunction Photodetector. *Scientific Reports* **2013**, *3*, 23-45.
79. Mak, K. F.; Shan, J., Photonics and Optoelectronics of 2d Semiconductor Transition Metal Dichalcogenides. *Nature Photonics* **2016**, *10* (4), 216-226.
80. Addou, R.; McDonnell, S.; Barrera, D.; Guo, Z.; Azcatl, A.; Wang, J.; Zhu, H.; Hinkle, C. L.; Quevedo-Lopez, M.; Alshareef, H. N., Impurities and Electronic Property Variations of Natural Mos₂ Crystal Surfaces. *ACS Nano* **2015**, *9* (9), 9124-9133.
81. Pirkle, A.; Chan, J.; Venugopal, A.; Hinojos, D.; Magnuson, C.; McDonnell, S.; Colombo, L.; Vogel, E.; Ruoff, R.; Wallace, R., The Effect of Chemical Residues on the Physical and Electrical Properties of Chemical Vapor Deposited Graphene Transferred to Sio₂. *Applied Physics Letters* **2011**, *99* (12), 122108-122101-122108-122103.
82. McDonnell, S.; Brennan, B.; Azcatl, A.; Lu, N.; Dong, H.; Buie, C.; Kim, J.; Hinkle, C. L.; Kim, M. J.; Wallace, R. M., Hfo₂ on Mos₂ by Atomic Layer Deposition: Adsorption Mechanisms and Thickness Scalability. *ACS Nano* **2013**, *7* (11), 10354-10361.
83. Terrones, H.; Lv, R.; Terrones, M.; Dresselhaus, M. S., The Role of Defects and Doping in 2d Graphene Sheets and 1d Nanoribbons. *Reports on Progress in Physics* **2012**, *75* (6), 062501.
84. Fang, H.; Tosun, M.; Seol, G.; Chang, T. C.; Takei, K.; Guo, J.; Javey, A., Degenerate N-Doping of Few-Layer Transition Metal Dichalcogenides by Potassium. *Nano Letters* **2013**, *13* (5), 1991-1995.

85. Du, Y.; Liu, H.; Neal, A. T.; Si, M.; Peide, D. Y., Molecular Doping of Multilayer Mos₂ Field-Effect Transistors: Reduction in Sheet and Contact Resistances. *IEEE Electron Device Letters* **2013**, *34* (10), 1328-1330.
86. Das, S.; Chen, H.-Y.; Penumatcha, A. V.; Appenzeller, J., High Performance Multilayer Mos₂ Transistors with Scandium Contacts. *Nano Letters* **2013**, *13* (1), 100-105.
87. Neal, A. T.; Liu, H.; Gu, J.; Ye, P. In *Metal Contacts to Mos 2: A Two-Dimensional Semiconductor*, Device Research Conference (DRC), 2012 70th Annual, IEEE: 2012; pp 65-66.
88. Amani, M.; Chin, M. L.; Birdwell, A. G.; O'Regan, T. P.; Najmaei, S.; Liu, Z.; Ajayan, P. M.; Lou, J.; Dubey, M., Electrical Performance of Monolayer Mos₂ Field-Effect Transistors Prepared by Chemical Vapor Deposition. *Applied Physics Letters* **2013**, *102* (19), 19310-19311- 19310-19314.
89. Zhu, W.; Low, T.; Lee, Y.-H.; Wang, H.; Farmer, D. B.; Kong, J.; Xia, F.; Avouris, P., Electronic Transport and Device Prospects of Monolayer Molybdenum Disulphide Grown by Chemical Vapour Deposition. *Nature Communications* **2014**, *5*, 1-8.
90. Feng, Q.; Zhu, Y.; Hong, J.; Zhang, M.; Duan, W.; Mao, N.; Wu, J.; Xu, H.; Dong, F.; Lin, F., Growth of Large-Area 2d Mos₂(1-x)Se_{2x} Semiconductor Alloys. *Advanced Materials* **2014**, *26* (17), 2648-2653.
91. Van Der Zande, A. M.; Huang, P. Y.; Chenet, D. A.; Berkelbach, T. C.; You, Y.; Lee, G.-H.; Heinz, T. F.; Reichman, D. R.; Muller, D. A.; Hone, J. C., Grains and Grain Boundaries in Highly Crystalline Monolayer Molybdenum Disulphide. *Nature Materials* **2013**, *12* (6), 554-561.
92. Zhou, W.; Zou, X.; Najmaei, S.; Liu, Z.; Shi, Y.; Kong, J.; Lou, J.; Ajayan, P. M.; Yakobson, B. I.; Idrobo, J.-C., Intrinsic Structural Defects in Monolayer Molybdenum Disulfide. *Nano Letters* **2013**, *13* (6), 2615-2622.
93. Huang, Y. L.; Chen, Y.; Zhang, W.; Quek, S. Y.; Chen, C.-H.; Li, L.-J.; Hsu, W.-T.; Chang, W.-H.; Zheng, Y. J.; Chen, W., Bandgap Tunability at Single-Layer Molybdenum Disulphide Grain Boundaries. *Nature Communications* **2015**, *6*, 1-8.
94. Hong, J.; Hu, Z.; Probert, M.; Li, K.; Lv, D.; Yang, X.; Gu, L.; Mao, N.; Feng, Q.; Xie, L., Exploring Atomic Defects in Molybdenum Disulphide Monolayers. *Nature Communications* **2015**, *6*, 1-8.
95. Liu, D.; Guo, Y.; Fang, L.; Robertson, J., Sulfur Vacancies in Monolayer Mos₂ and Its Electrical Contacts. *Applied Physics Letters* **2013**, *103* (18), 183113-183111-183113-183114.
96. Desai, S. B.; Madhvapathy, S. R.; Amani, M.; Kiriya, D.; Hettick, M.; Tosun, M.; Zhou, Y.; Dubey, M.; Ager III, J. W.; Chrzan, D., Gold-Mediated Exfoliation of Ultralarge Optoelectronically-Perfect Monolayers. *Advanced Materials* **2016**, *28* (21), 4053-4058.
97. Shim, J.; Bae, S.-H.; Kong, W.; Lee, D.; Qiao, K.; Nezich, D.; Park, Y. J.; Zhao, R.; Sundaram, S.; Li, X., Controlled Crack Propagation for Atomic Precision Handling of Wafer-Scale Two-Dimensional Materials. *Science* **2018**, eaat8126.
98. Magda, G. Z.; Petó, J.; Dobrik, G.; Hwang, C.; Biró, L. P.; Tapasztó, L., Exfoliation of Large-Area Transition Metal Chalcogenide Single Layers. *Scientific Reports* **2015**, *5*, 14714.

99. Zhang, S.; Hill, H. M.; Moudgil, K.; Richter, C. A.; Hight Walker, A. R.; Barlow, S.; Marder, S. R.; Hacker, C. A.; Pookpanratana, S. J., Controllable, Wide-Ranging N-Doping and P-Doping of Monolayer Group 6 Transition-Metal Disulfides and Diselenides. *Advanced Materials* **2018**, *30* (36), 1-8.
100. Kim, S. Y.; Yang, H. I.; Choi, W., Photoluminescence Quenching in Monolayer Transition Metal Dichalcogenides by Al₂O₃ Encapsulation. *Applied Physics Letters* **2018**, *113* (13), 133104-133101-133104-133105.
101. Qiu, H.; Pan, L.; Yao, Z.; Li, J.; Shi, Y.; Wang, X., Electrical Characterization of Back-Gated Bi-Layer Mos₂ Field-Effect Transistors and the Effect of Ambient on Their Performances. *Applied Physics Letters* **2012**, *100* (12), 123104-123101-123104-123103.
102. Zhao, P.; Azcatl, A.; Bolshakov, P.; Moon, J.; Hinkle, C. L.; Hurley, P. K.; Wallace, R. M.; Young, C. D., Effects of Annealing on Top-Gated Mos₂ Transistors with HfO₂ Dielectric. *Journal of Vacuum Science & Technology B, Nanotechnology and Microelectronics: Materials, Processing, Measurement, and Phenomena* **2017**, *35* (1), 01A118-111-101A118-115.
103. Azcatl, A.; Santosh, K.; Peng, X.; Lu, N.; McDonnell, S.; Qin, X.; De Dios, F.; Addou, R.; Kim, J.; Kim, M. J., HfO₂ on Uv-O₃ Exposed Transition Metal Dichalcogenides: Interfacial Reactions Study. *2D Materials* **2015**, *2* (1), 1-9.
104. Yang, H. I.; Park, S.; Choi, W., Modification of the Optoelectronic Properties of Two-Dimensional Mos₂ Crystals by Ultraviolet-Ozone Treatment. *Applied Surface Science* **2018**, *443*, 91-96.
105. Azcatl, A.; McDonnell, S.; KC, S.; Peng, X.; Dong, H.; Qin, X.; Addou, R.; Mordi, G. I.; Lu, N.; Kim, J., Mos₂ Functionalization for Ultra-Thin Atomic Layer Deposited Dielectrics. *Applied Physics Letters* **2014**, *104* (11), 111601-111601-111601-111604.
106. Wang, F.; Stepanov, P.; Gray, M.; Lau, C. N., Annealing and Transport Studies of Suspended Molybdenum Disulfide Devices. *Nanotechnology* **2015**, *26* (10), 1-5.
107. Ma, N.; Jena, D., Carrier Statistics and Quantum Capacitance Effects on Mobility Extraction in Two-Dimensional Crystal Semiconductor Field-Effect Transistors. *2D Materials* **2015**, *2* (1), 1-8.
108. Li, H.; Zhang, Q.; Yap, C. C. R.; Tay, B. K.; Edwin, T. H. T.; Olivier, A.; Baillargeat, D., From Bulk to Monolayer Mos₂: Evolution of Raman Scattering. *Advanced Functional Materials* **2012**, *22* (7), 1385-1390.
109. Pirkle, A.; McDonnell, S.; Lee, B.; Kim, J.; Colombo, L.; Wallace, R., The Effect of Graphite Surface Condition on the Composition of Al₂O₃ by Atomic Layer Deposition. *Applied Physics Letters* **2010**, *97* (8), 082901-082901-082901-082903.
110. Van Zeghbroeck, B., *Principles of Semiconductor Devices*. Colorado University, 2004; Vol. 34.
111. Bolshakov, P.; Khosravi, A.; Zhao, P.; Hurley, P. K.; Hinkle, C. L.; Wallace, R. M.; Young, C. D., Dual-Gate Mos₂ Transistors with Sub-10 Nm Top-Gate High-K Dielectrics. *Applied Physics Letters* **2018**, *112* (25), 253502-253501-253502-253505.
112. Liu, W.; Kang, J.; Cao, W.; Sarkar, D.; Khatami, Y.; Jena, D.; Banerjee, K. In *High-Performance Few-Layer-Mos₂ Field-Effect-Transistor with Record Low Contact-Resistance*, Electron Devices Meeting (IEDM), IEEE International, 2013.

113. Abraham, M.; Mohny, S. E., Annealed Ag Contacts to Mos₂ Field-Effect Transistors. *Journal of Applied Physics* **2017**, *122* (11), 115306.
114. Yu, L.; El-Damak, D.; Ha, S.; Rakheja, S.; Ling, X.; Kong, J.; Antoniadis, D.; Chandrakasan, A.; Palacios, T. In *Mos₂ Fet Fabrication and Modeling for Large-Scale Flexible Electronics*, 2015 Symposium on VLSI Technology, IEEE: 2015.
115. Jeong, S. H.; Liu, N.; Park, H.; Hong, Y. K.; Kim, S., Temperature-Dependent Electrical Properties of Al₂O₃-Passivated Multilayer Mos₂ Thin-Film Transistors. *Applied Sciences* **2018**, *8* (3), 424-433.
116. Velický, M.; Donnelly, G. E.; Hendren, W. R.; McFarland, S.; Scullion, D.; DeBenedetti, W. J.; Correa, G. C.; Han, Y.; Wain, A. J.; Hines, M. A., Mechanism of Gold-Assisted Exfoliation of Centimeter-Sized Transition Metal Dichalcogenide Monolayers. *ACS Nano* **2018**, *12* (10), 10463-10472.
117. Shim, J.; Bae, S.-H.; Kong, W.; Lee, D.; Qiao, K.; Nezich, D.; Park, Y. J.; Zhao, R.; Sundaram, S.; Li, X., Controlled Crack Propagation for Atomic Precision Handling of Wafer-Scale Two-Dimensional Materials. *Science* **2018**, *362* (6415), 665-670.
118. Lindvall, N.; Kalabukhov, A.; Yurgens, A., Cleaning Graphene Using Atomic Force Microscope. *Journal of Applied Physics* **2012**, *111* (6), 064904-064901-064904-064904.
119. Rajan, N. K.; Brower, K.; Duan, X.; Reed, M. A., Limit of Detection of Field Effect Transistor Biosensors: Effects of Surface Modification and Size Dependence. *Applied Physics Letters* **2014**, *104* (8), 084106.
120. Bhalla, N.; Di Lorenzo, M.; Pula, G.; Estrela, P., Protein Phosphorylation Detection Using Dual-Mode Field-Effect Devices and Nanoplasmonic Sensors. *Scientific Reports* **2015**, *5*, 8687.
121. Freeman, R.; Gill, R.; Willner, I., Following a Protein Kinase Activity Using a Field-Effect Transistor Device. *Chemical Communications* **2007**, (33), 3450-3452.
122. Wang, W. U.; Chen, C.; Lin, K.-h.; Fang, Y.; Lieber, C. M., Label-Free Detection of Small-Molecule-Protein Interactions by Using Nanowire Nanosensors. *Proceedings of the National Academy of Sciences* **2005**, *102* (9), 3208-3212.
123. Johnson, K. S.; Jannasch, H. W.; Coletti, L. J.; Elrod, V. A.; Martz, T. R.; Takeshita, Y.; Carlson, R. J.; Connery, J. G., Deep-Sea Durafet: A Pressure Tolerant Ph Sensor Designed for Global Sensor Networks. *Analytical Chemistry* **2016**, *88* (6), 3249-3256.
124. Demuth, C.; Varonier, J.; Jossen, V.; Eibl, R.; Eibl, D., Novel Probes for Ph and Dissolved Oxygen Measurements in Cultivations from Millilitre to Benchtop Scale. *Applied Microbiology and Biotechnology* **2016**, *100* (9), 3853-3863.
125. Rothberg, J. M.; Hinz, W.; Rearick, T. M.; Schultz, J.; Mileski, W.; Davey, M.; Leamon, J. H.; Johnson, K.; Milgrew, M. J.; Edwards, M., An Integrated Semiconductor Device Enabling Non-Optical Genome Sequencing. *Nature* **2011**, *475* (7356), 348.
126. Tarrant, M. K.; Cole, P. A., The Chemical Biology of Protein Phosphorylation. *Annual Review of Biochemistry* **2009**, *78*, 797-825.
127. Mu, L.; Droujinine, I. A.; Rajan, N. K.; Sawtelle, S. D.; Reed, M. A., Direct, Rapid, and Label-Free Detection of Enzyme-Substrate Interactions in Physiological Buffers Using Cmos-Compatible Nanoribbon Sensors. *Nano Letters* **2014**, *14* (9), 5315-5322.

128. Dhavan, R. T., L.-H., A Decade of Cdk5. *Nature Reviews Molecular Cell Biology* **2001**, *2*, 749-759.
129. Feldmann, G.; Mishra, A.; Hong, S.-M.; Bisht, S.; Strock, C. J.; Ball, D. W.; Goggins, M.; Maitra, A.; Nelkin, B. D., Inhibiting the Cyclin-Dependent Kinase Cdk5 Blocks Pancreatic Cancer Formation and Progression through the Suppression of Ras-Ral Signaling. *Cancer Research* **2010**, *70* (11), 4460-4469.
130. Moutal, A.; Luo, S.; Largent-Milnes, T. M.; Vanderah, T. W.; Khanna, R., Cdk5-Mediated Crmp2 Phosphorylation Is Necessary and Sufficient for Peripheral Neuropathic Pain. *Neurobiology of Pain* **2019**, *5*, 100022.
131. Peterson, D. W.; Ando, D. M.; Taketa, D. A.; Zhou, H.; Dahlquist, F. W.; Lew, J., No Difference in Kinetics of Tau or Histone Phosphorylation by Cdk5/P25 Versus Cdk5/P35 in Vitro. *Proceedings of the National Academy of Sciences* **2010**, *107* (7), 2884-2889.
132. Van Slyke, D. D., On the Measurement of Buffer Values and on the Relationship of Buffer Value to the Dissociation Constant of the Buffer and the Concentration and Reaction of the Buffer Solution. *Journal of Biological Chemistry* **1922**, *52* (2), 525-570.
133. McLaughlin, K.; Dickson, A.; Weisberg, S. B.; Coale, K.; Elrod, V.; Hunter, C.; Johnson, K. S.; Kram, S.; Kudela, R.; Martz, T., An Evaluation of Isfet Sensors for Coastal Ph Monitoring Applications. *Regional Studies in Marine Science* **2017**, *12*, 11-18.
134. Dhavan, R.; Tsai, L.-H., A Decade of Cdk5. *Nature Reviews Molecular Cell Biology* **2001**, *2* (10), 749.
135. Niranjana D. Amin, W. A., and Harish C. Pant, Cyclin-Dependent Kinase 5 (Cdk5) Activation Requires Interaction with Three Domains of P35. *Journal of Neuroscience Research* **2002**, *67*, 354-362.
136. Lee, M.-s.; Kwon, Y. T.; Li, M.; Peng, J.; Friedlander, R. M.; Tsai, L.-H., Neurotoxicity Induces Cleavage of P35 to P25 by Calpain. *Nature* **2000**, *405* (6784), 360.
137. Noble, W.; Olm, V.; Takata, K.; Casey, E.; Mary, O.; Meyerson, J.; Gaynor, K.; LaFrancois, J.; Wang, L.; Kondo, T., Cdk5 Is a Key Factor in Tau Aggregation and Tangle Formation in Vivo. *Neuron* **2003**, *38* (4), 555-565.
138. Patching, S. G., Surface Plasmon Resonance Spectroscopy for Characterisation of Membrane Protein-Ligand Interactions and Its Potential for Drug Discovery. *Biochimica et Biophysica Acta (BBA)-Biomembranes* **2014**, *1838* (1), 43-55.
139. Cahen, D.; Naaman, R.; Vager, Z., The Cooperative Molecular Field Effect. *Advanced Functional Materials* **2005**, *15* (10), 1571-1578.
140. Williams, E. H.; Davydov, A. V.; Motayed, A.; Sundaresan, S. G.; Bocchini, P.; Richter, L. J.; Stan, G.; Steffens, K.; Zangmeister, R.; Schreifels, J. A., Immobilization of Streptavidin on 4h-Sic for Biosensor Development. *Applied Surface Science* **2012**, *258* (16), 6056-6063.
141. Duan, X.; Rajan, N. K.; Izadi, M. H.; Reed, M. A., Complementary Metal Oxide Semiconductor-Compatible Silicon Nanowire Biofield-Effect Transistors as Affinity Biosensors. *Nanomedicine* **2013**, *8* (11), 1839-1851.
142. Elfström, N.; Karlström, A. E.; Linnros, J., Silicon Nanoribbons for Electrical Detection of Biomolecules. *Nano Letters* **2008**, *8* (3), 945-949.

143. Cui, Y.; Wei, Q.; Park, H.; Lieber, C. M., Nanowire Nanosensors for Highly Sensitive and Selective Detection of Biological and Chemical Species. *Science* **2001**, 293 (5533), 1289-1292.
144. Weber, P. C.; Ohlendorf, D.; Wendoloski, J.; Salemme, F., Structural Origins of High-Affinity Biotin Binding to Streptavidin. *Science* **1989**, 243 (4887), 85-88.
145. Duan, X.; Li, Y.; Rajan, N. K.; Routenberg, D. A.; Modis, Y.; Reed, M. A., Quantification of the Affinities and Kinetics of Protein Interactions Using Silicon Nanowire Biosensors. *Nature Nanotechnology* **2012**, 7 (6), 401.
146. Sperling, R. A.; Parak, W. J., Surface Modification, Functionalization and Bioconjugation of Colloidal Inorganic Nanoparticles. *Philosophical Transactions of the Royal Society A: Mathematical, Physical and Engineering Sciences* **2010**, 368 (1915), 1333-1383.
147. Gupta, S.; Elias, M.; Wen, X.; Shapiro, J.; Brillson, L.; Lu, W.; Lee, S. C., Detection of Clinically Relevant Levels of Protein Analyte under Physiologic Buffer Using Planar Field Effect Transistors. *Biosensors and Bioelectronics* **2008**, 24 (4), 505-511.
148. Buck, R.; Rondinini, S.; Covington, A.; Baucke, F.; Brett, C. M.; Camoes, M.; Milton, M.; Mussini, T.; Naumann, R.; Pratt, K., Measurement of Ph. Definition, Standards, and Procedures (Iupac Recommendations 2002). *Pure and Applied Chemistry* **2002**, 74 (11), 2169-2200.
149. Loucaides, S.; R  rolle, V. M.; Papadimitriou, S.; Kennedy, H.; Mowlem, M. C.; Dickson, A. G.; Gledhill, M.; Achterberg, E. P., Characterization of Meta-Cresol Purple for Spectrophotometric Ph Measurements in Saline and Hypersaline Media at Sub-Zero Temperatures. *Scientific Reports* **2017**, 7 (1), 2481.
150. Gotor, R. I.; Ashokkumar, P.; Hecht, M.; Keil, K.; Rurack, K., Optical Ph Sensor Covering the Range from Ph 0–14 Compatible with Mobile-Device Readout and Based on a Set of Rationally Designed Indicator Dyes. *Analytical Chemistry* **2017**, 89 (16), 8437-8444.
151. Wu, T. A., A.; You, K.-D.; Kisslinger, K.; Stach, E. A.; Shahrjerdi D., Experimental Study of the Detection Limit in Dual-Gate Biosensors Using Ultrathin Silicon Transistors. *ACS Nano* **2017**, 11, 7142-7147.
152. Zafar, S.; D'Emic, C.; Afzali, A.; Fletcher, B.; Zhu, Y.; Ning, T., Optimization of Ph Sensing Using Silicon Nanowire Field Effect Transistors with Hfo2 as the Sensing Surface. *Nanotechnology* **2011**, 22 (40), 405501.
153. Tarasov, A.; Campbell, P. M.; Tsai, M. Y.; Hesabi, Z. R.; Feirer, J.; Graham, S.; Ready, W. J.; Vogel, E. M., Highly Uniform Trilayer Molybdenum Disulfide for Wafer-Scale Device Fabrication. *Advanced Functional Materials* **2014**, 24 (40), 6389-6400.
154. Accastelli, E.; Scarbolo, P.; Ernst, T.; Palestri, P.; Selmi, L.; Guiducci, C., Multi-Wire Tri-Gate Silicon Nanowires Reaching Milli-Ph Unit Resolution in One Micron Square Footprint. *Biosensors* **2016**, 6 (1), 9.
155. Bhalla, N.; Di Lorenzo, M.; Pula, G.; Estrela, P., Protein Phosphorylation Analysis Based on Proton Release Detection: Potential Tools for Drug Discovery. *Biosensors and Bioelectronics* **2014**, 54, 109-114.

156. Hahm, J.-i.; Lieber, C. M., Direct Ultrasensitive Electrical Detection of DNA and DNA Sequence Variations Using Nanowire Nanosensors. *Nano Letters* **2004**, *4* (1), 51-54.
157. Knopfmacher, O.; Tarasov, A.; Fu, W.; Wipf, M.; Niesen, B.; Calame, M.; Schonberger, C., Nernst Limit in Dual-Gated Si-Nanowire Fet Sensors. *Nano Letters* **2010**, *10* (6), 2268-2274.
158. Terrones, H.; Lv, R.; Terrones, M.; Dresselhaus, M. S., The Role of Defects and Doping in 2d Graphene Sheets and 1d Nanoribbons. *Reports on Progress in Physics* **2012**, *75* (6), 1-30.
159. Im, H.; Huang, X.-J.; Gu, B.; Choi, Y.-K., A Dielectric-Modulated Field-Effect Transistor for Biosensing. *Nature Nanotechnology* **2007**, *2* (7), 430.
160. Im, M.; Ahn, J.-H.; Han, J.-W.; Park, T. J.; Lee, S. Y.; Choi, Y.-K., Development of a Point-of-Care Testing Platform with a Nanogap-Embedded Separated Double-Gate Field Effect Transistor Array and Its Readout System for Detection of Avian Influenza. *IEEE Sensors Journal* **2010**, *11* (2), 351-360.
161. Iverson, G. K.; Salmons, J. C., Filling the Gap. *Journal of English Linguistics* **2005**, *33* (3), 207-221.
162. Perera, M. M.; Lin, M.-W.; Chuang, H.-J.; Chamlagain, B. P.; Wang, C.; Tan, X.; Cheng, M. M.-C.; Tománek, D.; Zhou, Z., Improved Carrier Mobility in Few-Layer Mos₂ Field-Effect Transistors with Ionic-Liquid Gating. *ACS Nano* **2013**, *7* (5), 4449-4458.
163. Zhang, Y.; Oka, T.; Suzuki, R.; Ye, J.; Iwasa, Y., Electrically Switchable Chiral Light-Emitting Transistor. *Science* **2014**, *344* (6185), 725-728.
164. Chu, L.; Schmidt, H.; Pu, J.; Wang, S.; Özyilmaz, B.; Takenobu, T.; Eda, G., Charge Transport in Ion-Gated Mono-, Bi-, and Trilayer Mos₂ Field Effect Transistors. *Scientific Reports* **2014**, *4*, 7293.
165. Niranjana D. Amin, Y. Z., Binukumar BK, Varsha Shukla, Susan Skuntz, Philip Grant, Joseph Steiner, Manju Bhaskar, and Harish C. Pant, The Interaction of Munc 18 (P67) with the P10 Domain of P35 Protects in Vivo Cdk5/P35 Activity from Inhibition by Tfp5, a Peptide Derived from P35. *Molecular Biology of the Cell* **2016**, *27*, 3221-3232.
166. Ortiz-Conde, A.; Sánchez, F. G.; Liou, J. J.; Cerdeira, A.; Estrada, M.; Yue, Y., A Review of Recent Mosfet Threshold Voltage Extraction Methods. *Microelectronics Reliability* **2002**, *42* (4-5), 583-596.
167. Yoon, Y.; Ganapathi, K.; Salahuddin, S., How Good Can Monolayer Mos₂ Transistors Be? *Nano Letters* **2011**, *11* (9), 3768-3773.
168. Wang, Y.; Ma, H., Protein Kinase Profiling Assays: A Technology Review. *Drug Discovery Today: Technologies* **2015**, *18*, 1-8.
169. Binukumar, B. K., Zheng, Y.-L., Shukla, V., Amin, N. D., Grant, P. & Pant, H. C., Tfp5, a Peptide Derived from P35, a Cdk5 Neuronal Activator, Rescues Cortical Neurons from Glucose Toxicity. *Journal of Alzheimer's Disease* **2014**, *39*, 899-898.
170. Chiriac, V.; Balea, G., Buffer Index and Buffer Capacity for a Simple Buffer Solution. *Journal of Chemical Education* **1997**, *74* (8), 937.
171. Liu, M.; Choi, S.; Cuny, G. D.; Ding, K.; Dobson, B. C.; Glicksman, M. A.; Auerbach, K.; Stein, R. L., Kinetic Studies of Cdk5/P25 Kinase: Phosphorylation of

- Tau and Complex Inhibition by Two Prototype Inhibitors. *Biochemistry* **2008**, *47* (32), 8367-8377.
172. Hashiguchi, M.; Saito, T.; Hisanaga, S.-i.; Hashiguchi, T., Truncation of Cdk5 Activator P35 Induces Intensive Phosphorylation of Ser202/Thr205 of Human Tau. *Journal of Biological Chemistry* **2002**, *277* (46), 44525-44530.
173. Dubois, B.; Feldman, H. H.; Jacova, C.; Hampel, H.; Molinuevo, J. L.; Blennow, K.; DeKosky, S. T.; Gauthier, S.; Selkoe, D.; Bateman, R., Advancing Research Diagnostic Criteria for Alzheimer's Disease: The Iwg-2 Criteria. *The Lancet Neurology* **2014**, *13* (6), 614-629.
174. Frisoni, G. B.; Boccardi, M.; Barkhof, F.; Blennow, K.; Cappa, S.; Chiotis, K.; Démonet, J.-F.; Garibotto, V.; Giannakopoulos, P.; Gietl, A., Strategic Roadmap for an Early Diagnosis of Alzheimer's Disease Based on Biomarkers. *The Lancet Neurology* **2017**, *16* (8), 661-676.
175. Briggs, C. A.; Chakroborty, S.; Stutzmann, G. E., Emerging Pathways Driving Early Synaptic Pathology in Alzheimer's Disease. *Biochemical and Biophysical Research Communications* **2017**, *483* (4), 988-997.
176. Hediger, M. A.; Romero, M. F.; Peng, J.-B.; Rolfs, A.; Takanaga, H.; Bruford, E. A., The Abscs of Solute Carriers: Physiological, Pathological and Therapeutic Implications of Human Membrane Transport Proteins. *Pflügers Archiv* **2004**, *447* (5), 465-468.
177. Alberts, B., *Molecular Biology of the Cell*. Garland science: 2017.
178. Sadava, D. E.; Hillis, D. M.; Heller, H. C.; Berenbaum, M., *Life: The Science of Biology*. Macmillan: 2009; Vol. 2.
179. Gamper, N.; Shapiro, M. S., Regulation of Ion Transport Proteins by Membrane Phosphoinositides. *Nature Reviews Neuroscience* **2007**, *8* (12), 921-934.
180. Deol, S. S.; Bond, P. J.; Domene, C.; Sansom, M. S., Lipid-Protein Interactions of Integral Membrane Proteins: A Comparative Simulation Study. *Biophysical Journal* **2004**, *87* (6), 3737-3749.
181. Rojko, N.; Anderluh, G., How Lipid Membranes Affect Pore Forming Toxin Activity. *Accounts of Chemical Research* **2015**, *48* (12), 3073-3079.
182. Praper, T.; Sonnen, A.; Viero, G.; Kladnik, A.; Froelich, C. J.; Anderluh, G.; Dalla Serra, M.; Gilbert, R. J., Human Perforin Employs Different Avenues to Damage Membranes. *Journal of Biological Chemistry* **2011**, *286* (4), 2946-2955.
183. Gurnev, P. A.; Nestorovich, E. M., Channel-Forming Bacterial Toxins in Biosensing and Macromolecule Delivery. *Toxins* **2014**, *6* (8), 2483-2540.
184. Benz, R.; Schmid, A.; Wiedmer, T.; Sims, P. J., Single-Channel Analysis of the Conductance Fluctuations Induced in Lipid Bilayer Membranes by Complement Proteins C5b-9. *Journal of Membrane Biology* **1986**, *94* (1), 37-45.
185. Tomita, N., Mohammad, M. M., Niedzwiecki, D. J., Ohta, M., & Movileanu, L, Does the Lipid Environment Impact the Open-State Conductance of an Engineered B-Barrel Protein Nanopore. *Biochimica et Biophysica Acta (BBA)-Biomembranes* **2013**, *1828* (3), 1057-1065.
186. Krasilnikov, O.; Sabirov, R., Ion Transport through Channels Formed in Lipid Bilayers by Staphylococcus Aureus Alpha-Toxin. *General Physiological Biophysics* **1989**, *8*, 213-222.

187. Kasianowicz, J. J.; Brandin, E.; Branton, D.; Deamer, D. W., Characterization of Individual Polynucleotide Molecules Using a Membrane Channel. *Proceedings of the National Academy of Sciences* **1996**, *93* (24), 13770-13773.
188. Menestrina, G.; Dalla Serra, M.; Pederzoli, C.; Bregante, M.; Gambale, F., Bacterial Hemolysins and Leukotoxins Affect Target Cells by Forming Large Exogenous Pores into Their Plasma Membrane. Escherichia Coli Hemolysin a as a Case Example. *Bioscience Reports* **1995**, *15* (6), 543-551.
189. Gu, L.-Q.; Bayley, H., Interaction of the Noncovalent Molecular Adapter, B-Cyclodextrin, with the Staphylococcal A-Hemolysin Pore. *Biophysical Journal* **2000**, *79* (4), 1967-1975.
190. Stoddart, D.; Heron, A. J.; Mikhailova, E.; Maglia, G.; Bayley, H., Single-Nucleotide Discrimination in Immobilized DNA Oligonucleotides with a Biological Nanopore. *Proceedings of the National Academy of Sciences* **2009**, *106* (19), 7702-7707.
191. Shendure, J.; Mitra, R. D.; Varma, C.; Church, G. M., Advanced Sequencing Technologies: Methods and Goals. *Nature Reviews Genetics* **2004**, *5* (5), 335-344.
192. Mikheyev, A. S.; Tin, M. M., A First Look at the Oxford Nanopore Minion Sequencer. *Molecular Ecology Resources* **2014**, *14* (6), 1097-1102.
193. De Biase, P. M.; Ervin, E. N.; Pal, P.; Samoylova, O.; Markosyan, S.; Keehan, M. G.; Barrall, G. A.; Noskov, S. Y., What Controls Open-Pore and Residual Currents in the First Sensing Zone of Alpha-Hemolysin Nanopore? Combined Experimental and Theoretical Study. *Nanoscale* **2016**, *9* (11571).
194. Aksimentiev, A.; Schulten, K., Imaging A-Hemolysin with Molecular Dynamics: Ionic Conductance, Osmotic Permeability, and the Electrostatic Potential Map. *Biophysical Journal* **2005**, *88* (6), 3745-3761.
195. Allen, T. W.; Andersen, O. S.; Roux, B., Molecular Dynamics—Potential of Mean Force Calculations as a Tool for Understanding Ion Permeation and Selectivity in Narrow Channels. *Biophysical chemistry* **2006**, *124* (3), 251-267.
196. Balijepalli, A.; Robertson, J. W. F.; Reiner, J. E.; Kasianowicz, J. J.; Pastor, R. W., Theory of Polymer–Nanopore Interactions Refined Using Molecular Dynamics Simulations. *Journal of the American Chemical Society* **2013**, *135* (18), 7064–7072.
197. Khalili-Araghi, F.; Gumbart, J.; Wen, P. C.; Sotomayor, M.; Tajkhorshid, E.; Schulten, K., Molecular Dynamics Simulations of Membrane Channels and Transporters. *Current Opinions of Structural Biology* **2009**, *19*, 128-137.
198. Kumar, S.; Tao, C.; Chien, M.; Hellner, B.; Balijepalli, A.; Robertson, J. W.; Li, Z.; Russo, J. J.; Reiner, J. E.; Kasianowicz, J. J., Peg-Labeled Nucleotides and Nanopore Detection for Single Molecule DNA Sequencing by Synthesis. *Scientific Reports* **2012**, *2*.
199. Desikan, R.; Patra, S. M.; Sarthak, K.; Maiti, P. K.; Ayappa, K., Comparison of Coarse-Grained (Martini) and Atomistic Molecular Dynamics Simulations of A and B Toxin Nanopores in Lipid Membranes. *Journal of Chemical Sciences* **2017**, *129* (7), 1017-1030.
200. McGillivray, D. J.; Valincius, G.; Heinrich, F.; Robertson, J. W.; Vanderah, D. J.; Febo-Ayala, W.; Ignatjev, I.; Lösche, M.; Kasianowicz, J. J., Structure of Functional Staphylococcus Aureus A-Hemolysin Channels in Tethered Bilayer Lipid Membranes. *Biophysical Journal* **2009**, *96* (4), 1547-1553.

201. Robertson, J. W.; Rodrigues, C. G.; Stanford, V. M.; Rubinson, K. A.; Krasilnikov, O. V.; Kasianowicz, J. J., Single-Molecule Mass Spectrometry in Solution Using a Solitary Nanopore. *Proceedings of the National Academy of Sciences* **2007**, *104* (20), 8207-8211.
202. Baaken, G.; Ankri, N.; Schuler, A.-K.; Rühle, J. r.; Behrends, J. C., Nanopore-Based Single-Molecule Mass Spectrometry on a Lipid Membrane Microarray. *ACS Nano* **2011**, *5* (10), 8080-8088.
203. Klauda, J. B., Venable, R.M., Freites, J.A., O'Connor, J.W., Tobias, D.J., Mondragon-Ramirez, C., Vorobyov, I., MacKerell, Jr., A.D., and Pastor, R.W., Update of the Charmm All-Atom Additive Force Field for Lipids: Validation on Six Lipid Types. *Journal of Physical Chemistry B* **2010**, *114*, 7830-7843.
204. S. Jo, T. K., V. G. Iyer, W. Im, Charmm-Gui: A Web-Based Graphical User Interface for Charmm. *Journal of Computational Chemistry* **2008**, *29* (11), 1859-1865.
205. L., S.; M.R., H.; C., S.; S., C.; H., B.; J.E., G., Structure of Staphylococcal Alpha-Hemolysin, a Heptameric Transmembrane Pore. *science* **1996**, *274* (5294).
206. Böckmann, R. A.; Hac, A.; Heimburg, T. G., H., Effect of Sodium Chloride on a Lipid Bilayer. *Biophysical Journal* **2003**, *85* (3), 1647-1655.
207. Durell, S. R.; Brooks, B. R.; Bennaim, A., Solvent-Induced Forces between Two Hydrophilic Groups. *Journal of Physical Chemistry* **1994**, *98*, 2198-2202.
208. Jorgensen, W. L.; Chandrasekhar, J.; Madura, J. D.; Impey, R. W.; Klein, M. L., Comparison of Simple Potential Functions for Simulating Liquid Water *Journal of Chemical Physics* **1983**, *79*, 926-935.
209. Klauda, J. B.; Venable, R. M.; Freites, J. A.; O'Connor, J. W.; Mondragon-Ramirez, C.; Vorobyov, I.; Tobias, D. J.; MacKerell, A. D.; Pastor, R. W., Update of the Charmm All-Atom Additive Force Field for Lipids: Validation on Six Lipid Types. *Journal of Physical Chemistry B* **2010**, *114*, 7830-7843.
210. Klauda, J. B.; Monje, V.; Kim, T.; Im, W., Improving the Charmm Force Field for Polyunsaturated Fatty Acid Chains. *Journal of Chemical Physics B* **2012**, *116*, 9424-9431.
211. Steinbach, P. J.; Brooks, B. R., New Spherical-Cutoff Methods for Long-Range Forces in Macromolecular Simulation. *Journal of Computational Chemistry* **1994**, *15*, 667-683.
212. J.P. Ryckaert, G. C., H.J.C. Berendsen, Numerical-Integration of Cartesian Equations of Motion of a System with Constraints -Molecular-Dynamics of N-Alkanes. *Journal of Computational Physics* **1977**, *23*, 327-341.
213. T. Darden, D. Y., L. Pedersen, Particle Mesh Ewald: An N·Log(N) Method for Ewald Sums in Large Systems. *Journal of Chemical Physics* **1993**, *98*, 10089-10092.
214. Martyna, G. J.; Tobias, D. J.; Klein, M. L., Constant Pressure Molecular Dynamics Algorithms. *The Journal of Chemical Physics* **1994**, *101* (5), 4177-4189.
215. Zhuang, X.; Makover, J. R.; Im, W.; Klauda, J. B., A Systematic Molecular Dynamics Simulation Study of Temperature Dependent Bilayer Structural Properties. *Biochimica et Biophysica Acta* **2014**, *1838*, 2520-2529.
216. Kucerka, N.; Nieh, M. P.; Katsaras, J., Fluid Phase Lipid Areas and Bilayer Thicknesses of Commonly Used Phosphatidylcholines as a Function of Temperature. *Biochimica Biophysica Acta Biomembrane* **2011**, *1808* (11), 2761-2771.

217. Smart, O. S.; Goodfellow, J. M.; Wallace, B. A., The Pore Dimensions of Gramicidin A. *Biophysical Journal* **1993**, *65*, 2455-2460.
218. Yoo, J.; Aksimentiev, A., Molecular Dynamics of Membrane-Spanning DNA Channels: Conductance Mechanism, Electro-Osmotic Transport, and Mechanical Gating. *The Journal of Physical Chemistry Letters* **2015**, *6* (23), 4680-4687.
219. Göpflich, K.; Li, C.-Y.; Ricci, M.; Bhamidimarri, S. P.; Yoo, J.; Gyenes, B.; Ohmann, A.; Winterhalter, M.; Aksimentiev, A.; Keyser, U. F., Large-Conductance Transmembrane Porin Made from DNA Origami. *ACS Nano* **2016**, *10* (9), 8207-8214.
220. Hoiles, W.; Krishnamurthy, V., Dynamic Modeling of Antimicrobial Pore Formation in Engineered Tethered Membranes. *IEEE Transactions on Molecular, Biological and Multi-Scale Communications* **2015**, *1* (3), 265-276.
221. van Uitert, I.; Le Gac, S.; van den Berg, A., The Influence of Different Membrane Components on the Electrical Stability of Bilayer Lipid Membranes. *Biochimica et Biophysica Acta Biomembranes* **2010**, *1798* (1), 21-31.
222. Lee, A. G., Lipid-Protein Interactions in Biological Membranes: A Structural Perspective. *Biochimica Biophysica Acta* **2003**, *1612*, 1-40.
223. Killian, J. A., Hydrophobic Mismatch between Proteins and Lipids in Membranes. *Biochimica et Biophysica Acta Biomembranes* **1998**, *1376* (3), 401-416.
224. Mondal, S.; George, K.; Lei, S.; Harel, W., The Cost of Living in the Membrane: A Case Study of Hydrophobic Mismatch for the Multi-Segment Protein Leut. *Chemistry and Physics of Lipids* **2013**, *169*, 27-38.
225. Ramadurai, S., Ria Duurkens, Victor V. Krasnikov, and Bert Poolman, Lateral Diffusion of Membrane Proteins: Consequences of Hydrophobic Mismatch and Lipid Composition. *Biophysical Journal* **2010**, *99* (5), 1482-1489.
226. Lomize, M. A.; Pogozheva, I. D.; Joo, H.; Mosberg, H. I.; Lomize, A. L., Opm Database and Ppm Web Server: Resources for Positioning of Proteins in Membranes. *Nucleic Acids Research* **2012**, *40* (D1), D370-D376.
227. Noskov, S. Y.; Im, W.; Roux, B., Ion Permeation through the A-Hemolysin Channel: Theoretical Studies Based on Brownian Dynamics and Poisson-Nernst-Planck Electrodiffusion Theory. *Biophysical Journal* **2004**, *87* (4), 2299-2309.
228. Stoddart, D.; Ayub, M.; Höfler, L.; Raychaudhuri, P.; Klingelhoefer, J. W.; Maglia, G.; Heron, A.; Bayley, H., Functional Truncated Membrane Pores. *Proceedings of the National Academy of Sciences* **2014**, *111* (7), 2425-2430.
229. Bond, P. J.; Guy, A. T.; Heron, A. J.; Bayley, H.; Khalid, S., Molecular Dynamics Simulations of DNA within a Nanopore: Arginine– Phosphate Tethering and a Binding/Sliding Mechanism for Translocation. *Biochemistry* **2011**, *50* (18), 3777-3783.
230. Guy, A. T., Thomas J. Piggot, and Syma Khalid, Single-Stranded DNA within Nanopores: Conformational Dynamics and Implications for Sequencing; a Molecular Dynamics Simulation Study. *Biophysical Journal* **2012**, *103* (5), 1028-1036.
231. Yakel, J., The 5-Ht₃ Receptor Channel: Function, Activation and Regulation. In *Pharmacology of Ionic Channel Function: Activators and Inhibitors*, Springer: 2000; pp 541-560.
232. Thompson, A. J.; R Lummis, S., 5-Ht₃ Receptors. *Current Pharmaceutical Design* **2006**, *12* (28), 3615-3630.

233. Yakel, J. L.; Jackson, M. B., 5-Ht3 Receptors Mediate Rapid Responses in Cultured Hippocampus and a Clonal Cell Line. *Neuron* **1988**, *1* (7), 615-621.
234. Gross, C.; Hen, R., Genetic and Environmental Factors Interact to Influence Anxiety. *Neurotoxicity Research* **2004**, *6* (6), 493-501.
235. Anguelova, M.; Benkelfat, C.; Turecki, G., A Systematic Review of Association Studies Investigating Genes Coding for Serotonin Receptors and the Serotonin Transporter: Ii. Suicidal Behavior. *Molecular Psychiatry* **2003**, *8* (7), 646.
236. Thompson, A. J.; Lummis, S. C., The 5-Ht3 Receptor as a Therapeutic Target. *Expert Opinion on Therapeutic Targets* **2007**, *11* (4), 527-540.
237. Walstab, J.; Rappold, G.; Niesler, B., 5-Ht 3 Receptors: Role in Disease and Target of Drugs. *Pharmacology & Therapeutics* **2010**, *128* (1), 146-169.
238. Gielen, M.; Corringer, P. J., The Dual-Gate Model for Pentameric Ligand-Gated Ion Channels Activation and Desensitization. *The Journal of Physiology* **2018**, *596* (10), 1873-1902.
239. Corradi, J.; Gumilar, F.; Bouzat, C., Single-Channel Kinetic Analysis for Activation and Desensitization of Homomeric 5-Ht3a Receptors. *Biophysical Journal* **2009**, *97* (5), 1335-1345.
240. Nemezc, A.; Prevost, M. S.; Menny, A.; Corringer, P.-J., Emerging Molecular Mechanisms of Signal Transduction in Pentameric Ligand-Gated Ion Channels. *Neuron* **2016**, *90* (3), 452-470.
241. Nury, H.; Poitevin, F.; Van Renterghem, C.; Changeux, J.-P.; Corringer, P.-J.; Delarue, M.; Baaden, M., One-Microsecond Molecular Dynamics Simulation of Channel Gating in a Nicotinic Receptor Homologue. *Proceedings of the National Academy of Sciences* **2010**.
242. Calimet, N.; Simoes, M.; Changeux, J.-P.; Karplus, M.; Taly, A.; Cecchini, M., A Gating Mechanism of Pentameric Ligand-Gated Ion Channels. *Proceedings of the National Academy of Sciences* **2013**, 201313785.
243. Chiodo, L.; Malliavin, T.; Maragliano, L.; Cottone, G., A Possible Desensitized State Conformation of the Human A7 Nicotinic Receptor: A Molecular Dynamics Study. *Biophysical Chemistry* **2017**, *229*, 99-109.
244. Martin, N. E.; Malik, S.; Calimet, N.; Changeux, J.-P.; Cecchini, M., Un-Gating and Allosteric Modulation of a Pentameric Ligand-Gated Ion Channel Captured by Molecular Dynamics. *PLoS Computational Biology* **2017**, *13* (10), e1005784.
245. Cerdan, A. H.; Martin, N. É.; Cecchini, M., An Ion-Permeable State of the Glycine Receptor Captured by Molecular Dynamics. *Structure* **2018**, *26* (11), 1555-1562. e1554.
246. Hassaine, G.; Deluz, C.; Grasso, L.; Wyss, R.; Tol, M. B.; Hovius, R.; Graff, A.; Stahlberg, H.; Tomizaki, T.; Desmyter, A., X-Ray Structure of the Mouse Serotonin 5-Ht3 Receptor. *Nature* **2014**, *512* (7514), 276-281.
247. Basak, S.; Gicheru, Y.; Samanta, A.; Molugu, S. K.; Huang, W.; la de Fuente, M.; Hughes, T.; Taylor, D. J.; Nieman, M. T.; Moiseenkova-Bell, V., Cryo-Em Structure of 5-Ht_{3a} Receptor in Its Resting Conformation. *Nature Communications* **2018**, *9* (1), 514.
248. Basak, S.; Gicheru, Y.; Rao, S.; Sansom, M. S.; Chakrapani, S., Cryo-Em Reveals Two Distinct Serotonin-Bound Conformations of Full-Length 5-Ht 3a Receptor. *Nature* **2018**, 1.

249. Yuan, S.; Filipek, S.; Vogel, H., A Gating Mechanism of the Serotonin 5-Ht 3 Receptor. *Structure* **2016**, *24* (5), 816-825.
250. Polovinkin, L.; Hassaine, G.; Perot, J.; Neumann, E.; Jensen, A. A.; Lefebvre, S. N.; Corringer, P.-J.; Neyton, J.; Chipot, C.; Dehez, F., Conformational Transitions of the Serotonin 5-Ht 3 Receptor. *Nature* **2018**, 1.
251. Best, R. B.; Zhu, X.; Shim, J.; Lopes, P. E.; Mittal, J.; Feig, M.; MacKerell Jr, A. D., Optimization of the Additive Charmm All-Atom Protein Force Field Targeting Improved Sampling of the Backbone ϕ , Ψ and Side-Chain X1 and X2 Dihedral Angles. *Journal of chemical theory and computation* **2012**, *8* (9), 3257-3273.
252. Shan, J.; Khelashvili, G.; Mondal, S.; Mehler, E. L.; Weinstein, H., Ligand-Dependent Conformations and Dynamics of the Serotonin 5-Ht_{2a} Receptor Determine Its Activation and Membrane-Driven Oligomerization Properties. *PLoS Computational Biology* **2012**, *8* (4), e1002473.
253. Fantini, J.; Barrantes, F. J., Sphingolipid/Cholesterol Regulation of Neurotransmitter Receptor Conformation and Function. *Biochimica et Biophysica Acta Biomembranes* **2009**, *1788* (11), 2345-2361.
254. Cecchini, M.; Changeux, J.-P., The Nicotinic Acetylcholine Receptor and Its Prokaryotic Homologues: Structure, Conformational Transitions & Allosteric Modulation. *Neuropharmacology* **2015**, *96*, 137-149.
255. Brannigan, G.; Hénin, J.; Law, R.; Eckenhoff, R.; Klein, M. L., Embedded Cholesterol in the Nicotinic Acetylcholine Receptor. *Proceedings of the National Academy of Sciences* **2008**, *105* (38), 14418-14423.
256. Barrantes, F. J., Cholesterol Effects on Nicotinic Acetylcholine Receptor. *Journal of Neurochemistry* **2007**, *103*, 72-80.
257. Baenziger, J. E.; Domville, J. A.; Therien, J. D., The Role of Cholesterol in the Activation of Nicotinic Acetylcholine Receptors. In *Current Topics in Membranes*, Elsevier: 2017; Vol. 80, pp 95-137.
258. Basak, S.; Gicheru, Y.; Rao, S.; Sansom, M. S.; Chakrapani, S., Cryo-Em Reveals Two Distinct Serotonin-Bound Conformations of Full-Length 5-Ht 3a Receptor. *Nature* **2018**, *563* (7730), 270.
259. B. Webb, A. S., Comparative Protein Structure Modeling Using Modeller. *Current Protocols in Bioinformatics* **2014**, 5.6.1-5.6.32.
260. Shaw, D. E.; Grossman, J.; Bank, J. A.; Batson, B.; Butts, J. A.; Chao, J. C.; Deneroff, M. M.; Dror, R. O.; Even, A.; Fenton, C. H. In *Anton 2: Raising the Bar for Performance and Programmability in a Special-Purpose Molecular Dynamics Supercomputer*, Proceedings of the international conference for high performance computing, networking, storage and analysis, IEEE Press: 2014; pp 41-53.
261. Trott, O.; Olson, A. J., Autodock Vina: Improving the Speed and Accuracy of Docking with a New Scoring Function, Efficient Optimization, and Multithreading. *Journal of Computational Chemistry* **2010**, *31* (2), 455-461.
262. Vanommeslaeghe, K.; Hatcher, E.; Acharya, C.; Kundu, S.; Zhong, S.; Shim, J.; Darian, E.; Guvench, O.; Lopes, P.; Vorobyov, I., Charmm General Force Field: A Force Field for Drug-Like Molecules Compatible with the Charmm All-Atom Additive Biological Force Fields. *Journal of Computational Chemistry* **2010**, *31* (4), 671-690.
263. Derkach, V.; Surprenant, A.; North, R., 5-Ht3 Receptors Are Membrane Ion Channels. *Nature* **1989**, *339* (6227), 706.

264. Lambert, J. J.; Peters, J. A.; Hales, T. G.; Dempster, J., The Properties of 5-Ht3 Receptors in Clonal Cell Lines Studied by Patch-Clamp Techniques. *British Journal of Pharmacology* **1989**, *97* (1), 27-40.
265. Lippert, R. A.; Predescu, C.; Ierardi, D. J.; Mackenzie, K. M.; Eastwood, M. P.; Dror, R. O.; Shaw, D. E., Accurate and Efficient Integration for Molecular Dynamics Simulations at Constant Temperature and Pressure. *The Journal of Chemical Physics* **2013**, *139* (16), 10B621_621.
266. Hoover, W. G., Canonical Dynamics: Equilibrium Phase-Space Distributions. *Physical Review A* **1985**, *31* (3), 1695.
267. Humphrey, W.; Dalke, A.; Schulten, K., Vmd: Visual Molecular Dynamics. *Journal of Molecular Graphics* **1996**, *14* (1), 33-38.
268. Alwarawrah, M.; Dai, J.; Huang, J., A Molecular View of the Cholesterol Condensing Effect in Dopc Lipid Bilayers. *The Journal of Physical Chemistry B* **2010**, *114* (22), 7516-7523.
269. Melis, C.; Bussi, G.; Lummis, S. C.; Molteni, C., Trans– Cis Switching Mechanisms in Proline Analogues and Their Relevance for the Gating of the 5-Ht3 Receptor. *The Journal of Physical Chemistry B* **2009**, *113* (35), 12148-12153.
270. Corradi, J.; Bouzat, C., Unraveling Mechanisms Underlying Partial Agonism in 5-Ht_{3a} Receptors. *Journal of Neuroscience* **2014**, *34* (50), 16865-16876.
271. Hénin, J.; Salari, R.; Murlidaran, S.; Brannigan, G., A Predicted Binding Site for Cholesterol on the Gabaa Receptor. *Biophysical Journal* **2014**, *106* (9), 1938-1949.
272. Yoluk, Ö.; Brömstrup, T.; Bertaccini, E. J.; Trudell, J. R.; Lindahl, E., Stabilization of the Glucl Ligand-Gated Ion Channel in the Presence and Absence of Ivermectin. *Biophysical Journal* **2013**, *105* (3), 640-647.
273. Gicheru, Y. W.; Basak, S.; Chakrapani, S., Structural Mechanisms Underlying Pufa Modulation in Pentameric Ligand Gated Ion Channels. *Biophysical Journal* **2017**, *112* (3), 320a.
274. Basak, S.; Schmandt, N.; Gicheru, Y.; Chakrapani, S., Crystal Structure and Dynamics of a Lipid-Induced Potential Desensitized-State of a Pentameric Ligand-Gated Channel. *Elife* **2017**, *6*, e23886.
275. Burzomato, V.; Beato, M.; Groot-Kormelink, P. J.; Colquhoun, D.; Sivilotti, L. G., Single-Channel Behavior of Heteromeric A1 β Glycine Receptors: An Attempt to Detect a Conformational Change before the Channel Opens. *Journal of Neuroscience* **2004**, *24* (48), 10924-10940.
276. Lape, R.; Colquhoun, D.; Sivilotti, L. G., On the Nature of Partial Agonism in the Nicotinic Receptor Superfamily. *Nature* **2008**, *454* (7205), 722.
277. Kudryashev, M.; Castaño-Díez, D.; Deluz, C.; Hassaine, G.; Grasso, L.; Graf-Meyer, A.; Vogel, H.; Stahlberg, H., The Structure of the Mouse Serotonin 5-Ht3 Receptor in Lipid Vesicles. *Structure* **2016**, *24* (1), 165-170.
278. Hamill, O. P.; Marty, A.; Neher, E.; Sakmann, B.; Sigworth, F., Improved Patch-Clamp Techniques for High-Resolution Current Recording from Cells and Cell-Free Membrane Patches. *Pflügers Archiv* **1981**, *391* (2), 85-100.
279. VAN HOOFT, J. A.; Vijverberg, H. P., Phosphorylation Controls Conductance of 5-Ht3 Receptor Ligand-Gated Ion. *Receptors and Channels* **1995**, *3*, 7-12.

280. Alghalayini, A.; Garcia, A.; Berry, T.; Cranfield, C. G., The Use of Tethered Bilayer Lipid Membranes to Identify the Mechanisms of Antimicrobial Peptide Interactions with Lipid Bilayers. *Antibiotics* **2019**, *8* (1), 12.
281. Giess, F.; Friedrich, M. G.; Heberle, J.; Naumann, R. L.; Knoll, W., The Protein-Tethered Lipid Bilayer: A Novel Mimic of the Biological Membrane. *Biophysical Journal* **2004**, *87* (5), 3213-3220.
282. Knoll, W.; Frank, C.; Heibel, C.; Naumann, R.; Offenhäusser, A.; Rühle, J.; Schmidt, E.; Shen, W.; Sinner, A., Functional Tethered Lipid Bilayers. *Reviews in Molecular Biotechnology* **2000**, *74* (3), 137-158.
283. Cranfield, C. G.; Cornell, B. A.; Grage, S. L.; Duckworth, P.; Carne, S.; Ulrich, A. S.; Martinac, B., Transient Potential Gradients and Impedance Measures of Tethered Bilayer Lipid Membranes: Pore-Forming Peptide Insertion and the Effect of Electroporation. *Biophysical Journal* **2014**, *106* (1), 182-189.
284. Valincius, G.; Meškauskas, T.; Ivanauskas, F., Electrochemical Impedance Spectroscopy of Tethered Bilayer Membranes. *Langmuir* **2011**, *28* (1), 977-990.

Publications, Awards, and Presentations

Accepted Publications

1. Guros, N.B., Klauda, J.B., and Balijepalli, A. The Role of Lipid Interactions in Simulations of the alpha-hemolysin Ion Channel-forming Toxin. *Biophysical Journal* **2018**, 115: 1720–1730.
2. Guros, N.B., Le, S.T., Zhang, S., Sperling, B., Klauda, J.B., and Balijepalli, A., Robust Fabrication of Transistor Arrays from Large-Area Monolayer MoS₂. *ACS Applied Materials and Interfaces*. **2019**, 11, 16683–16692.

Submitted Manuscripts

1. Le, S.T., Guros, N.B., Bruce, R.C., Cardone, A., Niranjana, A.D., Zhang, S., Klauda, J.B., Pant, H.C., Richter, C.A., and Balijepalli, A. Quantum Capacitance-Limited MoS₂ Biosensors Enable Remote Label-Free Enzyme Measurements. **2019**. Royal Society of Chemistry (*Accepted*).
2. Guros, N.B., Klauda, J.B., and Balijepalli, A., Microsecond Timescale Simulations Demonstrate 5-HT mediated Pre-activation of the 5-HT_{3A} Serotonin Receptor (*PNAS*)
3. Evans, R.M., Guros, N.B., Balijepalli, A., Kearsley, A.J. Transport Phenomena in Biological Field Effect Transistors. *Journal of the American Mathematical Society*.

Manuscripts in Preparation

1. Guros, N.B., Klauda, J.B., and Balijepalli, A., Microsecond Timescales of 5-HT_{3A} desensitization (Target: *Biophysical Journal*)
2. Guros, N.B., Le, S.T., Sperling, B., Klauda, J.B., and Balijepalli, A. Comparison of Liquid-gated and Solid-state Monolayer MoS₂ Field-effect Transistors. (Target: *ACS Nano*)

Awards

1. The Graduate Department of Chemical and Biomolecular Engineering's Outstanding Research Assistant (2018 – 2019)
2. 2nd place winner of the Dean's Ph.D. Competition (2019)
3. Vice President of the Department of Chemical and Biomolecular Engineering Graduate Association (2015)

Conference Presentations

1. Le, S.T., Guros, N.B., Bruce, R.C., Cardone, A., Niranjana, A.D., Zhang, S., Klauda, J.B., Pant, H.C., Richter, C.A., and Balijepalli, A., *Label-Free Enzyme Activity Measurements with Quantum-Limited Biosensors* – Biophysical Society (2019), Baltimore, MD
2. Guros, N.B., Klauda, J.B., and Balijepalli, A., *Microsecond-Scale Molecular Dynamics Simulations Reveal Desensitized Behavior of 5HT3* – Biophysical Society (2019), Baltimore, MD
3. Le, S.T., Guros, N.B., Bruce, R.C., Cardone, A., Niranjana, A.D., Zhang, S., Klauda, J.B., Pant, H.C., Richter, C.A., and Balijepalli, A., *2D-MoS2 Field Effect Transistor Enable Remote Label-Free Enzyme Measurements* – American Physical Society (2019), Boston, MA
4. Le, S.T., Guros, N.B., Bruce, R.C., Cardone, A., Niranjana, A.D., Zhang, S., Klauda, J.B., Pant, H.C., Richter, C.A., and Balijepalli, A., *Real-time and label-free electronic measurements of enzyme activity and kinetics* – Society for Neuroscience (2018), San Diego, CA
5. Guros, N.B., Klauda, J.B., and Balijepalli, A., *Fabrication of 2D Field Effect Transistors and Measurements of Enzymatic Activity* – American Vacuum Society (2018), Gaithersburg, MD
6. Guros, N.B., Klauda, J.B., and Balijepalli, A., *Analyzing the effects of membrane lipid type on transmembrane proteins (α HL and 5-HT3) using molecular dynamics simulations* – Biophysical Society (2018), San Francisco, CA
7. Le, S.T., Guros, N.B., Bruce, R.C., Cardone, A., Niranjana, A.D., Zhang, S., Klauda, J.B., Pant, H.C., Richter, C.A., and Balijepalli, A., *Measurements of Enzyme Activity with Field Effect Transistors* – Biophysical Society (2018), San Francisco, CA
8. Le, S.T., Guros, N.B., Bruce, R.C., Cardone, A., Niranjana, A.D., Zhang, S., Klauda, J.B., Pant, H.C., Richter, C.A., and Balijepalli, A., *Super Nernstian pH sensing using ionic liquid gated 2-dimensional transition metal dichalcogenide transistors* – American Physical Society (2018), Los Angeles, CA
9. Guros, N.B., Klauda, J.B., and Balijepalli, A., *The Importance of Equilibration Time, Structure Truncation, and Membrane Lipid Type in Molecular Dynamics Simulations of Ion Channels* – American Chemical Society (2017), Washington, D.C.

Conference Presentations (continued)

10. Guros, N.B., Klauda, J.B., and Balijepalli, A., *Measuring Biomolecular Interactions with Transistors* – Researchfest (2017), University of Maryland, College Park, MD
11. Guros, N.B., Klauda, J.B., and Balijepalli, A., *The Importance of Equilibration Time, Structure Truncation, and Membrane Lipid Type in Molecular Dynamics Simulations of Ion Channels* – Computational Biophysics Symposium (2017), Baltimore, MD
12. Guros, N.B., Klauda, J.B., and Balijepalli, A., *Characterizing the α -hemolysin Nanopore and 5HT3 Receptor Gating Using Molecular Dynamics Simulations* – International Conference on Molecular Simulation (2016), Shanghai, China
Best Poster Award Winner
13. Guros, N.B., Klauda, J.B., and Balijepalli, A., *Characterizing the α -hemolysin Nanopore and 5HT3 Receptor Gating Using Molecular Dynamics Simulations* – Delaware Membrane Protein Symposium (2016), Newark, DE
14. Guros, N.B., Klauda, J.B., and Balijepalli, A., *Characterizing the α -hemolysin Nanopore and 5HT3 Receptor Gating Using Molecular Dynamics Simulations* – Biophysical Society (2016), Los Angeles, CA